# CONTROL OF PRESYNAPTIC FUNCTION BY AXONAL DYNAMICS

EDITED BY: Shin-ya Kawaguchi and Federico F. Trigo
PUBLISHED IN: Frontiers in Cellular Neuroscience and
Frontiers in Synaptic Neuroscience

frontiers Research Topics

**Frontiers eBook Copyright Statement**

The copyright in the text of individual articles in this eBook is the property of their respective authors or their respective institutions or funders. The copyright in graphics and images within each article may be subject to copyright of other parties. In both cases this is subject to a license granted to Frontiers.

The compilation of articles constituting this eBook is the property of Frontiers.

Each article within this eBook, and the eBook itself, are published under the most recent version of the Creative Commons CC-BY licence. The version current at the date of publication of this eBook is CC-BY 4.0. If the CC-BY licence is updated, the licence granted by Frontiers is automatically updated to the new version.

When exercising any right under the CC-BY licence, Frontiers must be attributed as the original publisher of the article or eBook, as applicable.

Authors have the responsibility of ensuring that any graphics or other materials which are the property of others may be included in the CC-BY licence, but this should be checked before relying on the CC-BY licence to reproduce those materials. Any copyright notices relating to those materials must be complied with.

Copyright and source acknowledgement notices may not be removed and must be displayed in any copy, derivative work or partial copy which includes the elements in question.

All copyright, and all rights therein, are protected by national and international copyright laws. The above represents a summary only. For further information please read Frontiers' Conditions for Website Use and Copyright Statement, and the applicable CC-BY licence.

ISSN 1664-8714
ISBN 978-2-88963-411-8
DOI 10.3389/978-2-88963-411-8

## About Frontiers

Frontiers is more than just an open-access publisher of scholarly articles: it is a pioneering approach to the world of academia, radically improving the way scholarly research is managed. The grand vision of Frontiers is a world where all people have an equal opportunity to seek, share and generate knowledge. Frontiers provides immediate and permanent online open access to all its publications, but this alone is not enough to realize our grand goals.

## Frontiers Journal Series

The Frontiers Journal Series is a multi-tier and interdisciplinary set of open-access, online journals, promising a paradigm shift from the current review, selection and dissemination processes in academic publishing. All Frontiers journals are driven by researchers for researchers; therefore, they constitute a service to the scholarly community. At the same time, the Frontiers Journal Series operates on a revolutionary invention, the tiered publishing system, initially addressing specific communities of scholars, and gradually climbing up to broader public understanding, thus serving the interests of the lay society, too.

## Dedication to Quality

Each Frontiers article is a landmark of the highest quality, thanks to genuinely collaborative interactions between authors and review editors, who include some of the world's best academicians. Research must be certified by peers before entering a stream of knowledge that may eventually reach the public - and shape society; therefore, Frontiers only applies the most rigorous and unbiased reviews.
Frontiers revolutionizes research publishing by freely delivering the most outstanding research, evaluated with no bias from both the academic and social point of view. By applying the most advanced information technologies, Frontiers is catapulting scholarly publishing into a new generation.

## What are Frontiers Research Topics?

Frontiers Research Topics are very popular trademarks of the Frontiers Journals Series: they are collections of at least ten articles, all centered on a particular subject. With their unique mix of varied contributions from Original Research to Review Articles, Frontiers Research Topics unify the most influential researchers, the latest key findings and historical advances in a hot research area! Find out more on how to host your own Frontiers Research Topic or contribute to one as an author by contacting the Frontiers Editorial Office: researchtopics@frontiersin.org

# CONTROL OF PRESYNAPTIC FUNCTION BY AXONAL DYNAMICS

Topic Editors:
**Shin-ya Kawaguchi,** Kyoto University, Japan
**Federico F. Trigo,** Université Paris Descartes, France; Instituto de Investigaciones Biológicas Clemente Estable (IIBCE), Uruguay

**Citation:** Kawaguchi, S., Trigo, F. F., eds. (2020). Control of Presynaptic Function by Axonal Dynamics. Lausanne: Frontiers Media SA. doi: 10.3389/978-2-88963-411-8

# Table of Contents

frontiers in Cellular Neuroscience

EDITORIAL
published: 06 December 2019
doi: 10.3389/fncel.2019.00543

# Editorial: Control of Presynaptic Function by Axonal Dynamics

*Federico F. Trigo* [1,2]* *and Shin-ya Kawaguchi* [3]*

[1] CNRS UMR8003, SPPIN Laboratory, Cerebellar Neurophysiology Group, Faculté des Sciences Fondamentales et Biomédicales, Université de Paris, Paris, France, [2] Departamento de Neurofisiología Celular y Molecular, Instituto de Investigaciones Biológicas Clemente Estable, Montevideo, Uruguay, [3] Department of Biophysics, Graduate School of Science, Kyoto University, Kyoto, Japan

**Keywords: axonal dynamics, synaptic release, action potential (AP), imaging, patch-clamp**

## Editorial on the Research Topic

## Control of Presynaptic Function by Axonal Dynamics

Neurons are highly polarized cells: they possess a dendritic arbor, which is classically considered the input compartment of the cell; a cellular body, where incoming information is integrated; the axon, which is a transmission compartment and classically considered as a conducting line responsible for action potential (AP) propagation; and axonal varicosities, which are the output compartments and where transmitter release occurs. Axons of mammalian brain neurons are highly diverse: some are myelinated and others unmyelinated, some are only a few hundred microns long and others more than 1 m long, some are highly branched and others almost unbranched, etc. The same is true for the presynaptic terminals: some are extremely big, packing hundreds of individual synaptic release sites, while others possess only a single active zone. This morphological diversity is accompanied by molecular or subcellular diversity. The distribution and density of ion channels vary among different axonal locations: some are highly concentrated in the AIS (axon initial segment; Kole et al., 2007), for example, and others in presynaptic terminals (Rowan et al., 2016), which also possess a variety of receptors for different neurotransmitters and/or neuromodulators.

Although it is safe to assume that at some level all axons behave similarly, ignoring axonal diversity would run the risk of oversimplifying axonal function and misunderstanding axonal physiology. However, studying the axonal compartment and presynaptic terminals is often challenging because of the features that were already mentioned: axon and presynaptic terminals are usually small structures (in the sub-micrometer range), they function extremely rapidly, and they have a complex morphology. Understanding the physiology of these tiny structures therefore requires the development of new techniques and the contribution of different methodologies.

Numerous reviews have been published in the last decade highlighting the computational capabilities of the axon (Debanne, 2004; Debanne et al., 2011), notably in terms of its effects on transmitter release. The scope of this "Research Topic" is to bring together different researchers studying the axonal compartment and presynaptic terminals in order to document recent progress and, more importantly, to highlight that the function of the axon is more complicated than previously thought and that much remains to be done in order to understand axonal function.

Two of the reviews treat the rapidly growing topic of axonal analog signaling—soma-axon interactions in the subthreshold voltage range. In the CNS, information transfer is classically considered to be digital, but subthreshold voltage signals can propagate along long distances and they can affect neurotransmitter release by modulating presynaptic voltage-gated channels. In one review, Zbili and Debanne describe analog signaling both from a historical and from a physiological perspective, as well as analog signaling mechanisms and their potential benefits for

OPEN ACCESS

***Edited and reviewed by:***
*Arianna Maffei,*
*Stony Brook University, United States*

***Correspondence:**
*Federico F. Trigo*
*federico.trigo@parisdescartes.fr*
*Shin-ya Kawaguchi*
*kawaguchi.shinya.7m@kyoto-u.ac.jp*

***Specialty section:***
*This article was submitted to Cellular Neurophysiology, a section of the journal Frontiers in Cellular Neuroscience*

***Received:*** *21 October 2019*
***Accepted:*** *22 November 2019*
***Published:*** *06 December 2019*

***Citation:***
*Trigo FF and Kawaguchi S (2019) Editorial: Control of Presynaptic Function by Axonal Dynamics. Front. Cell. Neurosci. 13:543. doi: 10.3389/fncel.2019.00543*

network computation. In the other review, Trigo discusses another, less-studied form of analog transmission, whereby subthreshold voltage signals backpropagate from the axon toward the soma. This so-called antidromic analog transmission challenges the dynamic polarization theory of Ramón y Cajal, according to which information propagates unidirectionally from dendrites to soma, and from soma to axon.

In another study, Yang et al. perform electrophysiological recordings from the soma and axonal blebs of the AIS in midbrain dopaminergic neurons (substantia nigra pars compacta and ventral tegmental area) and compare the biophysical properties of voltage-gated sodium channels in the two sites. Although the general properties of axonal and somatic channels are similar, axonal channels inactivate at more hyperpolarized potentials and more slowly than somatic channels. Surprisingly, associated immunostaining results show that the AIS of dopaminergic cells only expresses the Nav1.2 sodium channel subunit, and not the other typical AIS subunits, Nav 1.1 and 1.6. These results indicate that in some cells, like the dopaminergic cells studied here by Yang et al., the exclusive expression of the Nav1.2 subunit ensures stable AP generation at the AIS.

The AP waveform at the release site is a key factor for neuronal communication because it influences neurotransmitter release and synaptic plasticity. Apart from the AP amplitude and time course, the after-spike potential (the membrane potential, either depolarizing or hyperpolarizing, after the AP) may have a strong impact on axonal excitability. Recently, Zorrilla de San Martin et al. (2017) showed that the after-spike depolarizations induced by the activation of axonal $GABA_A$ auto-receptors in Purkinje cells increase the presynaptic $Ca^{2+}$ current and hence release, and have a dramatic effect on short-term plasticity. In a "Theory and Hypothesis" article, Raastad examines the after-spike potential in CNS neuronal thin axons in terms of its mechanisms and functional implications. By simulating such a depolarizing after-spike potential in hippocampal mossy fibers, Kamiya demonstrates in another article the substantial contribution of the passive spread of the AP itself into neighboring axonal regions to the after-spike depolarization.

In addition to the electrical properties of the axon, the mechanisms that control the intracellular $Ca^{2+}$ by internal buffers tightly control transmitter release from presynaptic terminals. In a theoretical paper, Nakamura studies the effects of the calcium chelator EGTA on transmitter release. EGTA has been widely used by neurophysiologists to estimate the coupling distance between the calcium entry site (calcium channels) and the calcium sensor in presynaptic terminals. Contrary to what is usually expected, in the close proximity of the calcium channel EGTA can affect release if the sensor is not saturated, as may happen for brief calcium influxes like those induced by APs. Nakamura's paper emphasizes the importance of measuring the AP characteristics with direct axonal recordings.

In an elegant study, Bolshakov et al. describe the role of a $Ca^{2+}$ binding protein, calretinin, on synaptic transmission with a combination of molecular biology and electrophysiology methods. The authors infect newborn pups' somatosensory neurons with an AAV vector in order to exogenously induce calretinin expression in cells that do not normally express the protein. They then compare synaptic release in infected and non-infected cells. With this approach Bolshakov et al. show that calretinin changes short-term plasticity in cortical synapses.

Miki discusses how Variance to Mean analysis is used to understand synaptic release mechanisms, particularly at high frequency repetitive stimulations. In his study, Miki explains how fluctuations in the number of released vesicles per AP and in the cumulative number of released vesicles during an AP train can be used to distinguish between different docking (or release) site models. In his perspective, Miki also discusses how this method could be complemented by techniques that do not rely on electrophysiological recordings to assess release but rather on direct visualization of synaptic vesicle exocytosis and of vesicle movements, including super-resolution imaging (see, for example, the study of Funahashi et al. in this issue and also Midorikawa and Sakaba, 2017) and electron microscopy (Kusick et al., 2018) techniques.

Two of the research papers describe techniques for high resolution visualization of the dynamics of synaptic vesicle fusion. In an original research article, Funahashi et al. induce the formation of active zone like structures on a glass coverslip in order to image the fusion of synaptic vesicles with total internal reflection microscopy, a super-resolution technique that uses the evanescent field of an angled laser beam. This methodological tour de force allowed the authors to image single vesicle fusion and to follow vesicular movements, and will certainly be used in the future to study presynaptic physiology. In the second technical paper, Dobson et al. describe in detail a simple photoconversion setup that allows seeing the ultrastructure of presynaptic terminals with the high resolution of an electron microscope.

As already mentioned, axonal studies require the development of new techniques. Panzera and Hoppa review in detail the use of genetically-encoded voltage indicators for the study of axonal physiology. Imaging the axon with voltage indicators allows recording from multiple axonal locations simultaneously, fulfilling a goal that cannot be attained with electrophysiological techniques. Although voltage-sensitive fluorescent proteins lag behind electrophysiological techniques in terms of temporal resolution, their development is rapidly advancing and they will probably outcompete electrophysiological methods not only for axon studies but for neurophysiology in general.

Finally, Kawaguchi reviews the myriad of factors that may influence transmitter release from small CNS presynaptic terminals, notably by describing recent literature based on direct patch-clamp recordings from axonal varicosities. This review nicely summarizes this topic by highlighting the complex interactions existing between the axon and its synaptic terminals and how these interactions influence neuronal output and plasticity.

The aim of this "Research Topic" was to highlight recent advances in the field of axonal function, both from the physiological and methodological perspectives. More importantly, we intended to attract the reader's attention about the fact that much remains to be done in order to understand axonal function. We hope we have fulfilled this goal. We would

like to thank all the contributing authors and hope the readers will enjoy diving into the study of axonal function.

## AUTHOR CONTRIBUTIONS

All authors listed have made a substantial, direct and intellectual contribution to the work, and approved it for publication.

## FUNDING

This work was supported by the JCJC ANR grant (ANR-17-CE16-0011-01) to FT, the KAKENHI grants from the JSPS/MEXT, Japan to SK (18H02527 and 19H04750), the Naito Science Foundation to SK, the Takeda Science Foundation to SK.

## REFERENCES

Debanne, D. (2004). Information processing in the axon. *Nat. Rev. Neurosci.* 5, 304–316. doi: 10.1038/nrn1397

Debanne, D., Campanac, E., Bialowas, A., Carlier, E., and Alcaraz, G. (2011). Axon physiology. *Physiol. Rev.* 91, 555–602. doi: 10.1152/physrev.00048.2009

Kole, M. H., Letzkus, J. J., and Stuart, G. J. (2007). Axon initial segment Kv1 channels control axonal action potential waveform and synaptic efficacy. *Neuron* 55, 633–47. doi: 10.1016/j.neuron.2007.07.031

Kusick, G. F., Chin, M., Lippmann, K., Adula, K. P., Davis, M. W., Jorgensen, E. W., et al. (2018). Synaptic vesicles undock and then transiently dock after an action potential. *bioRxiv [Preprint]*. doi: 10.1101/509216

Midorikawa, M., and Sakaba, T. (2017). Kinetics of releasable synaptic vesicles and their plastic changes at hippocampal mossy fiber synapses. *Neuron* 96, 1033–1040.e3. doi: 10.1016/j.neuron.2017.10.016

Rowan, M. J., DelCanto, G., Yu, J. J., Kamasawa, N., and Christie, J. M. (2016). Synapse-level determination of action potential duration by K(+) channel clustering in axons. *Neuron* 91, 370–383. doi: 10.1016/j.neuron.2016.05.035

Zorrilla de San Martin, J., Trigo, F. F., and Kawaguchi, S.-Y. (2017). Axonal GABAA receptors depolarize presynaptic terminals and facilitate transmitter release in cerebellar Purkinje cells. *J. Physiol.* 595, 7477–7493. doi: 10.1113/JP275369

**Conflict of Interest:** The authors declare that the research was conducted in the absence of any commercial or financial relationships that could be construed as a potential conflict of interest.

*Copyright © 2019 Trigo and Kawaguchi. This is an open-access article distributed under the terms of the Creative Commons Attribution License (CC BY). The use, distribution or reproduction in other forums is permitted, provided the original author(s) and the copyright owner(s) are credited and that the original publication in this journal is cited, in accordance with accepted academic practice. No use, distribution or reproduction is permitted which does not comply with these terms.*

frontiers in Cellular Neuroscience

ORIGINAL RESEARCH
published: 23 May 2018
doi: 10.3389/fncel.2018.00140

# Visualization of Synchronous or Asynchronous Release of Single Synaptic Vesicle in Active-Zone-Like Membrane Formed on Neuroligin-Coated Glass Surface

*Junichiro Funahashi, Hiromitsu Tanaka and Tomoo Hirano**

*Department of Biophysics, Graduate School of Science, Kyoto University, Kyoto, Japan*

Fast repetitive synaptic transmission depends on efficient exocytosis and retrieval of synaptic vesicles around a presynaptic active zone. However, the functional organization of an active zone and regulatory mechanisms of exocytosis, endocytosis and reconstruction of release-competent synaptic vesicles have not been fully elucidated. By developing a novel visualization method, we attempted to identify the location of exocytosis of a single synaptic vesicle within an active zone and examined movement of synaptic vesicle protein synaptophysin (Syp) after exocytosis. Using cultured hippocampal neurons, we induced formation of active-zone-like membranes (AZLMs) directly adjacent and parallel to a glass surface coated with neuroligin, and imaged Syp fused to super-ecliptic pHluorin (Syp-SEP) after its translocation to the plasma membrane from a synaptic vesicle using total internal reflection fluorescence microscopy (TIRFM). An AZLM showed characteristic molecular and functional properties of a presynaptic active zone. It contained active zone proteins, cytomatrix at the active zone-associated structural protein (CAST), Bassoon, Piccolo, Munc13 and RIM, and showed an increase in intracellular $Ca^{2+}$ concentration upon electrical stimulation. In addition, single-pulse stimulation sometimes induced a transient increase of Syp-SEP signal followed by lateral spread in an AZLM, which was considered to reflect an exocytosis event of a single synaptic vesicle. The diffusion coefficient of Syp-SEP on the presynaptic plasma membrane after the membrane fusion was estimated to be 0.17–0.19 $\mu m^2/s$, suggesting that Syp-SEP diffused without significant obstruction. Synchronous exocytosis just after the electrical stimulation tended to occur at multiple restricted sites within an AZLM, whereas locations of asynchronous release occurring later after the stimulation tended to be more scattered.

**Keywords: active zone, total internal reflection fluorescence microscopy, neuroligin, synaptic vesicle, synaptophysin, asynchronous release, exocytosis**

**Abbreviations:** AZLM, active-zone-like membrane; CAST, cytomatrix at the active zone-associated structural protein; CNQX, 6-cyano-7-nitroquinoxaline-2,3-dione; NND, nearest neighbor distance; PBS, phosphate buffered saline; SEP, super-ecliptic pHluorin; Syp, synaptophysin; TIRFM, total internal reflection fluorescence microscopy.

OPEN ACCESS

***Edited by:***
*Federico F. Trigo, Université Paris Descartes, France*

***Reviewed by:***
*Mitsuharu Midorikawa, Tokyo Women's Medical University, Japan*
*Alain Marty, Université Paris Descartes, France*

****Correspondence:***
*Tomoo Hirano*
*thirano@neurosci.biophys.kyoto-u.ac.jp*

***Received:*** *05 April 2018*
***Accepted:*** *07 May 2018*
***Published:*** *23 May 2018*

***Citation:***
*Funahashi J, Tanaka H and Hirano T (2018) Visualization of Synchronous or Asynchronous Release of Single Synaptic Vesicle in Active-Zone-Like Membrane Formed on Neuroligin-Coated Glass Surface. Front. Cell. Neurosci. 12:140. doi: 10.3389/fncel.2018.00140*

## INTRODUCTION

Synaptic vesicles are exocytosed at a presynaptic active zone immediately after arrival of an action potential, and their exocytosis can be repeated at high frequencies. Efficient retrieval mechanisms of release-competent synaptic vesicles support repetitive synaptic transmission (Haucke et al., 2011; Wu et al., 2014; Kononenko and Haucke, 2015). Previous studies have shown characteristics of exocytosis, endocytosis and synaptic vesicle retrieval using electrophysiological membrane capacitance measurement (von Gersdorff and Matthews, 1994; Yamashita et al., 2005; He et al., 2006) and fluorescence imaging (Miesenböck et al., 1998; Zenisek et al., 2000; Wienisch and Klingauf, 2006; Kavalali and Jorgensen, 2014). Most studies used repetitive activation of presynaptic neurons to improve the signal to noise ratio of data by increasing the total number of exocytosed synaptic vesicles, although some studies reported phenomena reflecting exocytosis of a single synaptic vesicle (Zenisek et al., 2000; Aravanis et al., 2003; Gandhi and Stevens, 2003; Balaji and Ryan, 2007; Chen et al., 2008; Zhang et al., 2009; Midorikawa and Sakaba, 2015; Tang et al., 2016; Maschi and Klyachko, 2017; Sakamoto et al., 2018).

The relative amounts of membrane proteins are presumed to be constant among synaptic vesicles in a presynaptic terminal (Takamori et al., 2006). After full-fusion exocytosis, synaptic vesicle proteins might remain clustered on the cell surface membrane so that they can be endocytosed as a package (Willig et al., 2006; Opazo et al., 2010), or they might be once dispersed and then gathered either on the cell membrane or on endosomal membrane to form release-competent vesicles (Wienisch and Klingauf, 2006; Gimber et al., 2015). However, the dynamics of synaptic vesicle proteins after a single exocytosis event have remained enigmatic, partly because of the limited spatiotemporal resolution of imaging data. Clarification of synaptic vesicle protein movement on the plasma membrane after exocytosis would provide critical information to reveal these dynamics.

Recently, the location of exocytosis of a synaptic vesicle has been studied intensively, and the existence of multiple release sites within an active zone has been suggested (Tang et al., 2016; Maschi and Klyachko, 2017; Miki et al., 2017; Sakamoto et al., 2018). Synaptic vesicle exocytosis occurs not only immediately after an action potential (synchronous release) but also tens or hundreds of msec after an action potential (asynchronous release). The $Ca^{2+}$-dependence and molecular regulation mechanisms have been suggested to differ between the synchronous and asynchronous releases (Bacaj et al., 2013; Kaeser and Regehr, 2014). Relatively slow $Ca^{2+}$ chelator EGTA preferentially suppresses asynchronous release but not synchronous release, suggesting that asynchronous release locations are more distant from the $Ca^{2+}$ source than synchronous release sites. Thus, synchronous and asynchronous release locations could be differentially distributed within an active zone, but this has not been directly demonstrated.

We have addressed these unsettled questions about presynaptic mechanisms by developing a new visualization method with a high signal to noise ratio and high spatiotemporal resolution using total internal reflection fluorescence microscopy (TIRFM). We previously developed a method to induce formation of postsynaptic-like membrane on a glass surface coated with presynaptic cell-adhesion molecule neurexin, and analyzed exocytosis and endocytosis of glutamate receptor tagged with super-ecliptic pHluorin (SEP, a pH-sensitive variant of green fluorescent protein, Miesenböck et al., 1998) around the postsynaptic-like membrane (Tanaka and Hirano, 2012; Tanaka et al., 2014; Fujii et al., 2017). These studies prompted us to apply a similar method for analyses of presynaptic vesicle exocytosis. Presynaptic neurexin binds to postsynaptic neuroligin, and the interaction is involved in synaptic formation, maturation and/or maintenance. It has been demonstrated that the presence of neurexin or neuroligin on non-neuronal cell membrane can induce postsynaptic or presynaptic membrane differentiation in a nearby neurite, respectively (Scheiffele et al., 2000; Graf et al., 2004). Here, we report formation of a presynaptic active-zone-like membrane (AZLM) on a glass surface coated with neuroligin in a hippocampal neuronal culture preparation, and then show results of fluorescence imaging studies on the dynamics of a synaptic vesicle protein synaptophysin (Syp) after a single exocytosis event, and on the locations of synchronous and asynchronous releases in an AZLM.

## MATERIALS AND METHODS

### Plasmids

Expression vectors of neuroligin-Fc and HA-neurexin were prepared as described previously (Scheiffele et al., 2000; Chih et al., 2006; Pettem et al., 2013) with minor modifications. Complementary DNA encoding the extracellular region (amino acids 1–675) of neuroligin 1 (−A +B) was fused to the N-terminal of human immunoglobulin-Fc region in pCAGplayII expression vector (Kawaguchi and Hirano, 2006). Neurexin 1β (−4) cDNA without its signal sequence (amino acids 1–47) was fused to the C-terminal of HA tag following a signal sequence in pDisplay expression vector (Invitrogen). An expression vector of EGFP was obtained from Clontech. EGFP-cytomatrix at the active zone-associated structural protein (CAST) was a gift from Dr. T. Ohtsuka (Yamanashi Univ.), and CAST was inserted into pTagRFPt-C vector (Shaner et al., 2008) modified from pTagRFP-C vector (Evrogen) to form TagRFPt-tagged CAST (CAST-RFP) expression vector. GCaMP6f was a gift from Dr. D.S. Kim (Chen et al., 2013; Addgene plasmid #40755). The expression vector of Syp-SEP was prepared as described previously (Granseth et al., 2006) with the following modification. The enhancer region of the CMV promoter was truncated (base pairs −300 to −67 relative to the transcription start site (+1) were deleted; Isomura et al., 2004) to reduce the expression level.

### Coating of Glass With Neuroligin

Glass coverslips coated with Fc-tagged neuroligin were prepared using methods similar to those in previous studies (Tanaka and Hirano, 2012; Tanaka et al., 2014), except that neuroligin-Fc

was used instead of neurexin-Fc. In brief, neuroligin-Fc was prepared from transfected HEK293 cells (RRID:CVCL_0045) using nProtein A Sepharose (GE Healthcare). Glass coverslips were incubated with 43 μM biotinylated BSA (Thermo Scientific) in buffer A containing 100 mM KCl, 5 mM $MgCl_2$, 25 mM HEPES, pH adjusted to 7.4 with KOH overnight at 4°C, followed by incubation with 17 μM streptavidin (WAKO) in buffer A for 1 h at room temperature (20–25°C). The coverslips were then incubated with biotin-conjugated anti-human IgG (1:100, Jackson ImmunoResearch) in buffer A for 1 h, followed by incubation with 3–5 μg/ml neuroligin-Fc in buffer A for 5 h. The coverslips were washed three times with buffer A after each incubation. Finally, the coverslips were incubated with 0.2 mg/ml poly-D-lysine (Sigma) for 12–48 h at 37°C.

## Primary Neuronal Culture and Transfection

All experimental procedures were carried out in accordance with guidelines laid down by the National Institutes of Health of USA and Kyoto University, and approved by the local committee for handling experimental animals in the Graduate School of Science, Kyoto University.

Hippocampal neuronal cultures were prepared from E18–20 Wistar rats (RRID:RGD_13508588) and grown on neuroligin-Fc-coated coverslips using methods similar to those described in a previous report except that Neurobasal-Electro rather than Neurobasal was used as the culture medium (Tanaka and Hirano, 2012). Lipofectamine 2000 (Invitrogen) was used to transfect plasmids into neurons at 9–10 DIV, and all experiments were performed 2 days after transfection.

## Immunocytochemistry

Cultured neurons were fixed with 4% paraformaldehyde and 4% sucrose in phosphate buffered saline (PBS) for 5 min at room temperature, and washed with PBS three times. Neurons were permeabilized and non-specific binding of antibodies was blocked with 0.2% Triton X-100 and 5% goat serum in PBS, respectively. Then, the preparation was incubated with primary antibody overnight at 4°C, and with secondary antibody for 1 h at room temperature. Images were acquired using TIRFM. Antibodies used here were anti-Bassoon (1:1000, Enzo; RRID:AB_10618753); anti-Piccolo (1:1000, Synaptic Systems; RRID:AB_887759); anti-Munc13 (1:1000, Synaptic Systems; RRID:AB_887733); anti-RIM (RAB3A-interacting molecule) 1/2 (1:1000, Synaptic Systems; RRID:AB_887775); goat anti-mouse or goat anti-rabbit IgG conjugated with Alexa 488 (Invitrogen; RRID:AB_138404 or AB_2576217, respectively).

## Live-Cell Imaging With TIRFM

TIRFM imaging was performed using an inverted fluorescence microscopy IX71 (Olympus) equipped with ×150/1.45 TIRFM objective lens (Olympus), ×1.6 intermediate lens (Olympus), 488 nm laser (85-BCD-020, Melles Griot, Albuquerque, NM), 561 nm laser (Sapphire 561LP, Coherent, Santa Clara, CA) and EM-CCD camera (iXon+; Andor), yielding a final effective pixel size of 67 nm. The electrical field stimulation (1 ms, 20–30 V/cm) was applied through platinum electrodes as described previously (Tanaka et al., 2014). All live-cell imaging experiments were performed at room temperature in extracellular imaging solution (119 mM NaCl, 2.5 mM KCl, 4 mM $CaCl_2$, 1 mM $MgCl_2$, 30 mM glucose, 25 mM HEPES; adjusted to pH 7.4 with NaOH). The solution also contained 10 μM 6-cyano-7-nitroquinoxaline-2,3-dione (CNQX) to inhibit AMPA-type glutamate receptor.

## $Ca^{2+}$ Imaging

For $Ca^{2+}$ imaging, neurons were transfected with GCaMP6f (Chen et al., 2013), CAST-RFP and HA-neurexin, and observed with TIRFM. CAST-RFP images were acquired in 35 × 35 pixels surrounding an AZLM, and the GCaMP signal change induced by 100 Hz, five electrical pulses stimulation was recorded for 1 s. An image was recorded for 35 ms exposure time, and acquisition of the following image started after 4 ms transfer time. GCaMP fluorescence change was analyzed using ImageJ (NIH). First, a baseline image was generated by averaging six images recorded before the stimulation, and this baseline was subtracted from each image. A region of interest (ROI, 15 × 15 pixels) was set around a CAST-positive active zone, and the average intensity in the ROI was determined.

## Imaging of Syp-SEP Before and After Exocytosis

To record exocytosis events and also to monitor synaptic vesicle protein dynamics, Syp-SEP (synaptophysin-pHluorin) was co-transfected to neurons with CAST-RFP and HA-neurexin. 50 Hz, five electrical pulses stimulation was applied first, and a region (35 × 35 pixels) surrounding a CAST-RFP-positive area showing a clear increase in the SEP signal intensity was selected. Then, 488 nm light was applied for 30 s to photobleach the extracellular Syp-SEP signal. The SEP signal change induced by single pulse stimulation was recorded 140–300 times in each AZLM. In each trial, an image was recorded for 35 ms exposure time, and after 4 ms transfer time the following image was acquired. Three and six images respectively were captured before and after the stimulation in each trial. We waited for 6 s before starting the next trial to reduce the probability of recording the bounce event, which reflects radial movement of an intracellular fluorescent vesicle presumably formed by endocytosis of previously exocytosed Syp-SEP (Midorikawa and Sakaba, 2015). After about 140 trials the probability of detecting a Syp-SEP signal increase immediately after the stimulation decreased in most cases. The data obtained after the decrease were excluded from analyses. We also recorded CAST-RFP images every 2–3 min in order to correct the drift of the preparation in the off-line analyses.

Syp-SEP fluorescence change after the single pulse stimulation was analyzed using custom routines of MATLAB (Mathworks; RRID:SCR_001622) as described previously (Tang et al., 2016) with some modifications. First, the base line image was obtained by averaging three images recorded before the stimulation. This averaged image was subtracted from each image recorded in a single trial to diminish background signal. Then, a 2-dimensional Gaussian function was used to fit signal intensities of 15 × 15 pixels surrounding the peak in the image recorded during 2–37 ms after the stimulation. If the fitted

Gaussian function showed peak intensity > 100 a.u., and 0.4 < SD < 3 pixels, the trial was used for further analysis, and the 3 × 3 pixel area surrounding the fitted peak was selected as the ROI. When the total signal intensity of the ROI just after the stimulation was > the mean + 3 SD intensity of three baseline images recorded before the stimulation and also > 1000 a.u., we examined the time course of events. If the total Syp-SEP signal intensity of the ROI in the 2nd frame (41–76 ms) recorded after the stimulation was > 20% of that in the 1st frame (2–37 ms), we assumed that synchronous exocytosis occurred. We occasionally recorded an instantaneous Syp-SEP signal increase which showed a fast signal decrease (the intensity became < 20% in the next frame). We thought that most of these were bounce events of previously endocytosed vesicles (Midorikawa and Sakaba, 2015) and excluded them from data analyses. We thought that these were bounce events, because the frequency of their occurrence increased when the interval between trials was shorter, which should have increased the number of fluorescent intracellular vesicles containing endocytosed Syp-SEP. In four of the trials among all those performed in the experiments, the distribution of Syp-SEP signal intensity could be fitted with the sum of two Gaussian functions whose centers were > 300 nm apart. In these cases, we presumed that synchronous release occurred at two locations, and the data were excluded from analyses except for the count of the number of synchronous release events. Asynchronous exocytosis was analyzed similarly except that the peak timing of the event relative to the stimulation was different. We did not include data obtained from an AZLM showing < 15 synchronous release events for the analyses.

## Distribution of Exocytosis Locations

We assumed the center of the Gaussian fit of the Syp-SEP signal in 15 × 15 pixels in the image showing the highest intensity in a trial to be the location of exocytosis. To examine whether exocytosis locations were distributed randomly in an AZLM or not, we first determined an AZLM region with the intensity threshold of CAST-RFP signal obtained using the Otsu method (ImageJ, NIH). Next, Monte-Carlo simulation was performed to get random distribution of the same number of exocytosis locations in an AZLM, which was repeated 100 times. Then, the nearest neighbor distances (NND) were measured in both experimental and simulation data (Miki et al., 2017). The clustering tendency of synchronous release locations within an AZLM was evaluated using a previously established hierarchical clustering analysis with cluster diameter of 50 nm (Maschi and Klyachko, 2017). Then, the distance between each exocytosis location and the nearest center of a cluster was measured.

## Estimation of Syp-SEP Diffusion Coefficient

In order to estimate the diffusion coefficient of Syp-SEP, we performed simulation of particle movement as in a previous study (Sochacki et al., 2012) with MATLAB. Ten thousand particles were set randomly in an 80 nm-diameter circle, and each particle moved randomly to one of four directions, up, down, left, or right by $\sqrt{2D\Delta t}$ in one step. D is the assumed diffusion coefficient and $\Delta t$ is the step time (0.5 ms). Particle positions at each time were summed for 35 ms, which corresponded to each recording period. The simulation was performed with various values of D. Then, the time course of experimental Syp-SEP signal decay in 3 × 3 pixels was compared with the simulation results, and the diffusion coefficient was calculated with the least squares method. We also estimated the diffusion coefficient by comparing the signal distribution of experimental data recorded during 41–76 ms after the stimulation with the simulated signal distribution using the least squares method.

## Statistics

All values are presented as mean ± SEM unless otherwise stated. Statistical analyses were performed using MATLAB. The Mann-Whitney U-test was used to evaluate the significance of differences between 2 groups. The Wilcoxon signed-rank test or U-test with Bonferroni correction was used when means of more than two groups were compared.

# RESULTS

## Formation of AZLM on the Glass Surface

A piece of cover glass was coated with the extracellular domain of neuroligin 1 using a method similar to that used to coat a glass surface with neurexin (Tanaka and Hirano, 2012; Tanaka et al., 2014), and rat hippocampal neurons were cultured on it (**Figure 1A**). A marker protein of presynaptic active zone CAST (Ohtsuka et al., 2002) fused to red fluorescent protein tag-RFPt (CAST-RFP) and EGFP were expressed in cultured hippocampal neurons. In neurons on the neuroligin-coated glass, CAST-RFP positive puncta were found on axons under conventional epi-fluorescence illumination, and some of them were also observed with total internal reflection fluorescence (TIRF) illumination, indicating that they were located very close to the glass surface. Most of such CAST-RFP signals were well observed in a single focusing plane just above the glass surface, suggesting parallel formation of CAST-positive areas on the neuroligin-coated glass. In this study we focused on such areas formed by excitatory neurons possessing spines on the dendrites. On the other hand, neurons cultured on the non-coated glass showed CAST-RFP positive puncta under epi-fluorescence, most of which were undetectable under TIRF illumination (**Figure 1B**). We next examined whether other presynaptic active-zone proteins were concentrated in CAST-RFP-positive active-zone-like structures. Active-zone proteins, Bassoon, Piccolo, Munc13 and RIM (Schoch and Gundelfinger, 2006; Südhof, 2012) were co-localized with CAST-RFP under TIRF illumination (**Figure 1C**). Each CAST-RFP-positive area was larger than the respective areas for the other presynaptic active-zone-proteins, a difference that might have been caused by overexpression of CAST-RFP. In addition, electrical field stimulation induced a transient increase in intracellular $Ca^{2+}$ concentration in and around the CAST-RFP-positive area (**Figure 1D**). These results together suggest that a presynaptic active-zone-like membrane (AZLM) was formed directly on the neuroligin-coated glass.

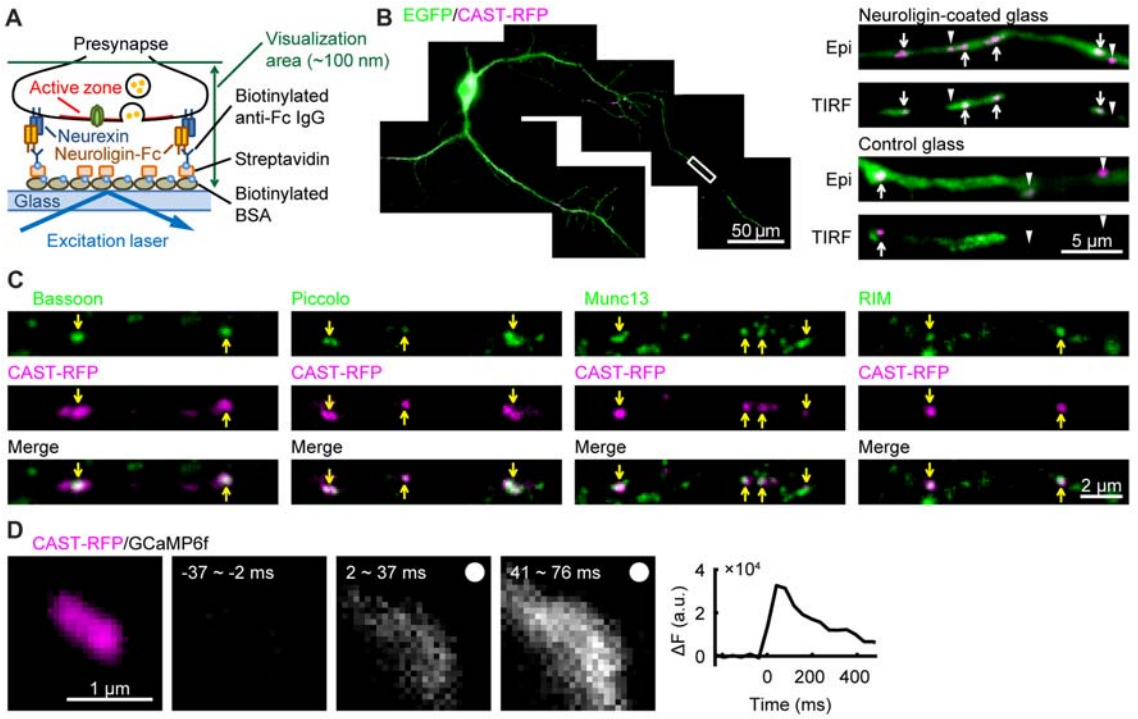


**FIGURE 1 |** Formation of active-zone-like membranes (AZLMs) on neuroligin-coated glass. **(A)** Schematic presentation of AZLM formation on a cover glass coated with neuroligin. **(B)** AZLMs and normal active zones observed with an epi-fluorescence (Epi) or total internal reflection fluorescence (TIRF) condition. White rectangular area in the left image was magnified in the right top. Green and magenta show EGFP and cytomatrix at the active zone-associated structural protein (CAST)-RFP signals, respectively. **(C)** Co-localization of CAST-RFP (magenta) with Bassoon, Piccolo, Munc13 or RIM (green). **(D)** GCaMP6f signal increase around an AZLM marked with CAST-RFP (left magenta). The right graph shows the time course of change of GCaMP signal intensity. Electrical stimulation (100 Hz, 5 pulses) was applied at 0 ms.

## Detection of Single Synaptic Vesicle Exocytosis

We then examined whether synaptic vesicle exocytosis occurred in AZLMs. Exocytosis of synaptic vesicles containing Syp-SEP can be detected as an increase of fluorescence signal, because SEP, which is non-fluorescent in the low pH intra-vesicular solution, becomes fluorescent after exposure to the neutral pH of extracellular solution (Kavalali and Jorgensen, 2014). Repetitive electrical field stimulation (50 Hz, 5 pulses) clearly increased the intensity of the Syp-SEP signal in an AZLM (**Figure 2A**), indicating that synaptic vesicles were exocytosed in an AZLM. Next, we tried to detect a single exocytosis event by one pulse stimulation, which sometimes induced a transient increase of Syp-SEP signal followed by signal dispersal (**Figure 2A**). In 0 mM $Ca^{2+}$ extracellular solution, such an increase of Syp-SEP signal was not recorded. The increase in Syp-SEP signal intensity occurred just after the electrical stimulation (synchronous release) in most cases (**Figure 2B**), although a slightly delayed signal increase (asynchronous release) was observed occasionally (**Figures 2B,C**). The asynchronous release event has been considered to reflect exocytosis of a single synaptic vesicle, and the signal intensities of asynchronous and synchronous events in 3 × 3 pixels were similar (synchronous, 2233 ± 72 a.u., $N$ = 226 events; asynchronous, 2115 ± 94 a.u., $N$ = 99 events; 10 AZLMs, $p$ = 0.50, U-test; **Figure 2D**). Taking this finding together with the relatively low probability of occurrence of synchronous release (17 ± 1%, 226/1340 total trials in 10 AZLMs), we concluded that most synchronous events reflect single vesicle exocytosis, although there could be some events (<3%) reflecting release of multiple vesicles. We recorded simultaneous synchronous releases at two locations with a distance of >300 nm only four times throughout our experiments (1.7%). In these cases, we presumed that synchronous release occurred at two locations, and the data were excluded from analyses except for the count of the number of synchronous release events. We note that definition of synchronous release here is a significant increase of the Syp-SEP signal detected in the first frame (2–37 ms) after the stimulation. Thus, some release events which we assumed to be synchronous could have occurred later in the time frame, which corresponded to asynchronous releases by a conventional electrophysiological criterion (Kaeser and Regehr, 2014).

## Lateral Diffusion of Syp-SEP After a Single Exocytosis Event

In most cases, relatively slow decay of Syp-SEP signal intensity was observed after single pulse stimulation (**Figure 2A**),

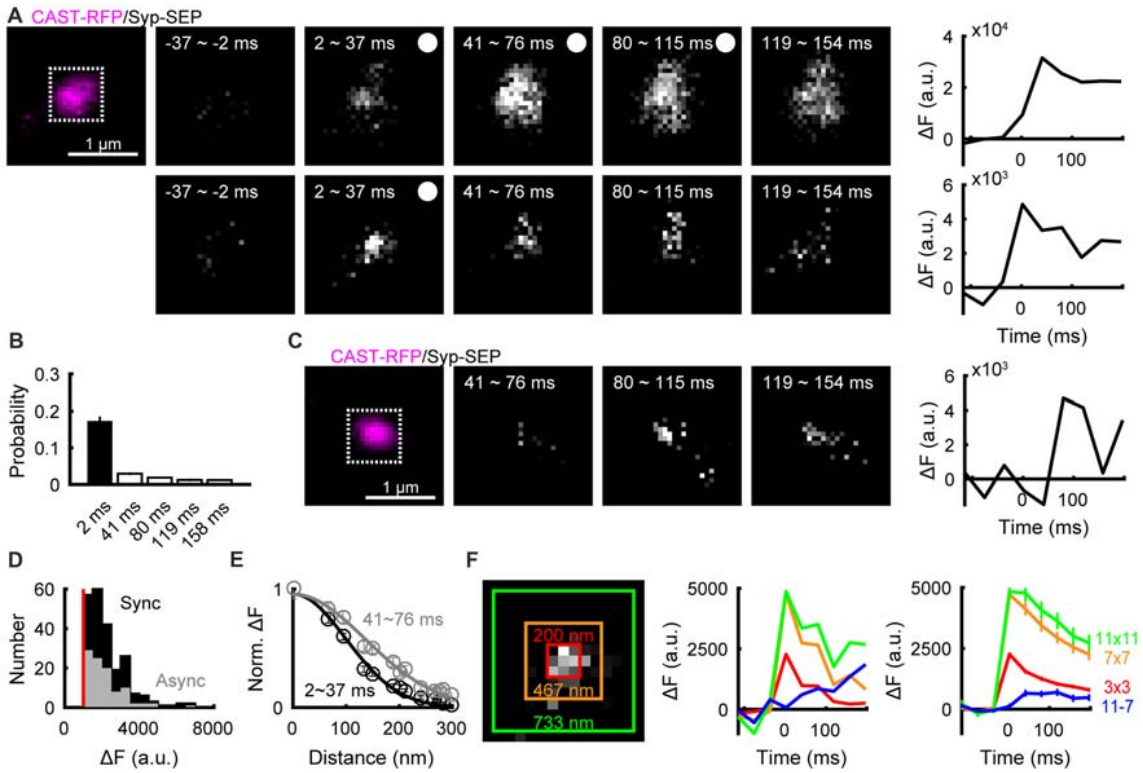


**FIGURE 2 |** Detection of exocytosis of a single synaptic vesicle and diffusion of synaptophysin (Syp)-super-ecliptic pHluorin (SEP) in AZLMs. **(A)** Images showing Syp-SEP signal increase after stimulation with 5 pulses at 50 Hz (upper) or after a single pulse stimulation (lower) in an AZLM (left, magenta), and the time courses of Syp-SEP signal intensity in 11 × 11 pixel areas (white square in the left image) after five pulse stimulation or a single pulse stimulation. The signal intensity is enhanced in the lower images compared with the upper. **(B)** Graph showing occurrence probability of a release event induced by a single pulse stimulation in each frame (2–37, 41–76, 80–115, 119–154, 158–193 ms) per trial throughout all experiments (10 AZLMs). **(C)** Asynchronous release in an AZLM (left, magenta) after a single pulse stimulation and the time course of Syp-SEP signal intensity in 11 × 11 pixels (white square). **(D)** Amplitude histograms of synchronous (black) or asynchronous (gray) release events in 3 × 3 pixels. **(E)** Distributions of Syp-SEP signal intensity in each pixel plotted against the distance from the center pixel at 2–37 ms (black) and 41–76 ms (gray). These are averaged data obtained from all synchronous events in 10 AZLMs. **(F)** Time courses of Syp-SEP signal intensity in 3 × 3 (red), 7 × 7 (orange), 11 × 11 (yellow green) and 11 × 11–7 × 7 (blue) pixels surrounding the center. The left graph shows data obtained in one trial in an AZLM shown in the left image, and the right one shows the averaged data from all synchronous release events in 10 AZLMs. Means and SEMS are shown in the right graph.

suggesting that full-fusion exocytosis rather than instantaneous kiss-and-run exocytosis (Aravanis et al., 2003; Zhang et al., 2009; Wu et al., 2014) took place. Next, we analyzed in detail how the Syp-SEP signal changed in a presumptive single exocytosis event. The center of the increased Syp-SEP signal was determined by fitting signal intensities with a two-dimensional Gaussian distribution in a frame recorded just after the electrical stimulation (2–37 ms; **Figure 2E**), and then the spatial distribution of the Syp-SEP signal was examined. The Syp-SEP signal recorded during 2–37 ms after the stimulation showed a larger peak and narrower distribution than that recorded during 41–76 ms, suggesting that lateral diffusion of Syp-SEP on the plasma membrane occurred after exocytosis (**Figures 2A,E**). Next, the total Syp-SEP signal intensities in 3 × 3, 7 × 7 and 11 × 11 pixels surrounding the center in the 2–37 ms image were measured in different time frames. After the increase in the 2–37 ms frame, the signal intensity decreased in all of the 3 × 3, 7 × 7 and 11 × 11 pixel areas, but the signal decay in 11 × 11 pixels was slowest (**Figure 2F**). In the 3 × 3, 7 × 7 and 11 × 11 pixel areas, the Syp-SEP signal intensity decreased to 35 ± 4%, 48 ± 5% and 56 ± 7%, respectively, of the peak value in the 197–232 ms frame. The decrease in the 11 × 11 pixel area was significantly slower than that in 7 × 7 pixels ($p$ = 0.003, Wilcoxon signed-rank test with Bonferroni correction) or in 3 × 3 pixels ($p < 0.001$). The total signal intensity in 11 × 11 pixels minus that in 7 × 7 pixels increased with time (**Figure 2F**, blue line), supporting the conclusion that lateral spread of Syp-SEP occurred by diffusion.

Fitting the time course of the Syp-SEP signal decrease in 3 × 3 pixels surrounding the center to the simulation results with the least squares method gave an estimate of the diffusion coefficient of 0.17 ± 0.02 $\mu m^2/s$ (**Figure 2F**, $N$ = 10 AZLMs). The diffusion coefficient was also estimated by comparing the lateral spread of the Syp-SEP signal in the 41–76 ms frame with the simulation data, which provided an estimate of 0.19 ± 0.02 $\mu m^2/s$.

An instantaneous Syp-SEP signal increase whose intensity rapidly decayed to <20% in the next time frame occurred just after the stimulation in 3% of trials. Such signal increases

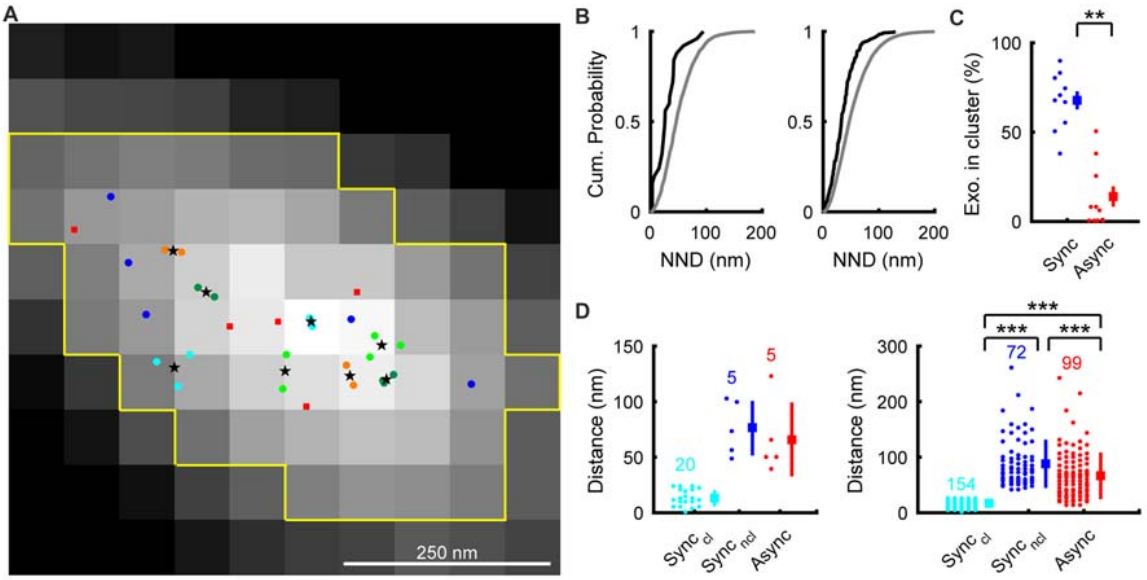


**FIGURE 3 |** Distribution of synchronous and asynchronous release locations in an AZLM. **(A)** Distribution of synchronous and asynchronous release locations in a representative AZLM. The AZLM area defined using the Otsu method was marked with yellow lines. Synchronous release events are categorized as those that occurred in clusters (marked with light blue, yellow green, dark green or orange circles) and those that occurred outside of any clusters (dark blue circles). Centers of individual cluster are marked with black stars. Asynchronous release locations are marked with red squares. **(B)** Cumulative probability plots of the nearest neighbor distances (NND) between synchronous release locations (black) and those obtained by Monte-Carlo simulation assuming random distribution (gray). The left graph shows data obtained from the AZLM shown in **(A)**, and the right one shows averaged data from all AZLMs. **(C)** Ratios of synchronous (dark blue) or asynchronous (red) release events occurring in synchronous release clusters in each AZLM. Small circles represent percentages in respective AZLMs and a square and a bar represent mean and SEM. $^{**}p < 0.01$, U-test. **(D)** Distribution of distances between each release location and the nearest center of a synchronous release cluster (light blue, synchronous release in a cluster; dark blue, synchronous release outside of any clusters; red, asynchronous release). The left graph shows data obtained from the AZLM shown in **(A)**, and the right one shows data from all AZLMs. Small circles represent individual data and a square and a bar represent mean and SD, respectively. Numbers in the graph indicate the numbers of respective release locations. $^{***}p < 0.001$, U-test with Bonferroni correction.

were also recorded in the 41–76 ms or 80–115 ms frame in 1.6 or 1.5% of trials, respectively. We think that most of these were due to bounce events of previously endocytosed vesicles (Midorikawa and Sakaba, 2015), and we excluded them from data analyses. We think that these were due to bounce events, because their frequency increased when the interval between trials was shorter, a condition which should have increased the number of fluorescent intracellular vesicles containing endocytosed Syp-SEP.

## Distribution of Synchronous and Asynchronous Release Locations

We assumed that the center of Gaussian fit in the Syp-SEP image showing the highest peak signal intensity was the location of exocytosis, in a similar manner to Tang et al. (2016). The estimated release locations were not distributed evenly, but rather were distributed in restricted regions within AZLMs (0.13–0.34 $\mu m^2$; **Figures 3A,B**). We also noticed that synchronous release locations tended to form clusters. We then performed hierarchical clustering analysis of release locations with a diameter of 50 nm as reported previously (Maschi and Klyachko, 2017). There were 5.9 ± 0.6 (3–8) clusters of synchronous release locations which presumably corresponded to release sites (Maschi and Klyachko, 2017; Miki et al., 2017; Sakamoto et al., 2018), and 68 ± 5.0% (6/16–17/19, 154/226 locations in 10 AZLM) of synchronous releases occurred in the clusters (**Figures 3C,D**). On the other hand, only 14 ± 6% (0/12–2/4, 12/99 locations in total, $p < 0.01$, U-test) of asynchronous releases occurred in the clusters of synchronous release locations. Thus, synchronous release tended to occur repeatedly in multiple restricted release sites, as has been suggested (Zenisek et al., 2000; Tang et al., 2016; Maschi and Klyachko, 2017; Miki et al., 2017; Sakamoto et al., 2018), whereas asynchronous release tended to occur outside of such clusters. Supporting this idea, the shortest distance between the center of a synchronous release cluster and each synchronous release location (40 ± 3 nm, $N = 226$) was significantly smaller than that between the center of a synchronous release cluster and each asynchronous release location (68 ± 4 nm, $N = 99$, 10 AZLM, $p < 0.001$, U-test; **Figure 3D**). We would like to note that synchronous release locations outside of clusters were more distant from the nearest center of a cluster (90 ± 5 nm, $N = 72$) than asynchronous release locations ($p < 0.001$, U-test; **Figure 3D**). These results might be in line with an idea that some releases we regarded as synchronous might have occurred later in the 2–37 ms frame and could have been asynchronous events by an electrophysiological standard (Kaeser and Regehr, 2014).

## DISCUSSION

Here, we detected exocytosis events of a single synaptic vesicle in AZLMs formed on neuroligin-coated glass and analyzed the dynamics of synaptic vesicle proteins upon exocytosis. Various presynaptic proteins were concentrated in an AZLM, and electrical stimulation induced intracellular $Ca^{2+}$ increase and fast synaptic vesicle exocytosis. Thus, AZLMs were equipped with active-zone molecules and showed basic functions of active zones. However, we should note that an AZLM is an artificial structure, might be somewhat immature and/or might not show all normal functions of mature hippocampal synapses. The release probability (0.17 per AZLM) in 4 mM $Ca^{2+}$ containing solution was lower than those reported previously. For example, Sakamoto et al. (2018) reported the release probability per release site was 0.51 in 4 mM $Ca^{2+}$ containing solution. The apparent low release probability in AZLMs might have been caused partly by the procedure of pre-bleaching of cell surface Syp-SEP before recording, which might have eliminated some signals derived from recently endocytosed vesicles. Thus, the release probability could have been underestimated in this study. We also note that it was difficult to stably record exocytosis events >150 times. The vesicle retrieval mechanism might have been somewhat immature. Insufficient interaction of presynaptic proteins with postsynaptic adhesive proteins other than neuroligin 1, such as SynCAM, LRRTM or cadherin (Gerrow and El-Husseini, 2006), might have been a cause of immaturity. We also noticed that sizes of AZLMs were larger than those of normal active zones (Tang et al., 2016; Maschi and Klyachko, 2017; Sakamoto et al., 2018), and that synaptic vesicle release did not occur in some areas of AZLMs. Over-expression of CAST-RFP might have expanded CAST-RFP-positive areas in our preparation, and some parts might not have been well-organized as release-competent areas, possibly due to an insufficient amount of active-zone proteins there. Nevertheless, we think that application of TIFRM on AZLMs formed in a single focus plane located very close to the bottom glass surface, has provided high spatiotemporal resolution images of fluorescence-tagged synaptic-vesicle protein Syp-SEP, and allowed us to precisely analyze Syp-SEP dynamics and the distribution of both synchronous and asynchronous release locations in AZLMs.

After full-fusion exocytosis, synaptic vesicle proteins could be endocytosed as a package without dispersion (Opazo et al., 2010) or diffused on the surface membrane and then endocytosed (Gimber et al., 2015). Our results support the latter hypothesis and suggest that synaptic vesicular membrane proteins become scattered on the plasma membrane after membrane fusion, although only Syp was examined in this study. Whether other synaptic vesicle proteins such as synaptobrevin, synaptotagmin and/or vesicular glutamate transporter move similarly to Syp is an important question to be addressed in the future. The estimated diffusion coefficient of Syp-SEP (0.17–0.19 $\mu m^2/s$) after single vesicle exocytosis was similar to the value reported in a previous study (Gimber et al., 2015) and to that of t-SNARE protein syntaxin (Ribrault et al., 2011), and was close to the fastest protein diffusion on the plasma membrane. Thus, it is suggested that synaptic vesicle protein Syp diffuses quickly on the plasma membrane upon vesicle exocytosis.

We found that locations of synchronous release of a synaptic vesicle tended to form clusters in an AZLM, and the number of such release sites was 3–8, which was similar to the number of release sites within an active zone reported in recent studies (Tang et al., 2016; Maschi and Klyachko, 2017; Sakamoto et al., 2018). Interestingly, we found that asynchronous release locations were distributed more widely than synchronous release locations. Thus, preferential synchronous and asynchronous release locations could be different. Zenisek et al. (2000) reported that synchronous releases tend to occur repeatedly at restricted sites and asynchronous releases do at isolated locations in a large presynaptic terminal of retinal bipolar cell. We found small fractions (32%) of synchronous release occurred outside of the release clusters. We might have failed to record repetitive synchronous releases in such locations because of the relatively small number of trials. Alternatively, such release events might not have been synchronous, but actually asynchronous ones, which occurred in the later time within the first frame (2–37 ms) after the stimulation. Asynchronous release might have occurred at locations not very close to $Ca^{2+}$ channels (Miki et al., 2017). It was also reported that different subtypes of synaptotagmin (syt1 and syt7) are involved in synchronous and asynchronous releases (Bacaj et al., 2013; Kaeser and Regehr, 2014). Different locations for synchronous and asynchronous releases might reflect sub-active-zonal molecular organization such as distributions of different types of synaptotagmin-interacting proteins in AZLMs.

The visualization methods we have developed here could easily be applied to other synaptic proteins and would provide useful information about the dynamics of respective presynaptic proteins in the future. In addition, the combination of these methods with rapid extracellular pH change methods (Fujii et al., 2017) might be able to visualize endocytosis of synaptic vesicle proteins around AZLMs. Thus, we think that AZLMs will be useful for studying basic functional properties of presynaptic active-zones.

## AUTHOR CONTRIBUTIONS

JF and TH contributed conception and design of the study and wrote the manuscript. JF performed most of experiments and all data analyses. HT performed some experiments in the early stage of study. All authors read and approved the submitted version.

## FUNDING

This work was supported by grants 15H04259 and 18H02526 to TH from Japan Society for the Promotion of Science, and a grant from Takeda Science Foundation in Japan.

## ACKNOWLEDGMENTS

We thank Drs. S. Fujii and E. Nakajima for comments on the manuscript.

## REFERENCES


Aravanis, A. M., Pyle, J. L., and Tsien, R. W. (2003). Single synaptic vesicles fusing transiently and successively without loss of identity. *Nature* 423, 643–647. doi: 10.1038/nature01686

Bacaj, T., Wu, D., Yang, X., Morishita, W., Zhou, P., Xu, W., et al. (2013). Synaptotagmin-1 and synaptotagmin-7 trigger synchronous and asynchronous phases of neurotransmitter release. *Neuron* 80, 947–959. doi: 10.1016/j.neuron.2013.10.026

Balaji, J., and Ryan, T. A. (2007). Single-vesicle imaging reveals that synaptic vesicle exocytosis and endocytosis are coupled by a single stochastic mode. *Proc. Natl. Acad. Sci. U S A* 104, 20576–20581. doi: 10.1073/pnas.0707574105

Chen, X., Barg, S., and Almers, W. (2008). Release of the styryl dyes from single synaptic vesicles in hippocampal neurons. *J. Neurosci.* 28, 1894–1903. doi: 10.1523/JNEUROSCI.4518-07.2008

Chen, T.-W., Wardill, T. J., Sun, Y., Pulver, S. R., Renninger, S. L., Baohan, A., et al. (2013). Ultrasensitive fluorescent proteins for imaging neuronal activity. *Nature* 499, 295–300. doi: 10.1038/nature12354

Chih, B., Gollan, L., and Scheiffele, P. (2006). Alternative splicing controls selective trans-synaptic interactions of the neuroligin-neurexin complex. *Neuron* 51, 171–178. doi: 10.1016/j.neuron.2006.06.005

Fujii, S., Tanaka, H., and Hirano, T. (2017). Detection and characterization of individual endocytosis of AMPA-type glutamate receptor around postsynaptic membrane. *Genes Cells* 22, 583–590. doi: 10.1111/gtc.12493

Gandhi, S. P., and Stevens, C. F. (2003). Three modes of synaptic vesicular recycling revealed by single-vesicle imaging. *Nature* 423, 607–613. doi: 10.1038/nature01677

Gerrow, K., and El-Husseini, A. (2006). Cell adhesion molecules at the synapse. *Front. Biosci.* 11, 2400–2419. doi: 10.2741/1978

Gimber, N., Tadeus, G., Maritzen, T., Schmoranzer, J., and Haucke, V. (2015). Diffusional spread and confinement of newly exocytosed synaptic vesicle proteins. *Nat. Commun.* 6:8392. doi: 10.1038/ncomms9392

Graf, E. R., Zhang, X., Jin, S.-X., Linhoff, M. W., and Craig, A. M. (2004). Neurexins induce differentiation of GABA and glutamate postsynaptic specializations via neuroligins. *Cell* 119, 1013–1026. doi: 10.1016/j.cell.2004.11.035

Granseth, B., Odermatt, B., Royle, S. J., and Lagnado, L. (2006). Clathrin-mediated endocytosis is the dominant mechanism of vesicle retrieval at hippocampal synapses. *Neuron* 51, 773–786. doi: 10.1016/j.neuron.2006.08.029

Haucke, V., Neher, E., and Sigrist, S. J. (2011). Protein scaffolds in the coupling of synaptic exocytosis and endocytosis. *Nat. Rev. Neurosci.* 12, 127–138. doi: 10.1038/nrn2948

He, L., Wu, X.-S., Mohan, R., and Wu, L.-G. (2006). Two modes of fusion pore opening revealed by cell-attached recordings at a synapse. *Nature* 444, 102–105. doi: 10.1038/nature05250

Isomura, H., Tsurumi, T., and Stinski, M. F. (2004). Role of the proximal enhancer of the major immediate-early promoter in human cytomegalovirus replication. *J. Virol.* 79, 12788–12799. doi: 10.1128/jvi.78.23.12788-12799.2004

Kaeser, P. S., and Regehr, W. G. (2014). Molecular mechanisms for synchronous, asynchronous, and spontaneous neurotransmitter release. *Annu. Rev. Physiol.* 76, 333–363. doi: 10.1146/annurev-physiol-021113-170338

Kavalali, E. T., and Jorgensen, E. M. (2014). Visualizing presynaptic function. *Nat. Neurosci.* 17, 10–16. doi: 10.1038/nn.3578

Kawaguchi, S.-Y., and Hirano, T. (2006). Integrin α3β1 suppresses long-term potentiation at inhibitory synapses on the cerebellar Purkinje neuron. *Mol. Cell. Neurosci.* 31, 416–426. doi: 10.1016/j.mcn.2005.10.012

Kononenko, N. L., and Haucke, V. (2015). Molecular mechanisms of presynaptic membrane retrieval and synaptic vesicle reformation. *Neuron* 85, 484–496. doi: 10.1016/j.neuron.2014.12.016

Maschi, D., and Klyachko, V. A. (2017). Spatiotemporal regulation of synaptic vesicle fusion sites in central synapses. *Neuron* 94, 65–73.e3. doi: 10.1016/j.neuron.2017.03.006

Midorikawa, M., and Sakaba, T. (2015). Imaging exocytosis of single synaptic vesicles at a fast CNS presynaptic terminal. *Neuron* 88, 492–498. doi: 10.1016/j.neuron.2015.09.047

Miesenböck, G., De Angelis, D. A., and Rothman, J. E. (1998). Visualizing secretion and synaptic transmission with pH-sensitive green fluorescent proteins. *Nature* 394, 192–195. doi: 10.1038/28190

Miki, T., Kaufmann, W. A., Malagon, G., Gomez, L., Tabuchi, K., Watanabe, M., et al. (2017). Numbers of presynaptic $Ca^{2+}$ channel clusters match those of functionally defined vesicular docking sites in single cell synapses. *Proc. Natl. Acad. Sci. U S A* 114, E5246–E5255. doi: 10.1073/pnas.1704470114

Ohtsuka, T., Takao-Rikitsu, E., Inoue, E., Inoue, M., Takeuchi, M., Matsubara, K., et al. (2002). CAST: a novel protein of the cytomatrix at the active zone of synapses that forms a ternary complex with RIM1 and Munc13–1. *J. Cell Biol.* 158, 577–590. doi: 10.1083/jcb.200202083

Opazo, F., Punge, A., Bückers, J., Hoopmann, P., Kastrup, L., Hell, S. W., et al. (2010). Limited intermixing of synaptic vesicle components upon vesicle recycling. *Traffic* 11, 800–812. doi: 10.1111/j.1600-0854.2010.01058.x

Pettem, K. L., Yokomaku, D., Takahashi, H., Ge, Y., and Craig, A. M. (2013). Interaction between autism-linked MDGAs and neuroligins suppresses inhibitory synapse development. *J. Cell Biol.* 200, 321–336. doi: 10.1083/jcb.201206028

Ribrault, C., Reingruber, J., Petkovic, M., Galli, T., Ziv, N. E., Holcman, D., et al. (2011). Syntaxin 1A lateral diffusion reveals transient and local SNARE interactions. *J. Neurosci.* 31, 17590–17602. doi: 10.1523/JNEUROSCI.4065-11.2011

Sakamoto, H., Ariyoshi, T., Kimpara, N., Sugao, K., Taiko, I., Takikawa, K., et al. (2018). Synaptic weight set by Munc13–1 supramolecular assemblies. *Nat. Neurosci.* 21, 41–49. doi: 10.1038/s41593-017-0041-9

Scheiffele, P., Fan, J., Choih, J., Fetter, R., and Serafini, T. (2000). Neuroligin expressed in nonneuronal cells triggers presynaptic development in contacting axons. *Cell* 101, 657–669. doi: 10.1016/s0092-8674(00)80877-6

Schoch, S., and Gundelfinger, E. D. (2006). Molecular organization of the presynaptic active zone. *Cell Tissue Res.* 326, 379–391. doi: 10.1007/s00441-006-0244-y

Shaner, N. C., Lin, M. Z., McKeown, M. R., Steinbach, P. A., Hazelwood, K. L., Davidson, M. W., et al. (2008). Improving the photostability of bright monomeric orange and red fluorescent proteins. *Nat. Methods* 5, 545–551. doi: 10.1038/nmeth.1209

Sochacki, K. A., Larson, B. T., Sengupta, D. C., Daniels, M. P., Shtengel, G., Hess, H. F., et al. (2012). Imaging the post-fusion release and capture of a vesicle membrane protein. *Nat. Commun.* 3:1154. doi: 10.1038/ncomms2158

Südhof, T. C. (2012). The presynaptic active zone. *Neuron* 75, 11–25. doi: 10.1016/j.neuron.2012.06.012

Takamori, S., Holt, M., Stenius, K., Lemke, E. A., Grønborg, M., Riedel, D., et al. (2006). Molecular anatomy of a trafficking organelle. *Cell* 127, 831–846. doi: 10.1016/j.cell.2006.10.030

Tanaka, H., Fujii, S., and Hirano, T. (2014). Live-cell imaging of receptors around postsynaptic membranes. *Nat. Protoc.* 9, 76–89. doi: 10.1038/nprot.2013.171

Tanaka, H., and Hirano, T. (2012). Visualization of subunit-specific delivery of glutamate receptors to postsynaptic membrane during hippocampal long-term potentiation. *Cell Rep.* 1, 291–298. doi: 10.1016/j.celrep.2012.02.004

Tang, A.-H., Chen, H., Li, T. P., Metzbower, S. R., MacGillavry, H. D., and Blanpied, T. A. (2016). A trans-synaptic nanocolumn aligns neurotransmitter release to receptors. *Nature* 536, 210–214. doi: 10.1038/nature19058

von Gersdorff, H., and Matthews, G. (1994). Dynamics of synaptic vesicle fusion and membrane retrieval in synaptic terminals. *Nature* 367, 735–739. doi: 10.1038/367735a0

Wienisch, M., and Klingauf, J. (2006). Vesicular proteins exocytosed and subsequently retrieved by compensatory endocytosis are nonidentical. *Nat. Neurosci.* 9, 1019–1027. doi: 10.1038/nn1739

Willig, K. I., Rizzoli, S. O., Westphal, V., Jahn, R., and Hell, S. W. (2006). STED microscopy reveals that synaptotagmin remains clustered after synaptic vesicle exocytosis. *Nature* 440, 935–939. doi: 10.1038/nature04592

Wu, L.-G., Hamid, E., Shin, W., and Chiang, H.-C. (2014). Exocytosis and endocytosis: modes, functions, and coupling mechanisms. *Annu. Rev. Physiol.* 76, 301–331. doi: 10.1146/annurev-physiol-021113-170305

Yamashita, T., Hige, T., and Takahashi, T. (2005). Vesicle endocytosis requires dynamin-dependent GTP hydrolysis at a fast CNS synapse. *Science* 307, 124–127. doi: 10.1126/science.1103631

Zenisek, D., Steyer, J. A., and Almers, W. (2000). Transport, capture and exocytosis of single synaptic vesicles at active zones. *Nature* 406, 849–854. doi: 10.1038/35022500

Zhang, Q., Li, Y., and Tsien, R. W. (2009). The dynamic control of kiss-and-run and vesicular reuse probed with single nanoparticles. *Science* 323, 1448–1453. doi: 10.1126/science.1167373

**Conflict of Interest Statement**: The authors declare that the research was conducted in the absence of any commercial or financial relationships that could be construed as a potential conflict of interest.

The reviewer AM and handling Editor declared their shared affiliation.

*Copyright © 2018 Funahashi, Tanaka and Hirano. This is an open-access article distributed under the terms of the Creative Commons Attribution License (CC BY). The use, distribution or reproduction in other forums is permitted, provided the original author(s) and the copyright owner are credited and that the original publication in this journal is cited, in accordance with accepted academic practice. No use, distribution or reproduction is permitted which does not comply with these terms.*

frontiers in Cellular Neuroscience

MINI REVIEW
published: 01 March 2019
doi: 10.3389/fncel.2019.00052

# Genetically Encoded Voltage Indicators Are Illuminating Subcellular Physiology of the Axon

*Lauren C. Panzera and Michael B. Hoppa**

*Department of Biological Sciences, Dartmouth College, Hanover, NH, United States*

Everything we see and do is regulated by electrical signals in our nerves and muscle. Ion channels are crucial for sensing and generating electrical signals. Two voltage-dependent conductances, $Na^+$ and $K^+$, form the bedrock of the electrical impulse in the brain known as the action potential. Several classes of mammalian neurons express combinations of nearly 100 different varieties of these two voltage-dependent channels and their subunits. Not surprisingly, this variability orchestrates a diversity of action potential shapes and firing patterns that have been studied in detail at neural somata. A remarkably understudied phenomena exists in subcellular compartments of the axon, where action potentials initiate synaptic transmission. Ion channel research was catalyzed by the invention of glass electrodes to measure electrical signals in cell membranes, however, progress in the field of neurobiology has been stymied by the fact that most axons in the mammalian CNS are far too small and delicate for measuring ion channel function with electrodes. These quantitative measurements of membrane voltage can be achieved within the axon using light. A revolution of optical voltage sensors has enabled exploring important questions of how ion channels regulate axon physiology and synaptic transmission. In this review we will consider advantages and disadvantages of different fluorescent voltage indicators and discuss particularly relevant questions that these indicators can elucidate for understanding the crucial relationship between action potentials and synaptic transmission.

**Keywords: genetically encoded voltage indicators, axon, synaptic transmission, voltage, action potentials**

OPEN ACCESS

***Edited by:***
*Shin-ya Kawaguchi,*
*Kyoto University, Japan*

***Reviewed by:***
*Dominique Debanne,*
*INSERM U1072 Neurobiologie des canaux Ioniques et de la Synapse, France*
*Dax Hoffman,*
*National Institutes of Health (NIH), United States*

***Correspondence:**
*Michael B. Hoppa*
*michael.b.hoppa@dartmouth.edu*

***Received:*** *17 December 2018*
***Accepted:*** *04 February 2019*
***Published:*** *01 March 2019*

***Citation:***
*Panzera LC and Hoppa MB (2019) Genetically Encoded Voltage Indicators Are Illuminating Subcellular Physiology of the Axon. Front. Cell. Neurosci. 13:52. doi: 10.3389/fncel.2019.00052*

## INTRODUCTION

### The AP Is a Flexible Currency of Cellular Communication

The linkage between electricity and signaling of the nervous system was first postulated by Galvani in 1791 after observing musculature contraction in the frog by applying electrical discharges directly onto nerve fibers (Ashcroft, 2012). It was not until the 1950s that Hodgkin and Huxley made the fateful recordings of membrane potential in the squid giant axon to discover voltage-gated ion channels give rise to propagating electrical signals known as action potentials (APs) (Hodgkin et al., 1952; Hodgkin and Huxley, 1952). The AP is the informal currency of information transfer between nerves that is enabled by the precisely timed flow of positively charged ions for both the depolarization ($Na^+$ influx) and repolarization ($K^+$ efflux) phases of the waveform. The invention of the patch-clamp enabled recordings of the AP from several small neurons across the nervous system of several species. Although the squid axon had a binary

firing response to different stimulations, several firing patterns were discovered that differed considerably between cell types (Llinas, 1988; Bean, 2007). This diversity includes the fast spiking inhibitory parvalbumin and Purkinje neurons compared to the slower firing of excitatory pyramidal neurons of the hippocampus and dopaminergic neurons in the substantia nigra (Grace and Bunney, 1984; McCormick et al., 1985; Connors and Gutnick, 1990; Raman and Bean, 1999; Brown et al., 2009; Gentet et al., 2010). Many of these differences in firing rates arise from different combinations of $Na^+$ and $K^+$ channels (Covarrubias et al., 1991; Dodson et al., 2002; Dodson and Forsythe, 2004; Engel and Jonas, 2005; Jan and Jan, 2012) which also give rise to different shapes of AP waveforms. APs in several fast firing neurons such as Purkinje neurons are characterized as having very narrow widths (∼180 μs) and fast rise times, while those of some slower firing neurons such as CA1 pyramidal neurons are much broader (∼810 μs) (Bean, 2007). This establishes the waveform as a plastic signal that encodes potentially interesting neurobiological information and rests upon the specific combinations of ion channels expressed at the cellular level. However, how different localization of channels within cells can modulate the shape of the AP at the subcellular scale is less well understood due to technical limitations of electrophysiology.

## The AP Waveform at Presynaptic Terminals Is Not Equivalent to the Somatic Waveform

After initiation in the axon initial segment adjacent to the soma, an AP rapidly propagates along the axon until it reaches the presynaptic terminals (Kole and Stuart, 2012). These terminals transduce incoming electrical signals (APs) into chemical signals (neurotransmitter release). Changes in transduction efficiency are the basis of memory formation, and chronic weakening of synaptic transduction is associated with pathologies such as Alzheimer's. The coordination of $Ca^{2+}$ entry that results in vesicle fusion is directed by the AP. The depolarizing event triggers the opening of voltage-gated $Ca^{2+}$ channels (Cavs) in a presynaptic terminal and subsequent vesicle fusion (Dodge and Rahamimoff, 1967; Llinas et al., 1981; Rosenmund et al., 1993; Schneggenburger and Neher, 2000). The AP is a command signal that sharply controls the open probability and open duration of Cavs and thus tightly regulates the synaptic concentration of $Ca^{2+}$ (Llinas et al., 1981; Schneggenburger and Neher, 2000; Lisman et al., 2007). Vesicle fusion is a supra-linear process that is steeply dependent (by a 3rd order power-law) on $Ca^{2+}$ entry at the synapse (Dodge and Rahamimoff, 1967; Augustine et al., 1985; Zucker and Fogelson, 1986; Schneggenburger and Neher, 2000). Thus, the AP is well positioned for modulating synaptic function, and small changes in the AP waveform have been shown to exert enormous impact on synaptic transmission (Sabatini and Regehr, 1997; Borst and Sakmann, 1999; Bischofberger et al., 2002; Rama et al., 2015).

An unexpected gap in the well-studied field of synaptic transmission is the measurement of the presynaptic AP waveform in small *en passant* synapses that dominate the central nervous system. Somatic recordings are generally not an accurate proxy for activity at nerve terminals, though the comparisons have been hard to come by using classic electrophysiology. The first detailed subcellular comparison of the AP waveform occurred in granule neurons from the dentate gyrus and their mossy fiber boutons which are large enough to allow electrical access (>3 μm). These recordings demonstrated a dramatically narrower AP at the mossy fiber terminal and provided the first physiological evidence that these two cellular compartments are quite independent with physiological consequences for synaptic transmission (Geiger and Jonas, 2000). More recently it was found that the nerve terminals of Purkinje neurons (∼3 μm) also have very different waveforms due to a unique balance of $Na^+$ and $K^+$ channels compared to the cell body and, more surprisingly, compared with adjacent axon (Kawaguchi and Sakaba, 2015). However, outside of these examples, whole-cell patch clamp is not technically feasible for decoding AP waveforms and molecular modulators in *en passant* synapses due to their sub-micron diameters (Shepherd and Harris, 1998; Mishchenko et al., 2010). Recordings from the few other large and accessible mammalian terminals has further demonstrated different AP waveform shapes when recorded from pituitary nerves (Jackson et al., 1991) and the calyx of Held (Sierksma and Borst, 2017). This divergence makes understanding the role of the AP in nerve terminals of even higher interest, especially given the host of recent channelopathies attributed to the presynaptic terminal and axon (Kullmann, 2010; Child and Benarroch, 2014; Vivekananda et al., 2017).

The development of optogenetic indicators other than voltage has provided new opportunities for imaging neural activity within the small *en passant* synapses of the central nervous system. The rapid advancements for improving genetically encoded $Ca^{2+}$ indicators (Chen et al., 2013) has revolutionized recording physiology with large signal-to-noise ratios (SNRs) that enable their use in defined compartments or cell types *in vitro* and *in vivo* (Sofroniew et al., 2016). This review will highlight the recent advances in voltage imaging specifically for the use of resolving APs within the axon and synaptic terminals. We will go on to highlight areas where optical measurements of voltage have recently been deployed to contribute to new knowledge of axon and synaptic physiology, as well as potentially interesting future directions.

## Ideal Properties of Genetically Encoded Voltage Indicators

Experimental use of genetically encoded voltage indicators (GEVIs) to record physiological voltage changes in the axon is still hindered at this time by low signal-to-noise ratios. While this is a consideration in all cells, it is particularly difficult for resolving the AP in small diameter (<300 nm) structures such as the axon that emit few photons due to limited surface area. This is made more difficult for recording transient APs that are fully resolved in 1–3 ms. Thus, photons emitted by fluorophores in response to voltage changes must be collected in very brief acquisition windows (<1 ms), making brightness paramount for accurate detection of the AP. It is also much easier to observe signals with a larger percentage change in

fluorescence ($\Delta F/F$) above any optical noise unrelated to your signal. We have reported the sensitivity and relative brightness of several recent iterations of reported GEVIs (**Table 1**). A second desired attribute for a GEVI, especially in the context of resolving an AP waveform, is that the indicator would have changes in fluorescence or kinetics for the depolarization and repolarization phases with taus on the order of 100 μs. Minimally, taus of fluorescent change need to be <1 ms for accurate detection of AP firing rates at 100 Hz; tau constants for both phases are also reported (**Table 1**). Final key considerations of GEVIs when combining with other optogenetic or fluorescent proteins, as well as determining potential use with 2-photon excitation, are their excitation and emission spectra. We have color-coded indicators in **Table 1** for clarity based on the single photon excitation energy/color (blue, green, and red) and divided by mechanism of fluorescence as detailed below.

## Voltage-Sensitive Dyes

Voltage-sensitive (VS) dyes already have many ideal characteristics for voltage-indicators: they are bright, photostable and have very fast kinetics (Zhou et al., 2007; Huang et al., 2015; Woodford et al., 2015), although many VS dyes alter properties of the membrane itself (Peterka et al., 2011). That important consideration aside, perhaps the most significant limitation of voltage-sensitive dyes is their lack of specificity. Lipophilic dyes stain all cell membranes when loaded extracellularly, so voltage-dependent fluorescence signals cannot be distinguished between cell types. Intracellular loading through glass electrodes gives excellent specificity and has been useful to studying axon physiology, but must be loaded cumbersomely through electrodes and allowed to diffuse through the cell, limiting their use *in vivo* or for measuring multiple adjacent cells.

## GEVIs in the Axon

There is a rich abundance of fluorescent voltage indicators available with different characteristics of speed, color, brightness, and sensitivity. When assessing indicators, each must be weighed for its inherent strengths and weaknesses in consideration of the research question being asked. Given the diversity of applications for voltage imaging and an explosion of engineered GEVIs, many reviews have been published comparing GEVIs and their applications (Emiliani et al., 2015; Knopfel et al., 2015; St-Pierre et al., 2015; Storace et al., 2016). Here we will focus solely on the current toolkit of GEVIs available as of this publication that are best suited for investigating voltage changes in the axon, with a focus on detecting and resolving AP waveforms. These GEVIs have historically fallen into two main classes: microbial rhodopsin-based indicators, and voltage-sensing domains (VSDs) of phosphatases fused to fluorescent proteins. We will follow the naming style of previous GEVI discussion (Nakajima et al., 2016) and label these two types Class I and Class II, respectively, and start our discussion with a brief timeline of GEVI development beginning with Class II probes. A final group of indicators currently in development, Class I-hybrids, use Förster resonance energy transfer between a microbial rhodopsin and a fluorescent protein to report changes in voltage (Gong et al., 2014).

# COMPARISON OF GEVIs

## Class II: VSD-Containing GEVIs

The earliest VSD GEVIs engineered contained voltage-sensing domains of naturally occurring ion channels fused with fluorescent proteins (Siegel and Isacoff, 1997; Ataka and Pieribone, 2002). Unfortunately, these initial probes suffered from limited plasma membrane expression and poor targeting which hindered their use in mammalian systems (Storace et al., 2016). Membrane expression was improved by replacing the voltage sensor of voltage-gated $K^+$ channels (Kvs) with a domain of the *Ciona intestinalis* voltage-sensitive phosphatase (Ci-VSP) (Murata et al., 2005).

There are two strategies used by Class II indicators to alter fluorescence. Probes including ArcLight (Jin et al., 2012) and an ArcLight derivative, Bongwoori (Lee et al., 2017), feature Ci-VSP fused to an intracellular super ecliptic pHluorin. Membrane depolarization induces a conformational change in the VSP which alters fluorescent emission. This approach yields reporters that are very bright yet also relatively slow, which makes them more suitable for detecting small changes such as graded potentials as opposed to APs. A second strategy for changing fluorescence takes advantage of an innovation in the engineering of fluorophores with the development of circularly permuted fluorescent proteins (cpFPs). The introduction of new termini into the tertiary structure of a fluorophore generates space for the fusion of a voltage sensing domain; conformational changes to the permuted protein alter fluorescence (Baird et al., 1999). ASAP1, a fusion construct of an extracellular cpGFP to the VSP of *Gallus gallus* (St-Pierre et al., 2014), improved upon the speed and sensitivity of previous VSP sensors including ArcLight. An ASAP variant, ASAP2f, demonstrated robust fluorescence changes ∼14% larger than ASAP1 in response to single stimuli (Yang et al., 2016); the current iteration, ASAP3, has sensitivity and speed enough to detect both subthreshold events and individual spiking up to 100 Hz in acute brain slices (Chavarha et al., 2018). A red-shifted variant, FlicR1, was generated by fusing a Ci-VSP domain to cpRFP (cpmApple) (Abdelfattah et al., 2016). One disadvantage of the previously mentioned GFP-based reporters is that the conformational changes that lead to photon emission suffer from slow kinetics ($\tau_{fast} > 3$ ms) that limit the accurate resolution of AP waveform dynamics. Notably, however, they have been engineered to have very high brightness which facilitates detection of both APs and subthreshold deflections.

## Class I: Rhodopsin-Based Indicators

The discovery of a light-driven proteorhodopsin found in marine bacteria (Beja et al., 2001) led to the development of an entirely new branch of GEVIs that uses the voltage-dependent protonation of a rhodopsin chromophore, retinal, to generate fluorescence. In the wild, light drives protons through the proteorhodopsin, resulting in a change in emission spectra of the protein. Mutagenesis eliminated light-induced proton pumping (Dioumaev et al., 2003) to yield a proteorhodopsin optical proton sensor (PROPS) that revealed electrical spiking

**TABLE 1 |** Comparison of contemporary GEVI characteristics.

| | | *Class I: Rhodopsin-based GEVIs* | | *Class I-hybrids: FRET-opsin GEVIs* | | |
|---|---|---|---|---|---|---|
| **GEVI name** | | **QuasAr2** | **Archon1** | **VARNAM** | **Voltron525** | **Ace2N-4AA-mNeon** |
| Fluorophore | | Retinal cofacor | Retinal cofacor | mRuby3 N81S | JF525 | mNeonGreen |
| ΔF/F per single stimulation | | 48 ± 3% | 30 ± 6% | −8.4 ± 0.3% | ~10%[6] | −12.0 ± 0.8% |
| Sensitivity (ΔF/F per 100 mV) | | 90 ± 2%[3] | 81 ± 8%[3] 43 ± 5% | −14.1 ± 0.4%[3,4] | −23.1 ± 1% | −13.4 ± 0.5%[2,3] |
| Linearity | | Yes | Yes | No | Yes | No |
| Brightness (relative to EGFP) | | Very dim | Dim | Equivalent | Very Bright | Bright |
| τ on (ms,−70 mV to +30 mV) at 32–34°C | τ 1 fast | 0.3 ± 0.05 ms | 0.61 ± 0.06 ms[5] | 0.88 ± 0.13 ms[1] | 0.64 ± 0.09 ms[5] | 0.37 ± 0.08 ms |
| | τ 2 slow | 3.2 ± 0.4 ms | 8.1 ± 0.5 ms | 5.2 ± 0.5 ms | 4.1 ± 0.6 ms | 5.5 ± 1.4 ms |
| | % τ 1 | 62% | 88% | n/a | 61 ± 4% | 58 ± 5% |
| τ off (ms, +30 mV to−70 mV) at 32–34°C | τ 1 fast | 0.3 ms | 1.1 ± 0.2 ms | 0.8 ± 0.44 ms | 0.78 ± 0.12 ms | 0.50 ± 0.09 ms |
| | τ 2 slow | 4.0 ms | 13 ± 3 ms | 4.7 ± 0.3 ms | 3.9 ± 0.2 ms | 5.9 ± 0.9 ms |
| | % τ 1 | 73% | 88% | n/a | 55 ± 7% | 60 ± 6% |
| Excitation λ 1P/2P | | 640 nm / n/a | 637 nm / n/a | 565 nm / n/a | 532 nm / n/a | 506 nm / n/a |
| References | | Hochbaum et al., 2014 | Piatkevich et al., 2018 | Kannan et al., 2018 | Abdelfattah et al., 2018 biorxiv | Gong et al., 2015 |
| | | *Class II: VSD-containing GEVIs* | | | | |
| **GEVI name** | | **FlicR1** | **ASAP2f** | **Bongwoori** | **ArcLight Q239** | **ASAP3** |
| Fluorophore | | cpmApple | cpGFP | sepHluorin A227D | sepHluorin A227D | cpGFP |
| ΔF/F per single stimulation | | 2.6 ± 0.8% | ~−5% | ~−5% | −3.2 ± 2.2% | −17.9 ± 1.2% |
| Sensitivity (ΔF/F per 100 mV) | | 6.6 ± 0.6%[3] | n/a | n/a | ~−40%[6] | −50.9 ± 1.1% |
| Linearity | | Yes | No | No | No | No |
| Brightness (relative to EGFP) | | Equivalent | Equivalent | Equivalent | Equivalent | Equivalent |
| τ on (ms,−70 mV to +30 mV) at 32–34°C | τ 1 fast | 0.74 ± 0.06 ms | 2.8 ± 0.1 ms | 10 ± 1 ms | 9 ± 1 ms | 0.94 ± 0.06 ms |
| | τ 2 slow | 27 ± 6 ms | 135 ± 16 ms | n/a | 48 ± 4 ms | 7.24 ± 0.38 ms |
| | % τ 1 | 90 ± 2% | 81 ± 2% | 91 ± 6% | 50 ± 3% | 72 ± 1% |
| τ off (ms, +30mV to −70mV) at 32–34°C | τ 1 fast | 0.93 ± 0.07 ms | 2.4 ± 0.2 ms | 7 ± 1 ms | 17 ± 1 ms | 3.79 ± 0.15 ms |
| | τ 2 slow | 14 ± 6 ms | 155 ± 16 ms | n/a | 60 ± 7 ms | 16.00 ± 1.21 ms |
| | % τ 1 | 79 ± 4% | 71 ± 3% | 100% | 79 ± 3% | 76 ± 5% |
| Excitation λ 1P/2P | | 560 nm/1120 nm | 470 nm / 920 nm | 472 nm / n/a | 480 nm / n/a | 480 nm/920 nm |
| References | | Abdelfattah et al., 2016 | Yang et al., 2016 | Piao et al., 2015 | Jin et al., 2012; Storace et al., 2015 | Ataka and Pieribone, 2002 |

*GEVIs are grouped according to their voltage-sensing mechanism and color-coded according to their single photon excitation wavelength (blue, green, red). Superscripts denote the following: (1) experiments to determine VARNAM kinetics performed at room temperature. (2) Experiments to determine sensitivity of Ace-mNeon published in Kannan et al. (2018) from a 120 mV depolarization. (3) Measured in HEK cells. (4) In response to a 120 mV depolarization. (5) Experiments performed at unknown temperature. (6) Value estimated from figure in cited paper.*

up to 1 Hz in *Escherichia coli* (Kralj et al., 2011b). Membrane localization of PROPS in eukaryotic cells failed, so the principle of reversing pump direction was applied to Archaerhodopsin 3 (Arch) from *Halorubrum sodomense*, which had known eukaryotic plasma membrane targeting (Kralj et al., 2011b). Site-directed mutagenesis of Arch yielded QuasArs ('quality superior to Arch'), which retained the rapid submillisecond kinetics of the original Arch voltage indicators but demonstrated much improved sensitivity and linear fluorescence responses to voltage changes (Hochbaum et al., 2014). The opsin core of QuasAr2 was enhanced to develop the Archon molecules (Piatkevich et al., 2018); compared to earlier Arch-derived sensors, Archon1 exhibits increased brightness, with high enough sensitivity to detect subthreshold voltage events as small as ∼5 mV with a SNR of 2 or greater and only a small decrease in speed compared to the original QuasAr2 GEVI (Piatkevich et al., 2018).

One significant limitation of microbial rhodopsin GEVIs is their low quantum efficiency which makes them at least 30 times dimmer than GFP (Hochbaum et al., 2014). Low photon release demands trial averaging to resolve AP waveforms and makes high frequency spike detection difficult. Dim fluorescence also necessitates increased laser power and risk of photobleaching and phototoxicity, however, this latter concern is minimized with red-shifted indicators due to the relative lack of autofluorescence in this spectrum. A significant advantage over Class II GEVIs is their fast kinetics and large dynamic ranges that enable resolution of individual AP waveforms even at high frequency firing rates akin to electrophysiological recordings.

### Class I-Hybrids: FRET-Opsin Indicators

To facilitate axonal AP recording, an ideal GEVI would combine the best characteristics of both classes: the speed of rhodopsin indicators with the brightness of VSD-containing probes. FRET-opsin hybrid reporters use bright fluorophores or synthetic dyes as donor molecules and rapid opsins as acceptor molecules, resulting in electrochromic FRET (eFRET). A promising recent hybrid probe fused a rhodopsin variant from *Acetabularia acetabulum* (Ace2N) with mNeonGreen (Gong et al., 2015). The resultant indicator has improved fluorophore brightness and fast (∼1 ms) kinetics with a more linear response to voltage than its predecessor (Gong et al., 2014). Ace2N-mNeon not only can resolve APs in single cells within live animals, but provides robust responses *in vivo* with resolution for single cell and single AP recording in mice and fruit flies (Gong et al., 2015). An exciting red-shifted indicator with comparable characteristics, VARNAM, couples Ace with mRuby3 (Kannan et al., 2018).

A variation of the FRET-opsin strategy is Voltron, which replaces the fluorescent protein FRET donor with a synthetic fluorescent dye. Dyes can be chosen based on their excitation and emission spectra and generally exhibit far superior optical properties of brightness or photostability. Voltron enables specific localization of the synthetic dyes by utilizing a self-labeling protein tag domain that covalently binds the donor dye and permanently couples it to an Ace2N voltage-sensing domain. Voltron bound to the dye molecule $JF_{525}$ (Grimm et al., 2017) ($Voltron_{525}$) exhibited the greatest sensitivity ($-23 \pm 1\%$ per 100 mV) of FRET-opsins (Abdelfattah et al., 2018).

Hybrid FRET-opsin indicators couple the superior brightness of VSD-containing GEVIs with speed approaching opsin-based GEVIs (∼1 ms). There are two significant disadvantages to FRET probes. First is a reduction in their sensitivity to voltage and curtailed response ranges. The second is that they use up much more of the excitation-emission spectrum that limits their combined expression with other genetically encoded indicators or actuators. The newest versions of these probes are bright enough for AP detection, but it will likely be challenging to resolve AP waveforms with their current kinetic properties in most nerve cells.

## OPTICAL APPROACHES TO PROBE MOLECULAR CONTROL OF PRESYNAPTIC APS

Bulk-loaded VS dyes have been successfully deployed to explore presynaptic APs from collections of fine terminals and axons emanating from parallel fibers of granule cells in the cerebellum (Sabatini and Regehr, 1997, 1999). These critical measurements established the impact that altering AP width has on $Ca^{2+}$ entry and neurotransmitter release in small nerve terminals that followed previous early electrophysiology in invertebrates (Byrne and Kandel, 1996). However, this technique of extracellular dye labeling is too non-specific to measure axonal responses as measurements are confounded by surrounding tissue including astrocytes, dendrites and heterogeneous axonal populations. The development of brighter VS dyes with fast kinetics (Yan et al., 2012) permitted single cell recording with intracellular loading. The "blue dye" type of VS dye (Zhou et al., 2007) was used to great effect to study axon collaterals and the cell bodies of layer 5 pyramidal cells, and pharmacological experiments demonstrated that narrow APs, as discussed above, are the result of a high density of Kv1 channels (Foust et al., 2011). 2-photon recording of hemicyanine VS dyes loaded into inhibitory stellate cells of the cerebellum revealed that Kv3 channels dominate the repolarization of fast APs in the presynaptic terminals while Kv1 channels were influential at the initial segment (Rowan et al., 2014). Adding to this diversity of $K^+$ channels modulating presynaptic APs are recordings from inhibitory neurons in the neocortex that identified different combinations of BK and Kv1 channels in fast-spiking and somatostatin-expressing interneurons (Casale et al., 2015).

The engineering of GEVIs with fast kinetics (Kralj et al., 2011a) has also enabled detailed measurements of the AP waveform in single cells with trial averaging. The first study to utilize the rhodopsin indicator Arch for measuring the presynaptic AP in *en passant* terminals leveraged its linear readout to calibrate the responses by forcing the membrane potential close to 0 mV with the cation-selective ionophore gramicidin. Excitatory hippocampal terminals were found to be rich in Kv1 channels and invaded by APs with low (+7 mV) overshoots that are ideally positioned for modulating Cav open probability (Hoppa et al., 2014). Arch was also used to robustly identify a dominant role for BK (Slo) channels at the *Drosophila* neuromuscular junction as a novel regulator of

synaptic transmission (Ford and Davis, 2014). Thus, both VS dyes and GEVIs have already begun contributing to our understanding of ion channel distributions in a variety of synaptic terminals.

## The Use of Optical Voltage Measurements to Study Compartmentalized Control and Temporal Aspects of the AP in the Axon

A recent review has highlighted various aspects of axon physiology to control the propagation of APs and compartmentalized signaling domains within the axon (Rama et al., 2018). Here, we discuss how VS dyes and GEVIs have contributed to our understanding of electrical signaling in the axon. The recent use of VS dyes has revealed remarkable levels of heterogeneity in the shape of the AP waveform between individual synapses of stellate neurons (Rowan et al., 2016). This paper convincingly introduces the AP as a plastic signal that modulates synaptic strength. *In vivo* recordings of voltage across the axonal arbors of Mi1 cells in the *Drosophila* visual system revealed incredible diversity between the AP waveforms that invaded presynaptic terminals depending on which cellular layer they innervated (Yang et al., 2016). These results were strongly correlated with differences in $Ca^{2+}$ imaging, indicative of an important role of the AP waveform in sensory physiology. Mechanisms underlying this heterogeneity are still being resolved. Toward this end, measurements of AP heterogeneity along the axon of excitatory hippocampal neurons *in vitro*

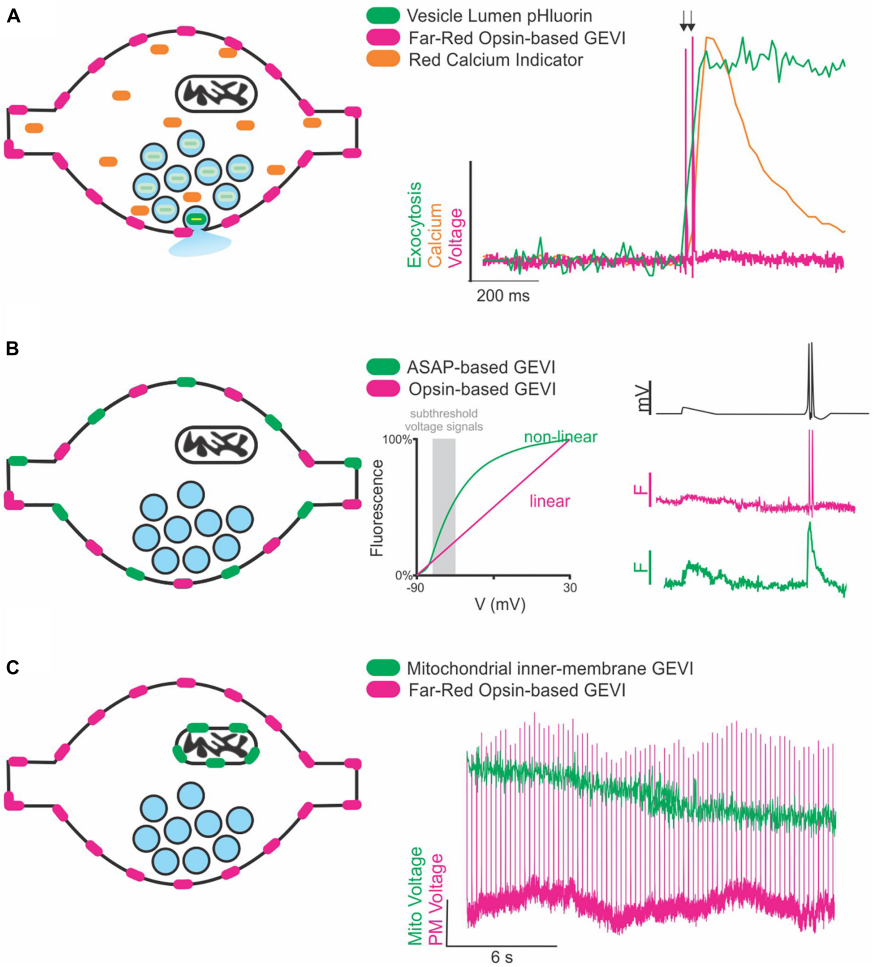


**FIGURE 1 |** Future directions of GEVIs to explore synaptic transmission. **(A)** Cartoon of a synapse expressing a far-red rhodopsin-based GEVI on the membrane and a cytosolic red $Ca^{2+}$ indicator. Vesicles (blue circles) contain pHluorin, a vesicular lumen-targeted pH-sensitive reporter of exocytosis (*left*). Theoretical traces (*right*) demonstrating recording of two single AP stimulations (arrows) superimposed with theoretical fluorescence traces of the $Ca^{2+}$ and exocytosis response in the same cell. **(B)** Cartoon of a synapse expressing two spectrally separate, membrane-targeted GEVIs (*left*). Subthreshold events (gray box, *center*) are in a voltage range better detected with large fluorescence changes by a non-linear indicator than a linear indicator. A theoretical voltage trace (*right, top*) of a subthreshold event followed by two single AP stimulations. Theoretical fluorescence traces of the linear (*middle*) and non-linear (*bottom*) indicators demonstrate how combining indicators could help resolve both sub- and suprathreshold events in the same cell. **(C)** Cartoon of a synapse expressing a membrane-targeted far-red GEVI, and a mitochondrial-targeted green GEVI (*left*). Theoretical fluorescence traces of both indicators demonstrate simultaneous recording of mitochondrial and membrane voltage dynamics in the same cell.

revealed a novel role for Navβ2 subunits in enabling successful propagation across axonal branch points (Cho et al., 2017). Thus, non-invasive multi-point recording along an axon is a distinct advantage of non-invasive optical voltage measurements. GEVIs have also contributed to our understanding of synaptic plasticity and how AP shape alterations during high frequency firing can depress or facilitate synaptic transmission (Jackman and Regehr, 2017). A recent publication was able to demonstrate *ex vivo* recordings of axons using GEVIs to explore AP broadening in the fine axons of mossy fibers (Ma et al., 2017), reminiscent of original recordings from terminals (Geiger and Jonas, 2000).

## Future Directions of GEVIs to Explore Synaptic Transmission

A recent review of voltage indicators predicted that the future of voltage indicators, especially regarding their use *in vivo*, is brighter, more sensitive, and redder; we would hasten to add faster as well for use in resolving an AP (Xu et al., 2017). Indeed, for many aspects of signal detection the use of red excitation and far-red emission GEVIs and VS dyes has distinct advantages as previously summarized (Xu et al., 2017). However, a host of fluorescent green (blue light excited) dyes and genetically encoded indicators exist to measure other properties of synaptic transmission including vesicle lumen pH, calcium, and neurotransmitters themselves. Therefore, thanks to the large spectral separation of far-red VS dyes and GEVIs from GFP-based reporters, future experiments can combine these green emission indicators with red voltage sensors to monitor not only how ion channels and their binding partners modulate voltage but how that translates to other aspects of synaptic function (**Figure 1A**). This spectral separation has already been combined with blue-light excited ion channels to investigate cellular (Emiliani et al., 2015) and subcellular aspects of neural excitation (Fan et al., 2018).

Multiple GEVIs with divergent spectral emission also be combined with great effect to study interesting aspects of axon physiology beyond the AP, especially if the two indicators have divergent sensitivities (linear and non-linear) to voltage. This situation could be exploited in future studies to detect different types of voltage signaling in the axon (**Figure 1B**). APs are difficult signals to measure due to their very rapid kinetics, but easy in terms of the large (>80 mV) voltage change, thus fast and linear indicators are optimal. However, there are also several types of subthreshold signals within the axon that do not initiate APs but do influence synaptic transmission that are slower and have smaller voltage changes (<10 mV) (Zbili et al., 2016; Rowan and Christie, 2017). Currently, small voltage changes in the axon are more challenging to detect using linear indicators with rapid kinetics such as an opsin-based GEVI including QuasAr, but less so for slower, brighter GEVIs that have non-linear responses to voltage such as ASAP (St-Pierre et al., 2014). These two indicators could be combined and simultaneously monitored to explore sub-threshold voltage in relation to AP propagation and modulation of waveform kinetics.

A third area of future interest measuring voltage with GEVIs would be to move beyond the plasma membrane. Given that light is not constrained by any size restriction, we can move much smaller than the synaptic terminal and explore how voltage might control other aspects of synaptic transmission at the level of organelles (**Figure 1C**). In theory, any membrane can use voltage for signaling or function including, but not limited to, synaptic vesicles and mitochondria. Voltage modulation in organelles is severely understudied and could benefit from adapting GEVIs to new forms of subcellular targeting such as those recently deployed for targeting Archaerhodopsins to synaptic vesicles and lysosomes (Rost et al., 2015). We are in the infancy of voltage detection with light and the future seems bright to learning new aspects of neurobiology in health and disease states.

## AUTHOR CONTRIBUTIONS

LP and MH conceptualized and designed the study, and drafted and revised the article.

## FUNDING

This work was supported by the Esther A. and Joseph Klingenstein Fund (LP and MH), National Science Foundations Grant IOS 1750199 (MH), and support from the GAANN Department of Education #P200A150059 (LP).

## ACKNOWLEDGMENTS

We thank Scott Alpizar for critically reading of the manuscript.

## REFERENCES

Abdelfattah, A. S., Farhi, S. L., Zhao, Y., Brinks, D., Zou, P., Ruangkittisakul, A., et al. (2016). A bright and fast red fluorescent protein voltage indicator that reports neuronal activity in organotypic brain slices. *J. Neurosci.* 36, 2458–2472. doi: 10.1523/JNEUROSCI.3484-15.2016

Abdelfattah, A. S., Kawashima, T., Singh, A., Novak, N., Liu, H., Svoboda, K., et al. (2018). Bright and photostable chemigenetic indicators for extended in vivo voltage imaging. *bioRxiv* [Preprint]. doi: 10.1101/436840

Ashcroft, F. M. (2012). *The Spark of Life: Electricity in the Human Body*. New York, NY: Norton.

Ataka, K., and Pieribone, V. A. (2002). A genetically targetable fluorescent probe of channel gating with rapid kinetics. *Biophys. J.* 82, 509–516. doi: 10.1016/S0006-3495(02)75415-5

Augustine, G. J., Charlton, M. P., and Smith, S. J. (1985). Calcium entry and transmitter release at voltage-clamped nerve terminals of squid. *J. Physiol.* 367, 163–181. doi: 10.1113/jphysiol.1985.sp015819

Baird, G. S., Zacharias, D. A., and Tsien, R. Y. (1999). Circular permutation and receptor insertion within green fluorescent proteins. *Proc. Natl. Acad. Sci. U.S.A.* 96, 11241–11246. doi: 10.1073/pnas.96.20.11241

Bean, B. P. (2007). The action potential in mammalian central neurons. *Nat. Rev. Neurosci.* 8, 451–465. doi: 10.1038/nrn2148

Beja, O., Spudich, E. N., Spudich, J. L., Leclerc, M., and DeLong, E. F. (2001). Proteorhodopsin phototrophy in the ocean. *Nature* 411, 786–789. doi: 10.1038/35081051

Bischofberger, J., Geiger, J. R., and Jonas, P. (2002). Timing and efficacy of Ca2+ channel activation in hippocampal mossy fiber boutons. *J. Neurosci.* 22, 10593–10602. doi: 10.1523/JNEUROSCI.22-24-10593.2002

Borst, J. G., and Sakmann, B. (1999). Effect of changes in action potential shape on calcium currents and transmitter release in a calyx-type synapse of the rat auditory brainstem. *Philos. Trans. R. Soc. Lond. B Biol. Sci.* 354, 347–355. doi: 10.1098/rstb.1999.0386

Brown, M. T., Henny, P., Bolam, J. P., and Magill, P. J. (2009). Activity of neurochemically heterogeneous dopaminergic neurons in the substantia nigra during spontaneous and driven changes in brain state. *J. Neurosci.* 29, 2915–2925. doi: 10.1523/JNEUROSCI.4423-08.2009

Byrne, J. H., and Kandel, E. R. (1996). Presynaptic facilitation revisited: state and time dependence. *J. Neurosci.* 16, 425–435. doi: 10.1523/JNEUROSCI.16-02-00425.1996

Casale, A. E., Foust, A. J., Bal, T., and McCormick, D. A. (2015). Cortical interneuron subtypes vary in their axonal action potential properties. *J. Neurosci.* 35, 15555–15567. doi: 10.1523/JNEUROSCI.1467-13.2015

Chavarha, M., Villette, V., Dimov, I., Pradhan, L., Evans, S., Shi, D., et al. (2018). Fast two-photon volumetric imaging of an improved voltage indicator reveals electrical activity in deeply located neurons in the awake brain. *bioRxiv* [Preprint]. doi: 10.1101/445064

Chen, T. W., Wardill, T. J., Sun, Y., Pulver, S. R., Renninger, S. L., Baohan, A., et al. (2013). Ultrasensitive fluorescent proteins for imaging neuronal activity. *Nature* 499, 295–300. doi: 10.1038/nature12354

Child, N. D., and Benarroch, E. E. (2014). Differential distribution of voltage-gated ion channels in cortical neurons: implications for epilepsy. *Neurology* 82, 989–999. doi: 10.1212/WNL.0000000000000228

Cho, I. H., Panzera, L. C., Chin, M., and Hoppa, M. B. (2017). Sodium channel beta2 subunits prevent action potential propagation failures at axonal branch points. *J. Neurosci.* 37, 9519–9533. doi: 10.1523/JNEUROSCI.0891-17.2017

Connors, B. W., and Gutnick, M. J. (1990). Intrinsic firing patterns of diverse neocortical neurons. *Trends Neurosci* 13, 99–104. doi: 10.1016/0166-2236(90)90185-D

Covarrubias, M., Wei, A. A., and Salkoff, L. (1991). Shaker, Shal, Shab, and Shaw express independent K+ current systems. *Neuron* 7, 763–773. doi: 10.1016/0896-6273(91)90279-9

Dioumaev, A. K., Wang, J. M., Balint, Z., Varo, G., and Lanyi, J. K. (2003). Proton transport by proteorhodopsin requires that the retinal Schiff base counterion Asp-97 be anionic. *Biochemistry* 42, 6582–6587. doi: 10.1021/bi034253r

Dodge, F. A. Jr., and Rahamimoff, R. (1967). Co-operative action a calcium ions in transmitter release at the neuromuscular junction. *J. Physiol.* 193, 419–432. doi: 10.1113/jphysiol.1967.sp008367

Dodson, P. D., Barker, M. C., and Forsythe, I. D. (2002). Two heteromeric Kv1 potassium channels differentially regulate action potential firing. *J. Neurosci.* 22, 6953–6961. doi: 10.1523/JNEUROSCI.22-16-06953.2002

Dodson, P. D., and Forsythe, I. D. (2004). Presynaptic K+ channels: electrifying regulators of synaptic terminal excitability. *Trends Neurosci.* 27, 210–217. doi: 10.1016/j.tins.2004.02.012

Emiliani, V., Cohen, A. E., Deisseroth, K., and Hausser, M. (2015). All-optical interrogation of neural circuits. *J. Neurosci.* 35, 13917–13926. doi: 10.1523/JNEUROSCI.2916-15.2015

Engel, D., and Jonas, P. (2005). Presynaptic action potential amplification by voltage-gated Na+ channels in hippocampal mossy fiber boutons. *Neuron* 45, 405–417. doi: 10.1016/j.neuron.2004.12.048

Fan, L. Z., Nehme, R., Adam, Y., Jung, E. S., Wu, H., Eggan, K., et al. (2018). All-optical synaptic electrophysiology probes mechanism of ketamine-induced disinhibition. *Nat. Methods* 15, 823–831. doi: 10.1038/s41592-018-0142-8

Ford, K. J., and Davis, G. W. (2014). Archaerhodopsin voltage imaging: synaptic calcium and BK channels stabilize action potential repolarization at the Drosophila neuromuscular junction. *J. Neurosci.* 34, 14517–14525. doi: 10.1523/JNEUROSCI.2203-14.2014

Foust, A. J., Yu, Y., Popovic, M., Zecevic, D., and McCormick, D. A. (2011). Somatic membrane potential and Kv1 channels control spike repolarization in cortical axon collaterals and presynaptic boutons. *J. Neurosci.* 31, 15490–15498. doi: 10.1523/JNEUROSCI.2752-11.2011

Geiger, J. R., and Jonas, P. (2000). Dynamic control of presynaptic Ca(2+) inflow by fast-inactivating K(+) channels in hippocampal mossy fiber boutons. *Neuron* 28, 927–939. doi: 10.1016/S0896-6273(00)00164-1

Gentet, L. J., Avermann, M., Matyas, F., Staiger, J. F., and Petersen, C. C. (2010). Membrane potential dynamics of GABAergic neurons in the barrel cortex of behaving mice. *Neuron* 65, 422–435. doi: 10.1016/j.neuron.2010.01.006

Gong, Y., Huang, C., Li, J. Z., Grewe, B. F., Zhang, Y., Eismann, S., et al. (2015). High-speed recording of neural spikes in awake mice and flies with a fluorescent voltage sensor. *Science* 350, 1361–1366. doi: 10.1126/science.aab0810

Gong, Y., Wagner, M. J., Zhong Li, J., and Schnitzer, M. J. (2014). Imaging neural spiking in brain tissue using FRET-opsin protein voltage sensors. *Nat. Commun.* 5:3674. doi: 10.1038/ncomms4674

Grace, A. A., and Bunney, B. S. (1984). The control of firing pattern in nigral dopamine neurons: single spike firing. *J. Neurosci.* 4, 2866–2876. doi: 10.1523/JNEUROSCI.04-11-02866.1984

Grimm, J. B., Muthusamy, A. K., Liang, Y., Brown, T. A., Lemon, W. C., Patel, R., et al. (2017). A general method to fine-tune fluorophores for live-cell and in vivo imaging. *Nat. Methods* 14, 987–994. doi: 10.1038/nmeth.4403

Hochbaum, D. R., Zhao, Y., Farhi, S. L., Klapoetke, N., Werley, C. A., Kapoor, V., et al. (2014). All-optical electrophysiology in mammalian neurons using engineered microbial rhodopsins. *Nat. Methods* 11, 825–833. doi: 10.1038/nmeth.3000

Hodgkin, A. L., and Huxley, A. F. (1952). The components of membrane conductance in the giant axon of Loligo. *J. Physiol.* 116, 473–496. doi: 10.1113/jphysiol.1952.sp004718

Hodgkin, A. L., Huxley, A. F., and Katz, B. (1952). Measurement of current-voltage relations in the membrane of the giant axon of Loligo. *J. Physiol.* 116, 424–448. doi: 10.1113/jphysiol.1952.sp004716

Hoppa, M. B., Gouzer, G., Armbruster, M., and Ryan, T. A. (2014). Control and plasticity of the presynaptic action potential waveform at small CNS nerve terminals. *Neuron* 84, 778–789. doi: 10.1016/j.neuron.2014.09.038

Huang, Y. L., Walker, A. S., and Miller, E. W. (2015). A photostable silicon rhodamine platform for optical voltage sensing. *J. Am. Chem. Soc.* 137, 10767–10776. doi: 10.1021/jacs.5b06644

Jackman, S. L., and Regehr, W. G. (2017). The mechanisms and functions of synaptic facilitation. *Neuron* 94, 447–464. doi: 10.1016/j.neuron.2017.02.047

Jackson, M. B., Konnerth, A., and Augustine, G. J. (1991). Action potential broadening and frequency-dependent facilitation of calcium signals in pituitary nerve terminals. *Proc. Natl. Acad. Sci. U.S.A.* 88, 380–384. doi: 10.1073/pnas.88.2.380

Jan, L. Y., and Jan, Y. N. (2012). Voltage-gated potassium channels and the diversity of electrical signalling. *J. Physiol.* 590, 2591–2599. doi: 10.1113/jphysiol.2011.224212

Jin, L., Han, Z., Platisa, J., Wooltorton, J. R., Cohen, L. B., and Pieribone, V. A. (2012). Single action potentials and subthreshold electrical events imaged in neurons with a fluorescent protein voltage probe. *Neuron* 75, 779–785. doi: 10.1016/j.neuron.2012.06.040

Kannan, M., Vasan, G., Huang, C., Haziza, S., Li, J. Z., Inan, H., et al. (2018). Fast, in vivo voltage imaging using a red fluorescent indicator. *Nat. Methods* 15, 1108–1116. doi: 10.1038/s41592-018-0188-7

Kawaguchi, S. Y., and Sakaba, T. (2015). Control of inhibitory synaptic outputs by low excitability of axon terminals revealed by direct recording. *Neuron* 85, 1273–1288. doi: 10.1016/j.neuron.2015.02.013

Knopfel, T., Gallero-Salas, Y., and Song, C. (2015). Genetically encoded voltage indicators for large scale cortical imaging come of age. *Curr. Opin. Chem. Biol.* 27, 75–83. doi: 10.1016/j.cbpa.2015.06.006

Kole, M. H., and Stuart, G. J. (2012). Signal processing in the axon initial segment. *Neuron* 73, 235–247. doi: 10.1016/j.neuron.2012.01.007

Kralj, J. M., Douglass, A. D., Hochbaum, D. R., Maclaurin, D., and Cohen, A. E. (2011a). Optical recording of action potentials in mammalian neurons using a microbial rhodopsin. *Nat. Methods* 9, 90–95. doi: 10.1038/nmeth.1782

Kralj, J. M., Hochbaum, D. R., Douglass, A. D., and Cohen, A. E. (2011b). Electrical spiking in *Escherichia coli* probed with a fluorescent voltage-indicating protein. *Science* 333, 345–348. doi: 10.1126/science.1204763

Kullmann, D. M. (2010). Neurological channelopathies. *Annu. Rev. Neurosci.* 33, 151–172. doi: 10.1146/annurev-neuro-060909-153122

Lee, S., Geiller, T., Jung, A., Nakajima, R., Song, Y. K., and Baker, B. J. (2017). Improving a genetically encoded voltage indicator by modifying the cytoplasmic charge composition. *Sci. Rep.* 7:8286. doi: 10.1038/s41598-017-08731-2

Lisman, J. E., Raghavachari, S., and Tsien, R. W. (2007). The sequence of events that underlie quantal transmission at central glutamatergic synapses. *Nat. Rev. Neurosci.* 8, 597–609. doi: 10.1038/nrn2191

Llinas, R., Steinberg, I. Z., and Walton, K. (1981). Relationship between presynaptic calcium current and postsynaptic potential in squid giant synapse. *Biophys. J.* 33, 323–351. doi: 10.1016/S0006-3495(81)84899-0

Llinas, R. R. (1988). The intrinsic electrophysiological properties of mammalian neurons: insights into central nervous system function. *Science* 242, 1654–1664. doi: 10.1126/science.3059497

Ma, Y., Bayguinov, P. O., and Jackson, M. B. (2017). Action potential dynamics in fine axons probed with an axonally targeted optical voltage sensor. *eNeuro* 4:ENEURO.0146–17. doi: 10.1523/ENEURO.0146-17.2017

McCormick, D. A., Connors, B. W., Lighthall, J. W., and Prince, D. A. (1985). Comparative electrophysiology of pyramidal and sparsely spiny stellate neurons of the neocortex. *J. Neurophysiol.* 54, 782–806. doi: 10.1152/jn.1985.54.4.782

Mishchenko, Y., Hu, T., Spacek, J., Mendenhall, J., Harris, K. M., and Chklovskii, D. B. (2010). Ultrastructural analysis of hippocampal neuropil from the connectomics perspective. *Neuron* 67, 1009–1020. doi: 10.1016/j.neuron.2010.08.014

Murata, Y., Iwasaki, H., Sasaki, M., Inaba, K., and Okamura, Y. (2005). Phosphoinositide phosphatase activity coupled to an intrinsic voltage sensor. *Nature* 435, 1239–1243. doi: 10.1038/nature03650

Nakajima, R., Jung, A., Yoon, B. J., and Baker, B. J. (2016). Optogenetic monitoring of synaptic activity with genetically encoded voltage indicators. *Front. Synaptic Neurosci.* 8:22. doi: 10.3389/fnsyn.2016.00022

Peterka, D. S., Takahashi, H., and Yuste, R. (2011). Imaging voltage in neurons. *Neuron* 69, 9–21. doi: 10.1016/j.neuron.2010.12.010

Piao, H. H., Rajakumar, D., Kang, B. E., Kim, E. H., and Baker, B. J. (2015). Combinatorial mutagenesis of the voltage-sensing domain enables the optical resolution of action potentials firing at 60 Hz by a genetically encoded fluorescent sensor of membrane potential. *J. Neurosci.* 35, 372–385. doi: 10.1523/JNEUROSCI.3008-14.2015

Piatkevich, K. D., Jung, E. E., Straub, C., Linghu, C., Park, D., Suk, H. J., et al. (2018). A robotic multidimensional directed evolution approach applied to fluorescent voltage reporters. *Nat. Chem. Biol.* 14, 352–360. doi: 10.1038/s41589-018-0004-9

Rama, S., Zbili, M., Bialowas, A., Fronzaroli-Molinieres, L., Ankri, N., Carlier, E., et al. (2015). Presynaptic hyperpolarization induces a fast analogue modulation of spike-evoked transmission mediated by axonal sodium channels. *Nat Commun* 6:10163. doi: 10.1038/ncomms10163

Rama, S., Zbili, M., and Debanne, D. (2018). Signal propagation along the axon. *Curr. Opin. Neurobiol.* 51, 37–44. doi: 10.1016/j.conb.2018.02.017

Raman, I. M., and Bean, B. P. (1999). Ionic currents underlying spontaneous action potentials in isolated cerebellar Purkinje neurons. *J. Neurosci.* 19, 1663–1674. doi: 10.1523/JNEUROSCI.19-05-01663.1999

Rosenmund, C., Clements, J. D., and Westbrook, G. L. (1993). Nonuniform probability of glutamate release at a hippocampal synapse. *Science* 262, 754–757. doi: 10.1126/science.7901909

Rost, B. R., Schneider, F., Grauel, M. K., Wozny, C., Bentz, C., Blessing, A., et al. (2015). Optogenetic acidification of synaptic vesicles and lysosomes. *Nat. Neurosci.* 18, 1845–1852. doi: 10.1038/nn.4161

Rowan, M. J., DelCanto, G., Yu, J. J., Kamasawa, N., and Christie, J. M. (2016). Synapse-level determination of action potential duration by k(+) channel clustering in axons. *Neuron* 91, 370–383. doi: 10.1016/j.neuron.2016.05.035

Rowan, M. J., Tranquil, E., and Christie, J. M. (2014). Distinct Kv channel subtypes contribute to differences in spike signaling properties in the axon initial segment and presynaptic boutons of cerebellar interneurons. *J. Neurosci.* 34, 6611–6623. doi: 10.1523/JNEUROSCI.4208-13.2014

Rowan, M. J. M., and Christie, J. M. (2017). Rapid state-dependent alteration in Kv3 channel availability drives flexible synaptic signaling dependent on somatic subthreshold depolarization. *Cell Rep.* 18, 2018–2029. doi: 10.1016/j.celrep.2017.01.068

Sabatini, B. L., and Regehr, W. G. (1997). Control of neurotransmitter release by presynaptic waveform at the granule cell to Purkinje cell synapse. *J. Neurosci.* 17, 3425–3435. doi: 10.1523/JNEUROSCI.17-10-03425.1997

Sabatini, B. L., and Regehr, W. G. (1999). Timing of synaptic transmission. *Annu. Rev. Physiol.* 61, 521–542. doi: 10.1146/annurev.physiol.61.1.521

Schneggenburger, R., and Neher, E. (2000). Intracellular calcium dependence of transmitter release rates at a fast central synapse. *Nature* 406, 889–893. doi: 10.1038/35022702

Shepherd, G. M., and Harris, K. M. (1998). Three-dimensional structure and composition of CA3– > CA1 axons in rat hippocampal slices: implications for presynaptic connectivity and compartmentalization. *J. Neurosci.* 18, 8300–8310. doi: 10.1523/JNEUROSCI.18-20-08300.1998

Siegel, M. S., and Isacoff, E. Y. (1997). A genetically encoded optical probe of membrane voltage. *Neuron* 19, 735–741. doi: 10.1016/S0896-6273(00)80955-1

Sierksma, M. C., and Borst, J. G. G. (2017). Resistance to action potential depression of a rat axon terminal in vivo. *Proc. Natl. Acad. Sci. U.S.A.* 114, 4249–4254. doi: 10.1073/pnas.1619433114

Sofroniew, N. J., Flickinger, D., King, J., and Svoboda, K. (2016). A large field of view two-photon mesoscope with subcellular resolution for in vivo imaging. *eLife* 5:e14472. doi: 10.7554/eLife.14472

Storace, D. A., Braubach, O. R., Jin, L., Cohen, L. B., and Sung, U. (2015). Monitoring brain activity with protein voltage and calcium sensors. *Sci. Rep.* 5, 1–15. doi: 10.1038/srep10212

Storace, D., Sepehri Rad, M., Kang, B., Cohen, L. B., Hughes, T., and Baker, B. J. (2016). Toward better genetically encoded sensors of membrane potential. *Trends Neurosci.* 39, 277–289. doi: 10.1016/j.tins.2016.02.005

St-Pierre, F., Chavarha, M., and Lin, M. Z. (2015). Designs and sensing mechanisms of genetically encoded fluorescent voltage indicators. *Curr. Opin. Chem. Biol.* 27, 31–38. doi: 10.1016/j.cbpa.2015.05.003

St-Pierre, F., Marshall, J. D., Yang, Y., Gong, Y., Schnitzer, M. J., and Lin, M. Z. (2014). High-fidelity optical reporting of neuronal electrical activity with an ultrafast fluorescent voltage sensor. *Nat. Neurosci.* 17, 884–889. doi: 10.1038/nn.3709

Vivekananda, U., Novak, P., Bello, O. D., Korchev, Y. E., Krishnakumar, S. S., Volynski, K. E., et al. (2017). Kv1.1 channelopathy abolishes presynaptic spike width modulation by subthreshold somatic depolarization. *Proc. Natl. Acad. Sci. U.S.A.* 114, 2395–2400. doi: 10.1073/pnas.1608763114

Woodford, C. R., Frady, E. P., Smith, R. S., Morey, B., Canzi, G., Palida, S. F., et al. (2015). Improved PeT molecules for optically sensing voltage in neurons. *J. Am. Chem. Soc.* 137, 1817–1824. doi: 10.1021/ja510602z

Xu, Y., Zou, P., and Cohen, A. E. (2017). Voltage imaging with genetically encoded indicators. *Curr. Opin. Chem. Biol.* 39, 1–10. doi: 10.1016/j.cbpa.2017.04.005

Yan, P., Acker, C. D., Zhou, W. L., Lee, P., Bollensdorff, C., Negrean, A., et al. (2012). Palette of fluorinated voltage-sensitive hemicyanine dyes. *Proc. Natl. Acad. Sci. U.S.A.* 109, 20443–20448. doi: 10.1073/pnas.1214850109

Yang, H. H., St-Pierre, F., Sun, X., Ding, X., Lin, M. Z., and Clandinin, T. R. (2016). Subcellular imaging of voltage and calcium signals reveals neural processing in vivo. *Cell* 166, 245–257. doi: 10.1016/j.cell.2016.05.031

Zbili, M., Rama, S., and Debanne, D. (2016). Dynamic control of neurotransmitter release by presynaptic potential. *Front. Cell Neurosci.* 10:278. doi: 10.3389/fncel.2016.00278

Zhou, W. L., Yan, P., Wuskell, J. P., Loew, L. M., and Antic, S. D. (2007). Intracellular long-wavelength voltage-sensitive dyes for studying the dynamics of action potentials in axons and thin dendrites. *J. Neurosci. Methods* 164, 225–239. doi: 10.1016/j.jneumeth.2007.05.002

Zucker, R. S., and Fogelson, A. L. (1986). Relationship between transmitter release and presynaptic calcium influx when calcium enters through discrete channels. *Proc. Natl. Acad. Sci. U.S.A.* 83, 3032–3036. doi: 10.1073/pnas.83.9.3032

**Conflict of Interest Statement:** The authors declare that the research was conducted in the absence of any commercial or financial relationships that could be construed as a potential conflict of interest.

*Copyright © 2019 Panzera and Hoppa. This is an open-access article distributed under the terms of the Creative Commons Attribution License (CC BY). The use, distribution or reproduction in other forums is permitted, provided the original author(s) and the copyright owner(s) are credited and that the original publication in this journal is cited, in accordance with accepted academic practice. No use, distribution or reproduction is permitted which does not comply with these terms.*

frontiers in Cellular Neuroscience

BRIEF RESEARCH REPORT
published: 13 March 2019
doi: 10.3389/fncel.2019.00091

# Overexpression of Calretinin Enhances Short-Term Synaptic Depression

*Alexey P. Bolshakov[1,2], Alexander Kolleker[3,4], Evgenia P. Volkova[2], Fliza Valiullina-Rakhmatullina[5], Peter M. Kolosov[1] and Andrei Rozov[5,6]**

[1]*Institute of Higher Nervous Activity and Neurophysiology, Russian Academy of Sciences (RAS), Moscow, Russia,* [2]*Research Laboratory of Electrophysiology, Pirogov Russian National Research Medical University, Moscow, Russia,* [3]*Max Planck Institute for Medical Research, Department of Molecular Neurobiology, Heidelberg, Germany,* [4]*Medical Institute, Buryat State University, Ulan-Ude, Russia,* [5]*Laboratory of Neurobiology, Institute of Fundamental Medicine and Biology, Kazan Federal University, Kazan, Russia,* [6]*Department of Physiology and Pathophysiology, University of Heidelberg, Heidelberg, Germany*

Analysis of the effects of various proteins on short-term synaptic plasticity is a difficult task, which may require the use of knockout animals. Here, we propose an alternative experimental approach for studying the roles of desired proteins in synaptic plasticity. We packed the $Ca^{2+}$-binding protein calretinin and the fluorescent protein Venus into AAV and injected the concentrated viral suspension into the neocortex of newborn rats. The infected layer 2/3 pyramidal cells were identified in rat cortical slices using Venus fluorescence. Analysis of short-term synaptic plasticity using paired patch clamp recordings between layer 2/3 pyramidal cells (presynaptic cell) and fast-spiking (FS) interneurons (post-synaptic cell) showed that calretinin expression in the pyramidal cells did not change the failure rate in this synapse but did decrease synaptic delay. Analysis of the parameters of short-term synaptic plasticity showed that the amplitude of the first EPSP in the train was not affected by calretinin, however, calretinin strongly enhanced short-term depression. In addition, we found that the effect of calretinin depended on the presynaptic firing frequency: an increase in frequency resulted in enhancement of synaptic depression.

**Keywords: interneuron, calretenin, release probability, viral expression, pyramidal cells, neocortex**

OPEN ACCESS

***Edited by:***
*Shin-ya Kawaguchi, Kyoto University, Japan*

***Reviewed by:***
*Yukihiro Nakamura, Jikei University School of Medicine, Japan*
*Takafumi Miki, Doshisha University Graduate School of Brain Science, Japan*

****Correspondence:***
*Andrei Rozov*
*andrei.rozov@physiologie.uni-heidelberg.de*

***Received:*** *02 December 2018*
***Accepted:*** *22 February 2019*
***Published:*** *13 March 2019*

***Citation:***
*Bolshakov AP, Kolleker A, Volkova EP, Valiullina-Rakhmatullina F, Kolosov PM and Rozov A (2019) Overexpression of Calretinin Enhances Short-Term Synaptic Depression. Front. Cell. Neurosci. 13:91. doi: 10.3389/fncel.2019.00091*

## INTRODUCTION

A large number of cytosolic proteins have the capacity to bind $Ca^{2+}$, however, traditionally three of them, parvalbumin, calbindin, and calretinin, are considered to act as the main $Ca^{2+}$-endogenous buffers. These proteins differ by $Ca^{2+}$-affinity, expression pattern, and binding kinetics, which determine their effect on synaptic efficacy and plasticity. Analysis of their functional role may be quite challenging because some of these proteins are predominantly expressed in interneurons constituting a relatively small neuronal population (<20%), which is further subdivided into numerous subtypes. Each subtype has its own unique connectivity pattern, synaptic properties, and $Ca^{2+}$-endogenous buffer expression profile. It would not be an exaggeration to say that for the vast majority of interneurons most of these parameters are not well studied when compared to the excitatory synapses formed by cortical glutamatergic neurons. The second complication arises from the classical investigation approach of the function of specific gene products by comparing WT and knockout animals. In the case of endogenous $Ca^{2+}$ buffers, this should be done on connections

where the identities of both pre- and post-synaptic neurons are constant in all experiments, this requirement greatly narrows experimental conditions. Moreover, it has been shown that the removal of some $Ca^{2+}$-binding proteins has more global consequences than simply reduction of endogenous buffer capacity. For instance, parvalbumin knockout leads to changes in short-term plasticity from depression to facilitation (Caillard et al., 2000), but also affects mitochondrial morphology (Henzi and Schwaller, 2015; Lichvarova et al., 2018). Ideally, the effects of chronic deletion of endogenous $Ca^{2+}$ buffers should be confirmed by wash-in experiments, where exogenously loaded buffer rescues the affected function (Blatow et al., 2003). In the case of calretinin, these research obstacles are multiplied by the fact that cortical interneurons expressing this protein predominantly innervate other GABAergic interneurons (Caputi et al., 2009). Consequently, both pre- and post-synaptic cells belong to "neuronal minorities," which make quite difficult to reliably find connected neuron pairs. However, the biophysical rules, by which endogenous buffers shape $Ca^{2+}$ dynamics, depend on $Ca^{2+}$ binding properties rather than the identity of the synapse. Indeed, partial activity-dependent saturation of calbindin underlies facilitation in both neocortical GABAergic and hippocampal glutamatergic terminals (Blatow et al., 2003). Thus, artificially expressed calretinin in terminals with initially low buffer capacity should affect intracellular $Ca^{2+}$ concentration ($[Ca^{2+}]_i$) in a similar way as it does in WT calretitin-positive interneurons. Pyramidal cells in layer 2/3 of the rat somatosensory cortex have low endogenous $Ca^{2+}$ capacity and some of the excitatory connections formed by these neurons are very well characterized (Rozov et al., 2001). Therefore, in order to study the effect of calretinin on synaptic release, the protein was virally introduced into these cells. As the "calretinin knockout neurons" we used either Venus-negative cells in the same slice or/and layer 2/3 pyramidal cells in slices from non-infected rats. Applying this approach we characterized the effects of calretinin on synaptic efficacy and plasticity at one of the most well studied neocortical synapses formed by presynaptic layer 2/3 pyramidal cells and postsynaptic fast-spiking (FS) interneurons (Gupta et al., 2000; Koester and Sakmann, 2000; Rozov et al., 2001; Blatow et al., 2003; Holmgren et al., 2003; Watanabe et al., 2005; Neske et al., 2015; Pala and Petersen, 2015; Voinova et al., 2015).

# MATERIALS AND METHODS

All experiments with animals were performed in line with the Russian rules regulating the use of animals for experimental studies and the European Communities Council Directive 86/609/EEC. The protocol of the experiment was approved by the Ethical Commission of the Institute of Higher Nervous Activity and Neurophysiology of the Russian Academy of Sciences.

## Cloning of the pAAV-Syn-Calr-IRES-Venus Plasmid

Total mouse mRNA from the forebrain was obtained with TRI Reagent (MRC) extraction and converted to cDNA with the reverse transcription reaction using a mixture of random oligonucleotides (N6) and 20-mer oligo(dT) primers._ORF of the calretinin precursor was amplified from cDNA with a pair of primers: ATGGATCCTTACACGGGGGGCTCACTGC and ATGCTAGCGCCGCCACCATGGCTGGCCCGCAGCAG. The PCR fragment was cloned into a pBluescript vector and sequenced from both ends. Clones confirmed with the proper sequence were used for further cloning; the fragment was excised with NheI and BamHI restriction enzymes and cloned into the pAAV-Syn-IRES-Venus plasmid (**Figure 1A**).

## Injection

An AAV cassette carrying mouse calretinin-IRES-Venus under a synapsin promoter was packed into AAV using a mix of pDp1 and pDp2 packing vectors (Grimm et al., 2003). The viral suspension was concentrated using a HiTrap Heparin HP affinity column (GE Health Care, Uppsala, Sweden). At P0-P1, rat pups were anesthetized using cold, and two injections (1 μl per site) were made in the somatosensory cortex as previously described (Pilpel et al., 2009). At P14–P23, the injected rat pups were decapitated and the injected half of the neocortex was used to prepare 300-μm-thick parasagittal cortical slices.

## Patch Clamp Recording

Neocortical brain slices were prepared and stored as described (Valiullina et al., 2016). Patch electrodes for both cells were filled with a solution which consisted of (in mM) K-gluconate, 140; KCl, 5; HEPES, 10; NaCl, 8; MgATP, 4; GTP, 0.3; and phosphocreatine, 10 (pH 7.3 with KOH). ACSF contained (in mM) 125 NaCl, 2.5 KCl, 25 glucose, 25 $NaHCO_3$, 1.25 $NaH_2PO_4$, 2 $CaCl_2$, and 1 $MgCl_2$ (carboxygenated with 5% $CO_2$/95% $O_2$). The infected layer 2/3 pyramidal cells were identified using Venus fluorescence and IR-DIC imaging. In paired recordings, postsynaptic putative FS basket cells in layer 2/3 were identified by location, morphology, and firing pattern (Reyes et al., 1998). All experiments were carried out at room temperature (23–25°C). Signals were recorded using a MultiClamp 700B amplifier, filtered at 3 kHz, and digitized at 10 kHz using a Digidata 1440a (Molecular Devices, USA) and Clampex 10.5 acquisition software (Molecular Devices/Axon Instruments, San Jose, USA).

Synaptic delay was measured as the time difference between an action potential (AP) peak and the onset of the corresponding postsynaptic EPSP, then the values obtained for the individual cell pairs were averaged to get the final estimate.

After electrophysiological recordings, slices were fixed in 4% paraformaldehyde and stained using anti-calretinin antibodies (Swant Inc., dilution 1:1,000). **Figure 1B** shows an image of an infected neocortex stained with anti-calretinin antibodies. Image analysis of images showed that Venus expression always colocalized with calretinin in layer 2/3 ($n = 52$ cells).

The statistical significance of differences was assessed with the Mann-Whitney rank sum test for two groups with unequal sample sizes and with the paired Student's $t$-test for pairwise comparison (for data shown on **Figure 2F**). The level of significance was set at $P < 0.05$. The data are presented as medians and 25th/75th percentile, unless otherwise stated.

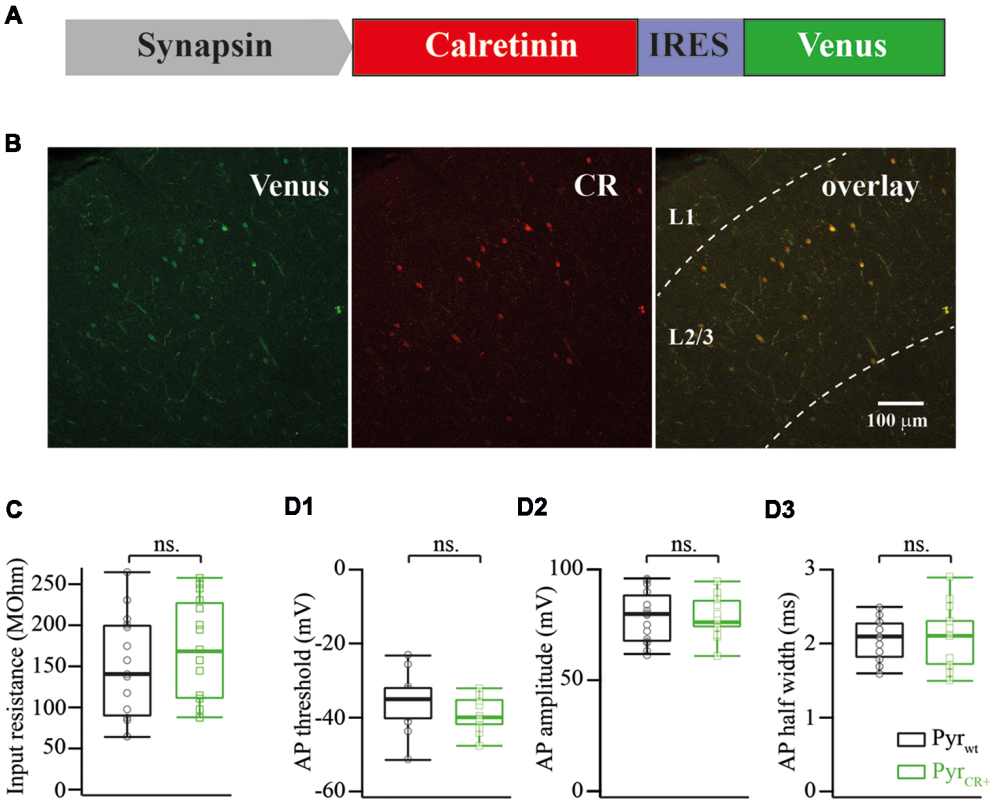


**FIGURE 1 | (A)** Schematic drawing of a viral cassette carrying calretinin and Venus. **(B)** Fluorescent images of a fixed cortical slice infected with AAV carrying calretinin and Venus. Left panel, Venus fluorescence; central panel, immunostaining against calretinin; right panel, overlay of both images. **(C)** Calretinin expression does not change the input resistance of layer 2/3 pyramidal cells (median WT vs. CR+: 143 vs. 173 MOhm; $n = 15$; $p = 0.319$ Mann-Whitney Test rank sum test). **(D)** Calretinin expression does not change the action potential (AP) properties of layer 2/3 pyramidal cells (median WT vs. CR+; $n = 15$ Mann-Whitney rank sum test): **(D1)** AP threshold −35 vs. −40 mV, $p = 0.12$; **(D2)** AP amplitude 79 vs. 76 mV, $p = 0.9$; **(D3)** AP half width 2.1 vs. 2.1, $p = 0.9$, ns, non-significant.

## RESULTS

### The Effect of Calretinin Expression on Intrinsic Properties and Excitability of Layer 2/3 Pyramidal Cells and Basic Release Properties at Layer 2/3 Pyramidal to FS Cell Synapses

First, we analyzed the consequences of calretinin overexpression on input resistance, AP threshold, AP amplitude and AP half-width of layer 2/3 pyramidal cells. None of the analyzed features were affected by calretinin expression. The pooled data from 15 calretinin-negative (WT) and 15 virally modified calretinin-positive (CR+) neurons are summarized in **Figure 1C,D1–3**, with exact median values (WT vs. CR+) provided in the figure legend.

To assess the effect of calretinin expression on basic synaptic properties we measured and analyzed the EPSP amplitude, synaptic delay, and failure rate at synapses between pyramidal cells and FS interneurons in layer 2/3 of the somatosensory cortex. Neurons were identified by their location, cell body shape (observed using infrared microscopy) and their firing pattern. Calretinin-expressing pyramidal cells were recognized by the presence of a fluorescence signal. Postsynaptic responses in the FS cells were triggered by 5 and 10 Hz trains of APs evoked in the presynaptic pyramidal neurons. At least 50 sweeps were collected in each neuronal pair for subsequent analysis (**Figure 2A**). First, we evaluated synaptic efficacy at the connections formed by WT and CR+ pyramidal neurons onto FS cells. To this end, we compared the averaged amplitudes of the first EPSP in the trains. The median values were very similar being 1.64 mV ($n = 12$) and 1.98 mV ($n = 12$) in WT and CR+ cell pairs respectively, ($p = 0.42$; Mann-Whitney rank sum test; **Figure 2B1**). This result was expected, since prior to every AP train calretinin was not bound to $Ca^{2+}$ and, therefore, was acting as a slow buffer. In agreement with this, the failure rate was slightly increased in the CR+ pyramidal cells, but this enhancement was not significant. The median value of failure rate in WT pyramidal cell terminals was 2% ($n = 12$) and, in CR+ terminals, 7.5% ($n = 10$, $p = 0.3$; Mann-Whitney rank sum test; **Figure 2B2**). However, even a slow buffer can shorten the temporal and spatial spread of the calcium microdomains and consequently reduce synaptic delay. Indeed, EPSPs recorded from the pairs where presynaptic pyramidal cell express calretinin were significantly better synchronized with APs as

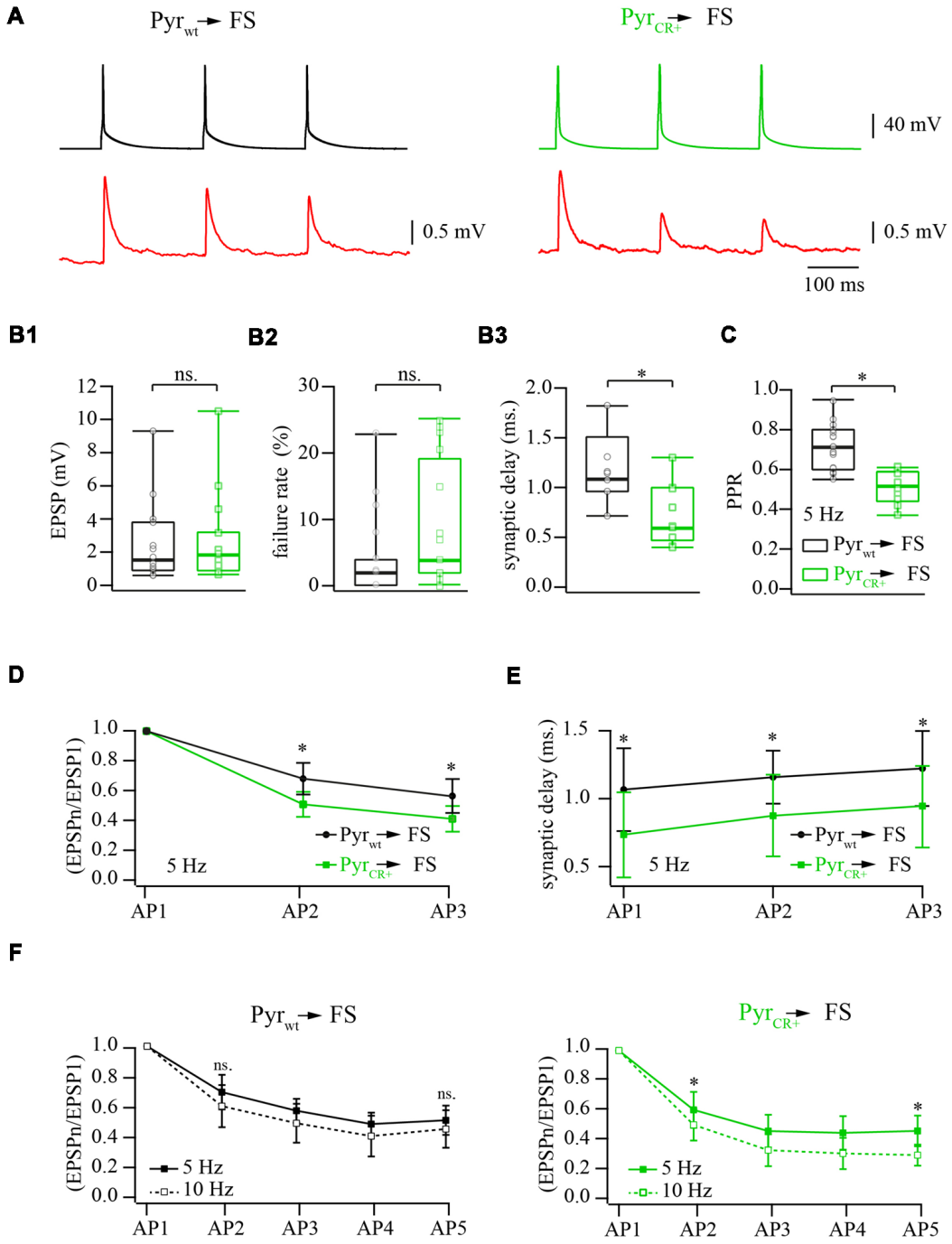


**FIGURE 2 |** Effect of calretinin expression in pyramidal cells, on the characteristics of layer 2/3 pyramidal neuron to fast-spiking (FS) interneuron synapses. **(A)** Representative averaged traces of presynaptic APs and postsynaptic EPSPs recorded from connected pairs of layer 2/3 pyramidal and FS neurons. Recordings obtained from WT neurons are shown on the left panel, the data from the pairs where presynaptic pyramidal cell was expressing calretinin are on the right. **(B)** Box plots show the effect of the calretinin expression (green box) on the basic release properties (**$B_1$**: EPSP amplitudes; **$B_2$**: failure rate; **$B_3$**: synaptic delay) in comparison to the WT data (black box). Open symbols represent the averaged value obtained in individual experiments. **(C)** Presynaptic calretinin expression reduces paired-pulse ratio (PPR) at layer 2/3 pyramidal to FS cell synapses (green box) relative to WT buffer-free synapses (black box). Open symbols represent the averaged value obtained in individual experiments. **(D)** Comparison of PPR for the second and the third responses in WT (calretinin-free; black) and calretinin-expressing (green) synapses. Data are shown as mean ± SD. **(E)** Reduction of synaptic delay remains significant for the second and the third responses in WT (calretinin-free; black) and calretinin-expressing (green) synapses. Data are shown as mean ± SD. **(F)** Differential effect of simulation frequency enhancement (from 5 to 10 Hz) on "immediate" ($EPSP_2/EPSP_1$) and steady-state depression ($EPSP_n/EPSP_1$) at WT (left panel) and calretinin-expressing synapses (right). Data are shown as mean ± SD. Significant difference is marked as (*), ns, non-significant.

indicated by the shorter synaptic delays. Median values were 1.08 ($n$ = 7) and 0.6 ($n$ = 9) milliseconds at WT and CR+ synapses, respectively ($p$ = 0.026; Mann-Whitney rank sum test; **Figure 2B3**).

## The Effect of Calretinin Expression on Short-Term Plasticity at Layer 2/3 Pyramidal to FS Cell Synapses

The binding of the first $Ca^{2+}$ ion to calretinin strongly increases the affinity of the remaining unoccupied binding sites converting calretinin from a slow calcium buffer to a fast calcium buffer. It has been shown that at layer 2/3 pyramidal to FS cell synapses slow buffers (EGTA) do not have a strong impact on short-term depression; this is in contrast with the fast buffer BAPTA which strongly reduces the amplitude of the first response and degree of depression (Rozov et al., 2001). Therefore, next we tested how the transition from the slow to fast $Ca^{2+}$ binding modes of calretinin affects short-term plasticity at these synapses. In WT animals the median value of paired-pulse ratio (PPR) of the second and the first EPSPs evoked by 5 Hz trains of three APs was 0.71 ($n$ = 17), however, PPR measured at CR+ synapses was significantly smaller, 0.52 ($n$ = 10; $p$ = 0.0009; Mann-Whitney rank sum test; **Figure 2C**). Significant enhancement of depression in the presence of calretinin persisted for the third EPSP ($p$ = 0.005; Mann-Whitney rank sum test; **Figure 2D**). Similarly to the first EPSP, the second and the third responses were more synchronized with APs in pairs formed by calretinin expressing pyramidal cells (EPSP2, $p$ = 0.008; EPSP3, $p$ = 0.009; Mann-Whitney rank sum test; **Figure 2E**).

At WT layer 2/3 pyramidal to FS cell synapses, a change in stimulation frequency from 5 to 10 Hz results in moderate and often not significant enhancement of both paired-pulse and steady state depression (Beck et al., 2005). However, at higher stimulation frequencies the ratio between the "slow" and "fast" forms of calretinin should be shifted towards the latter due to an increased level of residual intraterminal $Ca^{2+}$ concentration. Taking into account that "fast" calretinin promotes paired-pulse depression, we compared the frequency-dependent dynamics of EPSPs evoked by 5 and 10 Hz trains of five APs elicited in the same cell pairs. In WT animals, depression was slightly more pronounced for all APs in the train but these changes were not significant ($n$ = 6; $p > 0.05$ paired Student's $t$-test; **Figure 2F**). Contrarily, at CR+ synapses, the increase in the stimulation frequency caused strong enhancement of both paired-pulse and steady state depression. The EPSP2/EPSP1 ratios recorded at 5 and 10 Hz were 0.6 $\pm$ 0.11 and 0.5 $\pm$ 0.1, respectively, ($n$ = 7; $p$ = 0.04 paired Student's $t$-test; **Figure 2F**). At steady-state level, during the fifth AP, the difference between ratios were even more pronounced (EPSP5/EPSP1 at 5 Hz 0.46 $\pm$ 0.1 and at 10 Hz 0.29 $\pm$ 0.07; $p$ = 0.013 paired Student's $t$-test). Thus, in contrast to another fast-endogenous buffer, calbindin which has the main influence on the synaptic release during the first AP in the train and after partial saturation with $Ca^{2+}$ can cause synaptic facilitation, the calretinin effect on the first response is rather weak. However, "sensitization" of calretinin by $Ca^{2+}$ during the first AP increases its binding properties and therefore leads to the suppression of synaptic release.

# DISCUSSION

Synaptic transmission requires presynaptic $Ca^{2+}$ entry *via* voltage-gated $Ca^{2+}$ channels (VGCC) and subsequent vesicle fusion is triggered by $Ca^{2+}$ binding to the release calcium sensor. Synaptic release occurs at active zones in the close vicinity of presynaptic VGCC where $[Ca^{2+}]_i$ rapidly rises reaching levels sufficient for activation of exocytosis in a very short time. This spatially and temporally restricted elevation of $[Ca^{2+}]_i$ is known as a $Ca^{2+}$-concentration microdomain. Conversion of $Ca^{2+}$ entry into characteristic release properties (release probability, synaptic delay and short-term plasticity mode) at individual types of synapses crucially depends on diffusional distance, as well as on endogenous buffer capacity and buffering kinetics. It is commonly accepted that release probability ($Pr$) is negatively related to the distance between VGCCs and $Ca^{2+}$ vesicular release sensors (Neher, 1998), while synaptic latency is usually directly proportional to the diffusional distance (Rozov et al., 2001). In synapses, sparsely distributed VGCC and low endogenous buffer capacity accumulation of free residual $Ca^{2+}$ during frequency stimulation often leads to facilitation. In terminals where VGCC are more tightly coupled to the $Ca^{2+}$ sensor, high levels of $[Ca^{2+}]_i$ at the release site result in greater synchronization of release with APs and higher $Pr$. Synapses with a short diffusional distance are usually characterized by pronounced short-term depression (Neher, 1998). The effect of $Ca^{2+}$ buffers on synaptic release in these two types of terminals depends on their binding kinetics. Slow $Ca^{2+}$ buffers like exogenous EGTA and endogenous parvalbumin can efficiently reduce synaptic efficacy and block facilitation at low-$Pr$ synapses and do not have a significant effect on the amplitude of the postsynaptic responses and short-term plasticity at synapses with high-$Pr$. Buffers with fast binding kinetics (BAPTA or calbindin) can bind $Ca^{2+}$ before it reaches vesicular sensors, and therefore, significantly reduce $Pr$ at both types of terminals. The effect of a given buffer concentration is several fold stronger at low-$Pr$ compared to high-$Pr$ synapses. However, during repetitive high frequency presynaptic activity, fast buffers undergo partial saturation with $Ca^{2+}$ which attenuates the suppressant effect on release and leads to synaptic facilitation or a significant reduction in paired pulse depression (Rozov et al., 2001; Blatow et al., 2003; Voinova et al., 2015).

In contrast to calbindin, at low $[Ca^{2+}]_i$ calretinin behaves like a typical slow buffer with a binding rate lower than in EGTA (CR: $k_{on}$ 1.8 $\mu M^{-1}s^{-1}$; EGTA: $k_{on}$ 10 $\mu M^{-1}s^{-1}$). However, when the first pair of binding sites is occupied with $Ca^{2+}$, $k_{on}$ of the second pair drastically increases to 310 $\mu M^{-1}s^{-1}$ (Faas et al., 2007). For comparison, the fast buffer BAPTA has $k_{on}$ 400 $\mu M^{-1}s^{-1}$ (Naraghi and Neher, 1997; Meinrenken et al., 2002). Faas et al. (2007) described this phenomenon in terms of the positive cooperativity as ability to increase the ligand binding affinity of one site of a macromolecule by previous binding at another site of the same ligand to the

same molecule. Hence, during the first AP in the train when $[Ca^{2+}]_i$ is in the range of 100 nM, calretinin acts as a slow buffer and does not have a significant effect on release at least in high-*Pr* terminals. Indeed, both failure rate and amplitude of the unitary EPSPs were very similar in WT and calretinin expressing pyramidal cells. In addition, it suggests that in CR+ synapses the concentration of calretinin does not exceed a few hundred micromoles. However, AP-driven $Ca^{2+}$ entry (in the range of 5–20 μM in close vicinity to the VGCC) can partially saturate the first binding site of calretinin shifting its $Ca^{2+}$ binding affinity from "slow calretinin" to the "fast $1Ca^{2+}$-calretinin". "Fast" calretinin in turn can more effectively prevent $Ca^{2+}$ binding to the $Ca^{2+}$ sensor release suppressing vesicle fusion more efficiently during the second AP. Upon long lasting repetitive stimulation, the rate of "partial saturation" and, therefore, the ratio between "slow" and "fast" calretinins will depend on $K_{off}$ of $1Ca^{2+}$-calretinin and $2Ca^{2+}$-calretinin, calretinin diffusion rates, and most probably, on residual $[Ca^{2+}]_i$ and the $Ca^{2+}$ extrusion rate. There is evidence suggesting that residual $[Ca^{2+}]_i$ (>1 μM) remains in the terminals for hundreds of milliseconds after AP (Koester and Sakmann, 2000). Consequently, during bursts of presynaptic activity that are not long enough to cause complete saturation of calretinin, frequency-dependent accumulation of residual $[Ca^{2+}]_i$ can accelerate a transition from the "slow" calretinin to the "fast" $1Ca^{2+}$-calretinin resulting in stronger depression. However, in this case, the total $Ca^{2+}$-binding capacity of the buffer in the terminal should considerably exceed the amount of $Ca^{2+}$ coming with each AP. Thus, upon high frequency stimulation calretinin has a moderate effect on synaptic transmission during the first AP, but can greatly reduce information flow throughout the rest of the train.

## DATA AVAILABILITY

All datasets generated for this study are included in the manuscript.

## AUTHOR CONTRIBUTIONS

All authors listed have made a substantial, direct and intellectual contribution to the work, and approved it for publication.

## FUNDING

This research was supported by the subsidy allocated to Kazan Federal University for the state assignment in the sphere of scientific activities (6.2313.2017/4.6). The work was performed according to the Program of Competitive Growth of Kazan Federal University. The study was supported by the Russian Foundation for Basic Research (project no. 12-04-00632-a) and the Russian Academy of Sciences.

## ACKNOWLEDGMENTS

We thank David Jappy for useful comments on the manuscript. We are also grateful to Dr. Gorbacheva for technical help with confocal imaging.

## REFERENCES

Beck, O., Chistiakova, M., Obermayer, K., and Volgushev, M. (2005). Adaptation at synaptic connections to layer 2/3 pyramidal cells in rat visual cortex. *J. Neurophysiol.* 94, 363–376. doi: 10.1152/jn.01287.2004

Blatow, M., Caputi, A., Burnashev, N., Monyer, H., and Rozov, A. (2003). $Ca^{2+}$ buffer saturation underlies paired pulse facilitation in calbindin-D28k-containing terminals. *Neuron* 38, 79–88. doi: 10.3410/f.1012993.188364

Caillard, O., Moreno, H., Schwaller, B., Llano, I., Celio, M. R., and Marty, A. (2000). Role of the calcium-binding protein parvalbumin in short-term synaptic plasticity. *Proc. Natl. Acad. Sci. U S A* 97, 13372–13377. doi: 10.1073/pnas.230362997

Caputi, A., Rozov, A., Blatow, M., and Monyer, H. (2009). Two calretinin-positive GABAergic cell types in layer 2/3 of the mouse neocortex provide different forms of inhibition. *Cereb. Cortex* 19, 1345–1359. doi: 10.1093/cercor/bhn175

Faas, G. C., Schwaller, B., Vergara, J. L., and Mody, I. (2007). Resolving the fast kinetics of cooperative binding: $Ca^{2+}$ buffering by calretinin. *PLoS Biol.* 5:e311. doi: 10.1371/journal.pbio.0050311

Grimm, D., Kay, M. A., and Kleinschmidt, J. A. (2003). Helper virus-free, optically controllable and two-plasmid-based production of adeno-associated virus vectors of serotypes 1 to 6. *Mol. Ther.* 7, 839–850. doi: 10.1016/s1525-0016(03)00095-9

Gupta, A., Wang, Y., and Markram, H. (2000). Organizing principles for a diversity of GABAergic interneurons and synapses in the neocortex. *Science* 287, 273–278. doi: 10.1126/science.287.5451.273

Henzi, T., and Schwaller, B. (2015). Antagonistic regulation of parvalbumin expression and mitochondrial calcium handling capacity in renal epithelial cells. *PLoS One* 10:e0142005. doi: 10.1371/journal.pone.0142005

Holmgren, C., Harkany, T., Svennenfors, B., and Zilberter, Y. (2003). Pyramidal cell communication within local networks in layer 2/3 of rat neocortex. *J. Physiol.* 551, 139–153. doi: 10.1113/jphysiol.2003.044784

Koester, H. J., and Sakmann, B. (2000). Calcium dynamics associated with action potentials in single nerve terminals of pyramidal cells in layer 2/3 of the young rat neocortex. *J. Physiol.* 529 Pt 3, 625–646. doi: 10.1111/j.1469-7793.2000.00625.x

Lichvarova, L., Henzi, T., Safiulina, D., Kaasik, A., and Schwaller, B. (2018). Parvalbumin alters mitochondrial dynamics and affects cell morphology. *Cell. Mol. Life Sci.* 75, 4643–4666. doi: 10.1007/s00018-018-2921-x

Meinrenken, C. J., Borst, J. G., and Sakmann, B. (2002). Calcium secretion coupling at calyx of held governed by nonuniform channel-vesicle topography. *J. Neurosci.* 22, 1648–1667. doi: 10.1523/jneurosci.22-05-01648.2002

Naraghi, M., and Neher, E. (1997). Linearized buffered $Ca^{2+}$ diffusion in microdomains and its implications for calculation of $[Ca^{2+}]$ at the mouth of a calcium channel. *J. Neurosci.* 17, 6961–6973. doi: 10.1523/jneurosci.17-18-06961.1997

Neher, E. (1998). Vesicle pools and $Ca^{2+}$ microdomains: new tools for understanding their roles in neurotransmitter release. *Neuron* 20, 389–399. doi: 10.1016/s0896-6273(00)80983-6

Neske, G. T., Patrick, S. L., and Connors, B. W. (2015). Contributions of diverse excitatory and inhibitory neurons to recurrent network activity in cerebral cortex. *J. Neurosci.* 35, 1089–1105. doi: 10.1523/jneurosci.2279-14.2015

Pala, A., and Petersen, C. C. H. (2015). *In vivo* measurement of cell-type-specific synaptic connectivity and synaptic transmission in layer 2/3 mouse barrel cortex. *Neuron* 85, 68–75. doi: 10.1016/j.neuron.2014.11.025

Pilpel, N., Landeck, N., Klugmann, M., Seeburg, P. H., and Schwarz, M. K. (2009). Rapid, reproducible transduction of select forebrain regions by targeted recombinant virus injection into the neonatal mouse brain. *J. Neurosci. Methods* 182, 55–63. doi: 10.1016/j.jneumeth.2009.05.020

Reyes, A., Lujan, R., Rozov, A., Burnashev, N., Somogyi, P., and Sakmann, B. (1998). Target-cell-specific facilitation and depression in neocortical circuits. *Nat. Neurosci.* 1, 279–285. doi: 10.1038/1092

Rozov, A., Burnashev, N., Sakmann, B., and Neher, E. (2001). Transmitter release modulation by intracellular $Ca^{2+}$ buffers in facilitating and depressing nerve terminals of pyramidal cells in layer 2/3 of the rat neocortex indicates a target cell-specific difference in presynaptic calcium dynamics. *J. Physiol.* 531, 807–826. doi: 10.1111/j.1469-7793.2001.0807h.x

Valiullina, F., Zakharova, Y., Mukhtarov, M., Draguhn, A., Burnashev, N., and Rozov, A. (2016). The relative contribution of NMDARs to excitatory postsynaptic currents is controlled by $Ca^{2+}$-induced inactivation. *Front. Cell. Neurosci.* 10:12. doi: 10.3389/fncel.2016.00012

Voinova, O., Valiullina, F., Zakharova, Y., Mukhtarov, M., Draguhn, A., and Rozov, A. (2015). Layer specific development of neocortical pyramidal to fast spiking cell synapses. *Front. Cell Neurosci.* 9:518. doi: 10.3389/fncel.2015.00518

Watanabe, J., Rozov, A., and Wollmuth, L. P. (2005). Target-specific regulation of synaptic amplitudes in the neocortex. *J. Neurosci.* 25, 1024–1033. doi: 10.1523/jneurosci.3951-04.2005

**Conflict of Interest Statement**: The authors declare that the research was conducted in the absence of any commercial or financial relationships that could be construed as a potential conflict of interest.

*Copyright © 2019 Bolshakov, Kolleker, Volkova, Valiullina-Rakhmatullina, Kolosov and Rozov. This is an open-access article distributed under the terms of the Creative Commons Attribution License (CC BY). The use, distribution or reproduction in other forums is permitted, provided the original author(s) and the copyright owner(s) are credited and that the original publication in this journal is cited, in accordance with accepted academic practice. No use, distribution or reproduction is permitted which does not comply with these terms.*

frontiers in Cellular Neuroscience

REVIEW
published: 24 April 2019
doi: 10.3389/fncel.2019.00160

# Past and Future of Analog-Digital Modulation of Synaptic Transmission

*Mickael Zbili*[1,2]* *and Dominique Debanne*[1]*

[1]UNIS, UMR 1072, INSERM AMU, Marseille, France, [2]CRNL, INSERM U1028—CNRS UMR5292—Université Claude Bernard Lyon1, Lyon, France

Action potentials (APs) are generally produced in response to complex summation of excitatory and inhibitory synaptic inputs. While it is usually considered as a digital event, both the amplitude and width of the AP are significantly impacted by the context of its emission. In particular, the analog variations in subthreshold membrane potential determine the spike waveform and subsequently affect synaptic strength, leading to the so-called analog-digital modulation of synaptic transmission. We review here the numerous evidence suggesting context-dependent modulation of spike waveform, the discovery analog-digital modulation of synaptic transmission in invertebrates and its recent validation in mammals. We discuss the potential roles of analog-digital transmission in the physiology of neural networks.

**Keywords: axon, ion channels, synaptic transmission, brain circuits, short-term plasticity**

OPEN ACCESS

***Edited by:***
*Shin-ya Kawaguchi,*
*Kyoto University, Japan*

***Reviewed by:***
*Michael Blake Hoppa,*
*Dartmouth College, United States*
*Yousheng Shu,*
*Beijing Normal University, China*

***Correspondence:**
*Mickael Zbili*
*zbili.mickael@gmail.com*
*Dominique Debanne*
*dominique.debanne@inserm.fr*

***Received:*** *01 March 2019*
***Accepted:*** *08 April 2019*
***Published:*** *24 April 2019*

***Citation:***
*Zbili M and Debanne D (2019) Past and Future of Analog-Digital Modulation of Synaptic Transmission. Front. Cell. Neurosci. 13:160. doi: 10.3389/fncel.2019.00160*

## THE ACTION POTENTIAL IS NOT A DIGITAL EVENT

In the central nervous system (CNS), synaptic transmission is mainly supported by APs, i.e., it occurs when a spike has been emitted in the presynaptic cell. Classically, the analogy is made between the spike and the basic unit of information used in computers (bit), i.e., the spike is thought to be the minimal unit of information that a neuron can emit. In this view, the spike is seen as an "all-or-none" digital phenomenon whose shape is constant or whose shape modifications are not relevant for neuronal processing (Maley, 2018). These two assertions are wrong in most of the neuronal cell types, despite some cases showing very stable spike shape (Sierksma and Borst, 2017; **Figure 1A**).

In most neurons, the spike waveform is highly variable in function of the quantity of voltage-gated channels available at spike emission. This quantity depends on two parameters: the density and the level of inactivation of the channels. In this review, we will focus on variations in axonal spike shape that impact neurotransmitter release and synaptic strength.

The first source of spike shape modification is the neuronal firing rate. Repetitive firing may cause inactivation of both voltage-gated sodium channels (Nav) and voltage-gated potassium channels (Kv). Nav inactivation leads to a decrease in spike amplitude during AP trains (Brody and Yue, 2000; Prakriya and Mennerick, 2000; He et al., 2002; Kawaguchi and Sakaba, 2015; Ma et al., 2017; Ohura and Kamiya, 2018; **Figure 1B**), while Kv inactivation leads to an

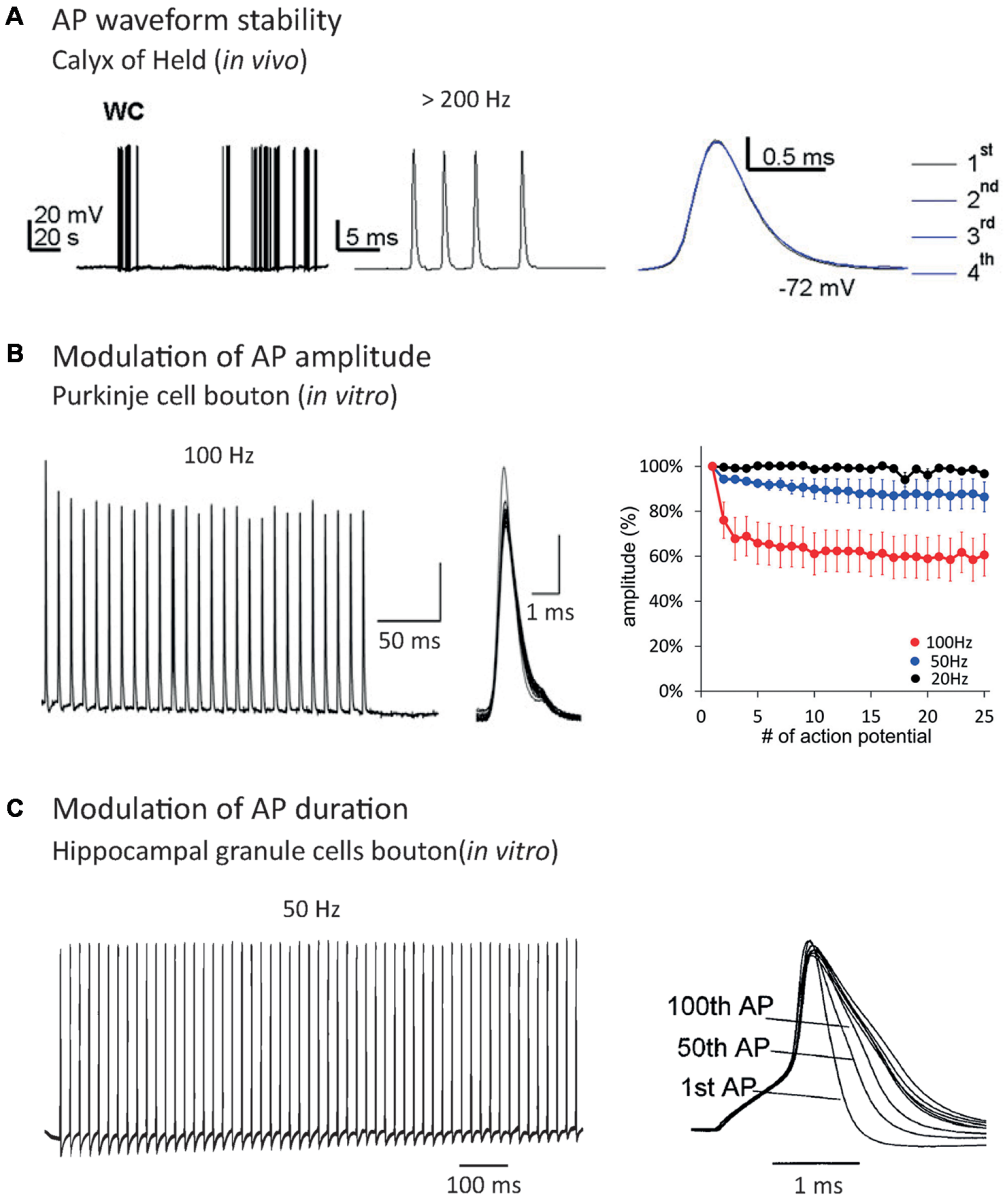


**FIGURE 1 |** Effect of repetitive firing on axonal Action Potential (AP) shape. **(A)** AP waveform is highly stable during high-frequency trains in the Calyx of Held recorded *in vivo*. Note that the APs are indistinguishable when they are superimposed. Adapted with permission from Sierksma and Borst (2017). **(B)** AP amplitude decrease during repetitive firing in Purkinje cells bouton. Note that increasing the frequency of AP train provokes an enhancement of AP amplitude decrease. Adapted with permission from Kawaguchi and Sakaba (2015). **(C)** AP duration increase during repetitive firing in hippocampal mossy fiber bouton. Adapted with permission from Geiger and Jonas (2000).

increase in spike width (Jackson et al., 1991; Park and Dunlap, 1998; Shao et al., 1999; Geiger and Jonas, 2000; Faber and Sah, 2003; Kim et al., 2005; Deng et al., 2013; Liu et al., 2017; Ma et al., 2017; **Figure 1C**). When it invades the presynaptic terminal, the spike provokes the opening of voltage-gated calcium channels (Cav), leading to an increase of $Ca^{2+}$ concentration in the bouton and the release of neurotransmitters. Due to the power law between intra-terminal $Ca^{2+}$ concentration and neurotransmitter release, small variations in presynaptic calcium entry, occurring through spike shape modifications, can lead to large changes in synaptic transmission (Sabatini and Regehr, 1997; Bollmann et al., 2000; Bischofberger et al., 2002; Fedchyshyn and Wang, 2005; Yang and Wang, 2006; Bucurenciu et al., 2008; Scott et al., 2008; Neishabouri and Faisal, 2014). In fact, spike broadening during repetitive firing entails synaptic transmission facilitation in the pituitary nerve (Jackson et al., 1991), dorsal root ganglion (Park and Dunlap, 1998) and mossy fiber bouton (Geiger and Jonas, 2000). Other studies showed that spike amplitude depression during repetitive firing provokes a decrease in synaptic transmission at hippocampal

(Brody and Yue, 2000; Prakriya and Mennerick, 2000; He et al., 2002) and cerebellar synapses (Kawaguchi and Sakaba, 2015). Therefore, spike shape variations participate in short-term synaptic plasticity produced by repetitive firing (Zucker and Regehr, 2002). In addition, Hebbian or homeostatic forms of synaptic plasticity may result from modulation of presynaptic spike waveform *via* long-term regulation of ion channel density (Gandhi and Matzel, 2000; Yang and Wang, 2006; Hoppa et al., 2014).

Another source of spike waveform variation is the presence of neuromodulators. Neuromodulation alters spike shape *via* subthreshold modifications of membrane potential or channel biophysics regulation. In hippocampal neurons, glutamate and GABA have been shown to depolarize axonal membrane potential leading to spike broadening, probably through Kv channel inactivation, inducing an increase in synaptic transmission (Ruiz et al., 2010; Sasaki et al., 2011). In cortical pyramidal neurons, dopamine fixation on D1 receptors causes a decrease in Kv1-dependent $I_D$ current, due to the hyperpolarization of its inactivation curve, leading to axonal spike broadening (Dong and White, 2003; Yang et al., 2013).

Action Potential (AP) waveform in neuronal compartments depends on the local density of voltage-gated ion channels. For example, the AP duration decreases during its axonal propagation in L5 pyramidal neurons due to axonal expression of Kv1 channels (Kole et al., 2007). Recent studies have shown that the density of voltage-gated channels is not homogenous all along the axon, leading to local variation of spike shape during its propagation. The density of peri-terminal Kv3 channels determines local spike width and synaptic release in terminals of cerebellar stellate cell interneurons (Rowan et al., 2016). In axons of cortical neurons, varying density of Nav channels determines branch-specific spike amplitude and spike-evoked presynaptic $Ca^{2+}$ entry (Cho et al., 2017). Therefore, the distribution of synaptic strength in neuronal networks is likely to be in part determined by the variability of AP waveform in the presynaptic terminals.

Finally, spike broadening and increased synaptic release due to Kv channel dysfunction or Kv channel down-regulation has been associated with various neurologic disorders such as schizophrenia, episodic ataxia type 1, fragile X syndrome, autism and epilepsy (Deng et al., 2013; Begum et al., 2016; Crabtree et al., 2017; Vivekananda et al., 2017; Scott et al., 2019).

Therefore, the spike waveform can be modified by neuronal firing rate, neuromodulation, variation in local voltage-gated channel density, voltage-gated channel long-term regulation and dysfunction of voltage-gated channels in the pathological context. All these spike waveform variations modify $Ca^{2+}$ entry and synaptic release at presynaptic terminals. As spike shape modifications alter the transmission of synaptic information, it should not be considered as a purely digital event.

In the following sections, we will focus on spike shape modulation by subthreshold variations of membrane potential. We will see that the spike waveform is determined by an analog information, the subthreshold neuronal activity, leading to synaptic release modulation. This phenomenon has been called Analog-Digital synaptic transmission (Clark and Häusser, 2006; Alle and Geiger, 2008; Debanne et al., 2013; Rama et al., 2015b; Zbili et al., 2016).

# BIRTH OF ANALOG-DIGITAL MODULATION OF SYNAPTIC TRANSMISSION AT INVERTEBRATE SYNAPSES

## AP Amplitude-Dependent Modulation of Synaptic Strength

The modulation of spike-evoked synaptic transmission by modulation of the presynaptic AP waveform has been first reported at the squid giant synapse by Hagiwara and Tasaki (1958). This pioneering study revealed that the amplitude of the presynaptic spike directly determines the amplitude of the postsynaptic response. The EPSP modulation was found to be extremely large, from virtually no detectable response to ∼7–8 mV (Hagiwara and Tasaki, 1958). The modulation of the presynaptic spike amplitude was simply obtained by varying the intensity of subthreshold depolarization. This spike-amplitude dependent modulation of synaptic transmission has been confirmed by subsequent studies at the squid giant synapse (Takeuchi and Takeuchi, 1962; Miledi and Slater, 1966; Kusano et al., 1967).

While it has been suspected for a long time that a presynaptic hyperpolarization increased spike-evoked synaptic transmission (Del Castillo and Katz, 1954), the study by Takeuchi and Takeuchi (1962) represents the first report to unambiguously show that transient hyperpolarization of the presynaptic membrane potential during induction of the presynaptic AP enhanced the presynaptic spike amplitude and, subsequently, the postsynaptic response (**Figure 2A**). Although the precise mechanisms underlying this modulation have not been addressed in this study, the facilitation may result from recovery of sodium current from inactivation (see also Rama et al., 2015a). This principle has been confirmed in many studies published later, including one in the squid (Miledi and Slater, 1966) and another in the crayfish (Dudel, 1971). Interestingly, this hyperpolarization-induced facilitation of synaptic transmission has also been reported at the rat neuromuscular junction (Hubbard and Willis, 1962, 1968).

The study by Kusano et al. (1967) was largely inspired by the work of Hagiwara and Tasaki (1958) but it represents the first clear demonstration that increasing the input current applied to trigger a spike leads to an increase in both the presynaptic spike amplitude and the postsynaptic response (**Figure 2B**). These two early studies are somehow without descendants since no other study has been undertaken since. Furthermore, the mechanism of this modulation has never been clearly identified but it may result from the minimization of sodium channel inactivation prior to spike emission.

## AP Duration-Dependent Modulation of Synaptic Strength

Modulation of synaptic strength by AP duration was reported later, after the discovery of enhancement of synaptic

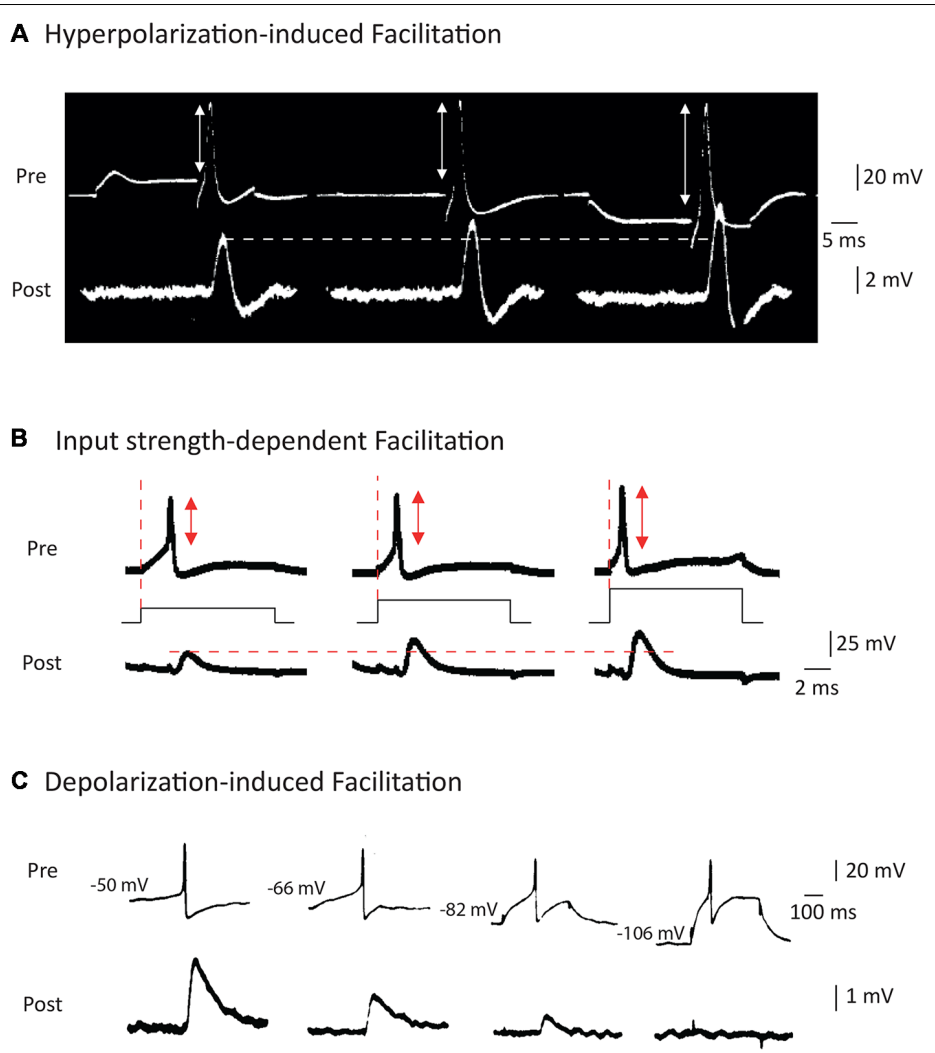


**FIGURE 2 |** Modulation of AP waveform and synaptic strength by presynaptic membrane potential in invertebrates. **(A)** Hyperpolarization of the presynaptic element leads to an increase in the spike amplitude and the post-synaptic potential amplitude at squid giant synapse. Adapted with permission from Takeuchi and Takeuchi (1962). **(B)** Increasing the current applied to emit the spike leads to a decrease in presynaptic spike latency, an increase in spike amplitude and an increased EPSP amplitude at the squid giant synapse. Adapted with permission from Kusano et al. (1967). **(C)** Depolarization of the presynaptic cell leads to an increase in spike-evoked synaptic transmission at the cholinergic synapse of Aplysia. Adapted with permission from Shapiro et al. (1980).

transmission by AP amplitude modulation. The first clear study stating context-dependent enhancement of synaptic transmission due to the broadening of presynaptic AP is that of Shapiro et al. (1980). The authors reported that in connected neurons from Aplysia, depolarization of the presynaptic neuron inactivates a potassium current, leading to a broadening of the spike and an enhancement of synaptic transmission (Shapiro et al., 1980; **Figure 2C**). One should note that this effect is exactly the opposite of that described in the squid where a presynaptic depolarization reduced spike-evoked transmission. Before this study, Shimahara and Tauc (1975) reported similar findings but the mechanism was not studied in this first report (Shimahara and Tauc, 1975). Later, Shimahara confirmed that blocking Kv channels with 4-aminopyridine suppressed the increase in synaptic transmission induced by depolarization (Shimahara, 1981, 1983). However, in these studies, it was unclear whether voltage was mainly acting on spike amplitude or spike duration.

## Presynaptic Voltage-Dependent Modulation: Role of Calcium Current

Beyond inactivation of Kv channels, a second mechanism had been identified in the Shapiro et al.'s (1980) study showing depolarization-induced enhancement of synaptic transmission. They showed that subthreshold depolarization of the presynaptic neuron to −55/−35 mV activated a steady-state $Ca^{2+}$ current that also contributed to the modulation of transmission, possibly by controlling release probability (Shapiro et al., 1980; Connor et al., 1986). Similar depolarization-induced enhancement of synaptic transmission has been reported at an inhibitory synapse

in the leech (Nicholls and Wallace, 1978). This study reports that small presynaptic depolarizations increase synaptic strength in an AP waveform independent way (probably due to basal $Ca^{2+}$ accumulation), while stronger depolarizations enhance synaptic release *via* broadening of the presynaptic spike. Therefore, depolarization-induced enhancement of synaptic transmission *via* basal $Ca^{2+}$ increase and *via* spike broadening can coexist at invertebrates' synapses. Recently, the depolarization-induced enhancement of synaptic transmission *via* basal $Ca^{2+}$ accumulation has been confirmed in heart interneurons of the leech (Ivanov and Calabrese, 2003) and B21 sensory neurons of the Aplysia (Ludwar et al., 2009, 2017; Evans et al., 2011).

Two main features should be noted in these pioneering studies. First, the modulation of synaptic transmission was found to be extremely large (about an order of magnitude). Second, only one type of modulation was found in a given presynaptic cell-type (i.e., only depolarization-induced facilitation in the Aplysia or hyperpolarization-induced facilitation in the squid).

## RECENT DEVELOPMENTS

From the early studies on spike-evoked release modulation *via* presynaptic membrane potential, we can conclude that spikes contain more information than usually thought. In fact, the synaptic strength depends on the subthreshold membrane potential of the presynaptic cell, indicating that the presynaptic spike transmits this analog information to the postsynaptic cell. However, the direction of this modulation of synaptic transmission seems to depend on the type of synapse. In fact, in some studies, the rule is: the more depolarized is the presynaptic cell, the bigger is the PSP (also called depolarization-induced Analog-Digital Facilitation or d-ADF), while in others the rule is the opposite (hyperpolarization-induced Analog-Digital Facilitation or h-ADF). We will see that the recent developments on the subject have extended the observations made on invertebrate preparations to mammalian synapses and have resolved this apparent paradox *via* the description of the ion channels responsible for the two types of ADF.

### Depolarization-Induced Analog-Digital Facilitation (d-ADF) in Mammalian Brain

The first descriptions of d-ADF in mammalian CNS have been made in Calyx of Held (Turecek and Trussell, 2001; Awatramani et al., 2005), CA3 area (Saviane et al., 2003), hippocampal mossy fibers (Alle and Geiger, 2006) and L5 pyramidal neurons (Shu et al., 2006; **Figures 3Ai,Bi**; **Table 1**). In all these cases, a depolarization of the presynaptic cell preceding the AP leads to an increase in synaptic transmission from 30% to 100% depending on the studies. However, a precise examination shows that different mechanisms are responsible for these d-ADFs.

#### d-ADF *via* Basal $Ca^{2+}$ Accumulation at the Terminal

The first mechanism described for d-ADF is not due to spike shape modulation. A weak opening of synaptic Cavs during the subthreshold depolarization leads to an increase in the basal $Ca^{2+}$ concentration at the terminal, and consequently, an enhancement of synaptic release when the spike invades the presynaptic terminal (Debanne et al., 2013; Rama et al., 2015b; Zbili et al., 2016). This mechanism has been described at the Calyx of Held (Turecek and Trussell, 2001; Awatramani et al., 2005; Hori and Takahashi, 2009), cerebellar molecular layer interneurons (Bouhours et al., 2011; Christie et al., 2011) and at the dendro-dendritic synapses between mitral cells of the olfactory bulb (Fekete et al., 2014). Due to the slow dynamics of $Ca^{2+}$ accumulation, several seconds of depolarization are needed to fully facilitate synaptic transmission. Interestingly, basal $Ca^{2+}$ accumulation induces synaptic release facilitation in two different ways. First, the increase in basal $Ca^{2+}$ concentration directly enhances the release probability, probably *via* the promotion of the vesicles priming and of the coupling between vesicles and Cav channels (Neher and Sakaba, 2008). Second, it can provoke a $Ca^{2+}$-dependent hyperpolarizing shift of Cav channel activation (Borst and Sakmann, 1998; Cuttle et al., 1998), leading to an increase of the spike-evoked $Ca^{2+}$ transient (Hori and Takahashi, 2009; Christie et al., 2011). Importantly, these two effects can occur at the same synapse (Hori and Takahashi, 2009).

#### d-ADF *via* Modulation of Presynaptic Spike Width

The second mechanism underlying d-ADF in mammals is the inactivation of Kv channels during the subthreshold depolarization. This phenomenon provokes broadening of the presynaptic spike (**Figures 3Aii,Bii**), leading to an increase in the spike-evoked $Ca^{2+}$ transient and an enhancement of synaptic release (Debanne et al., 2013; Rama et al., 2015b; Zbili et al., 2016; **Figures 3Ai,Bi**). Importantly, the time constant of this type of d-ADF depends on the inactivation time-constant of the Kv involved in the phenomenon. In L5 pyramidal neurons, CA3 pyramidal neurons and CA1 pyramidal neurons, slowly inactivating Kv1 channels are responsible for the d-ADF, and therefore the phenomenon presents a slow time constant (several seconds; Saviane et al., 2003; Shu et al., 2006, 2007; Kole et al., 2007; Sasaki et al., 2011, 2012; Zhu et al., 2011; Kim, 2014; Bialowas et al., 2015). In contrast, in inhibitory interneurons of the cerebellum (stellate cells), d-ADF depends on fast Kv3.4 inactivation and is, therefore, quicker to take place (100 ms of depolarization to have an effect and 1 s for a full increase in synaptic transmission; Rowan and Christie, 2017). Importantly, at invertebrates' synapses, the d-ADF *via* basal $Ca^{2+}$ accumulation and the d-ADF *via* Kv inactivation are not mutually exclusive and may occur at the same synapses (Bialowas et al., 2015; Rama et al., 2015b).

#### A Peculiar Case: d-ADF at Mossy Fiber Boutons

In granule cells of the Dentate Gyrus, an EPSP can propagate from the dendrites to the presynaptic bouton and increase spike-evoked synaptic transmission at mossy fiber bouton/CA3 synapses (Alle and Geiger, 2006). Surprisingly, this d-ADF seems to be $Ca^{2+}$-independent. In fact, it does not go along with an increase in basal $Ca^{2+}$ concentration or spike-evoked $Ca^{2+}$ transient (Scott et al., 2008), and it is not

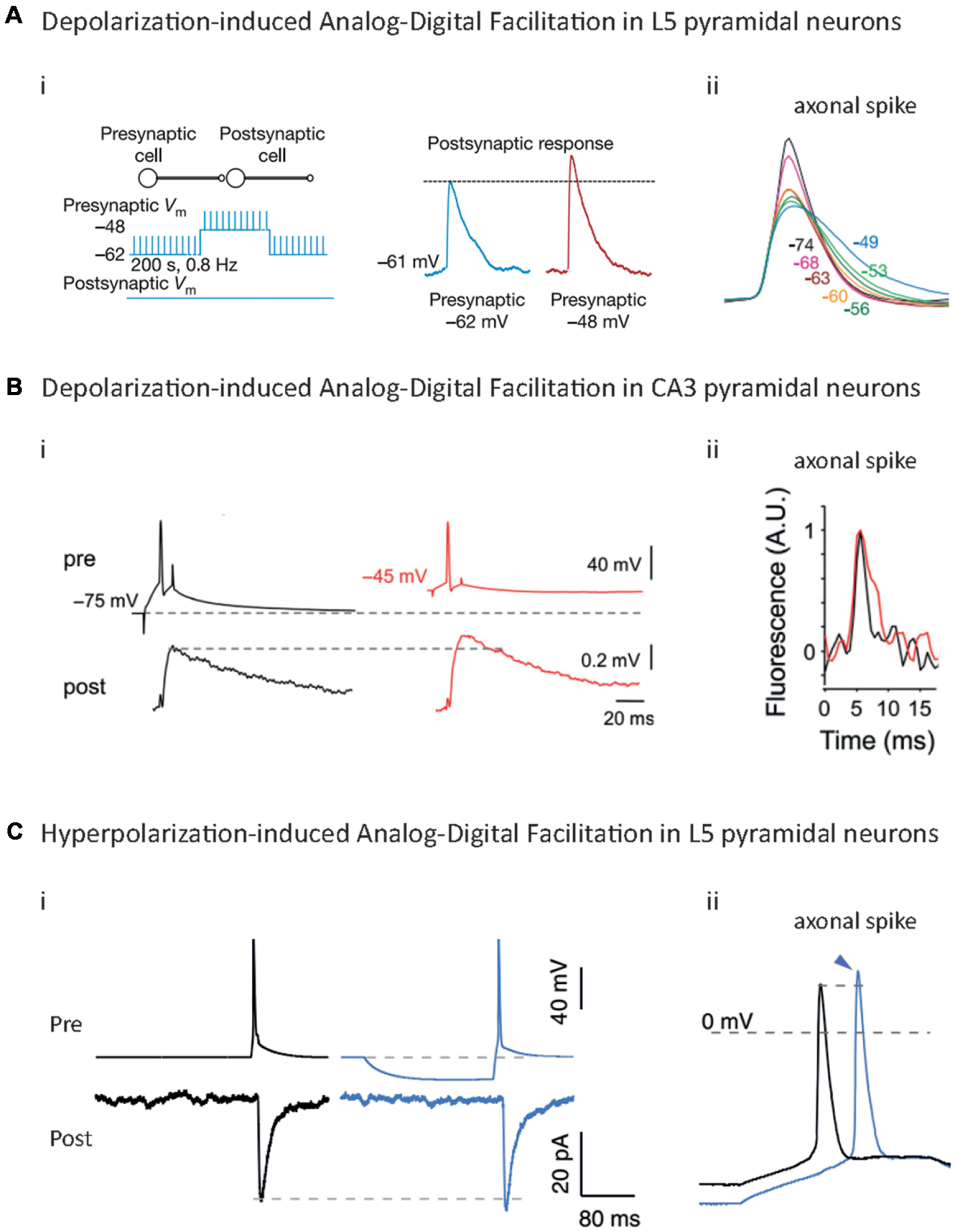


**FIGURE 3 |** Analog-Digital Facilitations at mammalian synapses. **(A)** Depolarization-induced Analog-Digital Facilitation (d-ADF) at L5-L5 synapses. Depolarization of the presynaptic cell leads to an increase in synaptic transmission at L5/L5 synapses (i) that is due to the broadening of the axonal spike measured by whole-cell recording from an axonal bleb (ii). Adapted with permission from Shu et al. (2006). **(B)** d-ADF at CA3/CA3 synapses. Long depolarization of the presynaptic cell leads to an increase in the synaptic transmission (i) that is mediated by the broadening of the axonal spike measured in voltage imaging (ii). Adapted with permission from Bialowas et al. (2015). **(C)** Hyperpolarization-induced Analog-Digital facilitation (h-ADF). Hyperpolarization of the presynaptic cell leads to an enhancement of synaptic transmission at L5/L5 synapses: (i) due to an increase in the spike amplitude measured by whole-cell recording from an axonal bleb, (ii) adapted with permission from Rama et al. (2015a).

blocked by application of 10 mM EGTA (Alle and Geiger, 2006) or 1 mM BAPTA (Scott et al., 2008). However, it should be noted that the increase in $Ca^{2+}$ entry can be too subtle to be seen with $Ca^{2+}$ fluorescent indicators. Moreover, at the Calyx of Held, it is necessary to apply 10 mM EGTA + 1 mM BAPTA to efficiently block d-ADF (Hori and Takahashi, 2009). Therefore, the mechanism of d-ADF at this synapse could be $Ca^{2+}$-dependent and needs further studies to be unraveled (Debanne et al., 2013).

## Hyperpolarization-Induced Analog-Digital Facilitation (h-ADF) in Mammalian Brain

Recent studies showed that a presynaptic hyperpolarization before the spike leads to an increase in spike-evoked

**TABLE 1** | Analog-digital facilitation.

| | Authors | Species | Cell type | Mechanism |
|---|---|---|---|---|
| **d-ADF** | Shimahara and Tauc (1975) | Aplysia | Interneuron | Not studied |
| | Nicholls and Wallace (1978) | Leech | Heart interneuron | • Basal $Ca^{2+}$<br>• Kv inactivation<br>• AP broadening |
| | Shimahara and Peretz (1978) | Aplysia | Interneuron | Not studied |
| | Alle and Geiger (2006) | Rat | Mossy fiber giant bouton | Unknown |
| | Scott et al. (2008) | Rat | Mossy fiber giant bouton | Unknown |
| | Zorrilla de San Martin et al. (2017) | Rat | Purkinje cells | Unknown |
| | Shapiro et al. (1980) | Aplysia | Cholinergic interneuron L10 | • Basal $Ca^{2+}$<br>• Kv inactivation<br>• AP broadening |
| | Shimahara (1981, 1983) | Aplysia | Left pleural ganglion | • Kv inactivation<br>• AP amplitude increase? |
| | Saviane et al. (2003) | Rat | CA3 pyramidal neuron | • Kv inactivation<br>• AP broadening |
| | Shu et al. (2006)/Shu et al. (2007) | Ferret/Rat | L5 pyramidal neuron | • Kv inactivation<br>• AP broadening |
| | Kole et al. (2007) | Rat | L5 pyramidal neuron | • Kv inactivation<br>• AP broadening |
| | Ruiz et al. (2010) | Rat | Mossy fiber giant bouton | • AP broadening |
| | Zhu et al. (2011) | Rat | L5 pyramidal neuron/interneuron synapses | • Kv inactivation |
| | Sasaki et al. (2011) | Rat | CA3 pyramidal neuron | • Kv inactivation<br>• AP broadening |
| | Sasaki et al. (2012) | Rat | CA3 pyramidal neuron | • Kv inactivation<br>• AP broadening |
| | Kim (2014) | Rat | CA1 pyramidal neuron/interneuron synapses | • Kv inactivation<br>• AP broadening |
| | Bialowas et al. (2015) | Rat | CA3 pyramidal neuron | • Basal $Ca^{2+}$<br>• Kv inactivation<br>• AP broadening |
| | Rowan and Christie (2017) | Mouse | Cerebellar interneuron (stellate cell) | • Kv inactivation<br>• AP broadening |
| | Connor et al. (1986) | Aplysia | Cholinergic interneuron L10 | • Basal $Ca^{2+}$ |
| | Turecek and Trussell (2001) | Rat | Calyx of Held | • Basal $Ca^{2+}$ |
| | Ivanov and Calabrese (2003) | Leech | Heart interneuron | • Basal $Ca^{2+}$ |
| | Ludwar et al. (2009) | Aplysia | Sensory neuron B21 | • Basal $Ca^{2+}$ |
| | Evans et al. (2011) | Aplysia | Sensory neuron B21 | • Basal $Ca^{2+}$ |
| | Ludwar et al. (2017) | Aplysia | Sensory neuron B21 | • Basal $Ca^{2+}$ |
| | Awatramani et al. (2005) | Rat | Calyx of Held | • Basal $Ca^{2+}$ |
| | Hori and Takahashi (2009) | Mouse/Rat | Calyx of Held | • Basal $Ca^{2+}$ |
| | Christie et al. (2011) | Rat | Cerebellar interneuron (Molecular Layer) | • Basal $Ca^{2+}$ |
| | Bouhours et al. (2011) | Rat | Cerebellar interneuron (Molecular Layer) | • Basal $Ca^{2+}$ |
| **h-ADF** | Del Castillo and Katz (1954) | Frog | Neuromuscular junction | Unknown |
| | Takeuchi and Takeuchi (1962) | Squid | Giant synapse | • AP amplitude increase |
| | Miledi and Slater (1966) | Squid | Stellate ganglion | • AP amplitude increase |
| | Dudel (1971) | Crayfish | Motor nerve | • AP amplitude increase |
| | Hubbard and Willis (1968) | Rat | Neuromuscular junction | • AP amplitude increase |
| | Hubbard and Willis (1962) | Rat | Neuromuscular junction | • AP amplitude increase |
| | Thio and Yamada (2004) | Rat | Hippocampal neurons | Unknown |
| | Cowan and Stricker (2004) | Rat | L4 pyramidal neuron | Unknown |
| | Ruiz et al. (2003) | Guinea pig | Bouton *en passant*, mossy fiber | Unknown |
| | Rama et al. (2015a) | Rat | CA3 and L5 pyramidal neuron | • Nav deinactivation<br>• AP amplitude increase |

neurotransmitter release in hippocampal cultures (Thio and Yamada, 2004), L4 pyramidal neurons (Cowan and Stricker, 2004), CA3 pyramidal neurons and L5 pyramidal neurons (Rama et al., 2015a; **Figure 3Ci**; **Table 1**). This facilitation ranges between 10% and 100% depending on the studies and the cell type. At CA3/CA3 and L5/L5 synapses, the mechanism underlying h-ADF has been fully described: a presynaptic hyperpolarization results in the recovery from inactivation of presynaptic Nav channels, which provokes an increase in presynaptic spike amplitude (**Figure 3Cii**), leading to an enhancement of spike-evoked $Ca^{2+}$ entry and synaptic release (Rama et al., 2015a; **Figure 3Ci**). This phenomenon

is likely to occur at hippocampal mossy fiber, in which a somatic hyperpolarization results in an increase of spike-evoked $Ca^{2+}$ transient at small axonal varicosities (Ruiz et al., 2003). Interestingly, due to the fast biophysics of Nav channels, h-ADF is extremely fast and occurs within 15–50 ms of hyperpolarization. Therefore, it can be induced by a unique IPSP preceding the spike. Hence, rebound spiking should have a bigger impact on the postsynaptic cell if h-ADF is present at the synapse. One can think that h-ADF is a widespread phenomenon because it depends on Nav channels which are present in all spiking neuron types. However, it should be noted that a strong Nav channel density should attenuate the impact of their de-inactivation on the spike amplitude, and therefore decrease the h-ADF (Rama et al., 2015a). Moreover, Nav1.6 channels, which are the main subtype in pyramidal cells axons, are strongly inactivated at resting potential (Hu et al., 2009), and therefore are suited to underlie h-ADF. Parvalbumin positive ($PV^+$) fast-spiking interneurons contain axonal Nav1.1 channels, a subtype that display less inactivation at resting membrane potential than Nav1.6 (Patel et al., 2015), and a much higher density of axonal Nav channels than pyramidal cells (Hu and Jonas, 2014; Hu et al., 2014). Therefore, one can expect that this type of interneuron lacks spike amplitude modulation and h-ADF.

## Coexistence of d-ADF and h-ADF at the Same Synapses

d-ADF and h-ADF are due to different mechanisms and present different time constants (100 ms to several seconds for d-ADF, 15–50 ms for h-ADF). It has been shown that d-ADF and h-ADF coexist and can be summed at CA3/CA3 synapses (Rama et al., 2015a). In fact, a long depolarization (10 s) followed by a brief hyperpolarization (200 ms) entails a bigger increase in spike-evoked synaptic transmission than a long depolarization or a brief hyperpolarization alone. Why has this coexistence not been shown in early studies in invertebrates? For synapses that display h-ADF but not d-ADF, we can assume a lack of inactivating potassium channels at the synapses studied, which prevents spike broadening by depolarization (giant synapse of the squid and frog neuromuscular junction). In the case of studies that report only d-ADF, it should be noted that the protocol used is not relevant to observe h-ADF. In fact, a brief hyperpolarization (15–200 ms) is needed to unravel h-ADF at synapses that also present d-ADF. A long hyperpolarization (several seconds) can induce de-inactivation of Kv1 channels and spike sharpening, which can thwart h-ADF (Bialowas et al., 2015; Rama et al., 2015a). In the studies made on invertebrates that report d-ADF but no h-ADF, the resting membrane potential was modified for several seconds before spike emission, which may explain why the h-ADF has not been reported. Therefore, additional studies are needed to unravel the degree of coexistence of d-ADF and h-ADF at invertebrates and mammals synapses.

## Physiological Consequences of ADFs

### Spatial Extent of ADFs

One of the main issues concerning Analog-Digital Facilitations is the spatial extent of these phenomena along the axon. In fact, ADFs are produced by subthreshold modifications of the somatic potential that spreads to the presynaptic terminal and modifies presynaptic spike shape or basal $Ca^{2+}$ (Debanne et al., 2013; Rama et al., 2015b). Therefore, the axonal space constant is a major determinant of the spatial extent of ADF. The axonal space constant varies among neuronal types, depending on the axonal diameter, the density of axonal branching and the axonal membrane resistance (Sasaki et al., 2012).

In CA3 hippocampal neurons, the axonal space constant has been evaluated around 200–500 μm (Sasaki et al., 2012; Bialowas et al., 2015; Rama et al., 2015a). In L5 pyramidal neurons, the value estimated ranges between 500 μm (Shu et al., 2006; Kole et al., 2007) and 1,000 μm (Christie and Jahr, 2009). In CA1 pyramidal neurons, the axonal space constant was found to be around 700 μm (Kim, 2014). Therefore, ADFs seem to be restricted to local brain circuits. For example, d-ADF has been found between CA3 neurons but not at the synapses between CA3 and CA1 neurons (Sasaki et al., 2012). However, several lines of evidence suggest that ADFs could also occur between more distant neurons. First, most of the recordings have been made in young animals (14–30 days after birth), in which the myelin sheet is still in development, and may have underestimated the axonal space constant in myelinated axons, such as CA1 and L5 pyramidal neurons. In fact, cortical myelin has been shown to develop up to 22 months after birth (Hill et al., 2018). Moreover, in myelinated axons of cat motoneurons, the axonal space constant was found to be 1,700 μm (Gogan et al., 1983). Second, neuromodulation can induce direct subthreshold potential modifications of presynaptic terminals by presynaptic receptor activation. Presynaptic glycinergic receptor activation depolarizes the Calyx of Held, leading to an increase in spike-evoked synaptic release (Turecek and Trussell, 2001). Similarly, presynaptic $GABA_A$ receptor activation depolarizes the presynaptic terminal, leading to an enhancement of spike-evoked synaptic transmission at mossy fiber giant bouton and Purkinje cells (Ruiz et al., 2010; Zorrilla de San Martin et al., 2017). In contrast, in L5 pyramidal neurons, axonal $GABA_A$ receptor activation leads to a hyperpolarization, a decrease of axonal spike width and a decrease of spike-evoked $Ca^{2+}$ entry (Xia et al., 2014). Finally, glutamate released by astrocytes depolarizes terminals in CA3 pyramidal neurons, leading to an increase in spike width and synaptic release (Sasaki et al., 2011). In these latter cases, ADFs are not dependent on subthreshold membrane potential spreading from the soma and could occur even at long range connections.

### Time Constant of ADFs

ADFs present various time constants which determine their potential roles in network physiology. In fact, in most of the studies, d-ADF needs 100 ms to several seconds of presynaptic depolarization to occur. On the contrary, h-ADF can be produced by fast presynaptic hyperpolarization (15–50 ms; Rama et al., 2015a). This difference is well explained by the underlying mechanism of d-ADF and h-ADF: slow accumulation of basal $Ca^{2+}$ (Bouhours et al., 2011; Christie et al., 2011) or slow Kv inactivation for d-ADF (Shu et al., 2006, 2007; Kole et al., 2007; Bialowas et al., 2015), fast recovery from inactivation of Nav for

h-ADF (Rama et al., 2015a; Zbili et al., 2016). Therefore, d-ADF and h-ADF should have different consequences on information transfer in neuronal networks.

### d-ADF May Maintain Excitatory Synaptic Strength During Cortical Up-States

It has been proposed that d-ADF, due to its slow time-constant, occurs during global network state modifications such as slow-wave sleep associated cortical up and down states (Shu et al., 2006). During an up state, all the neurons of a network will depolarize leading to a global increase in synaptic release through d-ADF. At the same time, the global depolarization should decrease the driving force associated with synaptic excitatory current. In fact, while d-ADF increases synaptic strength by a factor around 1% per mV of presynaptic depolarization (Kole et al., 2007; Bialowas et al., 2015), calculations of driving force for AMPA-driven synaptic current predict a synaptic strength decrease of around 1.5% per mV of postsynaptic depolarization. Therefore, in the case of a globally depolarized neuronal network, d-ADF can be considered as a homeostatic process that maintains an excitatory synaptic strength constant despite the decrease of the driving force.

### d-ADF May Maintain Excitatory-Inhibitory Balance During Up-States

Interestingly, at connections between L5 pyramidal neurons, a depolarization of the presynaptic pyramidal neuron entails both an increase of the monosynaptic EPSP (i.e., classical d-ADF) and an increase in disynaptic inhibition (Zhu et al., 2011). This depolarization-induced facilitation of disynaptic inhibition results from d-ADF occurring at a synapse between L5 pyramidal neurons and neighboring interneurons, leading to an increase in interneuron firing. This phenomenon has been proposed to be important for the persistence of excitatory-inhibitory balance during up-states where d-ADF may increase excitatory and inhibitory activity at the same time (Zhu et al., 2011).

### h-ADF May Participate to Network Synchronization

Because of the fast de-inactivation time constant of Nav channels, h-ADF can be induced by a single IPSP preceding the presynaptic spike (Rama et al., 2015a). Therefore, h-ADF modulates synaptic strength on a short time scale and may participate in fast network processing. First, it is well known that hyperpolarization produced by interneurons is able to synchronize the spiking of neighboring pyramidal neurons. Usually, one explains this phenomenon by a transient silencing of the pyramidal cells as a whole, causing the post-hyperpolarization spiking to occur in synchrony. It can also be enhanced by the so-called "rebound spiking," which is often due to the recovery from inactivation of T-type $Ca^{2+}$ channels and Nav channels during the hyperpolarization. Interestingly, the h-ADF, which increases the inter-pyramidal synaptic strength after a transient hyperpolarization, has been shown to increase the interneuron-driven network synchronization (Rama et al., 2015a). Second, it has been shown that sequences of co-activated pyramidal neurons are often preceded and can be produced by inter-neuronal firing (Sasaki et al., 2014). It would be interesting to examine whether the increase in inter-pyramidal synaptic strength through h-ADF participates in the production of neuronal ensembles by interneurons. Third, h-ADF could be a detection mechanism for unexpected spikes. In fact, when the neuron is hyperpolarized, the spiking probability decreases. However, due to h-ADF, if a spike occurs during a low spiking probability state, the synaptic release is increased, compared to a spike produced at the resting membrane potential. Therefore, h-ADF increases the informational content of unexpected spikes in cortical networks. Finally, it has been proposed that h-ADF participates in the increase of synaptic transmission during silent states of the slow wave sleep, in which cortical neurons can be hyperpolarized by 5–15 mV (Timofeev and Chauvette, 2017).

## CONCLUSION AND FUTURE DIRECTIONS

We have reviewed evidence showing that the informational content of the spike is dependent on the context of its emission. In fact, the presynaptic spike waveform varies as a function of the neuronal firing rate, the neuro-modulatory state or the subthreshold voltage fluctuations. Moreover, this information is transmitted to postsynaptic neurons by modulation of spike-evoked calcium entry and neurotransmitter release. In this view, the neurotransmission in mammalian CNS needs the occurrence of a digital signal (the spike), whose waveform is modulated by the sub-threshold signal. It has been proposed that synaptic transmission relies on a hybrid between analog and digital signaling, called Analog-Digital synaptic transmission (Clark and Häusser, 2006; Alle and Geiger, 2008). Consequently, the description of APs as purely digital events to study information processing of neuronal networks should be abandoned. In fact, it has been shown that an "AP waveform code" is highly reliable and more informative than a purely digital code (de Polavieja et al., 2005; Juusola et al., 2007). Several issues have to be solved to unravel the physiological implications of context-dependent spike waveform modulation. First, ADFs should be tested at various stages of neuronal development. One could expect that context-dependent modulation of spike waveform is larger in developing networks, which present a lower density of voltage-gated channels and therefore a less stable spike shape. Second, d-ADF and h-ADF have to be studied in adult networks, in which the myelination process is completed, to confirm the spatial extent of these phenomena. In fact, two published studies report paired recordings of thalamo-cortical connections (Bruno and Sakmann, 2006; Hu and Agmon, 2016), making it possible to test if ADFs occur at long range connections when the axon is myelinated. Third, it would be interesting to observe the extent of ADFs in interneurons. In fact, due to their high voltage-gated channel density, it seems that fast-spiking cortical interneurons do not present spike waveform modulation in function of the membrane potential (Tateno and Robinson, 2006; Goldberg et al., 2008). In contrast, cerebellar stellate cells present depolarization-induced spike broadening and an increase in synaptic release (Rowan and Christie, 2017). Therefore, GABAergic transmission may undergo ADF, depending on the type of interneuron studied. Finally, the spike

waveform effects may not be restricted to synaptic release and may affect dendritic computing. In fact, it has been proposed that a spike broadening causes a shunting of incoming PSPs and a decrease in their summation, promoting a low firing rate (Hausser et al., 2001; Juusola et al., 2007). Interestingly, in L5 pyramidal neurons, depolarization-induced spike broadening has been shown to have a shorter time-constant in the soma than in the axon (Shu et al., 2007), due to local differences in potassium current expression (fast inactivating $I_A$ current in the somato-dendritic compartment and slow inactivating $I_D$ current in the axon). Moreover, in contrast with the axonal spike broadening, it seems that the dendritic spike broadening reduces the $Ca^{2+}$ entry through the decrease of the driving force promoting the $Ca^{2+}$ tail current in granule cells of the dentate gyrus (Brunner and Szabadics, 2016). Therefore, it is likely that subthreshold depolarization has different effects on somato-dendritic and axonal computing. The pursuit of the investigation on neuronal computation *via* spike waveform will certainly unravel the physiological importance of this phenomenon on networks dynamics.

## AUTHOR CONTRIBUTIONS

MZ and DD wrote the manuscript and built the figures.

## FUNDING

This work was supported by ANR (AXODE-14-CE-13-0003-02 to DD), FRM (FDT20150-0532147 to MZ) and LABEX Cortex of Université de Lyon (NR-11-LABX-0042).

## REFERENCES

Alle, H., and Geiger, J. R. (2006). Combined analog and action potential coding in hippocampal mossy fibers. *Science* 311, 1290–1293. doi: 10.1126/science.1119055

Alle, H., and Geiger, J. R. (2008). Analog signalling in mammalian cortical axons. *Curr. Opin. Neurobiol.* 18, 314–320. doi: 10.1016/j.conb.2008.08.006

Awatramani, G. B., Price, G. D., and Trussell, L. O. (2005). Modulation of transmitter release by presynaptic resting potential and background calcium levels. *Neuron* 48, 109–121. doi: 10.1016/j.neuron.2005.08.038

Begum, R., Bakiri, Y., Volynski, K. E., and Kullmann, D. M. (2016). Action potential broadening in a presynaptic channelopathy. *Nat. Commun.* 7:12102. doi: 10.1038/ncomms12102

Bialowas, A., Rama, S., Zbili, M., Marra, V., Fronzaroli-Molinieres, L., Ankri, N., et al. (2015). Analog modulation of spike-evoked transmission in CA3 circuits is determined by axonal Kv1.1 channels in a time-dependent manner. *Eur. J. Neurosci.* 41, 293–304. doi: 10.1111/ejn.12787

Bischofberger, J., Geiger, J. R., and Jonas, P. (2002). Timing and efficacy of $Ca^{2+}$ channel activation in hippocampal mossy fiber boutons. *J. Neurosci.* 22, 10593–10602. doi: 10.1523/JNEUROSCI.22-24-10593.2002

Bollmann, J. H., Sakmann, B., and Borst, J. G. (2000). Calcium sensitivity of glutamate release in a calyx-type terminal. *Science* 289, 953–957. doi: 10.1126/science.289.5481.953

Borst, J. G., and Sakmann, B. (1998). Facilitation of presynaptic calcium currents in the rat brainstem. *J. Physiol.* 513, 149–155. doi: 10.1111/j.1469-7793.1998.149by.x

Bouhours, B., Trigo, F. F., and Marty, A. (2011). Somatic depolarization enhances GABA release in cerebellar interneurons via a calcium/protein kinase C pathway. *J. Neurosci.* 31, 5804–5815. doi: 10.1523/JNEUROSCI.5127-10.2011

Brody, D. L., and Yue, D. T. (2000). Release-independent short-term synaptic depression in cultured hippocampal neurons. *J. Neurosci.* 20, 2480–2494. doi: 10.1523/JNEUROSCI.20-07-02480.2000

Brunner, J., and Szabadics, J. (2016). Analogue modulation of back-propagating action potentials enables dendritic hybrid signalling. *Nat. Commun.* 7:13033. doi: 10.1038/ncomms13033

Bruno, R. M., and Sakmann, B. (2006). Cortex is driven by weak but synchronously active thalamocortical synapses. *Science* 312, 1622–1627. doi: 10.1126/science.1124593

Bucurenciu, I., Kulik, A., Schwaller, B., Frotscher, M., and Jonas, P. (2008). Nanodomain coupling between $Ca^{2+}$ channels and $Ca^{2+}$ sensors promotes fast and efficient transmitter release at a cortical GABAergic synapse. *Neuron* 57, 536–545. doi: 10.1016/j.neuron.2007.12.026

Cho, I. H., Panzera, L. C., Chin, M., and Hoppa, M. B. (2017). Sodium channel β2 subunits prevent action potential propagation failures at axonal branch points. *J. Neurosci.* 37, 9519–9533. doi: 10.1523/JNEUROSCI.0891-17.2017

Christie, J. M., and Jahr, C. E. (2009). Selective expression of ligand-gated ion channels in L5 pyramidal cell axons. *J. Neurosci.* 29, 11441–11450. doi: 10.1523/JNEUROSCI.2387-09.2009

Christie, J. M., Chiu, D. N., and Jahr, C. E. (2011). $Ca^{2+}$-dependent enhancement of release by subthreshold somatic depolarization. *Nat. Neurosci.* 14, 62–68. doi: 10.1038/nn.2718

Clark, B., and Häusser, M. (2006). Neural coding: hybrid analog and digital signalling in axons. *Curr. Biol.* 16, R585–R588. doi: 10.1016/j.cub.2006.07.007

Connor, J. A., Kretz, R., and Shapiro, E. (1986). Calcium levels measured in a presynaptic neurone of Aplysia under conditions that modulate transmitter release. *J. Physiol.* 375, 625–642. doi: 10.1113/jphysiol.1986.sp016137

Cowan, A. I., and Stricker, C. (2004). Functional connectivity in layer IV local excitatory circuits of rat somatosensory cortex. *J. Neurophysiol.* 92, 2137–2150. doi: 10.1152/jn.01262.2003

Crabtree, G. W., Sun, Z., Kvajo, M., Broek, J. A., Fénelon, K., McKellar, H., et al. (2017). Alteration of neuronal excitability and short-term synaptic plasticity in the prefrontal cortex of a mouse model of mental illness. *J. Neurosci.* 37, 4158–4180. doi: 10.1523/JNEUROSCI.4345-15.2017

Cuttle, M. F., Tsujimoto, T., Forsythe, I. D., and Takahashi, T. (1998). Facilitation of the presynaptic calcium current at an auditory synapse in rat brainstem. *J. Physiol.* 512, 723–729. doi: 10.1111/j.1469-7793.1998.723bd.x

de Polavieja, G. G., Harsch, A., Kleppe, I., Robinson, H. P., and Juusola, M. (2005). Stimulus history reliably shapes action potential waveforms of cortical neurons. *J. Neurosci.* 25, 5657–5665. doi: 10.1523/JNEUROSCI.0242-05.2005

Debanne, D., Bialowas, A., and Rama, S. (2013). What are the mechanisms for analogue and digital signalling in the brain? *Nat. Rev. Neurosci.* 14, 63–69. doi: 10.1038/nrn3361

Del Castillo, J., and Katz, B. (1954). Changes in end-plate activity produced by presynaptic polarization. *J. Physiol.* 124, 586–604. doi: 10.1113/jphysiol.1954.sp005131

Deng, P. Y., Rotman, Z., Blundon, J. A., Cho, Y., Cui, J., Cavalli, V., et al. (2013). FMRP regulates neurotransmitter release and synaptic information transmission by modulating action potential duration via BK channels. *Neuron* 77, 696–711. doi: 10.1016/j.neuron.2012.12.018

Dong, Y., and White, F. J. (2003). Dopamine D1-class receptors selectively modulate a slowly inactivating potassium current in rat medial prefrontal cortex pyramidal neurons. *J. Neurosci.* 23, 2686–2695. doi: 10.1523/JNEUROSCI.23-07-02686.2003

Dudel, J. (1971). The effect of polarizing current on action potential and transmitter release in crayfish motor nerve terminals. *Pflugers Arch.* 324, 227–248. doi: 10.1007/bf00586421

Evans, C. G., Ludwar, B., Askanas, J., and Cropper, E. C. (2011). Effect of holding potential on the dynamics of homosynaptic facilitation. *J. Neurosci.* 31, 11039–11043. doi: 10.1523/JNEUROSCI.2361-11.2011

Faber, E. S., and Sah, P. (2003). $Ca^{2+}$-activated $K^+$ (BK) channel inactivation contributes to spike broadening during repetitive firing in the rat lateral amygdala. *J. Physiol.* 552, 483–497. doi: 10.1111/j.1469-7793.2003.00483.x

Fedchyshyn, M. J., and Wang, L. Y. (2005). Developmental transformation of the release modality at the calyx of Held synapse. *J. Neurosci.* 25, 4131–4140. doi: 10.1523/JNEUROSCI.0350-05.2005

Fekete, A., Johnston, J., and Delaney, K. R. (2014). Presynaptic T-type $Ca^{2+}$ channels modulate dendrodendritic mitral-mitral and mitral-periglomerular connections in mouse olfactory bulb. *J. Neurosci.* 34, 14032–14045. doi: 10.1523/JNEUROSCI.0905-14.2014

Gandhi, C. C., and Matzel, L. D. (2000). Modulation of presynaptic action potential kinetics underlies synaptic facilitation of type B photoreceptors after associative conditioning in Hermissenda. *J. Neurosci.* 20, 2022–2035. doi: 10.1523/JNEUROSCI.20-05-02022.2000

Geiger, J. R., and Jonas, P. (2000). Dynamic control of presynaptic $Ca^{2+}$ inflow by fast-inactivating $K^+$ channels in hippocampal mossy fiber boutons. *Neuron* 28, 927–939. doi: 10.1016/s0896-6273(00)00164-1

Gogan, P., Gueritaud, J. P., and Tyc-Dumont, S. (1983). Comparison of antidromic and orthodromic action potentials of identified motor axons in the cat's brain stem. *J. Physiol.* 335, 205–220. doi: 10.1113/jphysiol.1983.sp014529

Goldberg, E. M., Clark, B. D., Zagha, E., Nahmani, M., Erisir, A., and Rudy, B. (2008). $K^+$ channels at the axon initial segment dampen near-threshold excitability of neocortical fast-spiking GABAergic interneurons. *Neuron* 58, 387–400. doi: 10.1016/j.neuron.2008.03.003

Hagiwara, S., and Tasaki, I. (1958). A study on the mechanism of impulse transmission across the giant synapse of the squid. *J. Physiol.* 143, 114–137. doi: 10.1113/jphysiol.1958.sp006048

Hausser, M., Major, G., and Stuart, G. J. (2001). Differential shunting of EPSPs by action potentials. *Science* 291, 138–141. doi: 10.1126/science.291.5501.138

He, Y., Zorumski, C. F., and Mennerick, S. (2002). Contribution of presynaptic $Na^+$ channel inactivation to paired-pulse synaptic depression in cultured hippocampal neurons. *J. Neurophysiol.* 87, 925–936. doi: 10.1152/jn.00225.2001

Hill, R. A., Li, A. M., and Grutzendler, J. (2018). Lifelong cortical myelin plasticity and age-related degeneration in the live mammalian brain. *Nat. Neurosci.* 21, 683–695. doi: 10.1038/s41593-018-0120-6

Hoppa, M. B., Gouzer, G., Armbruster, M., and Ryan, T. A. (2014). Control and plasticity of the presynaptic action potential waveform at small CNS nerve terminals. *Neuron* 84, 778–789. doi: 10.1016/j.neuron.2014.09.038

Hori, T., and Takahashi, T. (2009). Mechanisms underlying short-term modulation of transmitter release by presynaptic depolarization. *J. Physiol.* 587, 2987–3000. doi: 10.1113/jphysiol.2009.168765

Hu, H., and Agmon, A. (2016). Differential excitation of distally versus proximally targeting cortical interneurons by unitary thalamocortical bursts. *J. Neurosci.* 36, 6906–6916. doi: 10.1523/JNEUROSCI.0739-16.2016

Hu, H., Gan, J., and Jonas, P. (2014). Interneurons. Fast-spiking, parvalbumin$^+$ GABAergic interneurons: from cellular design to microcircuit function. *Science* 345:1255263. doi: 10.1126/science.1255263

Hu, H., and Jonas, P. (2014). A supercritical density of $Na^+$ channels ensures fast signaling in GABAergic interneuron axons. *Nat Neurosci* 17, 686–693. doi: 10.1038/nn.3678

Hu, W., Tian, C., Li, T., Yang, M., Hou, H., and Shu, Y. (2009). Distinct contributions of $Na_v1.6$ and $Na_v1.2$ in action potential initiation and backpropagation. *Nat. Neurosci.* 12, 996–1002. doi: 10.1038/nn.2359

Hubbard, J. I., and Willis, W. D. (1962). Hyperpolarization of mammalian motor nerve terminals. *J. Physiol.* 163, 115–137. doi: 10.1113/jphysiol.1962.sp006961

Hubbard, J. I., and Willis, W. D. (1968). The effects of depolarization of motor nerve terminals upon the release of transmitter by nerve impulses. *J. Physiol.* 194, 381–405. doi: 10.1113/jphysiol.1968.sp008414

Ivanov, A. I., and Calabrese, R. L. (2003). Modulation of spike-mediated synaptic transmission by presynaptic background $Ca^{2+}$ in leech heart interneurons. *J. Neurosci.* 23, 1206–1218. doi: 10.1523/JNEUROSCI.23-04-01206.2003

Jackson, M. B., Konnerth, A., and Augustine, G. J. (1991). Action potential broadening and frequency-dependent facilitation of calcium signals in pituitary nerve terminals. *Proc. Natl. Acad. Sci. U S A* 88, 380–384. doi: 10.1073/pnas.88.2.380

Juusola, M., Robinson, H. P., and de Polavieja, G. G. (2007). Coding with spike shapes and graded potentials in cortical networks. *Bioessays* 29, 178–187. doi: 10.1002/bies.20532

Kawaguchi, S. Y., and Sakaba, T. (2015). Control of inhibitory synaptic outputs by low excitability of axon terminals revealed by direct recording. *Neuron* 85, 1273–1288. doi: 10.1016/j.neuron.2015.02.013

Kim, S. (2014). Action potential modulation in CA1 pyramidal neuron axons facilitates OLM interneuron activation in recurrent inhibitory microcircuits of rat hippocampus. *PLoS One* 9:e113124. doi: 10.1371/journal.pone.0113124

Kim, J., Wei, D. S., and Hoffman, D. A. (2005). Kv4 potassium channel subunits control action potential repolarization and frequency-dependent broadening in rat hippocampal CA1 pyramidal neurones. *J. Physiol.* 569, 41–57. doi: 10.1113/jphysiol.2005.095042

Kole, M. H., Letzkus, J. J., and Stuart, G. J. (2007). Axon initial segment Kv1 channels control axonal action potential waveform and synaptic efficacy. *Neuron* 55, 633–647. doi: 10.1016/j.neuron.2007.07.031

Kusano, K., Livengood, D. R., and Werman, R. (1967). Correlation of transmitter release with membrane properties of the presynaptic fiber of the squid giant synapse. *J. Gen. Physiol.* 50, 2579–2601. doi: 10.1085/jgp.50.11.2579

Liu, P. W., Blair, N. T., and Bean, B. P. (2017). Action potential broadening in capsaicin-sensitive DRG neurons from frequency-dependent reduction of Kv3 current. *J. Neurosci.* 37, 9705–9714. doi: 10.1523/JNEUROSCI.1703-17.2017

Ludwar, B. C., Evans, C. G., Cambi, M., and Cropper, E. C. (2017). Activity-dependent increases in $[Ca^{2+}]$i contribute to digital-analog plasticity at a molluscan synapse. *J. Neurophysiol.* 117, 2104–2112. doi: 10.1152/jn.00034.2017

Ludwar, B., Evans, C. G., Jing, J., and Cropper, E. C. (2009). Two distinct mechanisms mediate potentiating effects of depolarization on synaptic transmission. *J. Neurophysiol.* 102, 1976–1983. doi: 10.1152/jn.00418.2009

Ma, Y., Bayguinov, P. O., and Jackson, M. B. (2017). Action potential dynamics in fine axons probed with an axonally targeted optical voltage sensor. *eNeuro* 4:ENEURO.0146-17.2017. doi: 10.1523/eneuro.0146-17.2017

Maley, C. J. (2018). Toward analog neural computation. *Minds Mach.* 28, 77–91. doi: 10.1007/s11023-017-9442-5

Miledi, R., and Slater, C. R. (1966). The action of calcium on neuronal synapses in the squid. *J. Physiol.* 184, 473–498. doi: 10.1113/jphysiol.1966.sp007927

Neher, E., and Sakaba, T. (2008). Multiple roles of calcium ions in the regulation of neurotransmitter release. *Neuron* 59, 861–872. doi: 10.1016/j.neuron.2008.08.019

Neishabouri, A., and Faisal, A. A. (2014). Axonal noise as a source of synaptic variability. *PLoS Comput. Biol.* 10:e1003615. doi: 10.1371/journal.pcbi.1003615

Nicholls, J., and Wallace, B. G. (1978). Modulation of transmission at an inhibitory synapse in the central nervous system of the leech. *J. Physiol.* 281, 157–170. doi: 10.1113/jphysiol.1978.sp012414

Ohura, S., and Kamiya, H. (2018). Short-term depression of axonal spikes at the mouse hippocampal mossy fibers and sodium channel-dependent modulation. *eNeuro* 5:ENEURO.0415-17.2018. doi: 10.1523/eneuro.0415-17.2018

Park, D., and Dunlap, K. (1998). Dynamic regulation of calcium influx by G-proteins, action potential waveform, and neuronal firing frequency. *J. Neurosci.* 18, 6757–6766. doi: 10.1523/JNEUROSCI.18-17-06757.1998

Patel, R. R., Barbosa, C., Xiao, Y., and Cummins, T. R. (2015). Human Nav1.6 channels generate larger resurgent currents than human Nav1.1 channels, but the Navbeta4 peptide does not protect either isoform from use-dependent reduction. *PLoS One* 10:e0133485. doi: 10.1371/journal.pone.0133485

Prakriya, M., and Mennerick, S. (2000). Selective depression of low-release probability excitatory synapses by sodium channel blockers. *Neuron* 26, 671–682. doi: 10.1016/s0896-6273(00)81203-9

Rama, S., Zbili, M., Bialowas, A., Fronzaroli-Molinieres, L., Ankri, N., Carlier, E., et al. (2015a). Presynaptic hyperpolarization induces a fast analogue modulation of spike-evoked transmission mediated by axonal sodium channels. *Nat. Commun.* 6:10163. doi: 10.1038/ncomms10163

Rama, S., Zbili, M., and Debanne, D. (2015b). Modulation of spike-evoked synaptic transmission: the role of presynaptic calcium and potassium channels. *Biochim. Biophys. Acta* 1853, 1933–1939. doi: 10.1016/j.bbamcr.2014.11.024

Rowan, M. J., and Christie, J. M. (2017). Rapid state-dependent alteration in Kv3 channel availability drives flexible synaptic signaling dependent on somatic subthreshold depolarization. *Cell Rep.* 18, 2018–2029. doi: 10.1016/j.celrep.2017.01.068

Rowan, M. J., DelCanto, G., Yu, J. J., Kamasawa, N., and Christie, J. M. (2016). Synapse-level determination of action potential duration by $K^+$ channel clustering in axons. *Neuron* 91, 370–383. doi: 10.1016/j.neuron.2016.05.035

Ruiz, A., Campanac, E., Scott, R. S., Rusakov, D. A., and Kullmann, D. M. (2010). Presynaptic $GABA_A$ receptors enhance transmission and LTP induction at hippocampal mossy fiber synapses. *Nat. Neurosci.* 13, 431–438. doi: 10.1038/nn.2512

Ruiz, A., Fabian-Fine, R., Scott, R., Walker, M. C., Rusakov, D. A., and Kullmann, D. M. (2003). $GABA_A$ receptors at hippocampal mossy fibers. *Neuron* 39, 961–973. doi: 10.1016/s0896-6273(03)00559-2

Sabatini, B. L., and Regehr, W. G. (1997). Control of neurotransmitter release by presynaptic waveform at the granule cell to Purkinje cell synapse. *J. Neurosci.* 17, 3425–3435. doi: 10.1523/JNEUROSCI.17-10-03425.1997

Sasaki, T., Matsuki, N., and Ikegaya, Y. (2011). Action-potential modulation during axonal conduction. *Science* 331, 599–601. doi: 10.1126/science.1197598

Sasaki, T., Matsuki, N., and Ikegaya, Y. (2012). Effects of axonal topology on the somatic modulation of synaptic outputs. *J. Neurosci.* 32, 2868–2876. doi: 10.1523/JNEUROSCI.5365-11.2012

Sasaki, T., Matsuki, N., and Ikegaya, Y. (2014). Interneuron firing precedes sequential activation of neuronal ensembles in hippocampal slices. *Eur. J. Neurosci.* 39, 2027–2036. doi: 10.1111/ejn.12554

Saviane, C., Mohajerani, M. H., and Cherubini, E. (2003). An ID-like current that is downregulated by $Ca^{2+}$ modulates information coding at CA3-CA3 synapses in the rat hippocampus. *J. Physiol.* 552, 513–524. doi: 10.1113/jphysiol.2003.051045

Scott, R., Ruiz, A., Henneberger, C., Kullmann, D. M., and Rusakov, D. A. (2008). Analog modulation of mossy fiber transmission is uncoupled from changes in presynaptic $Ca^{2+}$. *J. Neurosci.* 28, 7765–7773. doi: 10.1523/JNEUROSCI.1296-08.2008

Scott, R., Sánchez-Aguilera, A., van Elst, K., Lim, L., Dehorter, N., Bae, S. E., et al. (2019). Loss of Cntnap2 causes axonal excitability deficits, developmental delay in cortical myelination, and abnormal stereotyped motor behavior. *Cereb. Cortex* 29, 586–597. doi: 10.1093/cercor/bhx341

Shao, L. R., Halvorsrud, R., Borg-Graham, L., and Storm, J. F. (1999). The role of BK-type $Ca^{2+}$-dependent $K^+$ channels in spike broadening during repetitive firing in rat hippocampal pyramidal cells. *J. Physiol.* 521, 135–146. doi: 10.1111/j.1469-7793.1999.00135.x

Shapiro, E., Castellucci, V. F., and Kandel, E. R. (1980). Presynaptic membrane potential affects transmitter release in an identified neuron in Aplysia by modulating the $Ca^{2+}$ and $K^+$ currents. *Proc. Natl. Acad. Sci. U S A* 77, 629–633. doi: 10.1073/pnas.77.1.629

Shimahara, T. (1981). Modulation of synaptic output by the transient outward potassium current in aplysia. *Neurosci. Lett.* 24, 139–142. doi: 10.1016/0304-3940(81)90237-8

Shimahara, T. (1983). Presynaptic modulation of transmitter release by the early outward potassium current in Aplysia. *Brain Res.* 263, 51–56. doi: 10.1016/0006-8993(83)91199-x

Shimahara, T., and Peretz, B. (1978). Soma potential of an interneurone controls transmitter release in a monosynaptic pathway in Aplisia. *Nature* 273, 158–160. doi: 10.1038/273158a0

Shimahara, T., and Tauc, L. (1975). Multiple interneuronal afferents to the giant cells in Aplysia. *J. Physiol.* 247, 299–319. doi: 10.1113/jphysiol.1975.sp010933

Shu, Y., Hasenstaub, A., Duque, A., Yu, Y., and McCormick, D. A. (2006). Modulation of intracortical synaptic potentials by presynaptic somatic membrane potential. *Nature* 441, 761–765. doi: 10.1038/nature04720

Shu, Y., Yu, Y., Yang, J., and McCormick, D. A. (2007). Selective control of cortical axonal spikes by a slowly inactivating $K^+$ current. *Proc. Natl. Acad. Sci. U S A* 104, 11453–11458. doi: 10.1073/pnas.0702041104

Sierksma, M. C., and Borst, J. G. G. (2017). Resistance to action potential depression of a rat axon terminal *in vivo*. *Proc. Natl. Acad. Sci. U S A* 114, 4249–4254. doi: 10.1073/pnas.1619433114

Takeuchi, A., and Takeuchi, N. (1962). Electrical changes in pre- and postsynaptic axons of the giant synapse of Loligo. *J. Gen. Physiol.* 45, 1181–1193. doi: 10.1085/jgp.45.6.1181

Tateno, T., and Robinson, H. P. (2006). Rate coding and spike-time variability in cortical neurons with two types of threshold dynamics. *J. Neurophysiol.* 95, 2650–2663. doi: 10.1152/jn.00683.2005

Thio, L. L., and Yamada, K. A. (2004). Differential presynaptic modulation of excitatory and inhibitory autaptic currents in cultured hippocampal neurons. *Brain Res.* 1012, 22–28. doi: 10.1016/s0006-8993(04)00467-6

Timofeev, I., and Chauvette, S. (2017). Sleep slow oscillation and plasticity. *Curr. Opin. Neurobiol.* 44, 116–126. doi: 10.1016/j.conb.2017.03.019

Turecek, R., and Trussell, L. O. (2001). Presynaptic glycine receptors enhance transmitter release at a mammalian central synapse. *Nature* 411, 587–590. doi: 10.1038/35079084

Vivekananda, U., Novak, P., Bello, O. D., Korchev, Y. E., Krishnakumar, S. S., Volynski, K. E., et al. (2017). Kv1.1 channelopathy abolishes presynaptic spike width modulation by subthreshold somatic depolarization. *Proc. Natl. Acad. Sci. U S A* 114, 2395–2400. doi: 10.1073/pnas.1608763114

Xia, Y., Zhao, Y., Yang, M., Zeng, S., and Shu, Y. (2014). Regulation of action potential waveforms by axonal $GABA_A$ receptors in cortical pyramidal neurons. *PLoS One* 9:e100968. doi: 10.1371/journal.pone.0100968

Yang, J., Ye, M., Tian, C., Yang, M., Wang, Y., and Shu, Y. (2013). Dopaminergic modulation of axonal potassium channels and action potential waveform in pyramidal neurons of prefrontal cortex. *J. Physiol.* 591, 3233–3251. doi: 10.1113/jphysiol.2013.251058

Yang, Y. M., and Wang, L. Y. (2006). Amplitude and kinetics of action potential-evoked $Ca^{2+}$ current and its efficacy in triggering transmitter release at the developing calyx of Held synapse. *J. Neurosci.* 26, 5698–5708. doi: 10.1523/JNEUROSCI.4889-05.2006

Zbili, M., Rama, S., and Debanne, D. (2016). Dynamic control of neurotransmitter release by presynaptic potential. *Front. Cell. Neurosci.* 10:278. doi: 10.3389/fncel.2016.00278

Zhu, J., Jiang, M., Yang, M., Hou, H., and Shu, Y. (2011). Membrane potential-dependent modulation of recurrent inhibition in rat neocortex. *PLoS Biol.* 9:e1001032. doi: 10.1371/journal.pbio.1001032

Zorrilla de San Martin, J., Trigo, F. F., and Kawaguchi, S. Y. (2017). Axonal $GABA_A$ receptors depolarize presynaptic terminals and facilitate transmitter release in cerebellar Purkinje cells. *J. Physiol.* 595, 7477–7493. doi: 10.1113/jp275369

Zucker, R. S., and Regehr, W. G. (2002). Short-term synaptic plasticity. *Annu. Rev. Physiol.* 64, 355–405. doi: 10.1146/annurev.physiol.64.092501.114547

**Conflict of Interest Statement**: The authors declare that the research was conducted in the absence of any commercial or financial relationships that could be construed as a potential conflict of interest.

*Copyright © 2019 Zbili and Debanne. This is an open-access article distributed under the terms of the Creative Commons Attribution License (CC BY). The use, distribution or reproduction in other forums is permitted, provided the original author(s) and the copyright owner(s) are credited and that the original publication in this journal is cited, in accordance with accepted academic practice. No use, distribution or reproduction is permitted which does not comply with these terms.*

frontiers in Cellular Neuroscience

ORIGINAL RESEARCH
published: 14 May 2019
doi: 10.3389/fncel.2019.00210

# Modeling Analysis of Axonal After Potential at Hippocampal Mossy Fibers

*Haruyuki Kamiya**

*Department of Neurobiology, Graduate School of Medicine, Hokkaido University, Sapporo, Japan*

Action potentials reliably propagate along the axons, and after potential often follows the axonal action potentials. After potential lasts for several tens of millisecond and plays a crucial role in regulating excitability during repetitive firings of the axon. Several mechanisms underlying the generation of after potential have been suggested, including activation of ionotropic autoreceptors, accumulation of $K^+$ ions in the surrounding extracellular space, the opening of slow voltage-dependent currents, and capacitive discharge of upstream action potentials passively propagated through axon cable. Among them, capacitive discharge is difficult to examine experimentally, since the quantitative evaluation of a capacitive component requires simultaneous recordings from at least two different sites on the connecting axon. In this study, a series of numerical simulation of the axonal action potential was performed using a proposed model of the hippocampal mossy fiber where morphological as well as electrophysiological data are accumulated. To evaluate the relative contribution of the capacitive discharge in axonal after potential, voltage-dependent $Na^+$ current as well as voltage-dependent $K^+$ current was omitted from a distal part of mossy fiber axons. Slow depolarization with a similar time course with the recorded after potential in the previous study was left after blockade of $Na^+$ and $K^+$ currents, suggesting that a capacitive component contributes substantially in axonal after potential following propagating action potentials. On the other hand, it has been shown that experimentally recorded after potential often showed clear voltage-dependency upon changes in the initial membrane potential, obviously deviating from voltage-independent nature of the capacitive component. The simulation revealed that activation of voltage-dependent $K^+$ current also contributes to shape a characteristic waveform of axonal after potential and reconstitute similar voltage-dependency with that reported for the after potential recorded from mossy fiber terminals. These findings suggest that the capacitive component reflecting passive propagation of upstream action potential substantially contributes to the slow time course of axonal after potential, although voltage-dependent $K^+$ current provided a characteristic voltage dependency of after potential waveform.

**Keywords: axon, action potential, after potential, capacitive discharge, simulation**

OPEN ACCESS

***Edited by:***
*Shin-ya Kawaguchi,*
*Kyoto University, Japan*

***Reviewed by:***
*Yousheng Shu,*
*Beijing Normal University, China*
*Mitsuharu Midorikawa,*
*Tokyo Women's Medical University, Japan*

***Correspondence:**
*Haruyuki Kamiya*
*kamiya@med.hokudai.ac.jp*

***Specialty section:***
*This article was submitted to Cellular Neurophysiology, a section of the journal Frontiers in Cellular Neuroscience*

***Received:*** *13 February 2019*
***Accepted:*** *25 April 2019*
***Published:*** *14 May 2019*

***Citation:***
*Kamiya H (2019) Modeling Analysis of Axonal After Potential at Hippocampal Mossy Fibers. Front. Cell. Neurosci. 13:210. doi: 10.3389/fncel.2019.00210*

## INTRODUCTION

The axon carries neuronal information reliably to the presynaptic terminal as a form of the action potential (Debanne et al., 2011). Propagation of action potential along axon has been considered as a highly reliable digital process (Bean, 2007), although the excitability of axons is slightly modulated for a short period after generation of action potential up to tens to hundreds of milliseconds (Gardner-Medwin, 1972; Zucker, 1974). This post-stimulus change in the excitability of axon was mediated, at least in part, by depolarizing after potential which often follows action potential in the axon (Barrett and Barrett, 1982). After potential in axon may be important for temporal integration of neuronal signaling in the brain by affecting short-term plasticity of presynaptic transmitter release (for review, Ohura and Kamiya, 2016). For the candidate cellular mechanisms of axonal after potential, several possibilities have been suggested so far. These include not only passive mechanism reflecting an intrinsic property of axonal membrane (i.e., capacitive discharge of upstream action potentials; Barrett and Barrett, 1982; Borst et al., 1995; David et al., 1995), but also active mechanism due to slow activation of voltage-dependent channels (i.e., persistent-type or resurgent-type $Na^+$-channels; Kim et al., 2010; Ohura and Kamiya, 2018b) or extrinsic mechanisms such as $K^+$ accumulation (Malenka et al., 1981; Meeks and Mennerick, 2004) or autoreceptor activation (Kamiya et al., 2002; de San Martin et al., 2017). The relative contribution of active and passive mechanisms varies among different type of axons (Barrett and Barrett, 1982; Borst et al., 1995; Kim et al., 2010; Ohura and Kamiya, 2018b), although passive mechanisms due to capacitive discharge commonly underlie axonal depolarizing after potential. Despite functional significance in temporal integration (Ohura and Kamiya, 2018a), however, the property and the underlying mechanism of after potential was not thoroughly studied experimentally, especially in thin axons in the central nervous system, because of the extremely small size of axon diameter does not allow direct recordings from the axonal membrane in thin axons.

So far, several studies tried to characterize the axonal after potential by direct recording from axon terminals exceptionally large enough for patch-clamp recording, i.e., calyx of Held (Borst et al., 1995; Kim et al., 2010) and hippocampal mossy fiber terminal (Ohura and Kamiya, 2018b). Although previous studies have suggested that after potential at soma was mediated by several different mechanisms (Raman and Bean, 1997; Yue and Yaari, 2004; Gu et al., 2005; Metz et al., 2005; Yue et al., 2005; D'Ascenzo et al., 2009; Martinello et al., 2015). In this study, it was attempted to describe the quantitative contribution of the capacitive component in axonal after potential by a numerical simulation of membrane potential. For this purpose, we adopted a realistic model of hippocampal mossy fiber (Engel and Jonas, 2005) assuming typical *en passant* structure with large boutons implemented with voltage-dependent $Na^+$- and $K^+$ conductance reflecting properties of those recorded from mossy fiber terminals. A series of simulation analysis revealed the relative contribution of the capacitive component due to the passive propagation of upstream action potential. The simulation also illustrated the characteristic voltage-dependency of after potential recorded from mossy fiber terminals (Ohura and Kamiya, 2018b). The early phase of after potential is mainly determined by voltage-dependent $K^+$ conductance (Storm, 1987; Geiger and Jonas, 2000; Dodson et al., 2003), while the later phase is mediated by capacitive discharges of the axonal membrane. The sequential contribution of voltage-dependent $K^+$ conductance and capacitive component nicely reconstructed the time course and voltage-dependency of axonal after potential observed experimentally (Geiger and Jonas, 2000; Ohura and Kamiya, 2018b).

## MATERIALS AND METHODS

### Simulation

The simulated membrane potential ($V_m$) was calculated according to the model suggested by Engel and Jonas (2005) based on the data recorded from mossy fiber boutons. The model basically assumed a Hodgkin Huxley-type gating model adapted to channels those recorded in mossy fiber terminals, and $K^+$ channel inactivation (Geiger and Jonas, 2000) was reconstructed by implementing multiplicatively with parameters of recombinant $K_V1.4$ channels (Wissmann et al., 2003). Simulations were performed using NEURON 7.5 for Windows (Hines and Carnevale, 1997). The passive electrical properties of the axon were assumed to be uniform, with a specific membrane capacitance Cm of 1 $\mu F\ cm^{-2}$, a specific membrane resistance Rm of 10,000 $\Omega\ cm^2$, and an intracellular resistivity Ri of 110 $\Omega$ cm. The structure of the mossy fiber (Acsády et al., 1998; Henze et al., 2000) was approximated by a soma (diameter, 10 $\mu$m), 10 axonal cylinders (diameter, 0.2 $\mu$m; length, 100 $\mu$m), and 10 *en passant* boutons (diameter, 4 $\mu$m). The number of segments was 1 $\mu m^{-1}$, and the time step (dt) was 5 $\mu$s in all simulations. The resting potential was assumed to be −80 mV, although it was changed to −90 or −100 mV in some series of simulation. The reversal potential of the leak conductance was set to −81 mV to maintain stability. Voltage-gated $Na^+$ channels, $K^+$ channels, and leakage channels were inserted into the soma, axon, and boutons, respectively. The $Na^+$ conductance density was set to 50 mS $cm^{-2}$ for the axon and boutons and 10 mS $cm^{-2}$ for the soma. The $K^+$ conductance density was set to 36 mS $cm^{-2}$ throughout all parts of the neurons. Action potentials were evoked by injection of depolarizing current into the 9th bouton (0.2 ms, 0.1 or 0.2 nA) or the soma (2 ms, 0.2 nA). The equilibrium potentials for $Na^+$ and $K^+$ ions were assumed to be +50 and −85 mV, respectively. In the simulation in **Figure 5**, equilibrium potentials of $K^+$ ions were varied from −65 to −105 mV,

## RESULTS

### Passive Propagation of Action Potential Along the Mossy Fiber Model

Capacitive discharge of axonal membrane due to upstream action potential might contribute to a downstream action

potential. To evaluate the relative contribution of components reflecting passive propagation, voltage-dependent $Na^+$- and $K^+$ conductance was removed from distal portions of mossy fibers, and spatial profile of depolarization was examined. In the control condition, reliable propagation of action potential was reconstructed by simulation (**Figure 1A**). A small increase in the peak amplitude at the 10th bouton is possibly due to the seal end effect at the last bouton in the model. When $Na^+$- and $K^+$ conductance was omitted from distal axons from the eighth axon and bouton, substantial depolarization propagated passively (**Figure 1B**), but the amplitude declined along with the distance and the time course was slowed (**Figure 1C**), possibly reflecting the electrical filtering property of axon cable. The amplitude was plotted against distance from the 7th bouton, end of the compartment which expresses normal $Na^+$ and $K^+$ conductance. Data points were fitted with single exponential, and the distance with a reduction to 1/e (37%) was evaluated as 53 μm (**Figure 1D**). These results suggest that passively propagated depolarization partly contributed to the after potential recorded from downstream boutons. Conversely, passive propagation from the downstream compartment may affect upstream action potential. Passive depolarization may spatially distribute both backward and forward directions at a certain time point, although ionic component travels only forward direction by propagation of action potential. In support of this notion, action potential recorded at the 7th bouton was slightly smaller than that recorded from the upstream bouton as illustrated in **Figure 1B**. The rising phase of action potentials at downstream bouton concurs with the peak of an action potential at the upstream bouton, and therefore affecting the peak of the upstream action potential.

The value of spatial decay constant of 53 μm for passive propagation was relatively short. This may partly due to the filtering of fast voltage transient of the action potential by axon cable. In line with this notion, the length constant of mossy fiber model, as measure by spatial decay of steady-state hyperpolarization in response to current injection of longer step-pulse (4 pA for 500 ms, **Figure 1E**) was estimated as 171 μm (**Figure 1F**). This value is much close to that evaluated for EPreSP (subthreshold passive propagated somatic EPSP at mossy fiber axon (430 μm, Alle and Geiger, 2006).

## Voltage-Dependency of Axonal After Potential in Mossy Fiber Model

Previous studies in the calyx of Held (Sierksma and Borst, 2017), in the cerebellar basket cells (Begum et al., 2016), and in the hippocampal mossy fibers (Ohura and Kamiya, 2018b), have shown that the amplitude of after potential was negatively correlated with the initial membrane potentials. To test if a similar voltage dependency is reconstructed in simulation, resting membrane potential was changed by altering the equilibrium potential of leak conductance. At resting potential of −80 mV, after potentials are hyperpolarizing in polarity (**Figures 2A,B**). At −90 or −100 mV, depolarizing after potential with similar time course with those recorded experimentally were reconstructed (**Figures 2C–F**).

Superimposed traces of the reconstructed action potentials and after potentials (**Figures 2G,H**) clearly illustrated that the early phase, the initial 5 ms, converges around equilibrium potential of $K^+$ ions (−85 mV) as shown by an asterisk. It should be noted that the action potential onset was delayed at −90 or −100 mV (**Figures 2G,H**), possibly reflecting the slightly slower conduction at these negative membrane potentials than at −80 mV.

Simulation at −80 to −100 mV in which voltage-dependent $Na^+$- and $K^+$ conductance was removed from distal portions of mossy fibers shown in red (**Figure 2I**) left capacitive component which basically shows no voltage-dependency as in **Figure 2G**, although the small difference in amplitude (**Figure 2J**) possibly reflect changes in the amplitude of upstream action potential at different membrane potentials (at −80 to −100 mV). In line with this notion, action potentials at the 9th bouton show similar changes in amplitude as in **Figures 2K,L**. The difference in onset of action potentials (**Figures 2K,L**) and the downstream capacitive components (**Figures 2K,L**) may also be caused by the slower conduction at −90 or −100 mV.

## Ionic and Capacitive Components Underlying Propagating Action Potential

To get insight into the relative contribution of ionic and capacitive mechanisms in shaping time course of axonal after potential, a series of simulation to replace voltage-dependent $Na^+$ and $K^+$ conductance in the axonal membrane were carried out. Propagating action potential recorded from the 10th bouton (**Figure 3A**, *black*) was broadened by removal of voltage-dependent $K^+$ conductance from the 10th axon and bouton as shown in *red* (**Figure 3A**, *blue*). Further removal of voltage-dependent $Na^+$ conductance reduced the amplitude substantially (**Figure 3A**, *green*), although substantial depolarization, which possibly reflects the capacitive component due to passive propagation of upstream action potential. Superimposed traces in **Figure 3B** shows crosspoint between *black* and *green* traces, suggesting that $K^+$ conductance curtails passive components to shape the characteristic waveform of after potential. Using these data, components of membrane potential changes due to activation of $Na^+$ channels ($V_{mNa}$, *orange*) or $K^+$ channels ($V_{mK}$, *purple*) were calculated by subtraction. Sum of $V_{mNa}$ and $V_{mK}$ was calculated and shown in *red* (**Figure 3C**). Superimposed traces in **Figure 3D** clearly illustrate the temporal relationship of these components.

Similar simulation analysis was also performed at the resting potential of −100 mV, in which the waveform of after potential (**Figures 3E,F**) closely resembles with those of the recorded waveform of depolarizing after potential in the experiment (Geiger and Jonas, 2000; Ohura and Kamiya, 2018b). $Na^+$- (*orange*) and $K^+$-channel dependent (*purple*) components were calculated (**Figure 3G**), and the time course was compared with capacitive component (*green*) isolated by removing $Na^+$- and $K^+$- conductance. **Figure 3H** also illustrated that the relative contribution of each component, although a small effect of shunting of passive depolarization by large ionic components could not be excluded entirely. The amplitude of the early

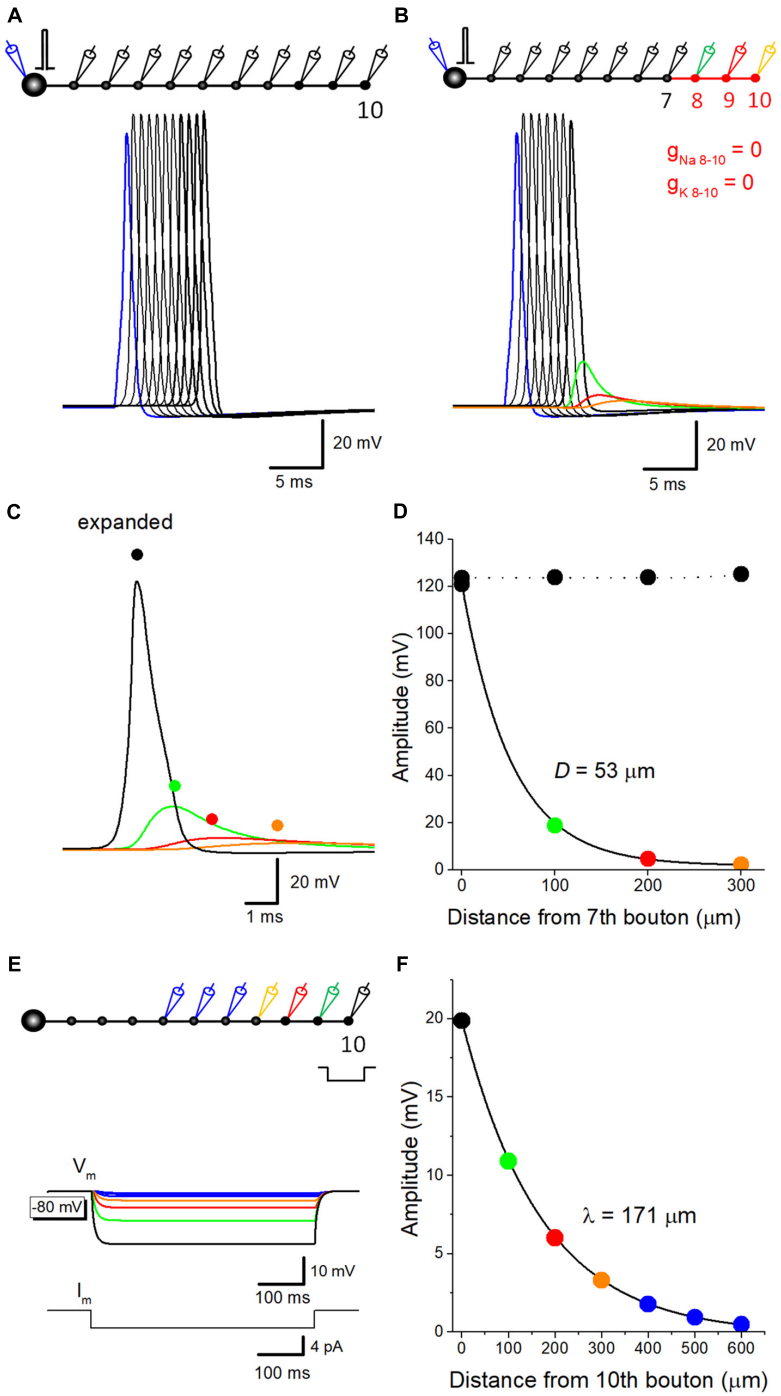


**FIGURE 1 |** Estimation of passive propagation of action potential along a hippocampal mossy fiber model. **(A)** Reliable propagation of action potential throughout *en passant* axon with 10 boutons evenly spaced every 100 μm ("a pearl chain model"). Brief current injection into the soma elicited action potential which propagates faithfully to the 10th bouton without attenuation. **(B)** Distance-dependent decay of the amplitude of action potential without voltage-dependent ionic conductance. Voltage-gated $Na^+$- and $K^+$-channels were omitted from the distal portion of mossy fiber axon from 8th (*green*) to 10th (*orange*) boutons and axon, as shown in *red*. The amplitude of depolarization decreased successively, and the time course was slowed down along the distance, consistent with the notion that it reflects passive propagation due to capacitive discharge by an upstream action potential. **(C)** Traces in **B** were expanded in time for comparison. **(D)** Spatial profiles of passive propagation. The decay of the peak amplitude along the distance was fitted by a single exponential with 53 μm for the length with a reduction to 1/e (37%). The amplitude of propagating action potentials with $Na^+$- and $K^+$-channels (*black*) was shown for comparison. **(E)** Hyperpolarizing responses to long pulse current injection of 4 pA for 500 ms into the 10th bouton, which were used for estimation of the length constant of steady-state hyperpolarization. **(F)** The decay of the peak amplitude along the distance was fitted by a single exponential with 171 μm.

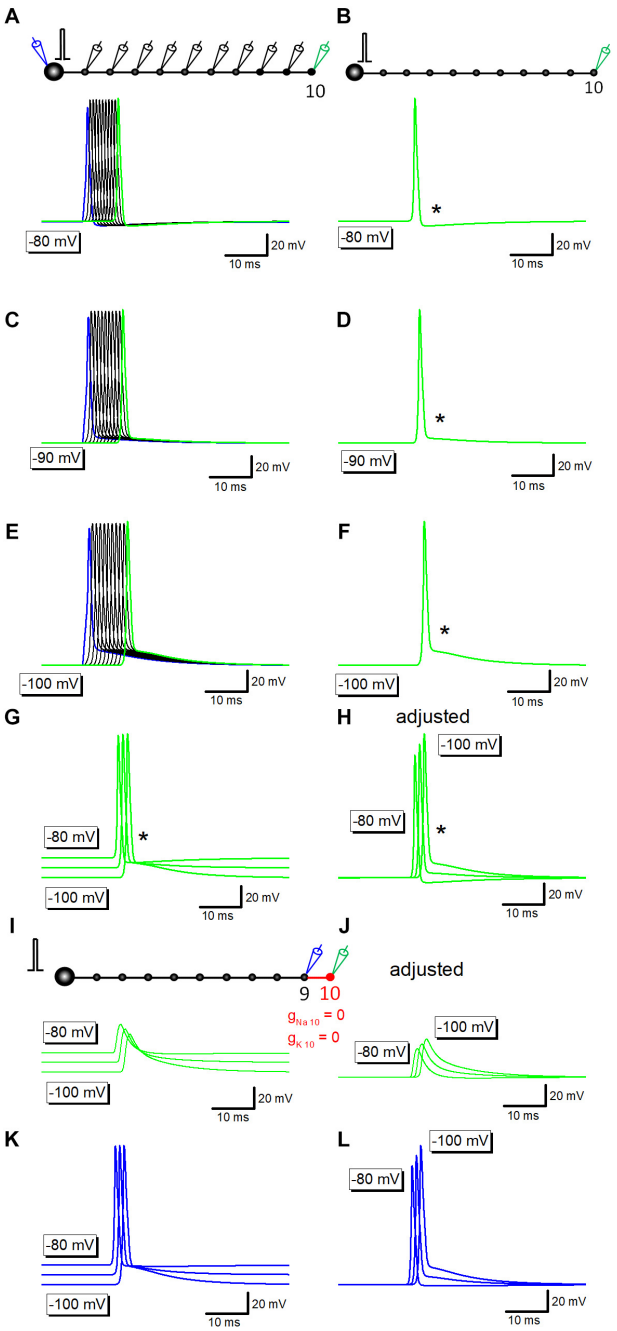


**FIGURE 2 |** Voltage-dependency of components of axonal after potential. **(A)** Propagating action potentials recorded from every bouton in which the resting potential was set at –80 mV. **(B)** Action potential at the 10th bouton was shown in *green*. An asterisk (*) shows the hyperpolarizing after potential. **(C–F)** Similar traces in which the resting potential was set at –90 mV **(C,D)** or at –100 mV **(E,F)**. After potential (*) was reversed in polarity to depolarizing one. **(G)** Superimposed traces in panels **(B,D,F)**. **(H)** Traces in panel **(G)** were aligned by subtracting baseline soon before the response to compare the time course of after potential at various membrane potentials. **(I)** Capacitive component due to passive propagation was calculated by removing $Na^+$- as well as $K^+$-channels from 10th axon and bouton (*red*). **(J)** Traces in panel **(I)** were adjusted for the baseline to compare the time course. **(K)** Action potential waveforms at the 9th bouton in the above simulation. **(L)** Traces in panel **(K)** were adjusted for the baseline to compare the time course.

phase of after potential is close to the equilibrium potential of $K^+$ ions ($E_K$, −85 mV), in line with the notion that the early phase is dominantly determined by the $K^+$ channel-dependent component.

## Capacitive Current Underlying Propagating Action Potential

To illustrate the exact time course and the sequence of activation of ionic and capacitive components, capacitive current ($I_{cap}$) propagating from upstream axon was simulated. Outward $I_{cap}$ (*red*) preceded the onset of inward $Na^+$-current ($I_{Na}$, *blue*) and outward $K^+$-current ($I_K$, *green*) during propagating action potential elicited by somatic stimulation (**Figure 4A**), as highlighted with an asterisk (*). The delay in activation of ionic currents reflects passive propagation due to capacitive discharge from the upstream axonal membrane. In contrast, when action potentials were evoked by current injection to the recorded bouton, there was no delay between the onsets of $I_{cap}$ and $I_{Na}$ (**Figure 4B**). Arrow indicates capacitive current due to current injection. The delay from capacitive to the ionic component is much obvious when the resting potential was set at −100 mV (**Figure 4C**). Direct stimulation at the recorded bouton also elicited $I_{cap}$ and $I_{Na}$ without delay at −100 mV (**Figure 4D**).

## Potassium Conductance Determines the Initial Phase of After Potential

Then it was examined whether potassium channel-dependent fast repolarization dominate time course of the initial phase of after potential. For this purpose, the equilibrium potential for $K^+$ ions around the 10th axon and bouton ($E_{K10}$) was changed systematically to vary the driving force of $K^+$ ions across the axonal membrane. Upon changes in $E_{K10}$ from −65 to −105 mV, initial phase (or breakpoint) was changed (**Figure 5A**). When $E_{K10}$ was set at more positive (−65 or −75 mV) than resting potential (−80 mV), after potential reversed polarity to depolarizing. A passive propagating component as measured by blocking voltage-dependent $Na^+$- and $K^+$ conductance was unchanged by an alteration in $E_{K10}$ (**Figure 5B**). Similar results were obtained when resting potentials were set at −100 mV (**Figures 5C,D**). These results suggest that activation of $K^+$ conductance determines fast repolarization and the breakpoint of the initial phase of after potential.

## The Contribution of Passive Capacitive Discharge in the Late Phase of After Potential

Time course of the slow phase of afterpotential seems to be slow enough to be explained by the passive properties of the axonal membrane. To test this notion, the simulation of propagating action potential with stepwise current injection was performed. Time course of slow relaxation of membrane potential upon current step injection (triangle) was quite similar to that of the late phase of afterpotential (asterisk) as shown in **Figure 6A**. The time constant of hyperpolarizing responses was 7.9 ms, while that of the late phase of afterpotential was 7.1 ms. The similarity in the time courses was also illustrated in the simulation data

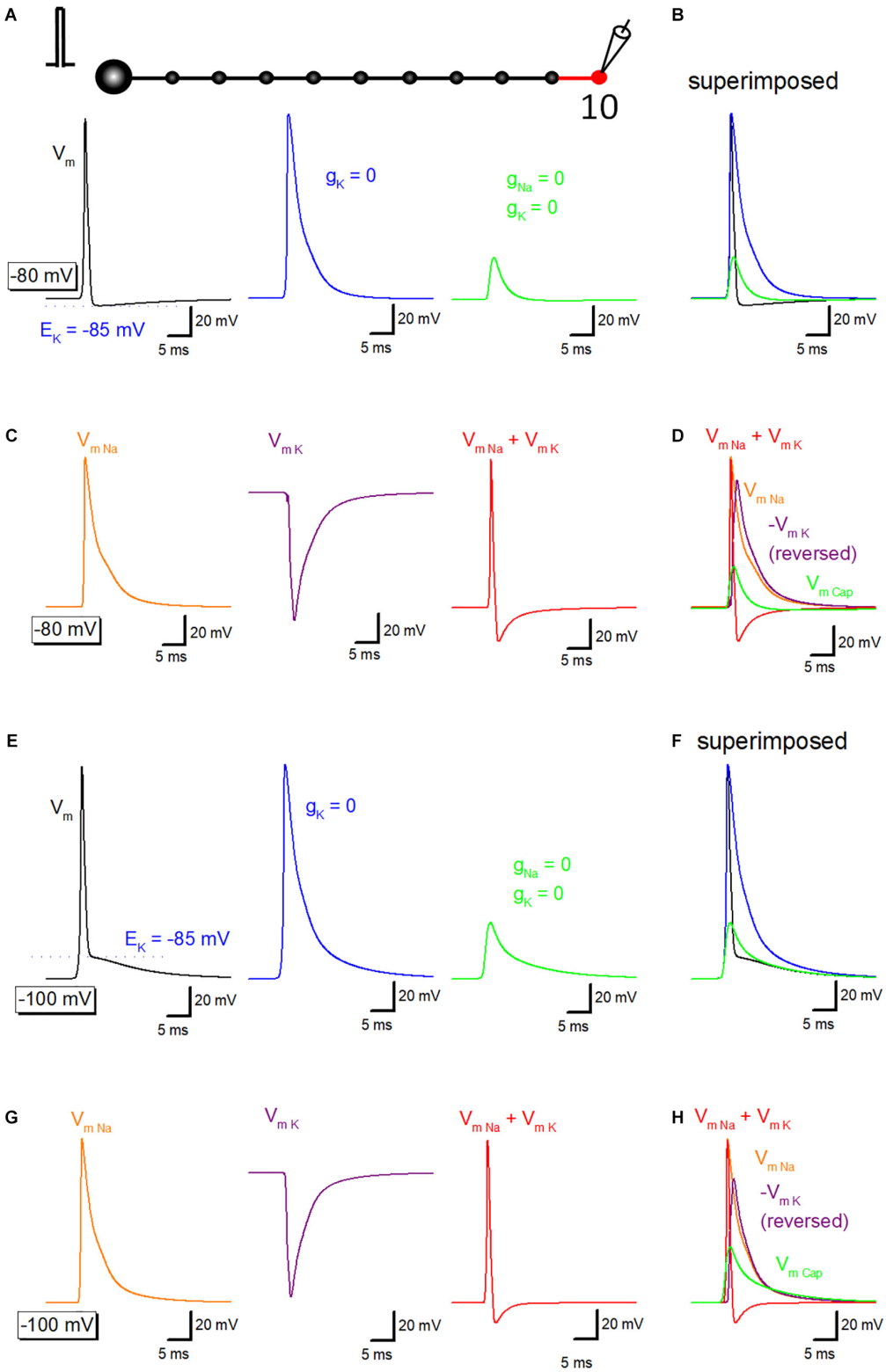


**FIGURE 3 |** Ionic and capacitive components underlying propagating action potential. **(A)** Reconstructed action potentials at the 10th boutons in the model (left, *black*). Equilibrium potential of $K^+$ ions ($E_K$, –85 mV) was shown as a *blue* dotted line. When voltage-dependent $K^+$ conductance was removed from 10th axon shaft and 10th bouton illustrating in the red, decay phase of the action potential was significantly delayed (middle, *blue*). Removal of voltage-dependent $Na^+$ conductance as well largely reduced the amplitude (right, *green*). **(B)** Superimposed traces in panel **(A)**. **(C)** Calculated components due to activation of voltage-dependent $Na^+$ channels ($V_{mNa}$, *orange*), $K^+$ channels ($V_{mK}$, *purple*) and the sum of them ($V_{mNa}$ + $V_{mK}$, *red*). **(D)** Superimposed traces in **C**. **(E–H)** Similar data from panels **(A–D)** except for the resting potential was set at –100 mV. $E_K$ (–85 mV) was also shown as a *blue* dotted line in Panel **(E)**.

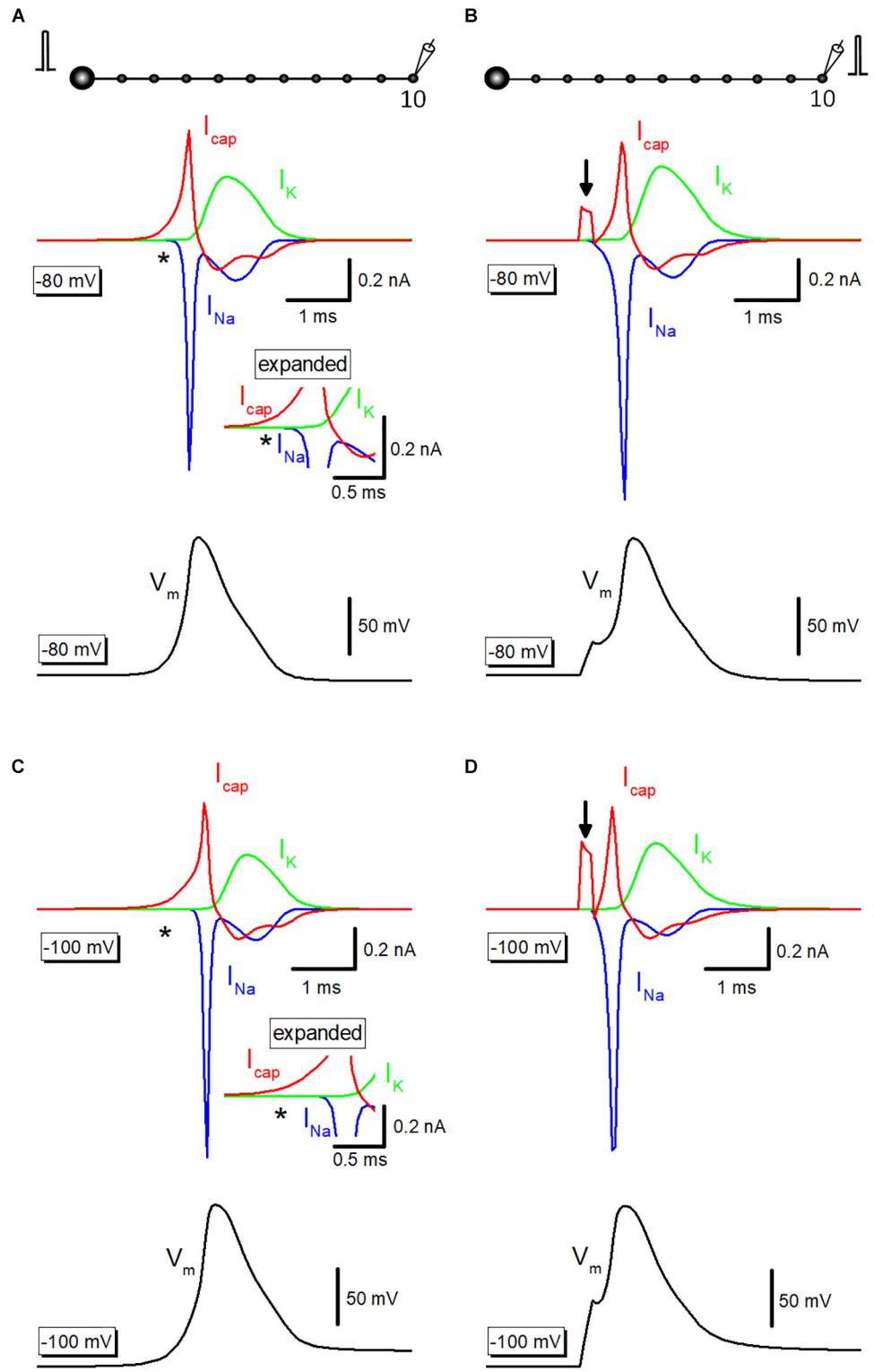


**FIGURE 4 |** Capacitive current during propagating an action potential. **(A)** Capacitive current ($I_{cap}$, *red*) during propagating action potential (*black*) were shown with $Na^+$- ($I_{Na}$, *blue*) and $K^+$-current ($I_K$, *green*). $I_{Na}$ initiated with a delay from the onset of $I_{cap}$ as shown by an asterisk (*). The inset represents the time-expanded traces showing the delay from capacitive ($I_{cap}$) to the ionic ($I_{Na}$ and $I_K$) components. **(B)** $I_{cap}$ (*red*), $I_{Na}$ (*blue*), and $I_K$ (*green*) during action potential elicited by current injection into the recorded bouton (*black*). Arrow indicates capacitive current due to injected current. **(C,D)** Similar data with **A,B** except for the resting potential was set at –100 mV.

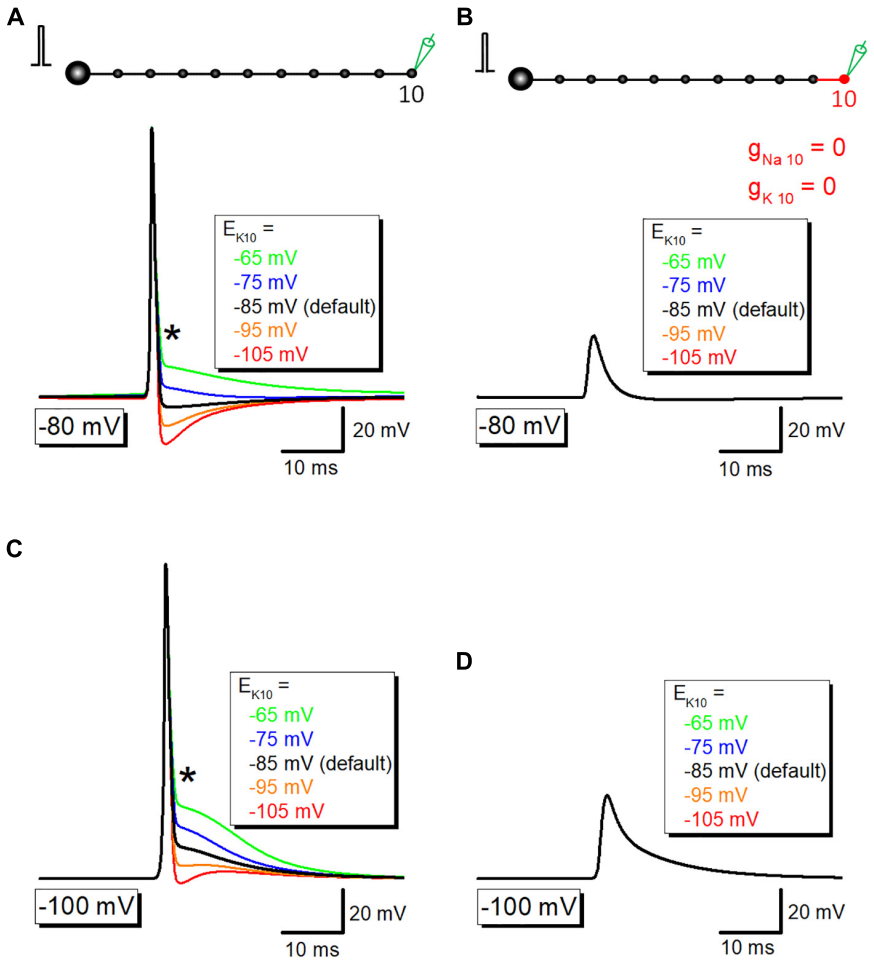


**FIGURE 5 |** The contribution of $K^+$ conductance in the initial phase of after potential. **(A)** The dependency of after potential on equilibrium potential for $K^+$ ions around the 10th axon and bouton ($E_{K10}$). The initial phase of after potential, as marked by an asterisk (*), was linearly changed with alteration of $E_K$. **(B)** Capacitive component of passive propagation, isolated by removal of $Na^+$-and $K^+$-conductance, was unchanged by alteration of $E_K$. **(C,D)** Similar data with panels **(A,B)** except for the resting potential was set at –100 mV.

with the initial membrane potential at −100 mV (**Figure 6B**). The contribution of capacitive components was also supported by the simulation changing the value of specific membrane capacitance (Cm) systematically. As expected from cable filtering by capacitance, increase in Cm reduce and prolonged the passive propagating component as shown in **Figure 6C**. Taking together, it was suggested that the capacitive component of passive propagation contribute substantially to the generation of depolarizing after potential.

## DISCUSSION

In this study, a series of numerical simulation using a realistic model of hippocampal mossy fiber was performed to illustrate the possible mechanisms underlying after potential following an axonal action potential. The early phase of after potential converges on the equilibrium potential of $K^+$ ions ($E_K$) and thereby the dominant contribution of voltage-dependent $K^+$ channels was suggested. On the other hand, the later phase was most likely explained by the passive capacitive discharge of the axonal membrane. A characteristic waveform of action potential-after potential sequence was nicely reconstructed by a combination of a breakpoint due to fast repolarization by the opening of $K^+$ channels and slow relaxation of polarization by the capacitive discharge of the axonal membrane.

### Evaluation of Passive Propagation of Action Potential Along the Mossy Fiber Model

In an experimental approach, it is difficult to estimate the spatial and temporal distribution of a passive component in a propagating action potential along the axon. Recordings from at least two distinct sites of the connecting axon, as well as spatially restricted blocking of voltage-gated conductance to eliminate an active component, are necessary for the evaluation of passive properties of axonal membranes (de San Martin et al., 2017).

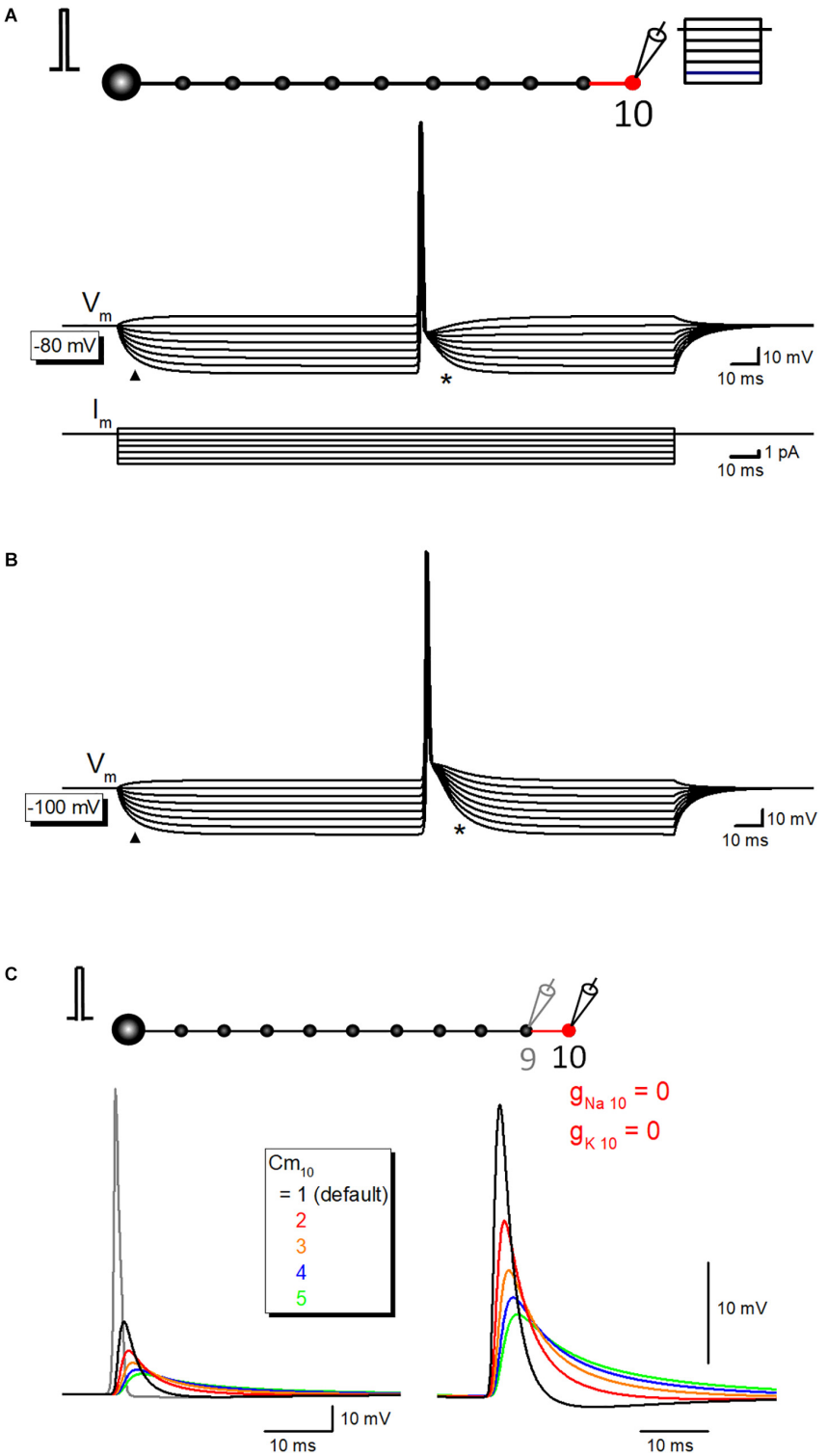


**FIGURE 6 |** The contribution of passive capacitive discharge in the late phase of after potential. **(A)** Propagating action potential-after potential sequence recorded at various membrane potentials in response to stepwise current injection (from +1 to –6 pA, 1 pA steps) to the recorded 10th bouton whose resting membrane potential was set at –80 mV. Note that the slow relaxation of membrane potential in response to stepwise current injection (triangle) shows a similar time course with that of after potential (asterisk). Lower traces are showing step-pulse current injection. **(B)** Similar records at –100 mV initial membrane potential. Again, time courses of hyperpolarization to step current injection (triangle) are similar to that of after potential. **(C)** Effect of the changes in the specific membrane capacitance Cm on passive capacitive component measured by removal of $g_{Na}$ and $g_K$ from the 10th axon and bouton.

These requirements are difficult to be achieved in the experimental conditions, while simulation readily figures out passive components in a propagating action potential.

The amplitude of passive components reflecting action potential at the next *en passant* bouton is estimated as 19 mV. The simulation also showed that the amplitude of the passive component declined along with the distance. The decay of the amplitude of passive components was fit with single exponential with the length for a reduction to 1/e as 53 μm. This value was similar to that estimated for $GABA_A$-receptor mediated response in axons of cerebellar molecular layer interneurons and in axons of cultured Purkinje cells (de San Martin et al., 2015, 2017). Passive component inevitably involves in a substantial fraction in propagating action potential-after potential sequence. This notion should be directly tested experimentally by subcellular recording approach from two distinct sites of a connecting mossy fiber axon.

The amplitudes of experimentally observed depolarizing after potentials at mossy fiber terminals are 6.9 ± 0.6 mV in the rat (Geiger and Jonas, 2000) and 15.3 ± 1.3 mV in the mouse (Ohura and Kamiya, 2018b). In our simulation, the action potential of 121 mV was decayed to 19 mV at 100 μm and 5 mV at 200 μm by passive propagation as shown in **Figure 1D**, suggesting that inter-bouton distances are ranged between 100 and 200 μm. Although the cable properties also depend on Cm value and the diameter of mossy fibers, the simple model suggested by Engel and Jonas (2005), which we adopted in this study, reasonably approximated the experimental values of after potential amplitude.

## Voltage-Dependent $K^+$ Channels Provide a Breakpoint in the Early Phase of After Potential

Previous studies consistently suggested that axonal after potential was mediated by the capacitive discharge of the axonal membrane. Contrary to expected from passive nature of capacitive component, however, it was shown that the amplitude of after potential shows clear voltage-dependency, i.e., after potential was smaller at depolarizing membrane potential, while it got bigger at hyperpolarizing membrane potential (Begum et al., 2016; Sierksma and Borst, 2017; Ohura and Kamiya, 2018b). The results of simulation in this study revealed that the characteristic waveform of after potential was reconstructed by a combination of fast repolarization by voltage-gated $K^+$-channels and by the passive capacitive discharge of the axonal membrane. Time course of the late phase of after potential was similar to those of slow relaxation of membrane potential in response to stepwise hyperpolarizing current injection, in consistent with the passive nature of the capacitive component.

Combination of voltage-dependent $K^+$ conductance and capacitive discharge might be a too simplified interpretation of the characteristic time course of after potential. Since previous studies pointed out that other voltage-dependent conductance, such as resurgent (Kim et al., 2010; Ohura and Kamiya, 2018b) as well as persistent $Na^+$ current (Yue et al., 2005), are involved in the late phase of after potential. These voltage-dependent currents might additionally involve in boosting up the after potential. Several previous studies reported that after potential waveform was altered upon changes in the recording membrane potentials, and sometimes reverse in polarity at depolarized membrane potentials. The reversal potentials estimated or extrapolated from the recorded after potential waveforms varies considerably (Begum et al., 2016; Sierksma and Borst, 2017; Ohura and Kamiya, 2018b), possibly reflecting the various contribution of active (voltage-dependent conductance) and passive (capacitive discharge) components. Overall voltage-dependency is consistent with the notion that early phase is predominantly governed by voltage-dependent $K^+$ conductance since the initial phase seems to reverse around $E_K$. The later phase is likely to reflect voltage-independent passive components of slow depolarization. These notions suggested that voltage-dependent $K^+$ channels and capacitive discharge involve as common mechanisms to shape the framework of after potential, while active conductance such as resurgent $Na^+$ current or T-type $Ca^{2+}$ current may additively contribute to the late phase of after potential.

One may argue that the model of hippocampal mossy fiber which we adopted in this study (Engel and Jonas, 2005) is too simple. For instance, if voltage-dependent conductance with activation voltage near resting potential like Ih or the persistent-type $Na^+$ channels is expressed in mossy fibers, depolarizing after potential might be affected by these voltage-dependent conductance. So far, there is no evidence for the presence of Ih on mossy fibers (Chevaleyre and Castillo, 2002; but see Mellor et al., 2002). Presence of persistent $Na^+$ channels on mossy fibers is also less likely since $Na^+$ current recorded from mossy fiber fully inactivate during prolonged depolarization step (Engel and Jonas, 2005).

Passive depolarization might be shunted by large ionic conductance increase during an action potential and thereby reduced passive depolarization to some extent. It should be mentioned, as demonstrated in **Figures 4A,C**, capacitive current (Icap) often precede $I_{Na}$ during an action potential, while still some fraction overlapped in the time domain. This implies shunting of passive depolarization, if any, is limited to the falling phase of Icap.

## Possible Contribution of Slow Activating Voltage-Dependent $Na^+$ Current in After Potential

Mossy fiber model adopted in this study assumes equilibrium potentials of $K^+$ ions ($E_K$) at −85 mV. In this model, action potentials were followed by hyperpolarizing after potential at resting potential of −80 mV. This is expected if the initial phase of after potentials is governed by the opening of voltage-gated $K^+$ channels and thereby approaching to $E_K$ more negative than resting membrane potential. However, experimentally recorded action potentials from mossy fiber terminals displays robust depolarizing after potential (Geiger and Jonas, 2000; Ohura and Kamiya, 2018b), and the waveforms are quite similar to those obtained in the simulation assuming more positive $E_K$ value than the resting potential of −80 mV. The reason for the difference in polarity between experiment (depolarizing) and the model (hyperpolarizing) needs to be clarified in future studies.

It seems to be reasonable to assume additional involvement of slow activating voltage-dependent $Na^+$ current such as resurgent $Na^+$ current (Ohura and Kamiya, 2018b) in boosting slow depolarization observed in the experiment.

In summary, systematic simulation analysis using a model of mossy fibers revealed that action potential propagates passively via axon cable substantially, and thereby consists of a part of after potential following an action potential. The characteristic waveform of axonal action potential-after potential sequence, as well as apparent voltage-dependency of after potential, are reconstructed with the simple combination voltage-dependent $K^+$ channel component and a passive capacitive component. An initial breakpoint after action potential may be controlled by fast repolarization by the opening of $K^+$ channels, while the later phase is dominantly mediated by the capacitive discharge of the axonal membrane. These notions may shed light on the common underlying mechanism of axonal after potential, although specific mechanisms may involve in fine-tuning of the axonal excitability.

## DATA AVAILABILITY

The raw data supporting the conclusions of this manuscript will be made available by the authors, without undue reservation, to any qualified researcher.

## AUTHOR CONTRIBUTIONS

HK performed the simulation, analyzed the data, and wrote the manuscript.

## FUNDING

This study was supported by Grant-in-Aid for Scientific Research (KAKENHI) from the Japan Society for the Promotion of Science (18K06514 to HK).

## REFERENCES

Acsády, L., Kamondi, A., Sík, A., Freund, T., and Buzsáki, G. (1998). GABAergic cells are the major postsynaptic targets of mossy fibers in the rat hippocampus. *J. Neurosci.* 18, 3386–3403. doi: 10.1523/jneurosci.18-09-03386.1998

Alle, H., and Geiger, J. R. P. (2006). Combined analog and action potential coding in hippocampal mossy fibers. *Science* 311, 1290–1293. doi: 10.1126/science.1119055

Barrett, E. F., and Barrett, J. N. (1982). Intracellular recording from vertebrate myelinated axons: mechanism of the depolarizing afterpotential. *J. Physiol.* 323, 117–144. doi: 10.1113/jphysiol.1982.sp014064

Bean, B. P. (2007). The action potential in mammalian central neurons. *Nat. Rev. Neurosci.* 8, 451–465. doi: 10.1038/nrn2148

Begum, R., Bakiri, Y., Volynski, K. E., and Kullmann, D. M. (2016). Action potential broadening in a presynaptic channelopathy. *Nat. Commun.* 7:12102. doi: 10.1038/ncomms12102

Borst, J. G., Helmchen, F., and Sakmann, B. (1995). Pre- and postsynaptic whole-cell recordings in the medial nucleus of the trapezoid body of the rat. *J. Physiol.* 489, 825–840. doi: 10.1113/jphysiol.1995.sp021095

Chevaleyre, V., and Castillo, P. E. (2002). Assessing the role of Ih channels in synaptic transmission and mossy fiber LTP. *Proc. Natl. Acad. Sci. U.S.A.* 99, 9538–9543. doi: 10.1073/pnas.142213199

D'Ascenzo, M., Podda, M. V., Fellin, T., Azzena, G. B., Haydon, P., and Grassi, C. (2009). Activation of mGluR5 induces spike afterdepolarization and enhanced excitability in medium spiny neurons of the nucleus accumbens by modulating persistent $Na^+$ currents. *J. Physiol.* 587, 3233–3250. doi: 10.1113/jphysiol.2009.172593

David, G., Modney, B., Scappaticci, K. A., Barrett, J. N., and Barrett, E. F. (1995). Electrical and morphological factors influencing the depolarizing after-potential in rat and lizard myelinated axons. *J. Physiol.* 489, 141–157. doi: 10.1113/jphysiol.1995.sp021037

de San Martin, J. Z., Jalil, A., and Trigo, F. F. (2015). Impact of single-site axonal GABAergic synaptic events on cerebellar interneuron activity. *J. Gen. Physiol.* 146, 477–493. doi: 10.1085/jgp.201511506

de San Martin, J. Z., Trigo, F. F., and Kawaguchi, S. Y. (2017). Axonal $GABA_A$ receptors depolarize presynaptic terminals and facilitate transmitter release in cerebellar Purkinje cells. *J. Physiol.* 595, 7477–7493. doi: 10.1113/JP275369

Debanne, D., Campanac, E., Bialowas, A., Carlier, E., and Alcaraz, G. (2011). Axon physiology. *Physiol. Rev.* 91, 555–602. doi: 10.1152/physrev.00048.2009

Dodson, P. D., Billups, B., Rusznák, Z., Szûcs, G., Barker, M. C., and Forsythe, I. D. (2003). Presynaptic rat Kv1.2 channels suppress synaptic terminal hyperexcitability following action potential invasion. *J. Physiol.* 550, 27–33. doi: 10.1113/jphysiol.2003.046250

Engel, D., and Jonas, P. (2005). Presynaptic action potential amplification by voltage-gated $Na^+$ channels in hippocampal mossy fiber boutons. *Neuron* 45, 405–417. doi: 10.1016/j.neuron.2004.12.048

Gardner-Medwin, A. R. (1972). An extreme supernormal period in cerebellar parallel fibres. *J. Physiol.* 222, 357–371. doi: 10.1113/jphysiol.1972.sp009802

Geiger, J. R., and Jonas, P. (2000). Dynamic control of presynaptic $Ca^{2+}$ inflow by fast-inactivating $K^+$ channels in hippocampal mossy fiber boutons. *Neuron* 28, 927–939. doi: 10.1016/s0896-6273(00)00164-1

Gu, N., Vervaeke, K., Hu, H., and Storm, J. F. (2005). Kv7/KCNQ/M and HCN/h, but not $K_{Ca}2$/SK channels, contribute to the somatic medium after-hyperpolarization and excitability control in CA1 hippocampal pyramidal cells. *J. Physiol.* 566, 689–715. doi: 10.1113/jphysiol.2005.086835

Henze, D. A., Urban, N. N., and Barrionuevo, G. (2000). The multifarious hippocampal mossy fiber pathway: a review. *Neuroscience* 98, 407–427. doi: 10.1016/s0306-4522(00)00146-9

Hines, M. L., and Carnevale, N. T. (1997). The NEURON simulation environment. *Neural. Comput.* 9, 1179–1209. doi: 10.1162/neco.1997.9.6.1179

Kamiya, H., Ozawa, S., and Manabe, T. (2002). Kainate receptor-dependent short-term plasticity of presynaptic $Ca^{2+}$ influx at the hippocampal mossy fiber synapses. *J. Neurosci.* 22, 9237–9243. doi: 10.1523/jneurosci.22-21-09237.2002

Kim, J. H., Kushmerick, C., and von Gersdorff, H. (2010). Presynaptic resurgent $Na^+$ currents sculpt the action potential waveform and increase firing reliability at a CNS nerve terminal. *J. Neurosci.* 30, 15479–15490. doi: 10.1523/JNEUROSCI.3982-10.2010

Malenka, R. C., Kocsis, J. D., Ransom, B. R., and Waxman, S. G. (1981). Modulation of parallel fiber excitability by postsynaptically mediated changes in extracellular potassium. *Science* 214, 339–341. doi: 10.1126/science.7280695

Martinello, K., Huang, Z., Lujan, R., Tran, B., Watanabe, M., Cooper, E. C., et al. (2015). Cholinergic afferent stimulation induces axonal function plasticity in adult hippocampal granule cells. *Neuron* 85, 346–363. doi: 10.1016/j.neuron.2014.12.030

Meeks, J. P., and Mennerick, S. (2004). Selective effects of potassium elevations on glutamate signaling and action potential conduction in hippocampus. *J. Neurosci.* 24, 197–206. doi: 10.1523/jneurosci.4845-03.2004

Mellor, J., Nicoll, R. A., and Schmitz, D. (2002). Mediation of hippocampal mossy fiber long-term potentiation by presynaptic Ih channels. *Science* 295, 143–147. doi: 10.1126/science.1064285

Metz, A. E., Jarsky, T., Martina, M., and Spruston, N. (2005). R-type calcium channels contribute to afterdepolarization and bursting in hippocampal CA1 pyramidal neurons. *J. Neurosci.* 25, 5763–5773. doi: 10.1523/jneurosci.0624-05.2005

Ohura, S., and Kamiya, H. (2016). Excitability tuning of axons in the central nervous system. *J. Physiol. Sci.* 66, 189–196. doi: 10.1007/s12576-015-0415-2

Ohura, S., and Kamiya, H. (2018a). Short-term depression of axonal spikes at the mouse hippocampal mossy fibers and sodium channel-dependent modulation. *eNeuro* 5:ENEURO.0415-17.2018. doi: 10.1523/ENEURO.0415-17.2018

Ohura, S., and Kamiya, H. (2018b). Sodium channel-dependent and -independent mechanisms underlying axonal afterdepolarization at mouse hippocampal mossy fibers. *eNeuro* 5:ENEURO.0254-18.2018. doi: 10.1523/ENEURO.0254-18.2018

Raman, I. M., and Bean, B. P. (1997). Resurgent sodium current and action potential formation in dissociated cerebellar Purkinje neurons. *J. Neurosci.* 17, 4517–4526. doi: 10.1523/jneurosci.17-12-04517.1997

Sierksma, M. C., and Borst, J. G. G. (2017). Resistance to action potential depression of a rat axon terminal in vivo. *Proc. Natl. Acad. Sci. U.S.A.* 114, 4249–4254. doi: 10.1073/pnas.1619433114

Storm, J. F. (1987). Action potential repolarization and a fast after-hyperpolarization in rat hippocampal pyramidal cells. *J. Physiol.* 385, 733–759. doi: 10.1113/jphysiol.1987.sp016517

Wissmann, R., Bildl, W., Oliver, D., Beyermann, M., Kalbitzer, H. R., Bentrop, D., et al. (2003). Solution structure and function of the "tandem inactivation domain" of the neuronal A-type potassium channel Kv1.4. *J. Biol. Chem.* 278, 16142–16150. doi: 10.1074/jbc.m210191200

Yue, C., Remy, S., Su, H., Beck, H., and Yaari, Y. (2005). Proximal persistent $Na^+$ channels drive spike afterdepolarizations and associated bursting in adult CA1 pyramidal cells. *J. Neurosci.* 25, 9704–9720. doi: 10.1523/jneurosci.1621-05.2005

Yue, C., and Yaari, Y. (2004). KCNQ/M channels control spike afterdepolarization and burst generation in hippocampal neurons. *J. Neurosci.* 24, 4614–4624. doi: 10.1523/jneurosci.0765-04.2004

Zucker, R. S. (1974). Excitability changes in crayfish motor neurone terminals. *J. Physiol.* 241, 111–126. doi: 10.1113/jphysiol.1974.sp010643

**Conflict of Interest Statement:** The author declares that the research was conducted in the absence of any commercial or financial relationships that could be construed as a potential conflict of interest.

*Copyright © 2019 Kamiya. This is an open-access article distributed under the terms of the Creative Commons Attribution License (CC BY). The use, distribution or reproduction in other forums is permitted, provided the original author(s) and the copyright owner(s) are credited and that the original publication in this journal is cited, in accordance with accepted academic practice. No use, distribution or reproduction is permitted which does not comply with these terms.*

frontiers in Cellular Neuroscience

HYPOTHESIS AND THEORY
published: 16 May 2019
doi: 10.3389/fncel.2019.00203

# The Slow Depolarization Following Individual Spikes in Thin, Unmyelinated Axons in Mammalian Cortex

*Morten Raastad**

*Department of Physiology, School of Medicine, Emory University, Atlanta, GA, United States*

An important goal in neuroscience is to understand how neuronal excitability is controlled. Therefore, Gardner-Medwin's 1972 discovery, that cerebellar parallel fibers were more excitable up to 100 ms after individual action potentials, could have had great impact. If this long-lasting effect were due to intrinsic membrane mechanisms causing a depolarizing after-potential (DAP) this was an important finding. However, that hypothesis met resistance because the use of $K^+$ sensitive electrodes showed that synchronous activation, as commonly used in excitability tests, increased extracellular $K^+$ concentration sufficiently to explain much of the hyperexcitability. It is still controversial because intra-axonal recordings, which could have settled the debate, have not been made from parallel fibers or other axons of similar calibers. If it had not been for the fact that such thin axons are, by far, the most common axon type in cortical areas and control almost all glutamate release, it would be tempting to ignore them until an appropriate intra-axonal recording technique is invented. I will go through the literature that, taken together, supports the hypothesis that a DAP is an intrinsic membrane mechanism in cerebellar parallel fibers and hippocampal Schaffer collaterals. It is most likely due to a well-controlled process that stops the fast repolarization at a membrane potential positive to resting membrane potential, leaving the membrane more excitable for ~100 ms during a slow, passive discharge of the membrane capacitance. The DAP helps reduce failures but can also cause uncontrolled bursting if it is not properly controlled. The voltage at which the fast repolarization stops, and the DAP starts, is close the activation range of both $Na^+$ and $Ca^{2+}$ voltage activated channels and is therefore essential for neuronal function.

**Keywords: action potential, axon, unmyelinated axons, after-potentials, depolarizing after-potential, conduction failures, presynaptic**

OPEN ACCESS

***Edited by:***
*Shin-ya Kawaguchi,*
*Kyoto University, Japan*

***Reviewed by:***
*Haruyuki Kamiya,*
*Hokkaido University, Japan*
*Lia Forti,*
*University of Insubria, Italy*
*Kenneth Paradiso,*
*Rutgers University, The State University of New Jersey, United States*

***Correspondence:**
*Morten Raastad*
*morten.raastad@emory.edu*

***Specialty section:***
*This article was submitted to Cellular Neurophysiology, a section of the journal Frontiers in Cellular Neuroscience*

***Received:*** *08 January 2019*
***Accepted:*** *23 April 2019*
***Published:*** *16 May 2019*

***Citation:***
*Raastad M (2019) The Slow Depolarization Following Individual Spikes in Thin, Unmyelinated Axons in Mammalian Cortex. Front. Cell. Neurosci. 13:203. doi: 10.3389/fncel.2019.00203*

## INTRODUCTION

The after-potentials of the action potentials ("spikes"), either hyper- or de-polarizing relative to resting membrane potential, are excitability-controlling mechanisms. Such after-potentials have been extensively studied in regions near the soma where some of their functions are obvious: they reduce or increase the amount of current needed to reach threshold for spike initiation at the axon initial segment (AIS). In the axon, after the spike is triggered at the AIS, the functions of

after-potentials are less obvious. That may be one of the reasons considerably less is known about after-potentials in axons, particularly in the very thin, typical cortical axons (TCAs).

Also, when spikes in TCAs have been studied the focus has been mostly on the fast rather than the slow part of the spike. This is because the shape of the fast spike has a well-established impact on transmitter release (Augustine, 1990; Sabatini and Regehr, 1997; Borst and Sakmann, 1999). In contrast, the study of effects of after-potentials on transmitter release is relatively new (Clarke et al., 2016; Sierksma and Borst, 2017), and their influences on conduction properties like speed, endurance, bursting, and failures, which are the main topics of this article, have received even less attention.

However, the most important reason for the lack of knowledge is that TCAs may be the worst preparations for investigating spike mechanisms because the tiny diameters of these axons (on average 0.17 μm, Westrum and Blackstad, 1962; Palay and Chan-Palay, 1974; Shepherd and Harris, 1998) have prevented the use of direct intracellular voltage recordings from intact axons. The revolution in genetic and molecular techniques has not solved this problem.

Unfortunately, we cannot get around the TCAs because they are by far the most common axon type in mammalian cortices (including hippocampal, cerebellar, and neo-cortex). Most of the brain's release of the excitatory transmitter glutamate is controlled by presynaptic "boutons" found along most of the paths of TCAs. They comprise the largest fractions of cortical volume (∼50%) and cellular membranes (∼60%) (Mishchenko et al., 2010) and are usually by far the largest part of neurons' volume and membrane surface (Braitenberg and Schüz, 1998; Wu et al., 2014).

The first data suggesting an after-potential in TCAs came from Gardner-Medwin in 1972 when he showed that cerebellar parallel fibers were more excitable up to 100 ms after individual action potentials. Although a depolarization after the spike was considered likely, the mechanism for this depolarization was suggested to be extracellular $K^+$ accumulation due to the synchronized activation of many parallel axons. Many years later, Wigström and Gustafsson (1981) used almost identical tests of TCAs in hippocampal slices and found the same excitability changes but concluded that the post-spike hyperexcitability was due to an intrinsic mechanism of the axons. One of the main aims of this article is to detangle the excitability-increasing effects of changes in extracellular $K^+$, and on the other hand the axon-intrinsic mechanism that creates a depolarizing after-potential (DAP) in TCAs.

Despite the limited opportunity to record intra-axonal potentials, it has over many years from a variety of technical approaches accumulated important data on the TCA spike, its propagation, and the DAP. Because of the slow accumulation of data some reports may have gone unnoticed, and this review will therefore summarize and synthesize knowledge about the TCA spike and their DAP. Almost all data are from cerebellar parallel fibers and hippocampal Schaffer collaterals, but I will refer to them as "TCAs," for convenience, but also as a reminder that they a similar to most axons in cortical regions with respect to calibers, boutons, and transmitter type. Also those pyramidal neurons that have myelin around their proximal axon usually end up as thin terminal axons that fit the description of a TCA, although their spike or after-potentials have not been investigated. We must therefore keep in mind that axons other than Schaffer collaterals and parallel fibers may be different.

I will focus on the DAP in the context of excitability control and spike propagation in TCAs, and mostly ignore the TCAs' transmitter releasing function which is covered elsewhere (for example (Debanne et al., 2011; Fioravante and Regehr, 2011)).

The sum of the available information strongly suggests that that hippocampal and cerebellar thin axons, examples of TCAs, have two distinct phases of repolarization; one fast that stops relatively abruptly at a well-controlled membrane potential more positive than the resting membrane potential, and thereafter the DAP which is a slow, passive decay back to resting membrane potential.

## TCA POST-SPIKE HYPEREXCITABILITY—AN AXONAL MEMBRANE MECHANISM OR THE RESULT OF UNSPECIFIC INCREASE IN EXTRACELLULAR $K^+$ CONCENTRATION?

### Hyperexcitability

The hyperexcitability that follows individual spikes in TCAs, which was the first hint of a DAP in such axons, can be reliably demonstrated through its effects on population spike amplitude and propagation speed (explained in **Figure 1**). These effects of a single conditioning stimulus were first shown by Gardner-Medwin (1972) in the cerebellar parallel fibers of the anesthetized cat, and by Wigström and Gustafsson (1981) in the Schaffer collaterals in hippocampal slices. Gardner-Medwin (1972) concluded that "The apparent increase of the conduction velocity of the parallel fibres is so marked that it distinguishes them from all the other fibres in the mammalian nervous system in which the after-effects of stimulation have been studied."

Both these studies found the maximal hyperexcitable effect around 20–30 ms after an electrical activation of the spikes, and they quantified the increase in excitability to 20–40% by studying how much they could reduce the strength of a second stimulus without losing any amplitude of the population spike amplitude. The similarity of these results, despite the large difference in the preparations, suggests that the hyperexcitability is a robust phenomenon.

### Hyperexcitability in Peripheral Axons

Excitability of *peripheral* axons in mammals and many other species has been extensively studied by recording changes in conduction speed. Particularly the thin, unmyelinated C-fibers have pronounced activity-dependent changes in conduction speed and may therefore help us understand mechanisms in TCAs. Many of these investigations use trains of stimuli at high frequency which activate many mechanisms, for example hyperpolarization due to the Na-K-pump (Ritchie and Straub, 1957) and depolarization due to increasing extracellular $K^+$ (Frankenhaeuser and Hodgkin, 1956). These factors can lead

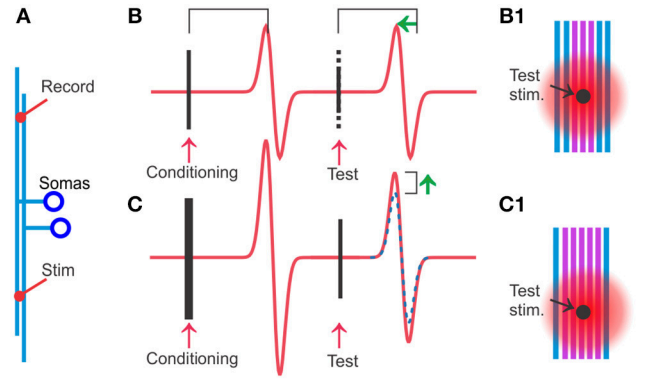


**FIGURE 1 |** Hyperexcitability specific to the activated axons can be detected and quantified by using conditioning and test stimuli on populations of TCAs. **(A)** Stimulation and recording electrodes are positioned typically 2–3 mm apart among the cerebellar parallel fibers or other TCAs. **(B)** A test stimulus is given 20 ms after the conditioning stimulus. When conditioning and test stimuli have equal strength, the test stimulus will activate the same axons as the conditioning stimulus and therefore the two spike population responses have similar amplitudes. However, the response to the test stimulus occurs at a shorter latency (green arrow) because the conditioned axons (violet in **B1**) are more excitable and the spike travels faster. This hyperexcitability can be quantified by reducing the stimulus strength of the test stimulus (dotted part of the stimulus artifact). At moderate reductions, typically 15–40%, the test response keeps its original amplitude. The interpretation is that the recently conditioned axons (violet in **B1**) have lower activation threshold, and even the reduced test stimulus is sufficient to activate all the violet, conditioned axons. **(C)** When the conditioning stimulus is stronger than the test (more violet, activated axons in **C1** than in **B1**), but the test strength is the same as in **(B)**, the test response will get a larger amplitude than in **(B)** (compare with dotted blue which is response to conditioning and test stimulus of equal strength). The interpretation is that the stronger conditioning stimulus leaves more axons with reduced threshold in **(C)** than in **(B)** (violet in **B1**) allowing the test stimulus in **(C)** to activate more axons than in **(B)**.

to periods of speeding, slowing and failures. Because of the difficulty in interpreting such mixtures of mechanisms, I will focus on the excitability changes that occur after single spikes ("post-spike hyperexcitability").

Many peripheral axon types show post-spike hyperexcitability, with duration similar to or sometimes longer than that observed in Schaffer collaterals and parallel fibers. Human sympathetic C-fibers have a hyperexcitable period of ∼1,000 ms (Bostock et al., 2003). Because of the long conduction distances that can be investigated in humans, the speeding-up due to this hyperexcitability can be considerable. For example, in human C-fibers of mechano- and heat-insensitive type, two spikes triggered 50 ms apart caught up >65% of that interval over ∼500 mm conduction distance (Weidner et al., 2003). Most increases after single spikes in humans are, however, small (often <5%), possibly due to masking of some of the effect by parts of the axon with different activity-dependent properties (discussed in Bostock et al., 2003). Myelinated axons have a DAP with an underlying mechanism that relies on a high-resistance pathway between the cell membrane and the myelin sheet (Barrett and Barrett, 1982) and is therefore not directly similar to the DAP in TCAs.

To summarize, increases in population propagation speed and amplitude are robustly demonstrated in whole animals (Gardner-Medwin, 1972), cerebellar and hippocampal slices (Wigström and Gustafsson, 1981), at temperatures between 22 and 35°C (Soleng et al., 2004; Pekala et al., 2016), and in peripheral cold-sensitive C-fibers and sympathetic axon in humans (Bostock et al., 2003).

## Does Extracellular Potassium Contribute to, or Even Fully Explain the Hyperexcitability?

Although there has not been doubt about the existence of the hyperexcitability in TCAs, there has been considerable uncertainty about its cause. The most likely causes are that the spike is followed by a depolarization due to (a) increased extracellular potassium concentration ($[K^+]_o$), or (b) an intrinsic membrane mechanism. This distinction is important because electrical activation synchronizing many axons may give $[K^+]_o$ increases ($\Delta[K^+]_o$) never occurring during normal brain activity, while an intrinsic membrane mechanism is likely to be important for normal axonal function.

Around the time Gardner-Medwin published his excitability-increasing effects there was an emerging awareness of the excitability-modifying effects of neurons' $K^+$ efflux and accumulation in extracellular space (Frankenhaeuser and Hodgkin, 1956). Even individual bursting Purkinje cells could produce $\Delta[K^+]_o$ of ∼1 mM in their vicinity (in turtle, Hounsgaard and Nicholson, 1983). Much of the magnitude and time-course of the excitability increase seen with *repetitive* extracellular electrical stimulation could be explained by $[K^+]_o$ recorded by $K^+$-sensitive electrodes (Malenka et al., 1981, 1983; Kocsis et al., 1983), but the critical question of whether *single* spikes could raise $[K^+]_o$ enough to explain the large (15–20%) increase in conduction speed was not addressed.

If we as a starting point assume that the excitability-increasing effect of a fast rise in $\Delta[K^+]_o$ in response to electrical activation of axons is similar to the effect of a slower increase in $\Delta[K^+]_o$ achieved by increasing the bath concentration of $K^+$, the post-spike hyperexcitability cannot be explained by $\Delta[K^+]_o$. Estimated $\Delta[K^+]_o$ per stimulus in bundles of simultaneously activated unmyelinated axons in the brain is 0.2–0.5 mM (Fritz and Gardner-Medwin, 1976; Kocsis et al., 1983; Aitken and Somjen, 1986). In contrast, raising bath $[K^+]_o$ from 2.5 to 4 mM increased conduction speed by only 4.6% (Kocsis et al., 1983; Soleng et al., 2004). So, a $[K^+]_o$ 3–6 times higher than the single-stimulus concentration gives only 1/3 to ¼ of the speed increase caused by individual spikes.

However, fast stimulus induced $\Delta[K^+]_o$ may have larger effects on excitability that the slower bath-applied $\Delta[K^+]_o$ because with slow increase membrane stabilizing mechanisms like the H-current and the Na-K-pump will have time to counteract the depolarizing effect of $\Delta[K^+]_o$. This idea may be possible to test because postsynaptic structures contribute significantly to the stimulus-induced $\Delta[K^+]_o$. Around 50% reduction of $\Delta[K^+]_o$ was reported when synaptic signals were blocked by low $Ca^{2+}$ and high $Mg^{2+}$, or $Mn^{2+}$ in hippocampal slices, cerebellum *in vivo*, and dorsal horn of rat spinal cord slices (Nicholson et al., 1978; Urbán et al., 1985; Aitken and Somjen,

1986). One publication reported that post-spike hyperexcitability (speed) was not changed after block of synaptic signals with adenosine (Kocsis et al., 1984). If also adenosine-block of synaptic signals reduces $\Delta[K^+]_o$, that finding would suggest that $\Delta[K^+]_o$ is not responsible for all of the post-spike hyperexcitability.

A third argument against $K^+$ as a major factor is obtained by reducing $\Delta[K^+]_o$ around the tested axon by spatially separating the conditioning and testing stimulus. This was done by using different branches of the same neuron for conditioning and test stimulus (Soleng et al., 2004). The threshold reduction obtained by this approach were similar to that of cerebellar axons in whole animals (14% reduction at 34°C and 30 ms interval).

### Single Axon

The critical experiment to test if the hyperexcitability is specific to the activated axon is of course to measure the excitability when only one axon is activated. This was done on cerebellar parallel fibers with a somatic tight-seal electrode triggering a somatic spike and a separate electrode testing the threshold for spike activation of the axon (Palani et al., 2012). In this configuration the threshold reduction and its time course (maximal threshold reduction 25% at 20 ms after a spike) was similar to the post-spike hyperexcitability described for parallel fibers in whole animals (Gardner-Medwin, 1972), supporting the idea that the post-spike hyperexcitability is an intrinsic property of the parallel fibers.

### How Much Does the Combined $K^+$ Efflux From Many Adjacent Axons Influence the Excitability?

Although synchronous electrical activation of axons is unphysiological, its effect is relevant in experiments and clinical CNS stimulations using electrodes. One way to better understand the impact of such stimulation is to activate a bundle of axons and record the antidromic spike at the soma of only one of them. Then it is possible to find the axonal activation threshold of the recorded unit, obtaining both successful activations and failures with the same stimulation strength, while maintaining a relatively constant number of activated axons (Pekala et al., 2016). In such experiments, a failure at the first stimulus *increased* the failure rate at the second stimulus (changed from 50% to 75% failures at 30 ms interval), suggesting a slightly reduced excitability after a single stimulus. In contrast, a success on the first stimulus almost *eliminated* failures at the second stimulus (<0.1% failures, Pekala et al., 2016). This means that the excitability-increasing effect of a spike in the tested unit's axon was much stronger than the influence from adjacent synchronously activated axons. Similar results were reported from hippocampal CA3 cell's axons (Soleng et al., 2004).

## SHAPE OF THE DAP

The initial part of the DAP is important because, as I will explain below, evidence from grease-gap recordings and backpropagating spikes suggest that the DAP initial amplitude is close to the activation range for $Na^+$ and $Ca^{2+}$ channels. I will go through the background for those claims in the section called "How does the DAP influence axonal functions." The start of the DAP is difficult to investigate by studying excitability (speed or threshold) because the refractory period of a spike stretches into the hyperexcitable period. A further complication is that the refractory period varies between axons (Raastad and Shepherd, 2003).

Recording the membrane potential would give information during the early period but direct intracellular voltage recordings of the traveling spike in TCAs have not been possible yet. Various methods have been used to overcome the difficulty in recording intracellularly from TCA, particularly the distal parts of the axonal arbor. These include intracellular recordings from soma with backpropagating spikes, "grease gap" methods, recordings from the bleb that forms when the axon is cut, and voltage sensitive dye (VSD) recordings. Most of these recordings have focused on the amplitude and width of the fast part of the spike, well-motivated by the importance of those parameters for control of transmitter release. Few have investigated spike after-potentials and their influence on conduction properties like speed, endurance, bursting, and failures.

To illustrate the findings, interpretations and qualifications, I will use a simple cable model implemented with the simulator NEURON (Hines and Carnevale, 1997). This is meant as a minimalistic model that approximately reproduce spike propagation properties discussed in this article. Details of the model are explained in **Figure 2** and in section Methods.

### Backpropagating Spikes

One opportunity to get information about the TCA spike, at least in neurons that have TCAs attached directly to soma without interposed myelination, like the cerebellar granule cells and rodent hippocampal Schaffer collaterals, is to use tight-seal somatic voltage recordings with backpropagating, electrically triggered spikes. This is illustrated with the model neuron in **Figure 3A**. Contributions from near-soma regions can be reduced or avoided by hyperpolarizing the soma by current injection to prevent the fast part of the spike from invading the soma. If there is a DAP following the axonal spike it may still be recorded at the soma, as shown in **Figure 3A**, red curve.

That approach (Palani et al., 2012; Pekala et al., 2014) was used to show a DAP starting on average 12 mV positive to a −63 mV resting potential and a decay to 1/e in 52 ms (Palani et al., 2012). Those publications also utilized threshold activation of the axon, with ∼50% activation failures of the recorded neuron. The DAP never occurred without a spike (at somatic voltages that allowed the spikes to invade the soma), showing that the DAP is an integral part of the spike. Furthermore, at the stochastic stimulation failures there was no detectable depolarization even though many axons were activated by the constant stimulus. This means that the depolarizing effect from other axons or cells, for example by their $K^+$ efflux, was not contributing much to the DAP recorded at the soma.

### Grease-Gap

"Electrical gap" methods (Stampfli, 1954), like air-, sucrose-, or grease-gap have been useful for recording membrane potential changes of axons that are hard to record from

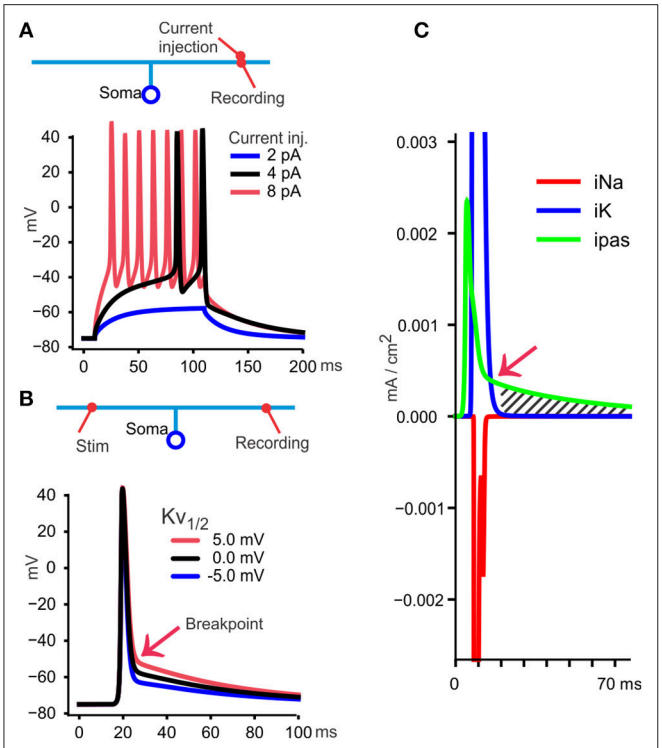


**FIGURE 2 |** A model to illustrate essential features of the DAP and post-spike hyperexcitability. **(A)** A simple model is used to illustrate findings and interpretations from various publications. A soma with 10 μm diameter connects to a 150 μm ascending axon with 0.3 μm diameter, and divides in two branches, each 1 mm long (~3 space constants each) and 0.2 μm diameter. Those dimensions resemble a granule cell in cerebellum and have axonal diameters compatible also with Schaffer collaterals (Palay and Chan-Palay, 1974; Shepherd and Harris, 1998). The neuron is given uniformly distributed conductances and other membrane properties (see section Methods). At 30°C, commonly used in slice experiments, small currents (100 ms square pulses) give firing, measured at the site of current injection in the axon, but a DAP cannot be identified because the spikes occur from a depolarized potential relative to resting membrane potential. **(B)** When measuring the traveling spike, a DAP becomes apparent because the spike starts at a membrane potential more negative than the voltage at which the fast repolarization stops ("breakpoint," red arrow). In this model, the breakpoint depends on the midpoint voltage for Kv's steady state activation curve (see section Methods), shown here with three values. For the rest of the simulations I used 0 mV (black curve) as midpoint. **(C)** With recording from the distal axon, as in **(B)**, the currents through $Na^+$, $K^+$, and passive channels (iNa, IK, ipas) are shown during the black spike in **(B)**. At one time point (red arrow) the passive current (green) becomes larger than iK and from there the DAP starts (hatched area) and follows the membrane time constant if, as here, the voltage sensitive iK is negligible.

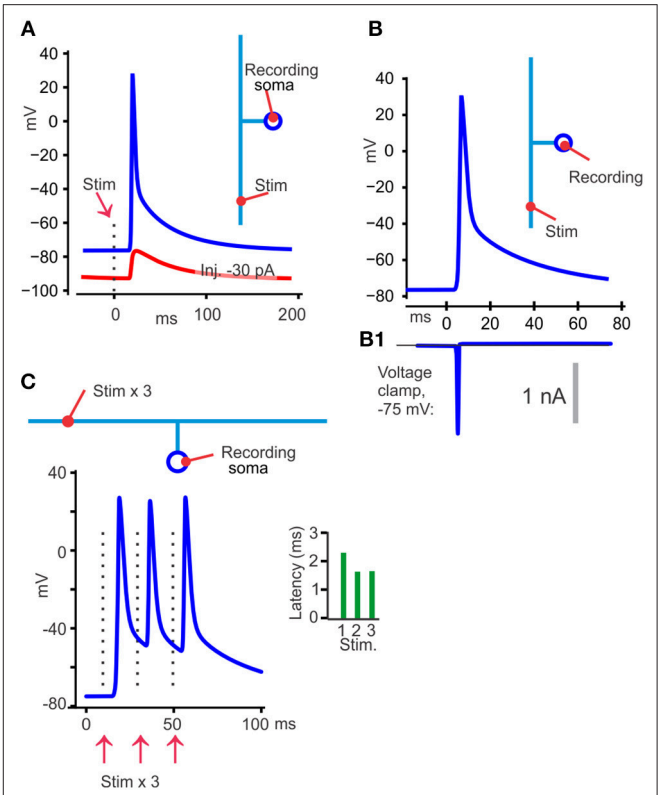


**FIGURE 3 |** Illustration of different findings from publications showing that TCA spikes have a DAP. **(A)** With the model at its uniform resting membrane potential of −75 mV, 30°C, an axonal electrical activation resulted in a back-propagating somatic spike (blue). When the soma was hyperpolarized to −90 mV (red) with current injection, the spike failed to invade the soma, but a DAP could still be detected. **(B)** Switching from voltage recording **(B)** to voltage clamp **(B1)** at the somatic recording site eliminated the DAP, which is compatible with a passive decay and similar to the results in Palani et al. (2012). **(C)** With three stimuli 20 ms apart the latency was shorter for the second than for the first spike, but similar for the second and third (green bars). One likely explanation is that the second and third spike traveled in an axon that was depolarized to the same voltage, by the DAP, in contrast to the first spike that had to overcome a more hyperpolarized axon.

with intracellular electrodes (Stys et al., 1991). With the grease-gap method the fast decay and the much slower DAP (in parallel fibers and hippocampal Schaffer collaterals) can be distinguished (Palani et al., 2012). The time course of the DAP recorded with the grease-gap method is similar to the decay of the hyperexcitability and to the antidromic somatically recorded potential. This supports the hypothesis that the hyperexcitability is caused by a slowly decaying axonal potential. With both grease-gap and somatically recorded back-propagating spikes, the DAP starts immediately when the fast repolarization stops (see **Figures 2B**, **3A**, blue), without any interposed hyperpolarization.

## Bleb Recordings

Although recordings from axonal blebs that form when axons are cut (Shu et al., 2007) have given very precise knowledge about spike initiation and membrane currents in the proximal 300–400 μm of axons, it has also become clear that this part of the axon is a specialized region different from more distal parts of the axons (Hu and Bean, 2018). Additionally, such recordings have been made mostly from layer 5 neocortical pyramidal cells which are myelinated (Shu et al., 2007) and relies less than the TCAs on voltage sensitive channels for fast spike repolarization (Chiu et al., 1979; Kaars and Faber, 1981). These differences in axonal mechanisms may explain that no DAP has been identified in bleb recordings.

## Voltage-Sensitive Dyes

Voltage sensitive dyes have the potential to report voltages from axons which are difficult to access with electrical recording electrodes. VSD recordings from relatively proximal parts of the TCAs, up to 200–400 μm from the soma, have not shown DAPs (Zhou et al., 2007; Foust et al., 2011; review by Popovic et al., 2015). In contrast, recordings that include distal parts of TCAs have shown apparently large DAPs (Sabatini and Regehr, 1997; Matsukawa et al., 2003). Hyperpolarizing after-potentials have not been reported with VSD recordings from TCAs, but there is one example of a small, fast repolarization that goes below the pre-spike level from cultured hippocampal neurons, using a light-activated proton pump as fluorophore (Hoppa et al., 2014).

One problem in interpreting these results is that proximal and distal VSD recordings have used different dyes and labeling methods. There is no example yet of recordings from both proximal and distal regions of TCAs that could have clarified if it is the axonal region, the recording method, or the neuron type that causes these different results. I will go through the few publications that have used VSDs to record from TCAs, and at the end suggest some factors that theoretically may influence the opportunity to record a DAP if one were present.

With bath-applied voltage sensitive fluorescent dyes (VSFD) and transmitted light voltage sensitive probes a large DAP, starting at ∼30% of the amplitude of the fast spike, was recorded in rat cerebellar parallel fibers (Sabatini and Regehr, 1997; Matsukawa et al., 2003). Synaptic transmission was eliminated but $[K^+]_o$, either directly influencing membrane potential of the axons or depolarizing glia cells, were discussed as possible mechanisms. This seems unlikely because there was no addition of the DAP amplitudes at 10 ms spike intervals (Sabatini and Regehr, 1997) even though $K^+$-sensitive electrode recordings show that $[K^+]_o$ ads at such intervals (Fritz and Gardner-Medwin, 1976; Malenka et al., 1981, 1983; Kocsis et al., 1983). Also, with axonally targeted genetically encoded hybrid voltage sensors there seems to be a small long-lasting DAP in mossy fibers and mossy cell axons, both unmyelinated, although this was not specifically commented or analyzed (Ma et al., 2017).

Although I focus on mammalian TCAs in this review, VSFD recordings from crayfish neuromuscular junction (Lin, 2008) are interesting because they show several features that resemble the VSFD recordings from Sabatini and Regehr (1997) and the grease-gap recordings from cerebellar parallel fibers (Palani et al., 2012). Common for these experiments is that they include the distal parts of thin, unmyelinated axons with *en passant* synapses, they have a hyperexcitable period after individual spikes (20–30% reduced activation threshold 15–25 ms after the spike, for the crayfish synapse see Zucker, 1974), and they have a slowly decaying DAP following *directly* after the fast part of the repolarization that is the likely cause of the hyperexcitability.

Because the crayfish neuromuscular synapse gives the opportunity to record presynaptically with intracellular micro-electrodes it has been extensively used to study how presynaptic mechanisms influence transmitter release. In such intra-axonal recordings, the DAP occurs only when the axon and its terminals are relatively *hyperpolarized* (Dudel, 1971). Because the occurrence of a DAP often required injection of hyperpolarizing current it has been unclear whether the DAP was a natural part of the spike in the crayfish preparation. However, since intact terminals have a large reduction of activation threshold after a spike (Zucker, 1974), and since the VSFD recordings (Lin, 2008) show a DAP, it is likely that the intact terminals do have DAPs.

These observations showing that the DAP required relatively hyperpolarized membrane potentials, and my model showing that the DAP disappears at depolarized levels (black curve in **Figure 2A**), give the idea that one reason some VSD recordings from TCAs do not show a DAP (in addition to the obvious reason that neocortical pyramidal neurons may not have an axonal DAP) is that the recording site was depolarized. Factors that may contribute to depolarization is that spikes were elicited by depolarizing currents at the soma (which often influences the axon at the recording site as pointed out in Foust et al., 2011), and phototoxicity. Because TCAs have a much higher surface-to-volume ratio than the soma, toxins produced by membrane-associated fluorophores will have a small cytoplasmic volume for dilution and may cause more phototoxicity in the TCA than at the soma.

# MECHANISMS CAUSING THE DAP IN TCAS

DAP mechanisms have been investigated at the soma, dendrites, large presynaptic terminals, and axons. Inward currents ($Na^+$ and $Ca^{2+}$) and passive components have been identified. For example, in hippocampal CA1 pyramidal neurons voltage sensitive R-type $Ca^{2+}$ channels are important (Metz et al., 2005); in cerebellar granule cells a resurgent $Na^+$ current contribute (Magistretti et al., 2006). In presynaptic structures large enough for intracellular recordings a DAP has been found in calyx of Held (Borst et al., 1995), and in mossy fiber boutons (Geiger and Jonas, 2000). In these terminals the DAP has both passive and active components (Kim et al., 2010; Lewis and Raman, 2014; Ohura and Kamiya, 2018). Myelinated axons usually have a passive DAP (Barrett and Barrett, 1982). The high resistance between the myelin sheet and the axonal membrane gives the DAP its slow decay and this mechanism is therefore unlikely to contribute in unmyelinated TCAs.

As I will explain in the following sections there is no evidence that inward currents contribute to the DAP in cerebellar parallel fibers or Schaffer collaterals. That does not mean that inward currents may not influence the DAP under conditions not yet tested, for example during longer spike trains. In the lack of data showing effects that need inward currents to be explained, I will exclude further discussions about the contribution of inward currents in other cells, presynaptic structures, or soma.

I will distinguish between mechanisms that determine the decay rate and those that determine the amplitude in TCAs. For all experiments referred in the three following sections, fast synaptic currents are blocked by CNQX, APV, and Picrotoxin.

Under such block the shape of the DAP did not change with the addition of 200 μM $Cd^{2+}$, showing that neither release nor voltage sensitive $Ca^{2+}$ currents contributed (Toda, 1976).

## DAP Decay in TCAs

Three observations suggest that the decay of the DAP is passive, meaning determined by the membrane capacitance and resistance. First, when the antidromic spike with its DAP is recorded at the granule cell's soma, and the recording is switched to voltage clamp, there is no detectable current that can explain the DAP, although a significant fast unclamped spike current persisted (Palani et al., 2012). This is expected from a capacitive current and can be illustrated with the model (somatic voltage clamp simulation in **Figures 3B,B1**).

Second, the decay rate of the post-spike hyperexcitability is not more than 20–30% different at 24 and 34°C (Soleng et al., 2004). This is compatible with the temperature effect on the membrane time constants of several cell types (Kim and Connors, 2012) but does not rule out other mechanisms with low temperature sensitivity.

Third, spike activity that probably induce changes in membrane resistance change the decay rate of the hyperexcitability (Soleng et al., 2004). The background for that experiment is that the Na-K-pump is electrogenic and hyperpolarizes the membrane as it pumps out excess $Na^{+}$ (Ritchie and Straub, 1957). In many axons this hyperpolarization is reduced by opening of HCN-channels, underlying the H-current (Eng et al., 1990). This added conductance (reduced membrane resistance) will reduce the membrane time constant. So, when the post-spike hyperexcitability decays ∼3 times faster at 2 Hz spike frequency compared to 0.1 Hz and becomes ∼2 times slower at those frequencies when HCN channels are blocked, a likely explanation is that an HCN conductance reduces the membrane resistance and the membrane time constant and therefore gives a faster DAP decay (Soleng et al., 2004).

## Amplitude of the TCA's DAP

The mechanisms governing the DAP amplitude has been explored by studying how it is influenced by activity, changes in membrane potential, and drugs (next section).

Several lines of evidence suggest that the voltage at which the fast repolarization stops, and the DAP starts (the "breakpoint" in **Figure 2B**) is relatively constant and insensitive to pre-spike potential, and spike activity. Voltage sensitive channels that inactivate fast at relatively depolarized levels, like the channel mechanism I implemented in the model, could explain these properties of the breakpoint (**Figure 3C**). The evidence for the breakpoint's insensitivity to pre-spike potential and spike activity comes from experiments similar to those referred under "Shape of the DAP" above but includes trains of axonal spikes. The constant, depolarized voltage for the breakpoint during such trains (illustrated in **Figure 3C**) has been observed by using VSFD, transmitted-light voltage sensitive probes, grease-gap recordings and somatic recordings with backpropagating spikes in cerebellar parallel fibers (Sabatini and Regehr, 1997; Matsukawa et al., 2003; Pekala et al., 2016). Those publications show that the second spike in such trains take off from the "back" of the DAP, a potential more depolarized than the resting membrane potential, but this difference in pre-spike voltage does not influence the breakpoint. The DAP also gives the spikes after the first one faster conduction speed, as seen in the green histogram in **Figure 3C**.

Those recordings from cerebellar parallel fibers are, with respect to constant breakpoint, very similar to recordings from the crayfish neuromuscular junction (Lin, 2008). A repolarization voltage relatively insensitive to pre-spike potential was also shown *in vivo* in the calyx of Held (Sierksma and Borst, 2017). Like spikes have a narrow voltage range for being triggered at the AIS, there may be a similarly narrow range for the end of their fast repolarization at the presynaptic structures in several neuron types and several species.

## Channels

The channels responsible for the fast repolarization which, according to data discussed above, also determine the DAP amplitude (measured from baseline to the breakpoint) have been explored by bath-applied drugs during grease-gap recordings (Pekala et al., 2014). The spike in cerebellar parallel fibers was not sensitive to 200 μM $Cd^{2+}$, ruling out $Ca^{+}$ currents and $Ca^{+}$-activated currents. Relative to baseline, the breakpoint moved 10% in depolarizing direction in response to 1 mM TEA, and 27% in response to 10 nM margatoxin (MgTX), when these drugs were applied alone. However, in combination these drugs took away most of the fast repolarization by moving the breakpoint 75% in depolarizing direction. The interpretation is that both MgTX-sensitive and TEA-sensitive channels contributed to the fast repolarization that stopped at the breakpoint and did a better job together than alone.

To interpret such grease-gap experiments it is important to be aware that by measuring the difference between baseline and the breakpoint we cannot, without further control experiments, know if it is the baseline (corresponding to resting membrane potential) or the breakpoint voltage that changes. Two additional observations help: First, conduction speed is sensitive to resting membrane potential, and no change was detected with either $Cd^{2+}$, TEA, or MgTX (Pekala et al., 2014). Second, MgTX enhanced the post-spike *hyperexcitability* (Palani et al., 2010), supporting the interpretation that TEA and MgTX pushed the breakpoint and the decay of the DAP in depolarizing direction.

Low concentrations of TEA (≤1 mM) have preferential effect on Kv3-family of channels (Rudy and McBain, 2001) and because Kv3.1 and Kv3.3 double knockout mice (Matsukawa et al., 2003) lack most TEA effects on cerebellar parallel fibers, these channels are likely to mediate the TEA effects at least in those axons. MgTX blocks Kv1.3 channels with high affinity, although others in the Kv1 family may also be blocked.

# HOW DOES THE DAP INFLUENCE AXONAL FUNCTIONS?

The data referred above suggest that the DAP is a robust process, starting at a voltage controlled by more than one channel family, relatively insensitive to activity and temperature, with a decay

determined mainly by the membrane time constant. How does a spike with those properties influence axonal function?

## The DAP Increases Reliability

The common view that TCAs never fail under physiological conditions may be biased by few rodent experiments using temperatures above 35–36°C, while rodents, including their brains, often raise above 38°C during moderate activity (Kiyatkin et al., 2002). Temperature dependent failures can be demonstrated by measuring populations of spikes at two sites along parallel fibers in cerebellum. When temperature increases just above 37°C the fraction of spikes arriving at the distal electrode falls (Pekala et al., 2016). VSDF recordings have also shown reduced spread of signals in hippocampal slices at temperatures >37°C (Takeya et al., 2002). Failures are provoked by higher temperature because Nav inactivation and Kv activation become faster (Hodgkin and Katz, 1949), both factors that reduce the spike amplitude and integral. Particularly fast activating Kv3 channels, present in Schaffer collaterals and cerebellar parallel fibers, would theoretically increase failure probability at high temperatures.

When spike propagation failures are provoked by temperature (illustrated with the model in **Figure 4A**), propagation reliability increases with the number of stimuli (**Figures 4B,C**). With somatic recordings and antidromic spikes some spikes occur only as a hump, but the next spike usually succeeds to propagate all the way to the soma (Pekala et al., 2016). This suggests that the post-spike hyperexcitability, due to the DAP, reduces the failures toward the end of the spike train. The proper test of that interpretation would be to move the "breakpoint" in hyperpolarizing direction to reduce its effect on failures. This has not been tested yet but may be possible using pharmacological tools (Kaczmarek and Zhang, 2017).

## Ca-Tail

Almost every bouton, which is one of the structures that defines a TCA, has machinery for transmitter release, including voltage sensitive $Ca^{2+}$ channels. This makes the shape of the *propagating* spike important for transmitter release and a broad range of normal and pathological processes (Debanne et al., 2011; Fioravante and Regehr, 2011). Since subthreshold potentials between −60 mV and spike threshold have been shown to give asynchronous transmitter release (in crayfish neuromuscular junction: Wojtowicz and Atwood, 1984) and to open $Ca^{2+}$ channels (mouse calyx of Held: (Awatramani et al., 2005); rat cerebellar interneurons: Christie et al., 2011) there is a theoretical possibility that the DAP may increase presynaptic $Ca^{2+}$ or slow the deactivation of Cav channels. This may contribute to the early phase of the delayed transmitter release occurring at some synapses, for example between parallel fibers and Purkinje cells (Atluri and Regehr, 1998). Whether Cav channels activate or not may also depend on a finetuned control between membrane potentials immediately before the spike and the amplitude of the DAP (Clarke et al., 2016), suggesting that DAP amplitude may be decisive in such delayed transmitter release.

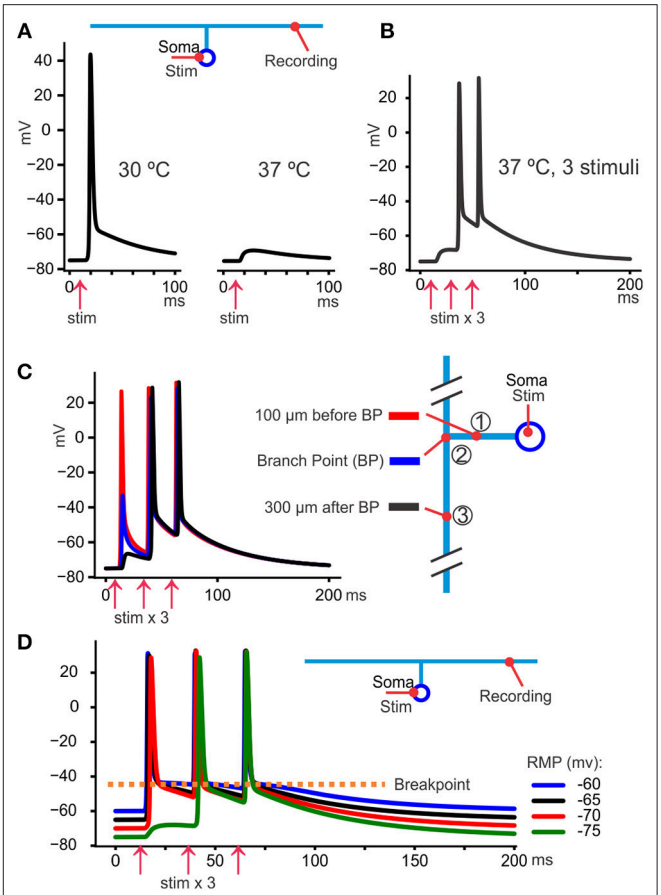


**FIGURE 4 |** The DAP reduces propagation failures. **(A)** At 30°C the spikes triggered at the soma by current injection always arrived at the axon. However, at 37°C they were still triggered at the soma (not shown) but failed to arrive at the distal axon where only a small voltage hump was seen. **(B)** Keeping the temperature at 37°C it was possible to overcome the propagation block by repeating the somatically triggered spikes, in this case with 20 ms intervals. One likely explanation is that the slow DAP spread passively further than the fast part of the spike (as can be seen as a hump in response to the first stimulus) and facilitated the propagation of the second and third spike. **(C)** By recording from three sites in the model axonal arbor we see that the first spike failed to propagate between site 1 and 3, but a depolarizing hump, due to the DAP, propagates even 300 µm past the branch point. That residual depolarization helped the second and third spike to propagate further than the first. **(D)** The resting membrane potential (RMP) was adjusted by changing the extracellular $K^+$ concentration to obtain values between −60 and −75 mV (color coded). We see that the fast-deactivating $K^+$ conductance implemented in the model gave very similar voltage levels for the breakpoint despite the large variation in RMP.

## Role in Bursting

It is not known if axonal (ectopic) bursts occur *in vivo*, but in slice experiments axonal bursts occurs in ∼30% of cerebellar granule cells. Such bursts come on the shoulder of the backpropagating spike's DAP, suggesting that the DAP is close to spike threshold (Pekala et al., 2014).

In the context of axonal bursting the temporal overlap between the refractory period (inhibiting bursting) and the DAP (promoting bursting) may be important. Since the post-spike hyperexcitability is relatively insensitive to temperature

(Soleng et al., 2004), but the refractory period is very temperature sensitive (Raastad and Shepherd, 2003), one hypothesis is that bursts occur with higher probability at high temperature because the Nav-channel inactivation becomes too short-lasting to protect against new spikes while the DAP is at its most depolarized levels. Theoretically, this could contribute to epileptic temperature-sensitive pathology, but that hypothesis has not been tested yet.

The stable voltage at which the fast repolarization stops has been shown to stabilize the shape of the spike during bursts, in crayfish neuromuscular junction (Lin, 2008) and in mouse calyx of Held (Sierksma and Borst, 2017). This may be important to minimize energy expenditure, and control transmitter release.

The constant breakpoint voltage will also, theoretically, stabilize the spike shape in situation where $[K^+]_o$ increases, particularly relevant in pathology like epileptic seizures. **Figure 4D** illustrates how the model behaves at different RMPs, manipulated by changing $[K^+]_o$. We see that during a train of spikes the individual spikes take off from similar potential despite great differences in RMPs, protecting the spiking mechanism from variations in $[K^+]_o$.

## CONCLUSION

The main conclusion of this article is that there is good support for the hypothesis proposing that individual spikes in cerebellar parallel fibers and hippocampal Schaffer collaterals are followed by a DAP, and that the DAP is a well-controlled process that stops the fast repolarization at a membrane potential positive to resting membrane potential, leaving the membrane more excitable for ∼100 ms during a slow, passive discharge of the membrane capacitance.

It is important that the presented model is intentionally simple but still qualitatively compatible with the selected data. The data I have selected is related to excitability, like activation threshold, conduction speed, and propagation failures. There is much data for example on transmitter release properties that the model is not intended to explain. The excitability control of the TCAs is probably enormously more complex, with interactions between changes in intracellular ion concentrations, the Na-K-pump, structural inhomogeneities along the TCAs, and participation of a large number of ion channels.

## METHODS

### Neuronal Model

Two voltage sensitive channels, Nav and Kv, and a leak conductance (gL) were used for the cell model. Both were implemented with the NMODL and NEURON languages (Hines and Carnevale, 1997) and inserted uniformly in the membrane of a neuron with dimensions given in **Figure 1**. Membrane capacitance and cytoplasmic resistivity were set to 1 μF/cm$^2$ and 150 Ωcm. The Nav had one variable for activation (m) and one for inactivation (h), and the Kv had one for activation (n), like the Hodgkin-Huxley (HH) model (Hodgkin and Huxley, 1952):

$$I = C\cdot\frac{dV}{dt} + gK\cdot n^4\cdot(V_m - V_K) + gNa\cdot m^3\cdot h\cdot(V_m - V_{Na}) + gL\,(V_m - V_L)$$

The gating variables were calculated as $\frac{dx}{dt} = \left(\frac{1}{xTau}\right)\cdot\left(xInf - x_0\right)$, where x is n, m or h.

The values of xInf was calculated as $xInf = \frac{1.0}{\left(1.0+\exp\left(\frac{v1}{-steepness}\right)\right)}$, and xTau as $xTau = \frac{Tmax}{qt}\cdot\left(0.05 + \left(\frac{1.9}{exp\left(\frac{v1}{Tc}\right)+exp\left(-\frac{v1}{Tc}\right)}\right)\right)$, using $qt = 2.3^{\frac{celcius-23}{10}}$, $v1 = v - \ midpoint$.

The "midpoint" for n, m, and h was 0, −25, −40. The "steepness" for n, m, and h was 18, 6, and 3. The "Tc" for n, m, and h was 25, 20, 10, and the "Tmax" for n, m, and h was 15, 0.51, and 7. Like HH, the conductance at each time step (0.01 ms) was calculated as gmax * n$^4$ for Kv, and gmax * m$^3$*$h$ for Nav, with gmax (the maximal conductance) 0.05 and 0.08 S/cm$^2$ for Nav and Kv, respectively. The parameters were chosen by manually selecting values that gave a fast $Na^+$ and $K^+$ current, and a fast deactivation of the $K^+$ current with the parameter "midpoint" set to a sufficiently depolarized value (0 mV) to give an almost complete deactivation at −45 mV.

The gL was set to 0.00002 S/cm$^2$ (which gives a 50 ms membrane time constant, compatible with the decay of the DAP in grease-gap recordings in Palani et al., 2012). Equilibrium potentials were 50 mV for Nav, −85 mV for Kv, and −75 mV for gL, which are common values in the literature.

## AUTHOR CONTRIBUTIONS

The author confirms being the sole contributor of this work and has approved it for publication.

## REFERENCES


Aitken, P. G., and Somjen, G. G. (1986). The sources of extracellular potassium accumulation in the CA1 region of hippocampal slices. *Brain Res.* 369, 163–167. doi: 10.1016/0006-8993(86)90524-X

Atluri, P. P., and Regehr, W. G. (1998). Delayed release of neurotransmitter from cerebellar granule cells. *J. Neurosci.* 18, 8214–8227. doi: 10.1523/JNEUROSCI.18-20-08214.1998

Augustine, G. J. (1990). Regulation of transmitter release at the squid giant synapse by presynaptic delayed rectifier potassium current. *J. Physiol.* 431, 343–364. doi: 10.1113/jphysiol.1990.sp018333

Awatramani, G. B., Price, G. D., and Trussell, L. O. (2005). Modulation of transmitter release by presynaptic resting potential and background calcium levels. *Neuron* 48, 109–121. doi: 10.1016/j.neuron.2005.08.038

Barrett, E. F., and Barrett, J. N. (1982). Intracellular recording from vertebrate myelinated axons: mechanism of the depolarizing afterpotential. *J. Physiol.* 323, 117–144. doi: 10.1113/jphysiol.1982.sp014064

Borst, J. G., Helmchen, F., and Sakmann, B. (1995). Pre- and postsynaptic whole-cell recordings in the medial nucleus of the trapezoid body of the rat. *J. Physiol.* 489 (Pt 3), 825–840. doi: 10.1113/jphysiol.1995.sp021095

Borst, J. G., and Sakmann, B. (1999). Effect of changes in action potential shape on calcium currents and transmitter release in a calyx-type synapse of the rat auditory brainstem. *Philos. Trans. R. Soc. Lond. B Biol. Sci.* 354, 347–355. doi: 10.1098/rstb.1999.0386

Bostock, H., Campero, M., Serra, J., and Ochoa, J. (2003). Velocity recovery cycles of C fibres innervating human skin. *J. Physiol.* 553, 649–663. doi: 10.1113/jphysiol.2003.046342

Braitenberg, V., and Schüz, A. (1998). *Cortex: Statistics and Geometry of Neuronal Connectivity*. Berlin: Springer. doi: 10.1007/978-3-662-03733-1

Chiu, S. Y., Ritchie, J. M., Rogart, R. B., and Stagg, D. (1979). A quantitative description of membrane currents in rabbit myelinated nerve. *J. Physiol.* 292, 149–166. doi: 10.1113/jphysiol.1979.sp012843

Christie, J. M., Chiu, D. N., and Jahr, C. E. (2011). $Ca^{2+}$-dependent enhancement of release by subthreshold somatic depolarization. *Nat. Neurosci.* 14, 62–68. doi: 10.1038/nn.2718

Clarke, S. G., Scarnati, M. S., and Paradiso, K. G. (2016). Neurotransmitter release can be stabilized by a mechanism that prevents voltage changes near the end of action potentials from affecting calcium currents. *J. Neurosci.* 36, 11559–11572. doi: 10.1523/JNEUROSCI.0066-16.2016

Debanne, D., Campanac, E., Bialowas, A., Carlier, E., and Alcaraz, G. (2011). Axon physiology. *Physiol. Rev.* 91, 555–602. doi: 10.1152/physrev.00048.2009

Dudel, J. (1971). The effect of polarizing current on action potential and transmitter release in crayfish motor nerve terminals. *Pflugers Arch.* 324, 227–248. doi: 10.1007/BF00586421

Eng, D. L., Gordon, T. R., Kocsis, J. D., and Waxman, S. G. (1990). Current-clamp analysis of a time-dependent rectification in rat optic nerve. *J. Physiol.* 421, 185–202. doi: 10.1113/jphysiol.1990.sp017940

Fioravante, D., and Regehr, W. G. (2011). Short-term forms of presynaptic plasticity. *Curr. Opin. Neurobiol.* 21, 269–274. doi: 10.1016/j.conb.2011.02.003

Foust, A. J., Yu, Y., Popovic, M., Zecevic, D., and McCormick, D. A. (2011). Somatic membrane potential and Kv1 channels control spike repolarization in cortical axon collaterals and presynaptic boutons. *J. Neurosci.* 31, 15490–15498. doi: 10.1523/JNEUROSCI.2752-11.2011

Frankenhaeuser, B., and Hodgkin, A. L. (1956). The after-effects of impulses in the giant nerve fibres of Loligo. *J. Physiol.* 131, 341–376. doi: 10.1113/jphysiol.1956.sp005467

Fritz, L. C., and Gardner-Medwin, A. R. (1976). The effect of synaptic activation on the extracellular potassium concentration in the hippocampal dentate area, *in vitro*. *Brain Res.* 112, 183–187. doi: 10.1016/0006-8993(76)90348-6

Gardner-Medwin, A. R. (1972). An extreme supernormal period in cerebellar parallel fibres. *J. Physiol.* 222, 357–371. doi: 10.1113/jphysiol.1972.sp009802

Geiger, J. R., and Jonas, P. (2000). Dynamic control of presynaptic $Ca^{2+}$ inflow by fast-inactivating $K^+$ channels in hippocampal mossy fiber boutons. *Neuron* 28, 927–939. doi: 10.1016/S0896-6273(00)00164-1

Hines, M. L., and Carnevale, N. T. (1997). The NEURON simulation environment. *Neural Comput.* 9, 1179–1209. doi: 10.1162/neco.1997.9.6.1179

Hodgkin, A. L., and Huxley, A. F. (1952). A quantitative description of membrane current and its application to conduction and excitation in nerve. *J. Physiol.* 117, 500–544. doi: 10.1113/jphysiol.1952.sp004764

Hodgkin, A. L., and Katz, B. (1949). The effect of temperature on the electrical activity of the giant axon of the squid. *J. Physiol.* 109, 240–249. doi: 10.1113/jphysiol.1949.sp004388

Hoppa, M. B., Gouzer, G., Armbruster, M., and Ryan, T. A. (2014). Control and plasticity of the presynaptic action potential waveform at small CNS nerve terminals. *Neuron* 84, 778–789. doi: 10.1016/j.neuron.2014.09.038

Hounsgaard, J., and Nicholson, C. (1983). Potassium accumulation around individual purkinje cells in cerebellar slices from the guinea-pig. *J. Physiol.* 340, 359–388. doi: 10.1113/jphysiol.1983.sp014767

Hu, W., and Bean, B. P. (2018). Differential control of axonal and somatic resting potential by voltage-dependent conductances in cortical layer 5 pyramidal neurons. *Neuron* 97, 1315–1326.e3. doi: 10.1016/j.neuron.2018.02.016

Kaars, C., and Faber, D. S. (1981). Myelinated central vertebrate axon lacks voltage-sensitive potassium conductance. *Science* 212, 1063–1065. doi: 10.1126/science.7233201

Kaczmarek, L. K., and Zhang, Y. (2017). Kv3 channels: enablers of rapid firing, neurotransmitter release, and neuronal endurance. *Physiol. Rev.* 97, 1431–1468. doi: 10.1152/physrev.00002.2017

Kim, J. A., and Connors, B. W. (2012). High temperatures alter physiological properties of pyramidal cells and inhibitory interneurons in hippocampus. *Front. Cell Neurosci.* 6:27. doi: 10.3389/fncel.2012.00027

Kim, J. H., Kushmerick, C., and von Gersdorff, H. (2010). Presynaptic resurgent Na+ currents sculpt the action potential waveform and increase firing reliability at a CNS nerve terminal. *J. Neurosci.* 30, 15479–15490. doi: 10.1523/JNEUROSCI.3982-10.2010

Kiyatkin, E. A., Brown, P. L., and Wise, R. A. (2002). Brain temperature fluctuation: a reflection of functional neural activation. *Eur. J. Neurosci.* 16, 164–168. doi: 10.1046/j.1460-9568.2002.02066.x

Kocsis, J. D., Eng, D. L., and Bhisitkul, R. B. (1984). Adenosine selectively blocks parallel-fiber-mediated synaptic potentials in rat cerebellar cortex. *Proc. Natl. Acad. Sci. U.S.A.* 81, 6531–6534. doi: 10.1073/pnas.81.20.6531

Kocsis, J. D., Malenka, R. C., and Waxman, S. G. (1983). Effects of extracellular potassium concentration on the excitability of the parallel fibres of the rat cerebellum. *J. Physiol.* 334, 225–244. doi: 10.1113/jphysiol.1983.sp014491

Lewis, A. H., and Raman, I. M. (2014). Resurgent current of voltage-gated Na(+) channels. *J. Physiol.* 592, 4825–4838. doi: 10.1113/jphysiol.2014.277582

Lin, J. W. (2008). Electrophysiological events recorded at presynaptic terminals of the crayfish neuromuscular junction with a voltage indicator. *J. Physiol.* 586, 4935–4950. doi: 10.1113/jphysiol.2008.158089

Ma, Y., Bayguinov, P. O., and Jackson, M. B. (2017). Action potential dynamics in fine axons probed with an axonally targeted optical voltage sensor. *eNeuro* 4:ENEURO.0146-17.2017 doi: 10.1523/ENEURO.0146-17.2017

Magistretti, J., Castelli, L., Forti, L., and D'Angelo, E. (2006). Kinetic and functional analysis of transient, persistent and resurgent sodium currents in rat cerebellar granule cells *in situ*: an electrophysiological and modelling study. *J. Physiol.* 573, 83–106. doi: 10.1113/jphysiol.2006.106682

Malenka, R. C., Kocsis, J. D., Ransom, B. R., and Waxman, S. G. (1981). Modulation of parallel fiber excitability by postsynaptically mediated changes in extracellular potassium. *Science* 214, 339–341. doi: 10.1126/science.7280695

Malenka, R. C., Kocsis, J. D., and Waxman, S. G. (1983). The supernormal period of the cerebellar parallel fibers effects of [Ca2+]o and [K+]o. *Pflugers Arch.* 397, 176–183. doi: 10.1007/BF00584354

Matsukawa, H., Wolf, A. M., Matsushita, S., Joho, R. H., and Knöpfel, T. (2003). Motor dysfunction and altered synaptic transmission at the parallel fiber-Purkinje cell synapse in mice lacking potassium channels Kv3.1 and Kv3.3. *J. Neurosci.* 23, 7677–7684. doi: 10.1523/JNEUROSCI.23-20-07677.2003

Metz, A. E., Jarsky, T., Martina, M., and Spruston, N. (2005). R-type calcium channels contribute to afterdepolarization and bursting in hippocampal CA1 pyramidal neurons. *J. Neurosci.* 25, 5763–5773. doi: 10.1523/JNEUROSCI.0624-05.2005

Mishchenko, Y., Hu, T., Spacek, J., Mendenhall, J., Harris, K. M., and Chklovskii, D. B. (2010). Ultrastructural analysis of hippocampal neuropil from the connectomics perspective. *Neuron* 67, 1009–1020. doi: 10.1016/j.neuron.2010.08.014

Nicholson, C., Kraig, R. P., ten Bruggencate, G., Stöckle, H., and Steinberg, R. (1978). Potassium, calcium, chloride and sodium changes in extracellular space during spreading depression in cerebellum [proceedings]. *Arzneimittelforschung* 28, 874–875.

Ohura, S., and Kamiya, H. (2018). Sodium channel-dependent and -independent mechanisms underlying axonal afterdepolarization at mouse hippocampal mossy fibers. *eNeuro* 5:ENEURO.0254-18.2018. doi: 10.1523/ENEURO.0254-18.2018

Palani, D., Baginskas, A., and Raastad, M. (2010). Bursts and hyperexcitability in non-myelinated axons of the rat hippocampus. *Neuroscience* 167, 1004–1013. doi: 10.1016/j.neuroscience.2010.03.021

Palani, D., Pekala, D., Baginskas, A., Szkudlarek, H., and Raastad, M. (2012). Action potentials recorded from bundles of very thin, gray matter axons in rat cerebellar slices using a grease-gap method. *J. Neurosci. Methods* 208, 119–127. doi: 10.1016/j.jneumeth.2012.05.005

Palay, S. L., and Chan-Palay, V. (1974). *Cerebellar Cortex: Cytology and Organization*. Berlin; Heidelberg; New York, NY: Springer. doi: 10.1007/978-3-642-65581-4

Pekala, D., Baginskas, A., Szkudlarek, H. J., and Raastad, M. (2014). Components of action potential repolarization in cerebellar parallel fibres. *J. Physiol.* 592, 4911–4929. doi: 10.1113/jphysiol.2014.280719

Pekala, D., Szkudlarek, H., and Raastad, M. (2016). Typical gray matter axons in mammalian brain fail to conduct action potentials faithfully at fever-like temperatures. *Physiol. Rep.* 4:e12981. doi: 10.14814/phy2.12981

Popovic, M., Vogt, K., Holthoff, K., Konnerth, A., Salzberg, B. M., Grinvald, A., et al. (2015). Imaging submillisecond membrane potential changes from

individual regions of single axons, dendrites and spines. *Adv. Exp. Med. Biol.* 859, 57–101. doi: 10.1007/978-3-319-17641-3_3

Raastad, M., and Shepherd, G. M. (2003). Single-axon action potentials in the rat hippocampal cortex. *J. Physiol.* 548, 745–752. doi: 10.1113/jphysiol.2002.032706

Ritchie, J. M., and Straub, R. W. (1957). The hyperpolarization which follows activity in mammalian non-medullated fibres. *J. Physiol.* 136, 80–97. doi: 10.1113/jphysiol.1957.sp005744

Rudy, B., and McBain, C. J. (2001). Kv3 channels: voltage-gated K+ channels designed for high-frequency repetitive firing. *Trends Neurosci.* 24, 517–526. doi: 10.1016/S0166-2236(00)01892-0

Sabatini, B. L., and Regehr, W. G. (1997). Control of neurotransmitter release by presynaptic waveform at the granule cell to Purkinje cell synapse. *J. Neurosci.* 17, 3425–3435. doi: 10.1523/JNEUROSCI.17-10-03425.1997

Shepherd, G. M., and Harris, K. M. (1998). Three-dimensional structure and composition of CA3–>CA1 axons in rat hippocampal slices: implications for presynaptic connectivity and compartmentalization. *J. Neurosci.* 18, 8300–8310.

Shu, Y., Duque, A., Yu, Y., Haider, B., and McCormick, D. A. (2007). Properties of action-potential initiation in neocortical pyramidal cells: evidence from whole cell axon recordings. *J. Neurophysiol.* 97, 746–760. doi: 10.1152/jn.00922.2006

Sierksma, M. C., and Borst, J. G. G. (2017). Resistance to action potential depression of a rat axon terminal *in vivo*. *Proc. Natl. Acad. Sci. U.S.A.* 114, 4249–4254. doi: 10.1073/pnas.1619433114

Soleng, A. F., Baginskas, A., Andersen, P., and Raastad, M. (2004). Activity-dependent excitability changes in hippocampal CA3 cell Schaffer axons. *J. Physiol.* 560, 491–503. doi: 10.1113/jphysiol.2004.071225

Stampfli, R. (1954). A new method for measuring membrane potentials with external electrodes. *Experientia* 10, 508–509. doi: 10.1007/BF02166189

Stys, P. K., Ransom, B. R., and Waxman, S. G. (1991). Compound action potential of nerve recorded by suction electrode: a theoretical and experimental analysis. *Brain Res.* 546, 18–32. doi: 10.1016/0006-8993(91)91154-S

Takeya, M., Hasuo, H., and Akasu, T. (2002). Effects of temperature increase on the propagation of presynaptic action potentials in the pathway between the Schaffer collaterals and hippocampal CA1 neurons. *Neurosci. Res.* 42, 175–185. doi: 10.1016/S0168-0102(01)00317-0

Toda, N. (1976). Neuromuscular blocking action of cadmium and manganese in isolated frog striated muscles. *Eur. J. Pharmacol.* 40, 67–75. doi: 10.1016/0014-2999(76)90355-1

Urbán, L., Aitken, P. G., and Somjen, G. G. (1985). Interstitial potassium concentration, slow depolarization and focal potential responses in the dorsal horn of the rat spinal slice. *Brain Res.* 331, 168–171. doi: 10.1016/0006-8993(85)90729-2

Weidner, C., Schmidt, R., Schmelz, M., Torebjork, H. E., and Handwerker, H. O. (2003). Action potential conduction in the terminal arborisation of nociceptive C-fibre afferents. *J. Physiol.* 547, 931–940. doi: 10.1113/jphysiol.2002.028712

Westrum, L. E., and Blackstad, T. W. (1962). An electron microscopic study of the stratum radiatum of the rat hippocampus (regio superior, CA 1) with particular emphasis on synaptology. *J. Comp. Neurol.* 119, 281–309. doi: 10.1002/cne.901190303

Wigström, H., and Gustafsson, B. (1981). Increased excitability of hippocampal unmyelinated fibres following conditioning stimulation. *Brain Res.* 229, 507–513. doi: 10.1016/0006-8993(81)91013-1

Wojtowicz, J. M., and Atwood, H. L. (1984). Presynaptic membrane potential and transmitter release at the crayfish neuromuscular junction. *J. Neurophysiol.* 52, 99–113. doi: 10.1152/jn.1984.52.1.99

Wu, H., Williams, J., and Nathans, J. (2014). Complete morphologies of basal forebrain cholinergic neurons in the mouse. *eLife* 3:e02444. doi: 10.7554/eLife.02444

Zhou, W. L., Yan, P., Wuskell, J. P., Loew, L. M., and Antic, S. D. (2007). Intracellular long-wavelength voltage-sensitive dyes for studying the dynamics of action potentials in axons and thin dendrites. *J. Neurosci. Methods* 164, 225–239. doi: 10.1016/j.jneumeth.2007.05.002

Zucker, R. S. (1974). Excitability changes in crayfish motor neurone terminals. *J. Physiol.* 241, 111–126. doi: 10.1113/jphysiol.1974.sp010643

**Conflict of Interest Statement:** The author declares that the research was conducted in the absence of any commercial or financial relationships that could be construed as a potential conflict of interest.

*Copyright © 2019 Raastad. This is an open-access article distributed under the terms of the Creative Commons Attribution License (CC BY). The use, distribution or reproduction in other forums is permitted, provided the original author(s) and the copyright owner(s) are credited and that the original publication in this journal is cited, in accordance with accepted academic practice. No use, distribution or reproduction is permitted which does not comply with these terms.*

frontiers in Cellular Neuroscience

MINI REVIEW
published: 12 June 2019
doi: 10.3389/fncel.2019.00269

# Dynamic Factors for Transmitter Release at Small Presynaptic Boutons Revealed by Direct Patch-Clamp Recordings

*Shin-ya Kawaguchi*[1,2,3]*

[1] Society-Academia Collaboration for Innovation, Kyoto University, Kyoto, Japan, [2] Department of Biophysics, Graduate School of Science, Kyoto University, Kyoto, Japan, [3] Institute for Advanced Study, Kyoto University, Kyoto, Japan

Small size of an axon and presynaptic structures have hindered direct functional analysis of axonal signaling and transmitter release at presynaptic boutons in the central nervous system. However, recent technical advances in subcellular patch-clamp recordings and in fluorescent imagings are shedding light on the dynamic nature of axonal and presynaptic mechanisms. Here I summarize the functional design of an axon and presynaptic boutons, such as diversity and activity-dependent changes of action potential (AP) waveforms, $Ca^{2+}$ influx, and kinetics of transmitter release, revealed by the technical *tour de force* of direct patch-clamp recordings and the leading-edge fluorescent imagings. I highlight the critical factors for dynamic modulation of transmitter release and presynaptic short-term plasticity.

**Keywords: axon, patch-clamp, transmitter release, presynaptic terminal, action potential, short-term plasticity**

OPEN ACCESS

***Edited by:***
*Josef Bischofberger, University of Basel, Switzerland*

***Reviewed by:***
*Stefan Hallermann, Leipzig University, Germany*
*Dominique Debanne, INSERM U1072 Neurobiologie des Canaux Ioniques et de la Synapse, France*

***Correspondence:**
*Shin-ya Kawaguchi*
*kawaguchi.shinya.7m@kyoto-u.ac.jp*

***Specialty section:***
*This article was submitted to Cellular Neurophysiology, a section of the journal Frontiers in Cellular Neuroscience*

***Received:*** *26 April 2019*
***Accepted:*** *29 May 2019*
***Published:*** *12 June 2019*

***Citation:***
*Kawaguchi S-y (2019) Dynamic Factors for Transmitter Release at Small Presynaptic Boutons Revealed by Direct Patch-Clamp Recordings. Front. Cell. Neurosci. 13:269. doi: 10.3389/fncel.2019.00269*

## INTRODUCTION

Direct patch-clamp recording from an axonal compartment tells a lot about the axon physiology and mechanisms of synaptic transmission. Unfortunately an axon and presynaptic terminals are usually too small to apply patch-clamp technique, except for unusually large structures, such as synapses of calyx of Held in the auditory brainstem and presynaptic boutons of hippocampal mossy fiber (Forsythe, 1994; Borst et al., 1995; Geiger and Jonas, 2000). Most conventional synapses in the central nervous system have much smaller presynaptic boutons (~1 μm) containing only 1–2 active zones, from which direct recording has been almost impossible to perform. However, in this decade remarkable technical advances have been accomplished in recording even from conventional small presynaptic structures in primary culture system, such as boutons of hippocampal pyramidal cells (~1 μm, Novak et al., 2013), cerebellar Purkinje cell (PC) axon terminals (~2–3 μm, Kawaguchi and Sakaba, 2015), and cerebellar granule cell (GC) axon varicosities (~1 μm, Kawaguchi and Sakaba, 2017). These advancements have provided detailed information about the mechanisms of presynaptic function, such as dynamics of presynaptic membrane excitability, $Ca^{2+}$ influx and buffering, pool size of readily releasable synaptic vesicles, and functional coupling between $Ca^{2+}$ and release machinery. In this article, I like to overview these recently clarified presynaptic mechanisms for transmitter release, particularly focusing on small synapses.

## FACTORS TO DETERMINE PRESYNAPTIC TRANSMITTER RELEASE

Fluorescent labeling of axons and presynaptic boutons makes it possible to precisely position a thin tip of glass pipette at a small structure for patch-clamp recordings. Voltage-clamp of an axon terminal allows to study quantitative relationship between the $Ca^{2+}$ influx to a presynaptic bouton and the amount of exocytosis of synaptic vesicles (**Figure 1**). For example, a long-duration of depolarization pulse applied to a bouton triggers fusion of almost all release-ready synaptic vesicles to the cytoplasmic membrane, resulting in an increase of surface membrane area size which can be recorded as a sudden jump of membrane capacitance (Cm) (Lindau and Neher, 1988; **Figure 1**). The amount of Cm increase, that is, the number of synaptic vesicles in readily releasable pool (RRP) changes depending on the type of synapses. For example, calyx of Held synapse (diameter, ~10 μm) shows about 400 fF of Cm increase upon a large $Ca^{2+}$ influx as ~2 nA upon a presynaptic depolarization pulse to 0 mV (Sun and Wu, 2001). On the other hand, ~100 fF of Cm increase is caused by ~200 pA of $Ca^{2+}$ currents at mossy fiber boutons in hippocampus (~5 μm) and those in the cerebellum (~6 μm) (Hallermann et al., 2003; Delvendahl et al., 2013). Recently, an inhibitory neuronal presynaptic terminal, a PC bouton with a size of 2~3 μm was patched, and a Cm increase of 80 fF was observed upon depolarization-induced $Ca^{2+}$ influx of ~300 pA (Kawaguchi and Sakaba, 2015; **Figure 1**). Thus, given that a single synaptic vesicle has a Cm of ~ 0.1 fF, about 1,000 synaptic vesicles are exocytosed from a single presynaptic bouton of a mossy fiber or a PC within several hundred milliseconds. On the other hand, a much smaller conventional presynaptic structure (~1 μm), an axon varicosity of a cerebellar GC, exhibited a ~20 fF of Cm increase with ~60 pA of $Ca^{2+}$ currents upon the identical depolarization pulse (Kawaguchi and Sakaba, 2017; **Figure 1**). Thus, even at a small axon terminal about 200 synaptic vesicles rapidly undergo fusion, which surprisingly corresponds to one third of total synaptic vesicles in a single bouton, based on the estimation by an electron microscopic analysis (Xu-Friedman et al., 2001). It should be noted that the quality of patch-clamp recording (i.e., physical access to the cytosol reflected by the series resistance) is critical for precise activation and measurement (in the extent and time course) of $Ca^{2+}$ currents and vesicular release. These measurements of presynaptic Cm increase upon strong $Ca^{2+}$ influx suggests that substantial number of synaptic vesicles rapidly undergo exocytosis at most synapses irrespective of their being excitatory or inhibitory.

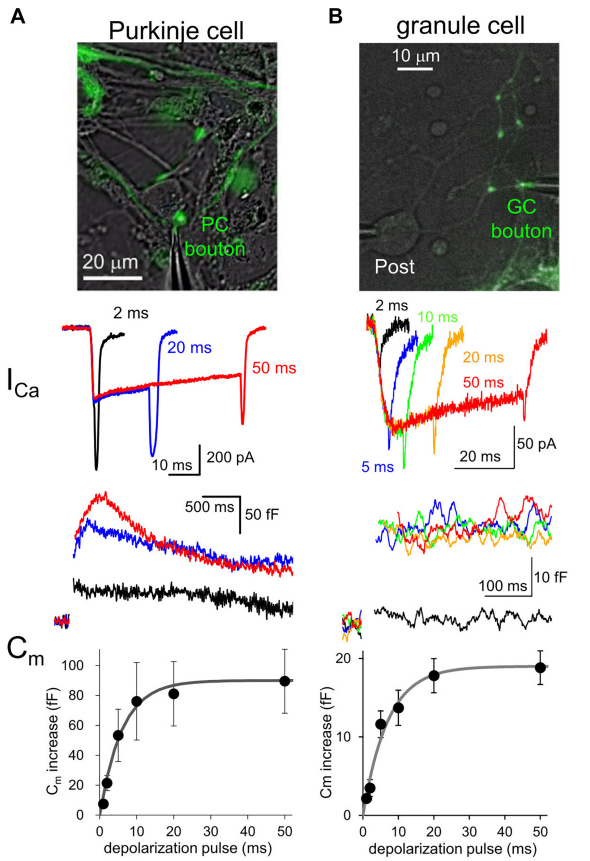


**FIGURE 1 |** Presynaptic transmitter releases studied by direct patch clamp recordings. **(A,B)** Patch-clamp recordings from a EGFP-labeled axon varicosity of a cerebellar PC **(A)** or of GC **(B)**, adapted from Kawaguchi and Sakaba (2015, 2017), respectively, with permission from Elsevier. Top, images of EGFP-labeled axon terminals of each neuron. Middle, presynaptic $Ca^{2+}$ currents ($I_{Ca}$) upon different durations of depolarization pulses to 0 mV. Bottom, presynaptic Cm increase triggered by $Ca^{2+}$ currents indicated in the middle. Average Cm increases plotted against duration of depolarization pulses are also shown.

Interestingly, comparison of various neuronal terminals implies a relationship that the maximal Cm increase and presynaptic $Ca^{2+}$ current amplitude likely depend on the first to second power of presynaptic diameter. Thus, we are tempted to assume that the RRP size estimated by Cm measurement simply reflects the surface area size of presynaptic structure, implying that the release machinery downstream of activation by $Ca^{2+}$ may operate in a similar manner at various neuronal boutons. However, it should be noted that the vesicular release estimated by Cm increases upon depolarization for tens of ms sometimes reflects the fusion of multiple states of synaptic vesicles, including those already primed at and those loosely coupled to the release sites (Sakaba and Neher, 2001), and even newly recruited ones at an extremely rapid rate (~ several ms) (Saviane and Silver, 2006; Kawaguchi and Sakaba, 2017). Recent elegant glutamate imaging coupled with super-resolution analysis of active zone proteins and electron microscopic analysis suggested that the exact number of release sites, which corresponds to synaptic vesicles maximally ready for immediate exocytosis upon $Ca^{2+}$ influx, is defined by the number of protein complex clusters consisting of $Ca^{2+}$ channels, and some active zone protein like Munc-13 (Miki et al., 2017; Sakamoto et al., 2018). Thus, the molecular organizations of presynaptic active zone and the vesicular recruitment mechanisms toward empty release sites determine the strength and sustainability of presynaptic transmitter release.

Different neuronal terminals show diversity in the process from $Ca^{2+}$ channel activation to triggering of vesicular release. First, $Ca^{2+}$ current is rapidly activated at a PC bouton (Kawaguchi and Sakaba, 2015) like a calyx of Held synapse (Borst et al., 1995), whereas a GC bouton exhibits slow activation of $Ca^{2+}$ current upon the identical depolarization pulses (Kawaguchi and Sakaba, 2017; **Figure 1**). In addition, the $Ca^{2+}$-release coupling estimated by the sensitivity to $Ca^{2+}$ chelators like EGTA varies in different neuronal boutons: a PC bouton shows tight coupling with low sensitivity to EGTA (Díaz-Rojas et al., 2015; Kawaguchi and Sakaba, 2015), as in other inhibitory interneurons (Bucurenciu et al., 2008; Eggermann et al., 2012); a GC bouton shows loose coupling with high EGTA sensitivity (Kawaguchi and Sakaba, 2017), in a similar manner to hippocampal mossy fiber boutons (Vyleta and Jonas, 2014). Furthermore, even action potential (AP) waveforms are quite different in axon terminals of PCs and GCs (see **Figure 2**).

Simultaneous recordings both from a presynaptic bouton and a postsynaptic cell provide more quantitative information about synaptic transmission (Sakaba and Neher, 2001; Sun and Wu, 2001). **Figure 2** illustrates time courses of presynaptic APs and $Ca^{2+}$ influx recorded from a PC or GC bouton, together with the kinetics of vesicular release estimated from postsynaptic responses (Kawaguchi and Sakaba, 2015, 2017). The remarkably different AP waveforms, when applied to the voltage-clamped bouton as voltage commands, cause clearly distinct kinetics of $Ca^{2+}$ influxes. This difference in $Ca^{2+}$ influx might be partly due to the slower activation of $Ca^{2+}$ channels in a GC than in a PC bouton (see **Figure 1**), in addition to the distinct AP kinetics (**Figure 2**). Furthermore, the initiation of transmitter release delays more in a GC axon varicosity after the $Ca^{2+}$ influx (~500 μs after the time of half-maximal $I_{Ca}$) than in a PC bouton (~300 μs), in spite that once started the release kinetics are similar (**Figure 2**). This distinct delay of release onset may partially reflect the different $Ca^{2+}$-release coupling: tight coupling at a PC bouton, whereas loose coupling in a GC bouton. On the other hand, similar time course of release rate by itself implies that release machinery may operate in a similar manner at these neurons. Thus, AP waveforms, the resultant activation of $Ca^{2+}$ channels, and the $Ca^{2+}$-driven activation of release machinery, seem to change depending on the neuronal type, and likely become as key factors to impact the transmitter release. Interestingly, recent imaging studies demonstrated that $Ca^{2+}$-release coupling becomes tighter after the chemical induction of presynaptic long-term potentiation (LTP) in hippocampal mossy fiber boutons (Midorikawa and Sakaba, 2017).

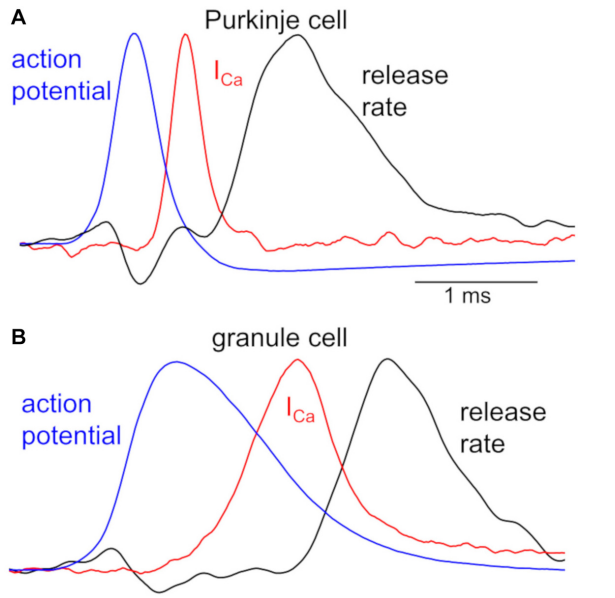


**FIGURE 2 |** Kinetics of APs, $Ca^{2+}$ influx, and transmitter release in a PC and GC bouton. Peak-scaled representative waveforms of APs, presynaptic $Ca^{2+}$ currents ($I_{Ca}$), and transmitter release rate obtained by simultaneous recordings from a representative pair of presynaptic bouton (**A**, PC; **B**, GC) and postsynaptic cell. Spontaneous APs (blue), recorded from an EGFP-labeled axon varicosity of a PC (**A**, peak of +30 mV) and of a GC (**B**, peak of +37 mV), were used as voltage commands for stimulation to the voltage-clamped bouton, and presynaptic $I_{Ca}$ (red, average of 5 traces from a pair) and postsynaptic currents were simultaneously recorded. Time courses of transmitter release rate (black, average of 5 traces recorded from a pair) were calculated by the deconvolution of the postsynaptic responses evoked by the presynaptic $I_{Ca}$, based on the miniature postsynaptic responses. Presynaptic recordings from a bouton of PC axon and that of GC axon had similar recording conditions, precluding the possibility of the distinct kinetics being due to the quality of patch-clamp recordings. All traces are adapted from Kawaguchi and Sakaba (2015, 2017) with permission from Elsevier.

## DIGITAL AND ANALOG SIGNALING IN AN AXON

Traditionally AP has been regarded as an all-or-none type of digital signal, reliably conveying information toward terminals in the central nervous system of vertebrates. However, direct recordings of APs by axonal patch-clamp methods and fluorescent imagings of membrane potential with a genetically encoded or chemical voltage indicator, have demonstrated activity-and/or location-dependent dynamic changes of AP waveforms in axon terminals (Kole et al., 2007; Hoppa et al., 2014; Kawaguchi and Sakaba, 2015; Rowan et al., 2016). In addition, sub-threshold electrical signals affect AP waveforms by modulating axonal $K^+$ channels and/or by passively propagating into an axon over hundreds μm even around distal regions (Pouzat and Marty, 1999; Alle and Geiger, 2006; Shu et al., 2006; Kole et al., 2007; Paradiso and Wu, 2009; Trigo et al., 2010; Pugh and Jahr, 2013; Zbili et al., 2016), which results in the modulation of transmitter release from presynaptic terminals (Rama et al., 2015; Rowan and Christie, 2017; Zorrilla de San Martin et al., 2017). Thus, the axonal AP signaling is modified in a manner like a hybrid of analog and digital transmission (Clark and Häusser, 2006; Debanne et al., 2011).

Because all $Ca^{2+}$ channels at a presynaptic structure are not necessarily activated by individual APs, change of an AP waveform potentially impacts the $Ca^{2+}$ influx into presynaptic cytoplasm, leading to modulation of transmitter release. In a cerebellar PC, high frequency AP firing results in attenuation of AP amplitude at a bouton, decreasing peak $Ca^{2+}$ influx,

and hence synaptic outputs (Kawaguchi and Sakaba, 2015). On the other hand, at hippocampal mossy fiber synapses, activity-dependent attenuation of AP is accompanied with the slower decay and hence causes larger net influx of $Ca^{2+}$, leading to augmented transmission (Geiger and Jonas, 2000). Distinct $Ca^{2+}$-release coupling in PC boutons and mossy fiber boutons might be partially responsible for the apparently opposite effects of activity-dependent AP changes on transmitter release (Vyleta and Jonas, 2014; Kawaguchi and Sakaba, 2015). The synapses with tighter $Ca^{2+}$-release coupling like PC boutons would show steeper dependence of transmitter release on the number of activated $Ca^{2+}$ channels rather than the total amount of $Ca^{2+}$ influx. Then, the AP amplitude controlling the maximal number of activated $Ca^{2+}$ channels could be more influential for the release in such tightly coupled synapses than the decay time course affecting the duration of $Ca^{2+}$ influx. In contrast, the total $Ca^{2+}$ influx would more preferentially control transmitter release in loosely coupled synapses. Thus, the impact of AP waveform modulation is determined how the synapse is functionally designed at the molecular level.

The presence of receptors for neurotransmitters in an axon has been demonstrated at various brain region and influences axonal excitability and neurotransmitter release (Debanne et al., 2011). Because of the substantial passive traveling of electrical signals in an axon, even a limited number of receptors in individual boutons could cooperatively contribute to changing the local membrane potential in an axon. For example, the axonal $GABA_A$Rs have been reported at various excitatory and inhibitory neurons, such as those in calyx of Held, posterior pituitary, cerebral cortex, hippocampus, and cerebellum (MacDermott et al., 1999; Trigo et al., 2008; Zorrilla de San Martin et al., 2017). Axonal $GABA_A$Rs may monitor the level of GABAergic inhibition around the postsynaptic target, locally adjusting the amount GABA release. Perforated patch-clamp technique using gramicidin clarified the reversal potential of GABA-mediated current ($E_{GABA}$) as $\sim -50$ mV in a terminal of the calyx of Held synapse (Price and Trussell, 2006) and −45 mV in a PC bouton (Zorrilla de San Martin et al., 2017). Because of the depolarized $E_{GABA}$, presynaptic $GABA_A$R activation depolarizes presynaptic boutons, facilitating $Ca^{2+}$ influx upon the subsequent AP arrival and hence synaptic transmission. In contrast, axonal $GABA_A$Rs also exert inhibitory effects in different neurons (Xia et al., 2014).

## SHORT-TERM PLASTICITY

Activity-dependent short-term plasticity of synaptic transmission lasting for milliseconds to minutes is an important element in the neuronal computation (Abbott and Regehr, 2004; Regehr, 2012). A lot of central synapses exhibit increase or decrease of strength, termed short-term synaptic facilitation, or depression, respectively, upon repetitive activity at short time intervals (Zucker and Regehr, 2002; Fioravante and Regehr, 2011). Dynamic changes of presynaptic $Ca^{2+}$ concentration and downstream processes of transmitter release mediate short-term plasticity. Residual $Ca^{2+}$ hypothesis is the simplest candidate mechanism for facilitation (Katz and Miledi, 1968). Temporal summation of residual $Ca^{2+}$ remaining in the cytoplasm after the first AP was suggested to facilitate the following AP-triggered transmitter release based on the ∼third power $Ca^{2+}$-dependence of release (Neher and Sakaba, 2008). However, the residual $Ca^{2+}$ increase is too small compared with the local $Ca^{2+}$ to explain synaptic facilitation in most cases.

P/Q-type of $Ca^{2+}$ channels, which predominantly mediates transmitter release at many synapses, exhibit remarkable facilitation of its current in a $Ca^{2+}$-dependent manner, resulting in facilitation of transmitter release (Catterall and Few, 2008; Ben-Johny and Yue, 2014). The association of $Ca^{2+}$ to C-lobe of calmodulin, which is basically bound with the P/Q-type channels, is thought to rapidly augment the $Ca^{2+}$ current by increasing the probability of channel opening. Exogenous expression of mutant $Ca^{2+}$ channels in superior cervical ganglion neurons in culture demonstrated a tight correlation between facilitation of $Ca^{2+}$ current and that of synaptic transmission (Mochida et al., 2008). Paired recordings from pre- and postsynaptic structures of a PC-PC pair showed that facilitation is almost exclusively mediated by the $Ca^{2+}$ current facilitation (Díaz-Rojas et al., 2015). Similar $Ca^{2+}$-dependent facilitation of presynaptic $Ca^{2+}$ influx takes place at glutamatergic boutons in the calyx of Held, which partly contributes to facilitation of synaptic transmission (Felmy et al., 2003; Müller et al., 2008; Hori and Takahashi, 2009). However, recently it was reported that a mutant mice lacking $Ca^{2+}$-facilitation of P-type channels still exhibit short-term facilitation at many synapses in a physiological condition, suggesting just a minor contribution of $Ca^{2+}$-current facilitation to short-term synaptic facilitation (Weyrer et al., 2019).

Another candidate mechanism for synaptic facilitation is the $Ca^{2+}$ buffer saturation hypothesis. If $Ca^{2+}$ buffer molecules remain occupied by $Ca^{2+}$ that entered into a bouton upon the first AP, cytoplasmic free $Ca^{2+}$ becomes more abundant upon the following APs, and leading to larger transmitter release. Indeed, calbindin contributes to the facilitation at hippocampal mossy fiber-CA3 excitatory synapses and inhibitory synapses in the cerebral cortex (Blatow et al., 2003). The buffer saturation model relies on the loose coupling between $Ca^{2+}$ and release machinery (Neher, 1998; Rozov et al., 2001; Vyleta and Jonas, 2014). Recently, direct recordings from a cerebellar GC axon varicosity demonstrated that $Ca^{2+}$-release coupling is indeed loose there, and facilitation depends on the presence of low concentration of fast $Ca^{2+}$ buffer in the terminal (Kawaguchi and Sakaba, 2017), in line with the $Ca^{2+}$ buffer saturation model.

The next hypothesis for short-term facilitation is the $Ca^{2+}$-dependent facilitation of release sensors (Regehr, 2012). Recent accumulating results indicate the critical role of Syt7 as such a facilitation sensor at various synapses (Jackman et al., 2016; Turecek and Regehr, 2018). The mechanism how Syt7 contributes to facilitation of transmitter release remains to be clarified in the future. However, it should be noted that some facilitation remains even with the genetic ablation of Syt7, implying that different combination of several facilitation mechanisms described above would operate together at distinct synapses.

In addition to facilitation, short-term depression has also been studied, and the RRP depletion is thought to be the major mechanism (Zucker and Regehr, 2002; Fioravante and Regehr, 2011). Other mechanisms, such as $Ca^{2+}$ current inactivation and AP conduction failure at axonal branches (Brody and Yue, 2000; Xu and Wu, 2005) and inactivation of release sites (Neher and Sakaba, 2008; Pan and Zucker, 2009), could also contribute. GABAergic synapses on deep cerebellar nuclei neurons innervated from PCs also exhibit short-term depression upon high frequency activation (Telgkamp and Raman, 2002; Pedroarena and Schwarz, 2003). Recently, direct axonal patch-clamp recordings together with fluorescent imaging of synapto-pHluorin demonstrated frequency-dependent attenuation of AP propagation from axonal tract toward the terminals in PCs (Kawaguchi and Sakaba, 2015). Smaller number of $Ca^{2+}$ channels activated by a smaller AP is responsible for the depression of transmitter release at high-frequency activation in a PC bouton. Importantly, the AP conduction faithfulness seems to increase in PC axons along with the development, resulting in smaller frequency-dependent depression at this synapse in mature animals (Turecek et al., 2016).

## CONCLUSION AND FUTURE DIRECTION

As overviewed here, recent technical advances to study axon physiology are shedding light on rich computational ability of an axon affecting synaptic outputs, rather than the classical view of an axon as a simple reliable digital signal conductor. Transmitter release from a presynaptic bouton is dynamically controlled by a variety of activity-dependent modulations of critical factors, such as AP waveforms, $Ca^{2+}$ channel activation, and $Ca^{2+}$-triggered release processes based on fine molecular organizations of release sites and vesicular replenishment systems. Different combinations of these dynamic elements would define the neuronal type-specific functional design of synapses and their short- and/or long-term plasticity. Rapid expansion of techniques for direct recording of axonal signaling with subcellular patch-clamp methods and/or fluorescent imagings is going to clarify neuron-specific and common functional designs of a variety of CNS synapses in the near future, which enriches our understanding of neuronal circuitry.

## AUTHOR CONTRIBUTIONS

S-yK wrote the manuscript and prepared the figures.

## FUNDING

This work was supported by the KAKENHI grants from the JSPS/MEXT, Japan (15KT0082, 18H02527, and the Grant-in Scientific Research on Innovation Areas 19H04750), the Naito Science Foundation, the Takeda Science Foundation, and by the JSPS Core-to-Core Program A Advanced Research Networks.

## REFERENCES

Abbott, L. F., and Regehr, W. G. (2004). Synaptic computation. *Nature* 431, 796–803.

Alle, H., and Geiger, J. R. P. (2006). Combined analog and action potential coding in hippocampal mossy fibers. *Science* 311, 1290–1293. doi: 10.1126/science.1119055

Ben-Johny, M., and Yue, D. T. (2014). Calmodulin regulation (calmodulation) of voltage-gated calcium channels. *J. Gen. Physiol.* 143, 679–692. doi: 10.1085/jgp.201311153

Blatow, M., Caputi, A., Burnashev, N., Monyer, H., and Rozov, A. (2003). Ca2+ buffer saturation underlies paired pulse facilitation in calbindin-D28k-containing terminals. *Neuron* 38, 79–88. doi: 10.1016/s0896-6273(03)00196-x

Borst, J. G., Helmchen, F., and Sakmann, B. (1995). Pre- and postsynaptic whole-cell recordings in the medial nucleus of the trapezoid body of the rat. *J. Physiol.* 489, 825–840. doi: 10.1113/jphysiol.1995.sp021095

Brody, D. L., and Yue, D. T. (2000). Release-independent short-term synaptic depression in cultured hippocampal neurons. *J. Neurosci.* 20, 2480–2494. doi: 10.1523/jneurosci.20-07-02480.2000

Bucurenciu, I., Kulik, A., Schwaller, B., Frotscher, M., and Jonas, P. (2008). Nanodomain coupling between Ca2+ channels and Ca2+ sensors promotes fast and efficient transmitter release at a cortical GABAergic synapse. *Neuron* 57, 536–545. doi: 10.1016/j.neuron.2007.12.026

Catterall, W. A., and Few, A. P. (2008). Calcium channel regulation and presynaptic plasticity. *Neuron* 59, 882–901. doi: 10.1016/j.neuron.2008.09.005

Clark, B., and Häusser, M. (2006). Neural coding: hybrid analog and digital signalling in axons. *Curr. Biol.* 16, R585–R588.

Debanne, D., Campanac, E., Bialowas, A., Carlier, E., and Alcaraz, G. (2011). Axon physiology. *Physiol. Rev.* 91, 555–602. doi: 10.1152/physrev.00048.2009

Delvendahl, I., Weyhersmüller, A., Ritzau-Jost, A., and Hallermann, S. (2013). Hippocampal and cerebellar mossy fibre boutons - same name, different function. *J. Physiol.* 591, 3179–3188. doi: 10.1113/jphysiol.2012.248294

Díaz-Rojas, F., Sakaba, T., and Kawaguchi, S. Y. (2015). Ca2+ current facilitation determines short-term facilitation at inhibitory synapses between cerebellar Purkinje cells. *J. Physiol.* 593, 4889–4904. doi: 10.1113/JP270704

Eggermann, E., Bucurenciu, I., Goswami, S. P., and Jonas, P. (2012). Nanodomain coupling between Ca2+ channels and sensors of exocytosis at fast mammalian synapses. *Nature Rev. Neurosci.* 13, 7–21. doi: 10.1038/nrn3125

Felmy, F., Neher, E., and Schneggenburger, R. (2003). Probing the intracellular calcium sensitivity of transmitter release during synaptic facilitation. *Neuron* 37, 801–811. doi: 10.1016/s0896-6273(03)00085-0

Fioravante, D., and Regehr, W. G. (2011). Short-term forms of presynaptic plasticity. *Curr. Opin. Neurobiol.* 21, 269–274. doi: 10.1016/j.conb.2011.02.003

Forsythe, I. D. (1994). Direct patch recording from identified presynaptic terminals mediating glutamatergic EPSCs in the rat CNS, in vitro. *J. Physiol.* 479, 381–387. doi: 10.1113/jphysiol.1994.sp020303

Geiger, J. R., and Jonas, P. (2000). Dynamic control of presynaptic Ca(2+) inflow by fast-inactivating k(+) channels in hippocampal mossy fiber boutons. *Neuron* 28, 927–939. doi: 10.1016/s0896-6273(00)00164-1

Hallermann, S., Pawlu, C., Jonas, P., and Heckmann, N. (2003). A large pool of releasable vesicles in a cortical glutamatergic synapse. *Proc. Natl. Acad. Sci. U.S.A.* 100, 8975–8980. doi: 10.1073/pnas.1432836100

Hoppa, M. B., Gouzer, G., Armbruster, M., and Ryan, T. A. (2014). Control and plasticity of the presynaptic action potential waveform at small CNS nerve terminals. *Neuron* 84, 778–789. doi: 10.1016/j.neuron.2014.09.038

Hori, T., and Takahashi, T. (2009). Mechanisms underlying short-term modulation of transmitter release by presynaptic depolarization. *J. Physiol.* 587, 2987–3000. doi: 10.1113/jphysiol.2009

Jackman, S. L., Turecek, J., Belinsky, J. E., and Regehr, W. G. (2016). The calcium sensor synaptotagmin 7 is required for synaptic facilitation. *Nature* 529, 88–91. doi: 10.1038/nature16507

Katz, B., and Miledi, R. (1968). The role of calcium in neuromuscular facilitation. *J. Physiol.* 195, 481–492. doi: 10.1113/jphysiol.1968.sp008469

Kawaguchi, S. Y., and Sakaba, T. (2015). Control of inhibitory synaptic outputs by low excitability of axon terminals revealed by direct recording. *Neuron* 85, 1273–1288. doi: 10.1016/j.neuron.2015.02.013

Kawaguchi, S. Y., and Sakaba, T. (2017). Fast Ca2+ buffer-dependent reliable but plastic transmission at small CNS synapses revealed by direct bouton recording. *Cell Rep.* 21, 3338–3345. doi: 10.1016/j.celrep.2017.11.072

Kole, M. H., Letzkus, J. J., and Stuart, G. J. (2007). Axon initial segment Kv1 channels control axonal action potential waveform and synaptic efficacy. *Neuron* 55, 633–647. doi: 10.1016/j.neuron.2007.07.031

Lindau, M., and Neher, E. (1988). Patch-clamp techniques for time-resolved capacitance measurements in single cells. *Pflugers. Arch.* 411, 137–146. doi: 10.1007/bf00582306

MacDermott, A. B., Role, L. W., and Siegelbaum, S. A. (1999). Presynaptic ionotropic receptors and the control of transmitter release. *Annu. Rev. Neurosci.* 22, 443–485. doi: 10.1146/annurev.neuro.22.1.443

Midorikawa, M., and Sakaba, T. (2017). Kinetics of releasable synaptic vesicles and their plastic changes at hippocampal mossy fiber synapses. *Neuron* 96, 1033–1040. doi: 10.1016/j.neuron.2017.10.016

Miki, T., Kaufmann, W. A., Malagon, G., Gomez, L., Tabuchi, K., Watanabe, M., et al. (2017). Numbers of presynaptic Ca2+ channel clusters match those of functionally defined vesicular docking sites in single central synapses. *Proc. Natl. Acad. Sci. U.S.A.* 114, E5246–E5255. doi: 10.1073/pnas.1704470114

Mochida, S., Few, A. P., Scheuer, T., and Catterall, W. A. (2008). Regulation of presynaptic Ca(V)2.1 channels by Ca2+ sensor proteins mediates short-term synaptic plasticity. *Neuron* 57, 210–216. doi: 10.1016/j.neuron.2007.11.036

Müller, M., Felmy, F., and Schneggenburger, R. (2008). A limited contribution of Ca2+ current facilitation to paired-pulse facilitation of transmitter release at the rat calyx of Held. *J. Physiol.* 586, 5503–5520. doi: 10.1113/jphysiol.2008.155838

Neher, E. (1998). Vesicle pools and Ca2+ microdomains: new tools for understanding their roles in neurotransmitter release. *Neuron* 20, 389–399. doi: 10.1016/s0896-6273(00)80983-6

Neher, E., and Sakaba, T. (2008). Multiple roles of calcium ions in the regulation of transmitter release. *Neuron* 59, 861–872. doi: 10.1016/j.neuron.2008.08.019

Novak, P., Gorelik, J., Vivekananda, U., Shevchuk, A. I., Ermolyuk, Y. S., Bailey, R. J., et al. (2013). Nanoscale-targeted patch-clamp recordings of functional presynaptic ion channels. *Neuron* 79, 1067–1077. doi: 10.1016/j.neuron.2013.07.012

Pan, B., and Zucker, R. S. (2009). A general model of synaptic transmission and short-term plasticity. *Neuron* 62, 539–554. doi: 10.1016/j.neuron.2009.03.025

Paradiso, K., and Wu, L.-G. (2009). Small voltage changes at nerve terminals travel up axons to affect action potential initiation. *Nat. Neurosci.* 12, 541–543. doi: 10.1038/nn.2301

Pedroarena, C. M., and Schwarz, C. (2003). Efficacy and short-term plasticity at GABAergic synapses between Purkinje and deep cerebellar nuclei neurons. *J. Neurophysiol.* 89, 704–716.

Pouzat, C., and Marty, A. (1999). Somatic recording of gabaergic autoreceptor current in cerebellar stellate and basket cells. *J. Neurosci.* 19, 1675–1690. doi: 10.1523/jneurosci.19-05-01675.1999

Price, G. D., and Trussell, L. O. (2006). Estimate of the chloride concentration in a central glutamatergic terminal: a gramicidin perforated-patch study on the calyx of held. *J. Neurosci.* 26, 11432–11436. doi: 10.1523/jneurosci.1660-06.2006

Pugh, J. R., and Jahr, C. E. (2013). Activation of axonal receptors by gaba spillover increases somatic firing. *J. Neurosci.* 33, 16924–16929. doi: 10.1523/JNEUROSCI.2796-13.2013

Rama, S., Zbili, M., Bialowas, A., Fronzaroli-Molinieres, L., Ankri, N., Carlier, E., et al. (2015). Presynaptic hyperpolarization induces a fast analogue modulation of spike-evoked transmission mediated by axonal sodium channels. *Nat. Commun.* 6:10163. doi: 10.1038/ncomms10163

Regehr, W. G. (2012). Short-term presynaptic plasticity. *Cold Spring Harb. Perspect. Biol.* 4:a005072. doi: 10.1101/cshperspect.a005702

Rowan, M. J., DelCanto, G., Yu, J. J., Kamasawa, N., and Christie, J. M. (2016). Synapse-Level determination of action potential duration by k(+) channel clustering in axons. *Neuron* 91, 370–383. doi: 10.1016/j.neuron.2016.05.035

Rowan, M. J. M., and Christie, J. M. (2017). Rapid state-dependent alteration in kv3 channel availability drives flexible synaptic signaling dependent on somatic subthreshold depolarization. *Cell Rep.* 18, 2018–2029. doi: 10.1016/j.celrep.2017.01.068

Rozov, A., Burnashev, N., Sakmann, B., and Neher, E. (2001). Transmitter release modulation by intracellular Ca2+ buffers in facilitating and depressing nerve terminals of pyramidal cells in layer 2/3 of the rat neocortex indicates a target cell-specific difference in presynaptic calcium dynamics. *J. Physiol.* 531, 807–826. doi: 10.1111/j.1469-7793.2001.0807h.x

Sakaba, T., and Neher, E. (2001). Calmodulin mediates rapid recruitment of fast-releasing synaptic vesicles at a calyx-type synapse. *Neuron* 32, 1119–1131. doi: 10.1016/s0896-6273(01)00543-8

Sakamoto, H., Ariyoshi, T., Kimpara, N., Sugao, K., Taiko, I., Takikawa, K., et al. (2018). Synaptic weight set by Munc13-1 supramolecular assemblies. *Nat. Neurosci.* 21, 41–49. doi: 10.1038/s41593-017-0041-9

Saviane, C., and Silver, R. A. (2006). Fast vesicle reloading and a large pool sustain high bandwidth transmission at a central synapse. *Nature* 439, 983–987. doi: 10.1038/nature04509

Shu, Y., Hasenstaub, A., Duque, A., Yu, Y., and McCormick, D. A. (2006). Modulation of intracortical synaptic potentials by presynaptic somatic membrane potential. *Nature* 441, 761–765. doi: 10.1038/nature04720

Sun, J. Y., and Wu, L. G. (2001). Fast kinetics of exocytosis revealed by simultaneous measurements of presynaptic capacitance and postsynaptic currents a central synapse. *Neuron* 30, 171–182. doi: 10.1016/s0896-6273(01)00271-9

Telgkamp, P., and Raman, I. M. (2002). Depression of inhibitory synaptic transmission between Purkinje cells and neurons of the cerebellar nuclei. *J. Neurosci.* 22, 8447–8457. doi: 10.1523/jneurosci.22-19-08447.2002

Trigo, F. F., Bouhours, B., Rostaing, P., Papageorgiou, G., Corrie, J. E. T., Triller, A., et al. (2010). Presynaptic miniature GABAergic currents in developing interneurons. *Neuron* 66, 235–247. doi: 10.1016/j.neuron.2010.03.030

Trigo, F. F., Marty, A., and Stell, B. M. (2008). Axonal GABAA receptors. *Eur. J. Neurosci.* 28, 841–848. doi: 10.1111/j.1460-9568.2008.06404.x

Turecek, J., Jackman, S. L., and Regehr, W. G. (2016). Synaptic specializations support frequency-independent purkinje cell output from the cerebellar cortex. *Cell Rep.* 17, 3256–3268. doi: 10.1016/j.celrep.2016.11.081

Turecek, J., and Regehr, W. G. (2018). Synaptotagmin 7 mediates both facilitation and asynchronous release at granule cell synapses. *J. Neurosci.* 38, 3240–3251. doi: 10.1523/JNEUROSCI.3207-17.2018

Vyleta, N. P., and Jonas, P. (2014). Loose coupling between Ca2+ channels and release sensors at a plastic hippocampal synapse. *Science* 343, 665–670. doi: 10.1126/science.1244811

Weyrer, C., Turecek, J., Niday, Z., Liu, P. W., Nanou, E., Catterall, W. A., et al. (2019). The role of cav2.1 channel facilitation in synaptic facilitation. *Cell Rep.* 26:2289-2297.e3. doi: 10.1016/j.celrep.2019.01.114

Xia, Y., Zhao, Y., Yang, M., Zeng, S., and Shu, Y. (2014). Regulation of action potential waveforms by axonal GABAA receptors in cortical pyramidal neurons. *PLoS One* 9:e100968. doi: 10.1371/journal.pone.0100968

Xu, J., and Wu, L. G. (2005). The decrease in the presynaptic calcium current is a major cause of short-term depression at a calyx synapse. *Neuron* 46, 633–645. doi: 10.1016/j.neuron.2005.03.024

Xu-Friedman, M. A., Harris, K. M., and Regehr, W. G. (2001). Three-dimensional comparison of ultrastructural characteristics at depressing and facilitating synapses onto cerebellar Purkinje cells. *J. Neurosci.* 21, 6666–6672. doi: 10.1523/jneurosci.21-17-06666.2001

Zbili, M., Rama, S., and Debanne, D. (2016). Dynamic control of neurotransmitter release by presynaptic potential. *Front. Cell. Neurosci.* 10:278. doi: 10.3389/fncel.2016.00278

Zorrilla de San Martin, J., Trigo, F. F., and Kawaguchi, S. Y. (2017). Axonal GABAA receptors depolarize presynaptic terminals and facilitate transmitter release in cerebellar Purkinje cells. *J. Physiol.* 595, 7477–7493. doi: 10.1113/JP275369

Zucker, R. S., and Regehr, W. G. (2002). Short-term synaptic plasticity. *Annu. Rev. Physiol.* 64, 355–405.

**Conflict of Interest Statement:** The author declares that the research was conducted in the absence of any commercial or financial relationships that could be construed as a potential conflict of interest.

*Copyright © 2019 Kawaguchi. This is an open-access article distributed under the terms of the Creative Commons Attribution License (CC BY). The use, distribution or reproduction in other forums is permitted, provided the original author(s) and the copyright owner(s) are credited and that the original publication in this journal is cited, in accordance with accepted academic practice. No use, distribution or reproduction is permitted which does not comply with these terms.*

frontiers in Cellular Neuroscience

PERSPECTIVE
published: 21 June 2019
doi: 10.3389/fncel.2019.00257

# What We Can Learn From Cumulative Numbers of Vesicular Release Events

*Takafumi Miki**

*Graduate School of Brain Science, Doshisha University, Kyoto, Japan*

Following action potential invasion in presynaptic terminals, synaptic vesicles are released in a stochastic manner at release sites (docking sites). Since neurotransmission occurs at frequencies up to 1 kHz, the mechanisms underlying consecutive vesicle releases at a docking site during high frequency bursts is a key factor for understanding the role and strength of the synapse. Particularly new vesicle recruitment at the docking site during neuronal activity is thought to be crucial for short-term plasticity. However current studies have not reached a unified docking site model for central synapses. Here I review newly developed analyses that can provide insight into docking site models. Quantal analysis using counts of vesicular release events provide a wealth of information not only to monitor the number of docking sites, but also to distinguish among docking site models. The stochastic properties of cumulative release number during bursts allow us to estimate the total number of releasable vesicles and to deduce the features of vesicle recruitment at docking sites and the change of release probability during bursts. This analytical method may contribute to a comprehensive understanding of release/replenishment mechanisms at a docking site.

**Keywords: synapse, neurotransmitter release, quantal analysis, release site, vesicle recruitment**

OPEN ACCESS

***Edited by:***
*Shin-ya Kawaguchi,*
*Kyoto University, Japan*

***Reviewed by:***
*Stefan Hallermann,*
*Leipzig University, Germany*
*Hartmut Schmidt,*
*Leipzig University, Germany*

***Correspondence:**
*Takafumi Miki*
*tmiki@mail.doshisha.ac.jp*

***Specialty section:***
*This article was submitted to Cellular Neurophysiology, a section of the journal Frontiers in Cellular Neuroscience*

***Received:*** *22 March 2019*
***Accepted:*** *23 May 2019*
***Published:*** *21 June 2019*

***Citation:***
*Miki T (2019) What We Can Learn From Cumulative Numbers of Vesicular Release Events. Front. Cell. Neurosci. 13:257. doi: 10.3389/fncel.2019.00257*

## INTRODUCTION

Synaptic vesicles fuse with the presynaptic membrane to release neurotransmitter into the synaptic cleft in a specific structure called active zone (AZ), where each AZ contains one or multiple vesicular docking/release sites (DSs). The DS number corresponds to the maximum number of vesicular release events following an action potential (AP) (review: Pulido and Marty, 2017). The number of released vesicles follows Poisson statistics under conditions of low release probability (e.g., low calcium and high magnesium concentrations extracellularly; Del Castillo and Katz, 1954). However, it was hypothesized that release with normal release probability under physiological conditions is a binomial process (Katz, 1969). Based on this hypothesis, the number of DSs have been estimated by fluctuation analyses using the peak amplitude of synaptic responses (Silver et al., 1998; Clements and Silver, 2000). Assumptions and corrections for heterogeneous release probability and quantal size within and across synapses, synaptic jitter, and quantal size distortion by desensitization and saturation of postsynaptic receptors, are needed to make an accurate estimate of synaptic parameters (DS number $N$, release probability per AZ $P$, and quantal size $Q$; Silver et al., 1998). An alternative approach, instead of using peak amplitudes of synaptic responses from multiple synapses, is to use for variance-mean analysis the number of vesicular release events detected from synaptic responses recorded from synapses having a single presynaptic AZ and a single postsynaptic density ('simple synapses': Malagon et al., 2016). In this alternative analysis, the parameter value for $Q$ in the analysis using peak amplitude of synaptic response is 1 since the number of vesicular events

is used. In this review, I will focus on the newly developed method to count vesicular events at single synapses and I will introduce analyses and model simulations to extract valuable information related to the number of DSs, the vesicle recruitment process, and the pool of releasable/suppliable vesicles. This approach allows us to predict a detailed DS model at a given synapse. Especially the mechanism of vesicle replenishment and the pool size of suppliable vesicles to DS are critical for short-term plasticity and sustained transmission. Experimental manipulations with in-depth electrophysiological examinations have uncovered changes and molecular/morphological correlates of synaptic parameters in DS models at synapses of the mammalian central nervous system (CNS) (e.g., Silver et al., 2003; Lou et al., 2005; Neher and Sakaba, 2008; Hallermann et al., 2010; Südhof, 2012; Liu et al., 2014; Chen et al., 2015; Montesinos et al., 2015; Jackman et al., 2016). More detailed description of DS models by the developed method may more clearly define molecular/morphological correlates of synaptic parameters. In addition, nanometer-resolution observations in mammalian CNS using super-resolution imaging and electron microscopy have revealed synaptic vesicle movement in presynaptic terminals (Midorikawa and Sakaba, 2015, 2017; Rothman et al., 2016; Maschi and Klyachko, 2017; Chang et al., 2018; Kusick et al., 2018), and distribution of synaptic vesicles and AZ proteins (Siksou et al., 2007; Imig et al., 2014; Nakamura et al., 2015; Tang et al., 2016), paving the way for a comparison between data and DS model simulations for a comprehensive understanding of vesicle release/replenishment at DSs if the vesicle recruitment process and the pool size of releasable/suppliable vesicles can be predicted accurately by the new method.

## COUNTING SV RELEASE

A simple approach for estimating synaptic parameters using fluctuation analysis is to utilize the number of released vesicles at single AZs instead of PSC amplitude, as the former method needs less corrections and assumptions than the latter. Recently we have developed a new method to detect individual vesicular release events using EPSCs recorded in simple synapses (Malagon et al., 2016). One requirement of the method is that PSCs should originate from a single AZ where unitary postsynaptic responses have little variability. Sharp synaptic responses, like those provided by activation of AMPA receptors, are optimal because they provide excellent time estimates of vesicular release events. While these conditions restrict the applicability of the method, the method is advantageous as it can cancel out receptor desensitization and saturation. Additionally, heterogeneity of quantal size and release probability, either within a synapse or across synapses, and asynchrony of vesicular release due to synaptic jitter, do not need to be taken into consideration in a fit of variance-mean plots. Altogether the method allows us to perform quantal analysis in a simple manner by using the number of release events, although some corrections are still required due to the time resolution of event detection (0.2 ms: Malagon et al., 2016). Although deconvolution techniques applied to large synapses provide valuable information, notably concerning mean values of vesicular release event number (Sakaba, 2006), obtaining variance values of the event number require corrections for heterogeneities of postsynaptic responses among AZs in the large synapses. The estimation error for variance in large synapses is further increased by confounders such as postsynaptic receptor desensitization and saturation, and heterogeneities of release probability among AZs. Additionally, the error is accumulated in cumulative number of vesicular events in a train (see next chapter). By contrast, our method essentially takes advantage of the quantal nature of synaptic currents to round up numbers associated with small signals. This eliminates uncertainties linked to quantal size variations, and results in a significant improvement of the accuracy of the results. Hence our method using simple synapses offers a large benefit for quantitative analysis.

The binomial model of vesicular release classically predicts a parabolic variance-mean relationship for synaptic response fluctuations (Katz, 1969). In variance-mean plots of release events numbers, the model parabola has an initial slope of 1, whereas its slope equals the quantal size in the classical analysis using PSC peak amplitudes, and it intersects the $x$ axis at the origin and at the DS number, $N$, according to the following formulas:

$$var = NP(1 - P)$$

$$mean = NP$$

so that:

$$var = mean(1 - mean/N)$$

where $var$ and $mean$ are the variance and mean of the number of vesicular release events, $N$ is the DS number, and $P$ is the release probability per DS. Note that in this formula, the parameter for quantal size $Q$ does not appear since event number is used instead of PSC amplitude.

Malagon et al. (2016) established this method at parallel fiber (PF)-molecular layer interneuron (MLI) synapses in the cerebellum. PFs contact MLIs at single synapses having almost always one AZ (Xu-Friedman et al., 2001). Thus single PF or single granule cell stimulation allows us to obtain responses from a single synapse (Malagon et al., 2016; Miki et al., 2017). When stimulating a PF-MLI synapse with an AP train, delayed release representing desynchronized miniature responses follows synchronized responses (Atluri and Regehr, 1998). By using repetitive trains of stimulations at a PF-MLI synapse, one can obtain from delayed release the average shape of miniature responses as a template of a unitary vesicular release event, as well as synaptic responses during AP trains. For decomposition of recorded EPSCs by the method, obtaining mEPSCs pertaining to the synapse under study is necessary because amplitude and time course of miniature events vary significantly among simple synapses (Auger and Marty, 1997; Crowley et al., 2007). In addition to obtaining miniature responses from asynchronous release such as delayed release, one could obtain miniature responses by lowering release probability that provide one/a few vesicular responses with frequent failures of the responses by stimulation in a

given synapse. Direct recording, spot $Ca^{2+}$ uncaging with appropriate flash intensity, and local application of α-Latrotoxin at a single bouton may also be able to provide miniature responses in a simple synapse (Auger and Marty, 1997; Trigo et al., 2012; Kawaguchi and Sakaba, 2017). After averaging mEPSCs, we fitted the average with a triple-exponential curve. Using the triple-exponential curve as a template, we applied deconvolution to the trace and the mEPSC average, thereby producing the deconvolved trace containing a series of spikes and the deconvolved mEPSC being a single 'spike' (**Figure 1A**). Fitting the deconvolved trace with vertically scaled spikes allowed us to detect vesicular release events in the trace. Decomposition of postsynaptic current into the contributions of individual vesicle events by methods including our method is based on the assumption that each vesicular event is a scaled version of a fixed template having the shape of mEPSCs (Clements and Bekkers, 1997; Andor-Ardó et al., 2012; Pernía-Andrade et al., 2012). After converting synaptic responses to vesicular release events by the decomposition of EPSCs, variance-mean analysis of the events reveals 3–10 DSs at one synapse (Malagon et al., 2016), a value comparable to that obtained by EPSC fluctuation analysis (Schmidt et al., 2013; Ishiyama et al., 2014).

## STOCHASTIC PROPERTIES OF CUMULATIVE RELEASE NUMBER

One key benefit of detecting vesicular release events in synaptic responses is to obtain the cumulative number of events in a train. Statistical analysis of the cumulative release number provides valuable information to evaluate release models. In this chapter, I will review several models derived on the basis of a classical binomial model and discuss the stochastic properties of the cumulative release number. Some models are described in a previous paper (Miki et al., 2016). In these models, DSs have a parameter $\delta$ that is the probability of occupancy by a synaptic vesicle in the resting state. I call $p$ the release probability of a DS that is occupied by a synaptic vesicle. Then the probability of release per DS is $\delta$ multiplied by $p$ ($P = \delta p$). A synapse is subject to trains of 8 action potentials (APs) at 200 Hz in all simulations. For each AP number within a train, variance and mean of the last vesicular release number, as well as variance and mean of the cumulative release number are calculated (**Figure 1**). The last vesicular release number for AP number (**i**) is defined as the number of detected events in response to **i**-th AP in a train (**Figures 1B,C**). The cumulative release number for AP number (**i**) is the total number of detected events in response to 1st-to-**i**-th APs in a train (**i** > 1; **Figure 1D**). The first point for cumulative release number (**i** = 1) is always the same as that for last release number (**Figures 1C,D**). These simulated results are plotted for each model in **Figure 2**; numbers next to individual points indicate AP numbers in red and gray for the last and cumulative release number, respectively. In all models, a DS number $N$ of 4 is assumed except for two-type-of DS model (model (vi) below). Therefore, the plots for the last release number can be fitted with a parabola with $N = 4$ in models (i), (ii), (iv), (v), and (viii).

### (i) One-Step Model

In this very simple model, there are four DSs that cannot be replenished with vesicles once they become empty (**Figure 2A**). In this case, all variance-mean points are located on a parabola with $N = 4$. The last vesicular release number follows a binomial process as expected. Since no replenishment takes place at DSs, the cumulated release number fluctuates with a maximum value of 4 among trains. Hence cumulative release points are also located on the same parabola ($N = 4$). Since some releasable vesicles are consumed for each stimulus number, while their maximal number remains limited to 4, the plot for the last release number goes toward the origin as stimulus number increases (open symbols). By contrast, cumulative release numbers move toward the $N$ value on the $x$ axis (closed symbols).

### (ii) Renewable One-Step Model

In this model, an empty DS is replenished with a rate constant $s$ (**Figure 2B**). The number of release events follows a binomial distribution ($N = 4$) as expected, while the cumulative number plot deviates from the parabola starting at the 2nd point, and becomes linear starting at the 4th point. The slope of the regression line (0.65) is less than 1, meaning that release in later stimuli is not a Poisson process.

### (iii) Parallel Model

In contrast to model (ii), in the parallel model release occurs following a Poisson process at DSs or somewhere else in the AZ, in addition to release at DSs without vesicle replenishment (**Figure 2C**). In this model, the vesicular pool is replenished following a Poisson process with a probability of $f$ per interspike interval, and vesicles in the pool release with a probability of $p2$. In this case, the plot for cumulative number deviates from the parabola, as we see in (ii), but the slope is now close to 1, showing that the release later in the stimulation is a random process described by a Poisson distribution. The plot for the last release number is close to the parabola $N = 4$. However, since release takes place in parallel following a Poisson process, a slight deviation from the parabolic curve occurs.

### (iv) Two-Step Model

This model introduces an additional site, called replacement site, for each DS (**Figure 2D**). Once a DS becomes empty, a vesicle coming from the associated replacement site replenishes the DS with a rate constant $r$. The last release number follows a binomial distribution with $N = 4$, while the variance for the cumulative release number increases at the 2nd point and approaches a second parabola with $N = 8$, corresponding to the sum of the numbers of DSs and replacement sites. Later points follow the second parabola. A fit of 2nd–8th points for cumulative release number with a parabolic curve shows a maximum mean value of 7.89, close to 8. Therefore, the total number of sites can be obtained from variance-mean plots of the cumulative release number, in addition to the number of DSs from those of the last release number.

### (v) Renewable Two-Step Model

This model is similar to the previous model (iv), except that a recruitment step is added to refill the replacement site

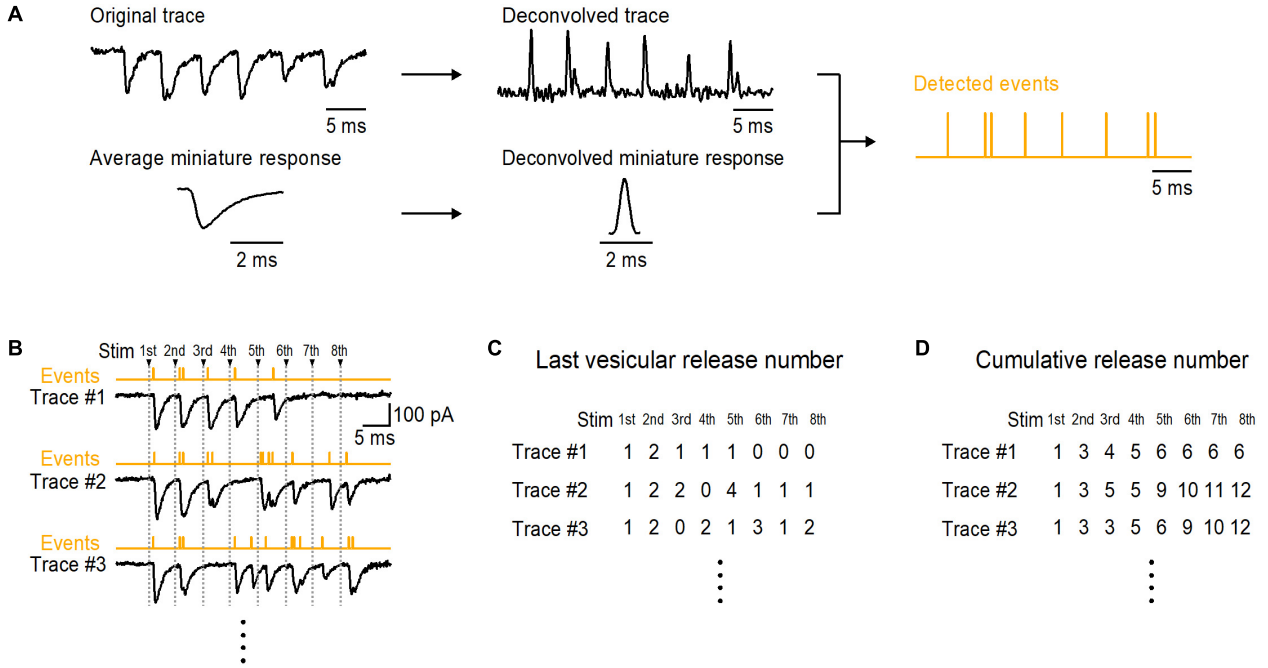


**FIGURE 1 |** Last and cumulative number of detected vesicular release events in a train at a simple synapse. **(A)** A brief flowchart shows a process to detect vesicular release events by decomposition of postsynaptic currents at a simple synapse. An original trace and miniature responses are obtained in a same experiment. The trace and average miniature response are deconvolved by a multi-exponential curve that is fitted to the average miniature response, producing a deconvolved trace and a deconvolved miniature response (spike). After fitting the deconvolved trace with appropriately time-positioned and vertically scaled spike, a series of events are detected. In detected events, vertical lines show time positions of the individual events. **(B)** Examples of traces in response to 8 APs at 200 Hz at a single PF-MLI synapse. Decomposition of EPSCs provides event detection (see Figures 1, 3 in Malagon et al., 2016). Counted numbers of vesicular events in response to each stimulus in each train are shown in **(C)**; these numbers are called 'last vesicular release number' in this report. The cumulative numbers of events for each stimulus are shown in **(D)**.

(**Figure 2E**). The plot for cumulative release number comes close to the second parabola $N = 8$ at 2nd and 3rd points as in (iv), however, according to this recruitment step it deviates later from the parabola. At the end of the train the plot becomes linear with a slope of 0.45, <1, meaning that release in later stimuli is not a Poisson process as shown in the scheme for the model. Last release numbers follow a binomial process. Because the statistical features of cumulative release were similar for glutamatergic and GABAergic synapses on MLIs (Miki et al., 2016), this renewable two-step model was proposed as a potential generally valid release model. For glutamatergic synapses on MLIs, the two-step model indicated that low $\delta$ (= 0.3–0.45) and large $r$ (= 0.6) produced initial facilitation followed by depression without change of $p$ (= 0.7; Miki et al., 2016). Actin- and myosin-disrupting drugs abolished the initial facilitation, suggesting actin- and myosin-dependent vesicle recruitment to DS. For GABAergic synapses on MLIs, small $r$ (= 0.15) produced depression. Interestingly, after prolonged presynaptic depolarization, synaptic responses showed an unusual form of depression/facilitation sequence that could be accounted for by the two-step model with low occupancy of replacement site ($\rho$ = 0.2; Pulido and Marty, 2018). Furthermore, this model can predict a large variety of time-dependent changes of synaptic strength by various combinations of parameter values (Doussau et al., 2017; Pulido and Marty, 2018) and can reproduce the kinetics of release (Miki et al., 2018).

## (vi) Two-Type-of DS Model

A different model also shows similar statistical properties of the cumulative release number. In this model derived from previous reports (e.g., Wu and Borst, 1999; Neher, 2006; Hallermann et al., 2010), two types of independent sites release vesicles with different probabilities (**Figure 2F**). One is characterized by high release probability without replenishment. The other is replenished from an infinite pool and has a low release probability that is initially 0 and becomes 0.4 starting with the 2nd stimulus. In this case, the cumulative release number plot jumps at the 2nd point to reach the second parabola, and then bends along this parabola. Then the plot gradually departs from the parabola and approaches a linear relation with a slope of 0.47, similar to (v). The last release plot for this model is rather remarkable (see red open circles). Initially second type DSs have a release probability of 0, thus the 1st point of the last release number plot is located on a parabola $N = 4$, whereas the 2nd–8th points are located near a parabola $N = 8$ due to the increase in release probability of second type sites to 0.4. The model is a simplified version compared with the model previously reported. In fact, instead of sudden increase in the release probability from the first to the second stimulus at the second type of sites and no vesicle

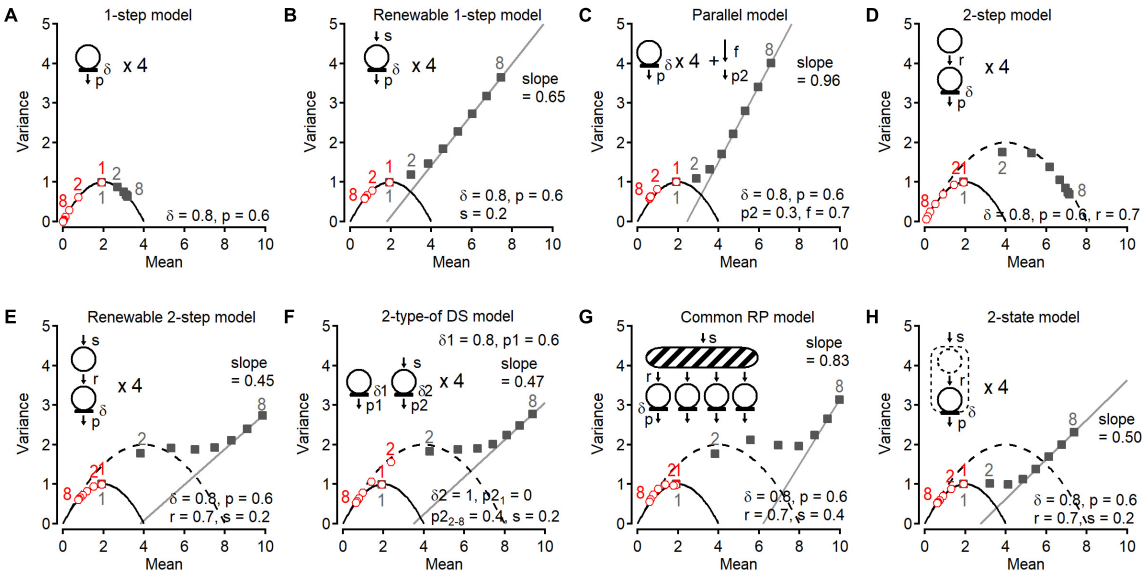


**FIGURE 2 |** Variance-Mean plots of last release number and cumulative release number in various models. A series of Monte Carlo simulations of variance-mean plots of last release number (red, open circles) and cumulative release number (gray, filled squares) (Miki et al., 2016). Synapses are subjected to trains of 8 APs at 200 Hz. In all panels, a parabola having $N$ of 4 is shown. In **(D–H)**, a parabolic curve having $N$ of 8 is also shown. In **(B,C,E–H)**, last two or three points for cumulative number were fitted with a line. Corresponding stimulus numbers for the plots of the last release number (red, open symbols) and of the cumulative release number (gray, closed symbols) are shown. **(A)** Simple 1-step model. There are four independent DSs that are occupied by synaptic vesicles with an initial occupancy $\delta = 0.8$ before the 1st stimulus. Docked vesicles have a release probability $p = 0.6$ per DS, for each stimulus. Once docked vesicles are released, no DS replenishment occurs. **(B)** In the renewable 1-step model, a replenishment step is added to the 1-step model in **(A)**. Emptied DSs are replenished from an infinite vesicle pool with a transition probability $s = 0.2$. **(C)** In the parallel model, in addition to the release from four DSs, release occurs as a Poisson process. **(D)** 2-step model. There are four replacement sites paired to four DSs. Once a DS becomes empty, a vesicle is supplied from the paired replacement site with a transition probability $r = 0.7$. There is no recruitment mechanism once a replacement site is depleted. **(E)** In the renewable 2-step model, a replenishment step with rate constant $s$ is added to the 2-step model. **(F)** In this model (one-step model + renewable one-step model), there are four 1-step DSs and four renewable 1-step DSs. Parameters in the one-step model are the same as those in **(A)**. **(G)** In another type of DSs, no release occurs upon the 1st stimulus ($p2_1 = 0$) but release occurs with a probability $p2_{2\text{-}8} = 0.4$ from the 2nd stimulus. **(H)** 2-state model. There are two states of vesicle docking at DSs. In contrast to replacement sites, vesicles cannot occupy both states at the same time.

replenishment to the first type of sites in the simplified model, the reported model assumed a gradual facilitation of the release probability of both type of sites and slow vesicle replenishment from the second to the first sites, reproducing large sets of data (e.g., Pan and Zucker, 2009; Ritzau-Jost et al., 2018). In general, however, parallel models do not provide separate parabolas for last release number and cumulative release number.

## (vii) Common RP Model

In the two-step or the renewable two-step model, a replacement site is associated to each DS. In the present model, a common replacement pool replaces individual replacement sites. Initially four vesicles in the pool are ready to replenish any empty DS (**Figure 2G**). This pool is replenished up to the permissible number of four with rate constant $s$. As in previous models, the cumulative release number plot jumps from a parabola $N = 4$ to reach a larger parabola representing replacement pool size plus DS number. The slope of the final linear fit is larger than that in the renewable two-step model and in the two-type of DS model. Hence vesicle replenishment through a common replacement pool at DS makes late release resemble a Poisson process. Finally, the last release number plot slightly deviates from the $N = 4$ parabola.

## (viii) Two-State Model

The last attractive model is a two-state model where a DS can accommodate one bound vesicle in two different states (loosely docked state and tightly docked state). This model was proposed based on the evidence that the docked/primed synaptic vesicle state is very dynamic (Neher and Brose, 2018; **Figure 2H**). In contrast to the two-step model, the two states cannot be simultaneously occupied by vesicles in this model: the second state is replenished from an infinite pool only if no vesicle is present on the site. In this model, the cumulative release number plot does not jump to a larger $N$ parabola. Rather, it gradually departs from the parabola with $N = 4$, eventually approaching a linear relation with a slope of 0.50.

The plots for the cumulative number among models (v), (vi), and (vii) are similar in shape. However the slope of the later points in model (vii) is larger than in models (v) and (vi), indicating more random release later in a train. In addition, a discrepancy between model (v) and (vi) appears in the plot for the last release number (red circle #2). Likewise, in the case of another proposed model where new release site recruit between stimulations instead of replenishment of vesicles to vacant DS (Valera et al., 2012; Brachtendorf et al., 2015), the second point for the last release number shift to a bigger parabola than

that for the first point. The increase in $N$ arises from the fast recruitment of reluctant synaptic vesicles into a fully releasable pool by high-frequency stimulation (Brachtendorf et al., 2015; Doussau et al., 2017).

As described above, there are similarities and discrepancies among models with certain sets of parameter values. In some sets of values the models are hardly distinguished but in the other sets they are distinguishable, since the shape of the plot for the cumulative number changes with the combination of the parameter values. Therefore, models need to be examined in different experimental conditions possibly changing the parameter values.

Stochastic properties of last and cumulative release number at PF-MLI synapses in cerebellum in 2-week-old rats were best fitted with model (v). Further support for this model was provided by pharmacological experiments (Miki et al., 2016). However it remains to be seen whether other synapses may be better depicted with other models of **Figure 2**.

In summary, when performing variance-mean analysis, the last release number provides information about the number of DSs and the release probability per DS; examination of the variance-mean plot for this number during an AP train provides information on whether release follows a binomial or a Poisson process. Comparing the statistical properties of the cumulative release number among various models, some features concerning replenishment steps are extracted. In certain models, the variance-mean plot displays a jump between the 1st and the 2nd point, implying the existence of an associated site (replacement site) or of an additional vesicle pool replenishing DSs for consecutive release. By contrast, a continuous increase in variance is displayed in other simpler models, like the renewable one-step model and the parallel model (**Figures 2B,C**). The slope of the fitted line for later points also gives indications concerning the docking/release model. A slope of 1 indicates that late release obeys a Poisson process, while a slope $< 1$ implies some kinetically limiting steps before DSs. If the cumulative release number plot forms a nearly complete parabola, this indicates little or no replenishment at the DSs. The parabola fit then provides a good estimate of the total number of vesicles associated with the AZ, as exemplified by the one-step model and the two-step model (**Figures 2A,D**). Even if there is a replenishment step with some rate constant, depending on the rate, the bended part of the cumulative release number plot may provide a rough estimate of the initial vesicle pool size in the model.

How reliably can we estimate the total number of releasable/suppliable vesicles using variance-mean plots for cumulative release? Further simulations related to the two-step model are shown in **Figure 3** to address this question. In **Figure 3A**, the occupancy $\delta$ of DSs is variable and the other parameters are fixed, including the release probability $p$, the rate constant for the recruitment step $r$, and the occupancy of replacement sites $\rho$ ($p = 0.6$, $r = 0.7$, and $\rho = 1$). If $\delta = 0$, all points are on the $N = 4$ parabola, corresponding to the exact total number of releasable/suppliable vesicles in DSs and replacement sites. If $\delta = 1$, as shown in **Figure 2D**, the 1st point is located on the $N = 4$ parabola since release occurs only at four DSs, whereas starting at the 2nd point the plot leaves the $N = 4$ parabola and

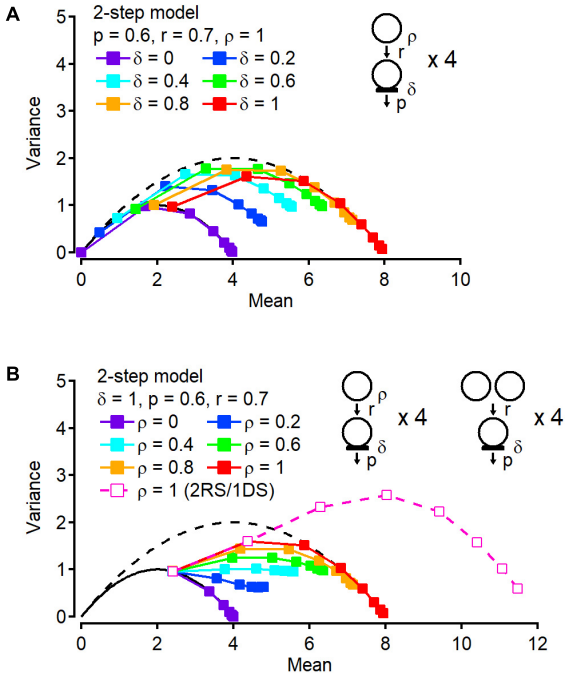


**FIGURE 3 |** Occupancy at docking and replacement sites affects stochastic properties of cumulative release number. **(A)** Variance-mean plots of cumulative release number with variable occupancy $\delta$ at DSs. Occupancy $\rho$ at replacement site is fixed to 1. **(B)** Instead of changing $\delta$, occupancy $\rho$ is changed (filled squares). A variance-mean plot from the model in which there are two replacement sites (RSs) paired to one DS is also shown (open squares).

approaches another parabola with $N = 8$, again corresponding to the total number of releasable/suppliable vesicles. Between $\delta = 0$ and 1, even though the total site number is always 8, the cumulative release plot provides different parabolas with different maximum numbers ($N = 5.52$, 6.72, 7.49, and 7.88 for $\delta = 0.2$, 0.4, 0.6, and 0.8, respectively). Hence not only the site number but also the occupancy of DSs affects the size of the parabola fitting the cumulative release number plot. And the value obtained from the parabola is closer to the total average number of releasable/suppliable vesicles ($= N\delta + N\rho$) than to the total number of available sites ($= 2N$). Likewise, changes of the occupancy at the replacement site instead of at the DS, affects the cumulative parabola (**Figure 3B**). In **Figure 3B**, only $r$ is changed and the other parameters are fixed ($p = 0.6$, $r = 0.7$, and $\delta = 1$). If $\rho = 0$ or 1, the cumulative number plots depict a parabola with $N = 4$ or 8, respectively. If $0 < \rho < 1$, extrapolated maximum values from a parabola fit are 5.30, 6.43, 7.25, and 7.75 for $\rho = 0.2$, 0.4, 0.6, and 0.8, respectively. As above, these numbers are closer to the total average number of releasable/suppliable vesicles ($= N\delta + N\rho$) than to the total number of available sites ($= 2N$). Finally, doubling the number of replenishment sites/vesicles per DS increases the maximum value of the parabola fit proportionally to the number of additional sites/vesicles (**Figure 3B**, open symbols). Taken together, a parabolic fit of the cumulative number plot provides us with

a rough estimate of the total number of releasable/suppliable vesicles, even though the value that is obtained is a slight over estimation in the cases $0 < \delta < 1$ and $0 < \rho < 1$.

## CONCLUDING REMARKS

Recently methods have been developed to count the number of released vesicles at single synapses using deconvolution analysis (Malagon et al., 2016). Reliable detection of vesicular events from synaptic responses allows us to estimate not only the number of DSs as in the conventional fluctuation analysis but also the total number of releasable/suppliable vesicles, and to understand features of the vesicle recruitment/release process by analysis of stochastic properties of cumulative release number. Comparing statistical properties of vesicular event number from data and models allows us to predict a possible DS model for a given synapse. Determining a release model and parameter values for synapses by the methods is crucial for understanding the limiting factor for the synaptic properties, such as short-term plasticity. Applying these analyses to various types of synapses has the potential to provide a comprehensive understanding of release models among synapses. Furthermore, the method of detecting individual vesicular release events, like the previously developed deconvolution analysis (Neher and Sakaba, 2001), also provides timing of the events (Miki et al., 2018). Models can predict speed and time course of vesicle replenishment to DSs, maturation of release machinery on DSs, pool size of synaptic vesicles, and DS number. Those could be investigated by recently developed techniques using super resolution microscopy and electron microscopy. It has been shown that the number of DSs correlates with the number of clusters of AZ proteins such as RIM, Munc13, and $Ca^{2+}$ channels (Tang et al., 2016; Miki et al., 2017; Sakamoto et al., 2018). Thus investigation of these AZ proteins may tell us localization, movement and regulation of DSs. In addition, nano-meter scale movements of synaptic vesicles have been observed after stimulation near the presynaptic membrane, indicating the speed and time course of vesicle recruitment (Midorikawa and Sakaba, 2015, 2017; Kusick et al., 2018). Those studies combined with the model simulation based on the quantal analysis may allow us to see the relationship between parameter values for predicted models and physical observations of DSs and synaptic vesicles. Future studies integrating multiple approaches will provide physical insight into the dynamics of interaction between release machineries and synaptic vesicles at a DS due to consecutive vesicle fusions during neuronal activity and eventually might lead to a unified model among synapses in CNS.

## DATA AVAILABILITY

The raw data supporting the conclusions of this manuscript will be made available by the authors, without undue reservation, to any qualified researcher.

## AUTHOR CONTRIBUTIONS

The author confirms being the sole contributor of this work and has approved it for publication.

## FUNDING

This work was supported by the Japan Society for the Promotion of Science KAKENHI grant (JP18K06472), the Uehara Memorial Foundation, Takeda Science Foundation, the Naito Foundation, Brain Science Foundation, and JSPS Core-to-core Program A Advanced Research Networks.

## ACKNOWLEDGMENTS

I thank Alain Marty for valuable comments and suggestions on the manuscript.

## REFERENCES

Andor-Ardó, D., Keen, E. C., Hudspeth, A. J., and Magnasco, M. O. (2012). Fast, automated implementation of temporally precise blind deconvolution of multiphasic excitatory postsynaptic currents. *PLoS One* 7:e38198. doi: 10.1371/journal.pone.0038198

Atluri, P. P., and Regehr, W. G. (1998). Delayed release of neurotransmitter from cerebellar granule cells. *J. Neurosci.* 18, 8214–8227. doi: 10.1523/jneurosci.18-20-08214.1998

Auger, C., and Marty, A. (1997). Heterogeneity of functional synaptic parameters among single release sites. *Neuron* 19, 139–150. doi: 10.1016/s0896-6273(00)80354-2

Brachtendorf, S., Eilers, J., and Schmidt, H. (2015). A use-dependent increase in release sites drives facilitation at calretinin-deficient cerebellar parallel-fiber synapses. *Front. Cell. Neurosci.* 9:27. doi: 10.3389/fncel.2015.00027

Chang, S., Trimbuch, T., and Rosenmund, C. (2018). Synaptotagmin-1 drives synchronous $Ca^{2+}$-triggered fusion by $C_2$B-domain-mediated synaptic-vesicle membrane attachment. *Nat. Neurosci.* 21, 33–40. doi: 10.1038/s41593-017-0037-5

Chen, Z., Das, B., Nakamura, Y., DiGregorio, D. A., and Young, S. M. Jr. (2015). $Ca^{2+}$ channel to synaptic vesicle distance accounts for the readily releasable pool kinetics at a functionally mature auditory synapse. *J. Neurosci.* 35, 2083–2100. doi: 10.1523/JNEUROSCI.2753-14.2015

Clements, J. D., and Bekkers, J. M. (1997). Detection of spontaneous synaptic events with an optimally scaled template. *Biophys. J.* 73, 220–229. doi: 10.1016/s0006-3495(97)78062-7

Clements, J. D., and Silver, R. A. (2000). Unveiling synaptic plasticity: a new graphical and analytical approach. *Trends Neurosci.* 23, 105–113. doi: 10.1016/s0166-2236(99)01520-9

Crowley, J. J., Carter, A. G., and Regehr, W. G. (2007). Fast vesicle replenishment and rapid recovery from desensitization at a single synaptic release site. *J. Neurosci.* 27, 5448–5460. doi: 10.1523/jneurosci.1186-07.2007

Del Castillo, J., and Katz, B. (1954). Quantal components of the end-plate potential. *J. Physiol.* 124, 560–573. doi: 10.1113/jphysiol.1954.sp005129

Doussau, F., Schmidt, H., Dorgans, K., Valera, A. M., Poulain, B., and Isope, P. (2017). Frequency-dependent mobilization of heterogeneous pools of synaptic vesicles shapes presynaptic plasticity. *eLife* 6:e28935. doi: 10.7554/eLife.28935

Hallermann, S., Fejtova, A., Schmidt, H., Weyhersmüller, A., Silver, R. A., Gundelfinger, E. D., et al. (2010). Bassoon speeds vesicle reloading at a central excitatory synapse. *Neuron* 68, 710–723. doi: 10.1016/j.neuron.2010.10.026

Imig, C., Min, S.-W., Krinner, S., Arancillo, M., Rosenmund, C., Südhof, T. C., et al. (2014). The morphological and molecular nature of synaptic

vesicle priming at presynaptic active zones. *Neuron* 84, 416–431. doi: 10.1016/j.neuron.2014.10.009

Ishiyama, S., Schmidt, H., Cooper, B. H., Brose, N., and Eilers, J. (2014). Munc13-3 superprimes synaptic vesicles at granule cell-to-basket cell synapses in the mouse cerebellum. *J. Neurosci.* 34, 14687–14696. doi: 10.1523/JNEUROSCI.2060-14.2014

Jackman, S. L., Turecek, J., Belinsky, J. E., and Regehr, W. G. (2016). The calcium sensor synaptotagmin 7 is required for synaptic facilitation. *Nature* 529, 88–91. doi: 10.1038/nature16507

Katz, B. (1969). *The Release of Neural Transmitter Substances*. Liverpool: Liverpool University Press.

Kawaguchi, S. Y., and Sakaba, T. (2017). Fast $Ca^{2+}$ buffer-dependent reliable but plastic transmission at small CNS synapses revealed by direct bouton recording. *Cell Rep.* 21, 3338–3345. doi: 10.1016/j.celrep.2017.11.072

Kusick, G. F., Chin, M., Lippmann, K., Adula, K. P., Davis, M. W., Jorgensen, E. M., et al. (2018). Synaptic vesicles undock and then transiently dock after an action potential. *bioRxiv* doi: 10.1101/509216

Liu, H., Bai, H., Hui, E., Yang, L., Evans, C. S., Wang, Z., et al. (2014). Synaptotagmin 7 functions as a $Ca^{2+}$-sensor for synaptic vesicle replenishment. *eLife* 3:e01524. doi: 10.7554/eLife.01524

Lou, X., Scheuss, V., and Schneggenburger, R. (2005). Allosteric modulation of the presynaptic $Ca^{2+}$ sensor for vesicle fusion. *Nature* 435, 497–501. doi: 10.1038/nature03568

Malagon, G., Miki, T., Llano, I., Neher, E., and Marty, A. (2016). Counting vesicular release events reveals binomial release statistics at single glutamatergic synapses. *J. Neurosci.* 36, 4010–4025. doi: 10.1523/JNEUROSCI.4352-15.2016

Maschi, D., and Klyachko, V. A. (2017). Spatiotemporal regulation of synaptic vesicle fusion sites in central synapses. *Neuron* 94, 65–73. doi: 10.1016/j.neuron.2017.03.006

Midorikawa, M., and Sakaba, T. (2015). Imaging exocytosis of single synaptic vesicles at a fast CNS presynaptic terminal. *Neuron* 88, 492–498. doi: 10.1016/j.neuron.2015.09.047

Midorikawa, M., and Sakaba, T. (2017). Kinetics of releasable synaptic vesicles and their plastic changes at hippocampal mossy fiber synapses. *Neuron* 96, 1033–1040. doi: 10.1016/j.neuron.2017.10.016

Miki, T., Kaufmann, W. A., Malagon, G., Gomez, L., Tabuchi, K., Watanabe, M., et al. (2017). Numbers of presynaptic $Ca^{2+}$ channel clusters match those of functionally defined vesicular docking sites in single central synapses. *Proc. Natl. Acad. Sci. U.S.A.* 114, E5246–E5255. doi: 10.1073/pnas.1704470114

Miki, T., Malagon, G., Pulido, C., Llano, I., Neher, E., and Marty, A. (2016). Actin- and myosin-dependent vesicle loading of presynaptic docking sites prior to exocytosis. *Neuron* 91, 808–823. doi: 10.1016/j.neuron.2016.07.033

Miki, T., Nakamura, Y., Malagon, G., Neher, E., and Marty, A. (2018). Two-component latency distributions indicate two-step vesicular release at simple glutamatergic synapses. *Nat. Commun.* 9:3943. doi: 10.1038/s41467-018-06336-5

Montesinos, M. S., Dong, W., Goff, K., Das, B., Guerrero-Given, D., Schmalzigaug, R., et al. (2015). Presynaptic deletion of GIT proteins results in increased synaptic strength at a mammalian central synapse. *Neuron* 88, 918–925. doi: 10.1016/j.neuron.2015.10.042

Nakamura, Y., Harada, H., Kamasawa, N., Matsui, K., Rothman, J. S., Shigemoto, R., et al. (2015). Nanoscale distribution of presynaptic $Ca^{2+}$ channels and its impact on vesicular release during development. *Neuron* 85, 145–158. doi: 10.1016/j.neuron.2014.11.019

Neher, E. (2006). A comparison between exocytic control mechanisms in adrenal chromaffin cells and a glutamatergic synapse. *Pflügers Arch.* 453, 261–268. doi: 10.1007/s00424-006-0143-9

Neher, E., and Brose, N. (2018). Dynamically primed synaptic vesicle states: key to understand synaptic short-term plasticity. *Neuron* 100, 1283–1291. doi: 10.1016/j.neuron.2018.11.024

Neher, E., and Sakaba, T. (2001). Combining deconvolution and noise analysis for the estimation of transmitter release rates at the calyx of held. *J. Neurosci.* 21, 444–461. doi: 10.1523/jneurosci.21-02-00444.2001

Neher, E., and Sakaba, T. (2008). Multiple roles of calcium ions in the regulation of neurotransmitter release. *Neuron* 59, 861–872. doi: 10.1016/j.neuron.2008.08.019

Pan, B., and Zucker, R. S. (2009). A general model of synaptic transmission and short-term plasticity. *Neuron* 62, 539–554. doi: 10.1016/j.neuron.2009.03.025

Pernía-Andrade, A. J., Goswami, S. P., Stickler, Y., Fröbe, U., Schlögl, A., and Jonas, P. (2012). A deconvolution-based method with high sensitivity and temporal resolution for detection of spontaneous synaptic currents in vitro and in vivo. *Biophys. J.* 103, 1429–1439. doi: 10.1016/j.bpj.2012.08.039

Pulido, C., and Marty, A. (2017). Quantal fluctuations in central mammalian synapses: functional role of vesicular docking sites. *Physiol. Rev.* 97, 1403–1430. doi: 10.1152/physrev.00032.2016

Pulido, C., and Marty, A. (2018). A two-step docking site model predicting different short-term synaptic plasticity patterns. *J. Gen. Physiol.* 150, 1107–1124. doi: 10.1085/jgp.201812072

Ritzau-Jost, A., Jablonski, L., Viotti, J., Lipstein, N., Eilers, J., and Hallermann, S. (2018). Apparent calcium dependence of vesicle recruitment. *J. Physiol.* 596, 4693–4707. doi: 10.1113/JP275911

Rothman, J. S., Kocsis, L., Herzog, E., Nusser, Z., and Silver, R. A. (2016). Physical determinants of vesicle mobility and supply at a central synapse. *eLife* 5:e15133. doi: 10.7554/eLife.15133

Sakaba, T. (2006). Roles of the fast-releasing and the slowly releasing vesicles in synaptic transmission at the calyx of Held. *J. Neurosci.* 26, 5863–5871. doi: 10.1523/jneurosci.0182-06.2006

Sakamoto, H., Ariyoshi, T., Kimpara, N., Sugao, K., Taiko, I., Takikawa, K., et al. (2018). Synaptic weight set by Munc13-1 supramolecular assemblies. *Nat. Neurosci.* 21, 41–49. doi: 10.1038/s41593-017-0041-9

Schmidt, H., Brachtendorf, S., Arendt, O., Hallermann, S., Ishiyama, S., Bornschein, G., et al. (2013). Nanodomain coupling at an excitatory cortical synapse. *Curr. Biol.* 23, 244–249. doi: 10.1016/j.cub.2012.12.007

Siksou, L., Rostaing, P., Lechaire, J.-P., Boudier, T., Ohtsuka, T., Fejtová, A., et al. (2007). Three-dimensinal architecture of presynaptic terminal cytomatrix. *J. Neurosci.* 27, 6868–6877. doi: 10.1523/jneurosci.1773-07.2007

Silver, R. A., Lübke, J., Sakmann, B., and Feldmeyer, D. (2003). High-probability uniquantal transmission at excitatory synapses in barrel cortex. *Science* 302, 1981–1984. doi: 10.1126/science.1087160

Silver, R. A., Momiyama, A., and Cull-candy, S. G. (1998). Locus of frequency-dependent depression identified with multiple-probability fluctuation analysis at rat climbing fibre-Purkinje cell synapses. *J. Physiol.* 510, 881–902. doi: 10.1111/j.1469-7793.1998.881bj.x

Südhof, T. C. (2012). The presynaptic active zone. *Neuron* 75, 11–25. doi: 10.1016/j.neuron.2012.06.012

Tang, A.-H., Chen, H., Li, T. P., Metzbower, S. R., MacGillavry, H. D., and Blanpied, T. A. (2016). A trans-synaptic nanocolumn aligns neurotransmitter release to receptors. *Nature* 536, 210–214. doi: 10.1038/nature19058

Trigo, F. F., Sakaba, T., Ogden, D., and Marty, A. (2012). Readily releasable pool of synaptic vesicles measured at single synaptic contacts. *Proc. Natl. Acad. Sci. U.S.A.* 109, 18138–18143. doi: 10.1073/pnas.1209798109

Valera, A. M., Doussau, F., Poulain, B., Barbour, B., and Isope, P. (2012). Adaptation of granule cell to Purkinje cell synapses to high-frequency transmission. *J. Neurosci.* 32, 3267–3280. doi: 10.1523/JNEUROSCI.3175-11.2012

Wu, L.-G., and Borst, J. G. G. (1999). The reduced release probability of releasable vesicles during recovery from short-term synaptic depression. *Neuron* 23, 821–832. doi: 10.1016/s0896-6273(01)80039-8

Xu-Friedman, M. A., Harris, K. M., and Regehr, W. G. (2001). Three-dimensional comparison of ultrastructural characteristics at depressing and facilitating synapses onto cerebellar Purkinje cells. *J. Neurosci.* 21, 6666–6672. doi: 10.1523/jneurosci.21-17-06666.2001

**Conflict of Interest Statement:** The author declares that the research was conducted in the absence of any commercial or financial relationships that could be construed as a potential conflict of interest.

*Copyright © 2019 Miki. This is an open-access article distributed under the terms of the Creative Commons Attribution License (CC BY). The use, distribution or reproduction in other forums is permitted, provided the original author(s) and the copyright owner(s) are credited and that the original publication in this journal is cited, in accordance with accepted academic practice. No use, distribution or reproduction is permitted which does not comply with these terms.*

frontiers in Cellular Neuroscience

ORIGINAL RESEARCH
published: 10 July 2019
doi: 10.3389/fncel.2019.00317

# Biophysical Properties of Somatic and Axonal Voltage-Gated Sodium Channels in Midbrain Dopaminergic Neurons

*Jun Yang, Yujie Xiao, Liang Li, Quansheng He, Min Li and Yousheng Shu**

*State Key Laboratory of Cognitive Neuroscience and Learning and IDG/McGovern Institute for Brain Research, Beijing Normal University, Beijing, China*

Spiking activities of midbrain dopaminergic neurons are critical for key brain functions including motor control and affective behaviors. Voltage-gated $Na^+$ channels determine neuronal excitability and action potential (AP) generation. Previous studies on dopaminergic neuron excitability mainly focused on $Na^+$ channels at the somatodendritic compartments. Properties of axonal $Na^+$ channels, however, remain largely unknown. Using patch-clamp recording from somatic nucleated patches and isolated axonal blebs from the axon initial segment (AIS) of dopaminergic neurons in mouse midbrain slices, we found that AIS channel density is approximately 4–9 fold higher than that at the soma. Similar voltage dependence of channel activation and inactivation was observed between somatic and axonal channels in both SNc and VTA cells, except that SNc somatic channels inactivate at more hyperpolarized membrane potentials ($V_m$). In both SNc and VTA, axonal channels take longer time to inactivate at a subthreshold depolarization $V_m$ level, but are faster to recover from inactivation than somatic channels. Moreover, we found that immunosignals of Nav1.2 accumulate at the AIS of dopaminergic neurons. In contrast, Nav1.1 and Nav1.6 immunosignals are not detectible. Together, our results reveal a high density of $Na^+$ channels at the AIS and their molecular identity. In general, somatic and axonal channels of both SNc and VTA dopaminergic neurons share similar biophysical properties. The relatively delayed inactivation onset and faster recovery from inactivation of axonal $Na^+$ channels may ensure AP initiation at high frequencies and faithful signal conduction along the axon.

**Keywords: voltage-gated sodium (Nav) channels, action potential, sodium channel subtype, axon, dopaminergic neuron**

OPEN ACCESS

***Edited by:***
*Federico F. Trigo, Université Paris Descartes, France*

***Reviewed by:***
*Mickael Zbili, INSERM U1028 Centre de Recherche en Neurosciences de Lyon, France*
*Haruyuki Kamiya, Hokkaido University, Japan*

****Correspondence:***
*Yousheng Shu*
*yousheng@bnu.edu.cn*

***Specialty section:***
*This article was submitted to Cellular Neurophysiology, a section of the journal Frontiers in Cellular Neuroscience*

***Received:*** *30 April 2019*
***Accepted:*** *27 June 2019*
***Published:*** *10 July 2019*

***Citation:***
*Yang J, Xiao Y, Li L, He Q, Li M and Shu Y (2019) Biophysical Properties of Somatic and Axonal Voltage-Gated Sodium Channels in Midbrain Dopaminergic Neurons. Front. Cell. Neurosci. 13:317. doi: 10.3389/fncel.2019.00317*

## INTRODUCTION

Dopaminergic neurons in the midbrain play critical roles in many key brain functions including motor control, motivation, reward, and cognition (Nieoullon, 2002; Wise, 2004; Fields, 2007; Tobler et al., 2007). Dysfunction of dopaminergic systems will lead to major brain disorders, such as Parkinson's disease, depression, schizophrenia, and addiction (Koob, 1998; Lewis and Lieberman, 2000; Dauer and Przedborski, 2003). There are two distinct groups of dopaminergic neurons located in substantia nigra pars compacta (SNc) and the ventral tegmental area (VTA). SNc neurons

are essential circuit elements for controlling movement and learning new motor skills, while VTA neurons play a central role in emotive and motivational brain functions. In comparison with those in VTA, dopaminergic neurons in SNc are more vulnerable to degeneration in Parkinson's disease.

Although they locate at different midbrain regions, dopaminergic neurons share similar electrophysiological properties. They discharge action potentials (APs) with broad voltage waveform in a pacemaking manner at a low frequency of 1–5 Hz and are able to generate bursts of APs at higher frequencies (10–30 Hz) *in vivo* (Grace et al., 2007; Tsai et al., 2009; Cao et al., 2010) and *in vitro* (Grace and Bunney, 1984; Hounsgaard et al., 1992; Johnson et al., 1992; Neuhoff et al., 2002; Korotkova et al., 2003; Kuwahara et al., 2006; Margolis et al., 2006; Khaliq and Bean, 2010). It has been proposed that tonic firing may determine the background dopamine level, while phasic (burst) firing is responsible for a large amount of dopamine release in response to reward signals (Grace et al., 2007; Tsai et al., 2009; Bermudez and Schultz, 2010). Optogenetic manipulation of the spiking activity in dopaminergic neurons would produce substantial behavior changes (Chaudhury et al., 2013; Tye et al., 2013; Gunaydin et al., 2014). Therefore, it is of interest to know what determines the excitability (i.e., AP generation) of dopaminergic neurons. Previous studies revealed differential mechanisms for pacemaking in these neurons. Spontaneous firing in VTA neurons is determined by a background $Na^+$ current (Khaliq and Bean, 2010), whereas that in SNc neurons is driven by a subthreshold $Ca^{2+}$ current (Chan et al., 2007, 2009). These findings suggest that ionic mechanisms governing AP generation in dopaminergic neurons could be different.

Voltage-gated $Na^+$ channels (Nav) are critical for AP generation in CNS neurons. Biophysical properties of Nav in dopaminergic neurons differ from those of midbrain GABAergic neurons (Seutin and Engel, 2010; Ding et al., 2011). The predominant pore-forming α subunits in the brain are Nav1.1, Nav1.2, and Nav1.6. Subunit Nav1.3 is also expressed but mainly during earlier development (Shah et al., 2001). Different channel subunits may have distinct biophysical properties. For example, Nav1.6 activates at much lower membrane potential ($V_m$) levels than Nav1.2 (Rush et al., 2005). In neocortical pyramidal cells, Nav1.6 accumulates at distal regions of the axon initial segment (AIS) and contributes to AP initiation, whereas Nav1.2 concentrates at peri-somatic regions and promotes AP backpropagation to the soma and dendrites (Hu et al., 2009). Previous findings from single-cell RT-PCR suggest expression of Nav1.1, Nav1.2, and Nav1.6 in substantia nigral dopaminergic neurons (Ding et al., 2011). It remains unknown whether midbrain dopaminergic neurons express these channel subunits at the protein level and whether there is any difference in the biophysical properties between SNc and VTA cells. Since AIS is the AP initiation site, it is of interest to examine whether AIS Nav channels differ from those at the soma.

To address these questions, we performed electrophysiological recording and channel subunit antibody staining experiments. We found that, in general, $Na^+$ channels of dopaminergic neurons share similar biophysical properties in both SNc and VTA. In comparison with those at soma, axonal channels take longer time to inactivate at a depolarizing $V_m$ level but show faster recovery from inactivation. As compared to those at the soma, AIS channels have a much higher density. These features ensure AP initiation at high frequencies at the AIS and faithful conduction. In contrast, properties of somatic channels may help gate AP backpropagation to the somatodendritic compartments. Interestingly, different from previous findings, our immunostaining experiments reveal a high-level expression of Nav1.2 at the AIS of both SNc and VTA dopaminergic neurons, while Nav1.6 and Nav1.1 immunosignals are undetectable.

# RESULTS

## AP Initiation and Propagation in Midbrain Dopaminergic Neurons

In acute midbrain slices from TH-GFP mice maintained at room temperature (24–26°C), we performed whole-cell recordings from the soma and/or the axon of GFP-positive cells. Most of the recorded neurons emitted axons from one of their proximal thick dendrites (**Figure 1A**), known as the axon-bearing dendrite (ABD). Axon recordings were obtained from the blebs formed at AIS, less than 120 μm away from the ABD branching site. In current-clamp mode, 56% of the recorded SNc cells ($n = 10/18$) showed spontaneous firing with an average frequency of 1.5 ± 0.6 Hz, 43% of VTA cells discharged spontaneously ($n = 6/14$) at a frequency of 1.35 ± 1.2 Hz. As shown in **Figure 1B**, the spontaneous APs of a SNc cell could be detected at both the somatic and axonal recording sites ($n = 10$ cells). Hyperpolarizing the $V_m$ by injecting a small constant negative current (−10 to −90 pA) to the soma would prevent spontaneous firing. Delivery of 500-ms positive current pulses to the axon (**Figure 1C**) or the soma (**Figure 1D**) could evoke trains of APs at both recording sites.

Close examination of the AP waveforms revealed that the AIS APs preceded the somatic APs no matter whether they are spontaneous and where the current pulses were applied (**Figure 1E**), indicating that AP initiated first at the axon. Previous studies (McCormick et al., 2007; Hu et al., 2009) indicated that, if APs initiate near the recording site, the $V_m$ will show smooth transition to the AP upstroke because of accumulative activation of voltage-gated $Na^+$ channels; however, if APs initiate at a remote site, the $V_m$ will first depolarize due to AP propagation and then generate a rapid upstroke due to the recruitment of local $Na^+$ channels. Indeed, the first derivative ($dV/dt$) of individual somatic APs showed two components in the AP rising phase, corresponding to the arrival of AIS potential and the generation of somatodendritic (SD) potential, respectively (blue, **Figure 1E**). In sharp contrast, there was no bump at the rising phase of AIS APs (red, **Figure 1E**). These observations agree well with an initiation zone at the AIS (McCormick et al., 2007).

Previous studies in other types of neurons showed that the voltage-gated $Na^+$ channels at the AIS possess higher density (Kole et al., 2008; Hu et al., 2009, 2014; Li et al., 2014) and unique biophysical properties (Hu et al., 2014), which are critical

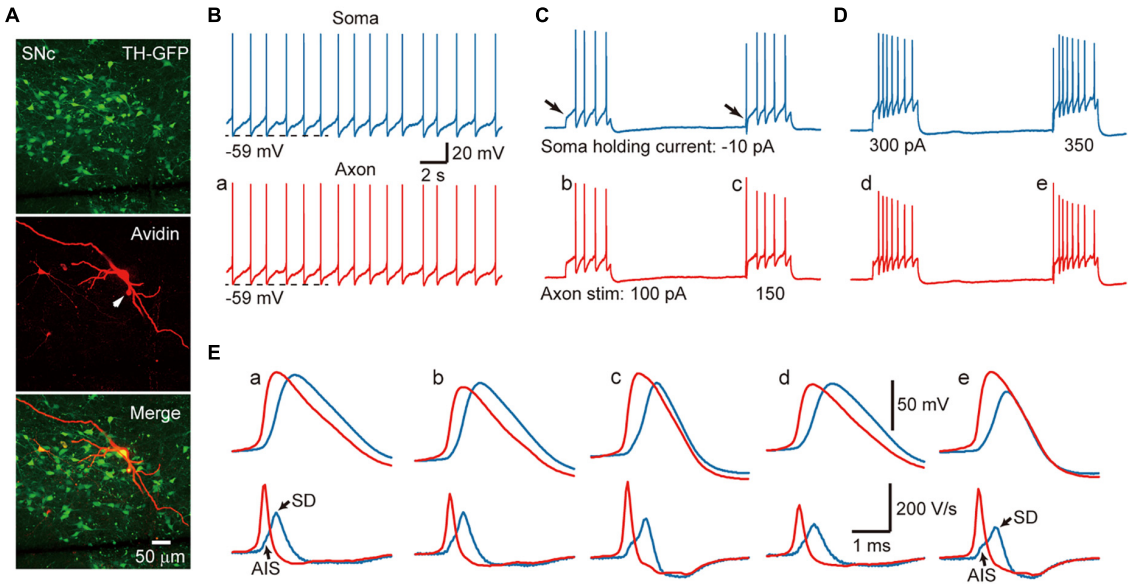


**FIGURE 1 |** Action potentials (APs) are initiated at the AIS of SNc TH-positive neurons. **(A)** An example recorded SNc TH-GFP neuron. **(B)** Dual whole-cell recording from the soma (blue) and the axon (red, 10 μm away from the soma) showing pace making activity at both recording sites. **(C)** Negative DC current injection to the soma prevents spontaneous firing. Positive current pulses (500 ms in duration) at the AIS cause repetitive firing at the axon and the soma. Note the absence and presence of the initial AP (arrows) in response to weak and strong current pulses (100 vs. 150 pA). **(D)** Injection of current pulses to the soma evoke repetitive firing at both recording sites. Also note the absence of presence of the initial AP. **(E)** Top, expansion of the APs indicated in **B–D**. Axonal APs precede the somatic APs in all cases. Bottom, the first derivative (d*V*/dt) of the corresponding APs. The two components at the rising phase of the somatic d*V*/dt trajectory (blue) correspond to the AIS and SD potentials, respectively. Note the difference of the rising phase between somatic and axonal d*V*/dt traces.

for AP initiation at the AIS. We, therefore, sought to investigate differences in the density and the voltage dependence between somatic and axonal $Na^+$ channels.

## Density of Somatic and AIS $Na^+$ Channels

We carried out voltage-clamp recordings from somatic nucleated patches and isolated AIS blebs of GFP-positive neurons in SNc and VTA (**Figure 2A**). Transient inward $Na^+$ currents were evoked by stepping the $V_m$ from a 35-ms prepulse at −120 mV to a series of testing pulses (25 ms in duration) from −70 to +25 mV. The maximal peak amplitudes of the evoked currents in isolated axonal blebs of SNc ($n$ = 22, **Figure 2B**) and VTA cells ($n$ = 22, **Figure 2C**) were 672 ± 70 and 402 ± 70 pA (Mean ± SEM, **Figures 2B–D**), and the calculated conductance densities were 44.9 ± 4.9 and 30.8 ± 5.0 pS/μm$^2$, respectively (**Figure 2E**). In contrast, currents obtained from somatic nucleated patches were much smaller (**Figures 2A–C**). The maximal current amplitudes of SNc ($n$ = 14) and VTA cells ($n$ = 10) were 56.0 ± 4.0 and 86.1 ± 10.7 pA, corresponding to conductance densities of 5.0 ± 0.3 and 6.8 ± 0.9 pS/μm$^2$, respectively (**Figures 2D,E**), which were approximately 9 and 4.5 fold lower than those in SNc ($p = 1.2 \times 10^{-6}$) and VTA AIS ($p = 1.9 \times 10^{-4}$).

Together, these results reveal a high density of $Na^+$ channels at the AIS in both SNc and VTA cells. Interestingly, the channel density in SNc AIS is significantly higher than that of VTA AIS ($p$ = 0.03), whereas the density of somatic channels in SNc is similar to that of VTA ($p$ = 0.15).

## Voltage-Dependent Activation and Deactivation

Examination of the $Na^+$ currents evoked by the activation voltage steps (**Figures 3A,B**) revealed similar voltage dependence between somatic and axonal $Na^+$ channels in both SNc and VTA cells (**Figure 3C**). Currents started to activate around −50 mV and reached complete activation around 0 mV. Fitting the activation curves with Boltzmann equation yielded the half-activation voltages ($V_{1/2}$) and slopes ($k$). The average $V_{1/2}$ for somatic and axonal channels of SNc cells were −25.7 ± 1.2 ($n$ = 8) and −23.0 ± 1.5 mV ($n$ = 14, $p$ = 0.18), respectively; the slopes were 6.4 ± 0.2 and 5.6 ± 0.3 mV ($p$ = 0.14, **Figure 3C**). Similar half-activation voltages were obtained from VTA cells (−27.1 ± 1.5 for soma and −25.7 ± 1.0 mV for axon, $p$ = 0.23); the slopes, however, showed a slight but significant difference (6.6 ± 0.3 vs. 5.4 ± 0.2 mV, $p$ = 0.004; $n$ = 8 for soma and 13 for axon, **Figure 3C**).

To examine the kinetics of channel activation and inactivation, we fitted the rising and the falling phases of transient currents with single exponential functions (**Figures 4A,B**). We observed no significant difference in the rise time between somatic and axonal currents evoked by steps to a range of voltage levels (−25 to +20 mV) in both SNc and VTA cells (SNc: $n$ = 8 nucleated patches and 14 isolated blebs; VTA: $n$ = 8 and 13, respectively, **Figures 4C,D**). However, the decay time constants of axonal

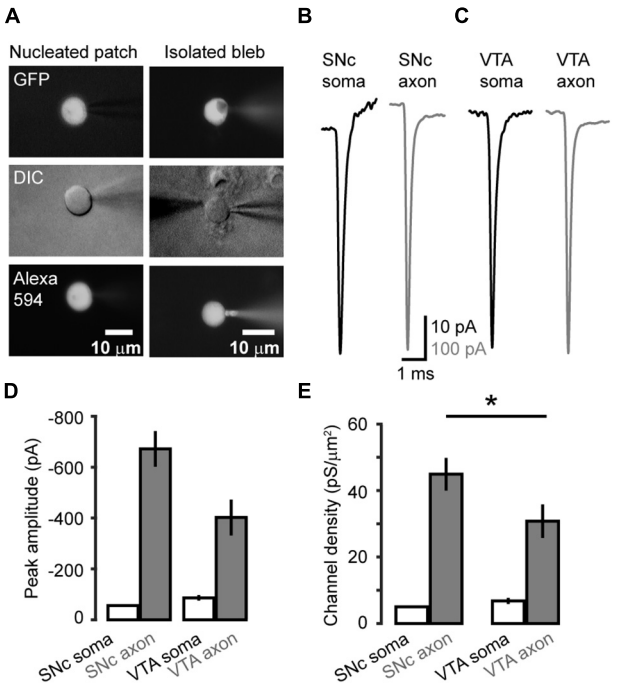


**FIGURE 2 |** $Na^+$ channel density at the soma and the AIS of midbrain TH neurons. **(A)** Fluorescence and DIC images of the recorded somatic nucleated patch and isolated AIS bleb. The recording pipettes contained Alexa Fluo-594, which could label the recorded nucleated patch and axonal bleb. **(B,C)** Example $Na^+$ currents obtained from SNc **(B)** and VTA cells **(C)** by stepping the holding voltage from −120 mV (35 ms) to 0 mV (25 ms). **(D)** Averaged peak amplitudes of $Na^+$ currents. **(E)** Averaged channel density at the soma and the AIS of SNc and VTA cells. $*p < 0.05$, comparison between SNc and VTA axonal channel density.

currents were significantly smaller than those of somatic currents for all the tested voltage levels (**Figures 4C,D**), indicating that axonal channels inactivate faster than somatic ones. These results indicate that, although somatic and axonal $Na^+$ channels share similar voltage dependence, they do differ in some aspects including the channel inactivation kinetics.

We next measured the time constant of channel deactivation. $Na^+$ channels were activated by stepping the $V_m$ from −120 to a 0.2-ms test pulse (0 mV), which was followed by a series of voltage steps (from −100 to −30 mV, **Figures 5A,B**). We fitted the tail currents with single exponential functions to obtain the time constants at different $V_m$ levels (**Figure 5C**) and found that axonal channels deactivate more rapidly than somatic channels. The time constant of axonal channels at −30 mV was significantly shorter than that of somatic channels in SNc cells (0.17 ± 0.02 vs. 0.23 ± 0.01 ms, $n = 5$ nucleated patches and 14 isolated blebs, $p = 0.04$, **Figure 5D**). Similar results were observed in VTA cells (soma: 0.27 ± 0.01 ms, $n = 5$; AIS: 0.17 ± 0.01 ms, $n = 14$, $p = 0.002$, **Figure 5D**).

## Steady-State Inactivation and Recovery

Next, we examined the steady-state inactivation (channel availability) at different $V_m$ levels. Transient $Na^+$ currents were evoked by stepping the $V_m$ from a series of conditioning pulses (from −120 to −20 mV, 35 ms) to the 20-ms test pulse at 0 mV (**Figures 6A,B**). The half-inactivation voltage of SNc somatic channels were −77.5 ± 2.0 mV ($n = 7$), significantly lower than that of axonal channels (−70.4 ± 2.0 mV, $p = 0.03$); no significant difference in the slope was observed (9.0 ± 0.8 mV for soma vs. 10.4 ± 1.2 mV for axon, $p = 0.4$, $n = 8$, **Figures 6A,C,D**). For VTA cells, the $V_{1/2}$ of inactivation and slope of somatic channels were −65.3 ± 3.1 mV and 8.7 ± 0.3 mV ($n = 6$), and those of axonal channels were −64.4 ± 2.5 mV ($p = 0.9$) and 8.4 ± 0.4 mV ($n = 12$, $p = 0.4$, **Figures 6B,D**), respectively. As shown in **Figure 6C**, the half-inactivation voltage of SNc somatic channels was also significantly hyperpolarized than that of VTA somatic ones ($p = 0.01$). These results suggest that, at subthreshold $V_m$ levels (from −80 to −55 mV), somatic channels of SNc cells show much lower availability for AP generation than their axonal channels; in addition, they are also less available than channels at both the soma and the axon of VTA cells.

To investigate the time course of the onset of channel inactivation, we applied a prepulse to −120 mV for 15 ms and then stepped the $V_m$ to −55 mV, followed by a test pulse to 0 mV after a delay ranging from 0 to 38 ms (**Figures 7A,B**). Single exponential fits of the normalized currents yielded time constants of 8.04 ± 0.52 and 6.40 ± 0.41 ms for SNc ($n = 8$ cells) and VTA somatic channels ($n = 7$ cells), respectively, significantly faster than those of axonal channels (SNc: 11.7 ± 1.2 ms, $n = 11$, $p = 0.02$; VTA: 10.6 ± 0.8 ms, $n = 15$, $p = 4.0 \times 10^{-4}$, **Figures 7C–E**).

We then examined the time course of recovery from channel inactivation. After the prepulse (−120 mV), paired pulses with different intervals (from 1 to 110 ms at −120 mV) were applied to the patches (**Figure 8**). Single exponential fits revealed a tendency of axonal Nav channels to be faster to recover from inactivation than somatic channels (soma: 1.2 ± 0.1 ms, $n = 10$, vs. axon: 0.9 ± 0.1 ms, $n = 14$, $p = 0.11$, **Figures 8A,C**). Similarly, somatic channels of VTA cells showed a slower recovery from inactivation than axonal channels (soma: 2.2 ± 0.2 ms vs. axon: 0.9 ± 0.1 ms, $n = 10$ nucleated patches and 19 isolated blebs, $p = 1.0 \times 10^{-5}$, **Figures 8B,D,E**) as well as SNc somatic channels (**Figure 8E**). These results suggest that axonal channels recover from inactivation faster than somatic channels, ensuring high-frequency AP generation and conduction.

## Molecular Identity of Axonal $Na^+$ Channels

We performed triple immunostaining using antibodies of TH, Ankyrin G (AnkG), and different $Na^+$ channel α subunits, including Nav1.2, Nav1.1, and Nav1.6. TH and AnkG were used to identify the dopaminergic neurites and AIS, respectively. We performed Nav1.2 antibody staining in the neocortex as a positive control (Hu et al., 2009; Li et al., 2014; **Figure 9A**). In both SNc and VTA (**Figures 9B,C**), most of the neurites positive to TH and AnkG were also positive to Nav1.2. Immunosignals of Nav1.2 were found in 93.9% and 96.4% of the neurites positive to both TH and AnkG ($n = 46$ in SNc and 54 in VTA from 6 mice, **Figure 9D**). However, none of the TH/AnkG-positive

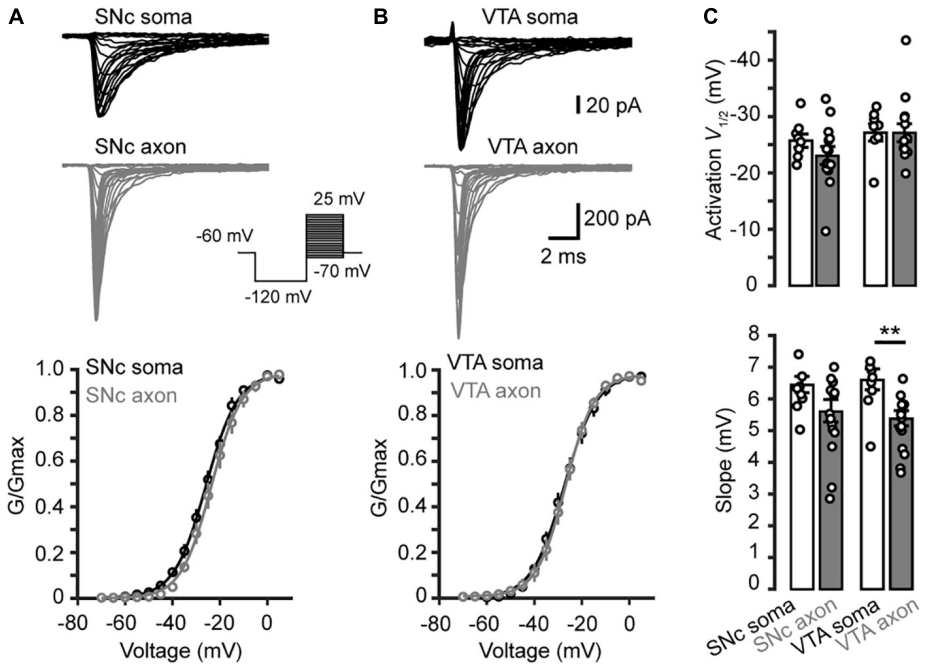


**FIGURE 3 |** Activation of transient $Na^+$ currents in somatic nucleated patches and isolated AIS blebs. **(A)** Top, $Na^+$ currents evoked by activation voltage commands (inset) in a somatic nucleated patch and an isolated axonal bleb in SNc. Bottom, activation curves from somatic and axonal $Na^+$ currents of SNc cells. The plots are fitted with Boltzmann functions. **(B)** Similar as in **A** but from VTA cells. **(C)** Group data showing the half-activation voltage ($V_{1/2}$) and the slope of $Na^+$ channel activation curves. $^{**}p < 0.01$.

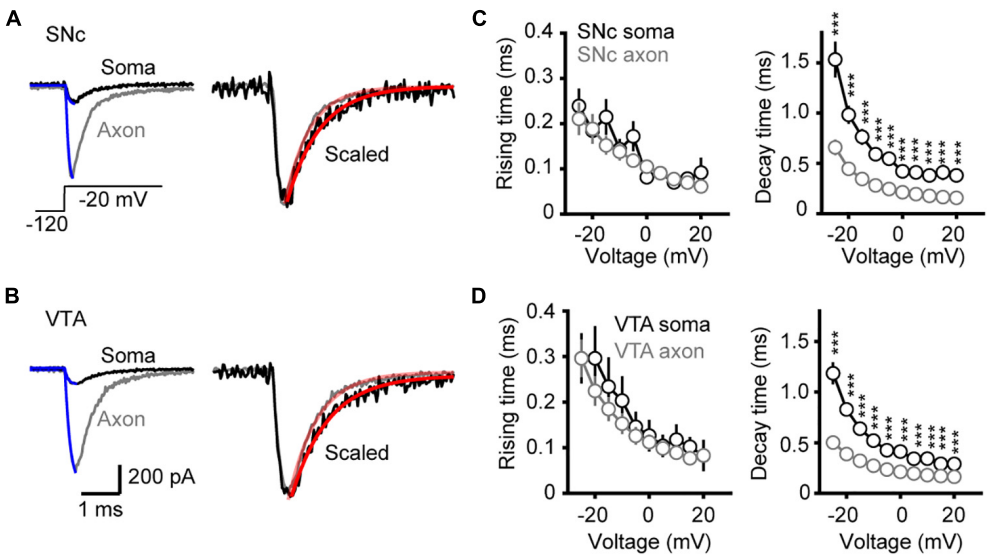


**FIGURE 4 |** Kinetics of activation and inactivation of $Na^+$ currents. **(A,B)** Example $Na^+$ currents of SNc **(A)** and VTA cells **(B)** evoked by stepping the voltage from a 35-ms prepulse of –120 to a test pulse of –20 mV. The rising phase of the currents was fitted by an exponential function with a delayed onset. The decay phase was fitted with a single exponential function. **(C,D)** Comparison of the rise and decay time between somatic and axonal $Na^+$ currents. $^{***}p < 0.001$.

neurites in both SNc and VTA showed Nav1.1 signals ($n$ = 50 from 3 mice, **Figures 10A–C**), although positive signals were found in the neocortex (**Figure 10A**) and in some of the neurites positive to AnkG but negative to TH (**Figures 10B,C**). These results indicate that the AIS of dopaminergic neurons express the α subunits Nav1.2 but not Nav1.1. Similar to that in the neocortex (Li et al., 2014) the AIS of TH-negative GABAergic neurons within SNc and VTA may express the subtype Nav1.1. Surprisingly, the most abundant α subunit Nav1.6 in the brain was not found in the AIS of TH-positive neurons ($n$ = 50

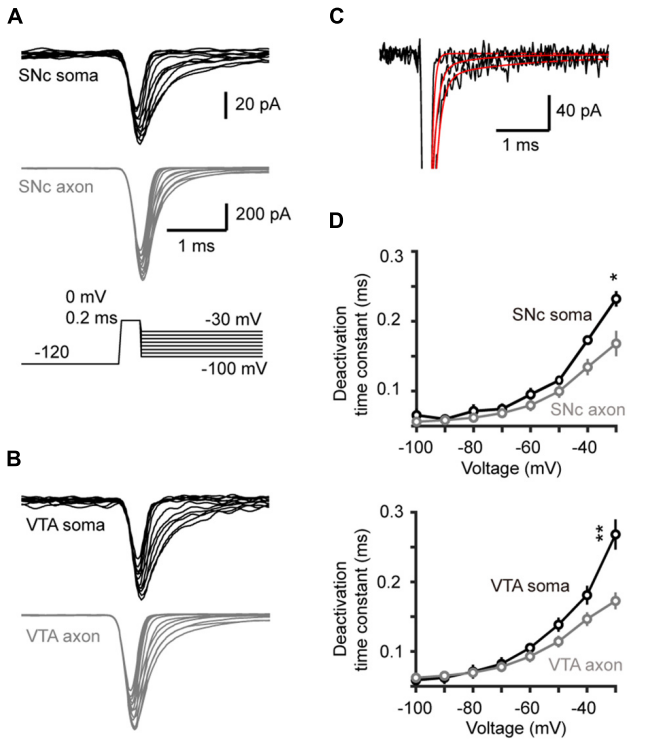


**FIGURE 5 |** Time course of $Na^+$ channel deactivation in TH neurons. **(A,B)** Families of $Na^+$ currents in SNc **(A)** and VTA cells **(B)** evoked by the channel deactivation voltage protocol (inset). Immediately after the test pulse (from a 30-ms –120 mV prepulse to 0 mV, 0.2 ms), the Vm was held at different levels (from –100 to –30 mV with increment of 10 mV). **(C)** Fitting the decay of the currents with single exponential functions. **(D)** The deactivation time constants at different voltage levels in SNc (top) and VTA cells (bottom). $^*p < 0.05$; $^{**}p < 0.01$.

from 3 mice, **Figures 10D–F**). Similar to the pattern of Nav1.1, Nav1.6 signals were found in TH-negative but AnkG-positive neurites, suggesting an expression of this channel subtype in other types of neurons in the midbrain. We found no detectible signals at the soma using channel antibodies, possibly due to the low abundance of channels. The molecular identity of somatic channels remains to be further examined. Together, these results indicate that Nav1.2 is the predominant α subunit in the AIS of midbrain dopaminergic neurons.

## DISCUSSION

In this study, we reveal a high density of voltage-gated $Na^+$ channels at the AIS of putative midbrain dopaminergic neurons, which may determine the AIS as the AP initiation zone. Although the activation of voltage-gated $Na^+$ channels at the soma and the AIS in midbrain dopaminergic neurons share similar voltage dependence, channel inactivation differs in many aspects. First, the inactivation of transient $Na^+$ currents at the axon is much faster than that of somatic channels. Second, at a subthreshold depolarizing $V_m$ level, inactivation onset of axonal channels is more delayed than that of somatic channels. Finally, axonal channels show faster recovery from inactivation. These inactivation properties allow higher channel availability, faster kinetics, and more rapid recovery from inactivation, to ensure the generation of APs at higher frequencies and depolarized $V_m$ levels. Interestingly, our immunostaining experiments indicate that Nav1.2 is the predominant channel subtype at the AIS that governs AP initiation.

### AP Initiation and Channel Density at the AIS

Similar to other types of neurons in the brain including neocortical pyramidal cells (Stuart et al., 1997; Chan et al., 2009) and cerebellar Purkinje cells (Clark et al., 2005), the AP initiation site of midbrain dopaminergic neurons locates at the AIS. Our dual whole-cell recordings at the soma and the AIS in both SNc and VTA neurons indicate that AIS APs always precede the somatic APs no matter whether the APs are generated spontaneously or evoked by current pulses (**Figure 1**). The phase plots of somatic APs have two components during the upstrokes, corresponding to the AIS potential and SD potential, respectively. However, the upstrokes of AIS APs show smooth initial depolarization and absence of the double components (McCormick et al., 2007), indicating that APs are initiated at the AIS. In agreement with this, simultaneous recordings from the soma and dendrites of dopaminergic neuron show that APs in ABD occur earlier than those at the soma and non-ABD, suggesting that APs originate at the axon (Hausser et al., 1995; Gentet and Williams, 2007).

Previous studies suggest roles of specific channel subtypes and high channel density in determining the AP initiation site (Stuart et al., 1997; Li et al., 2014). The $Na^+$ channel density at the AIS is about ∼34 fold higher than that at the soma in neocortical pyramidal cells (Hu et al., 2009). The AIS channel density is also higher in neocortical (∼60 fold) (Hu et al., 2009) and hippocampal parvalbumin-expressing neurons (Hu et al., 2009) ensuring fast signal conduction along the axon. In comparison with these types of cells, dopaminergic neurons express relatively less $Na^+$ channels at their AIS, the channel density is only 4–9 fold that of somatic ones. Distinct from our estimation of channel density at the soma, previous studies revealed a higher density in rat midbrain cells (Seutin and Engel, 2010; Moubarak et al., 2019). The discrepancy could be attributable to the identification of putative dopaminergic neuron, recording configuration, and animal species. Since dopaminergic neurons are spontaneously active, changes in mean frequency of their tonic firing may control and regulate the background dopamine level in the target brain regions (Sulzer et al., 2016), leading to relatively slow neuromodulation and alteration of brain states. Therefore, precision of individual APs could be not essential for dopaminergic neuron signaling. Activation of AIS channels not only initiates APs but also provides currents to charge the somatodendritic membrane and determine whether or not an AP can successfully backpropagate to the soma and dendrites. Considering that AP backpropagation play critical roles in mediating somatodendritic dopamine release (Geffen et al., 1976; Rice and Patel, 2015) and is subject to modulation by D2

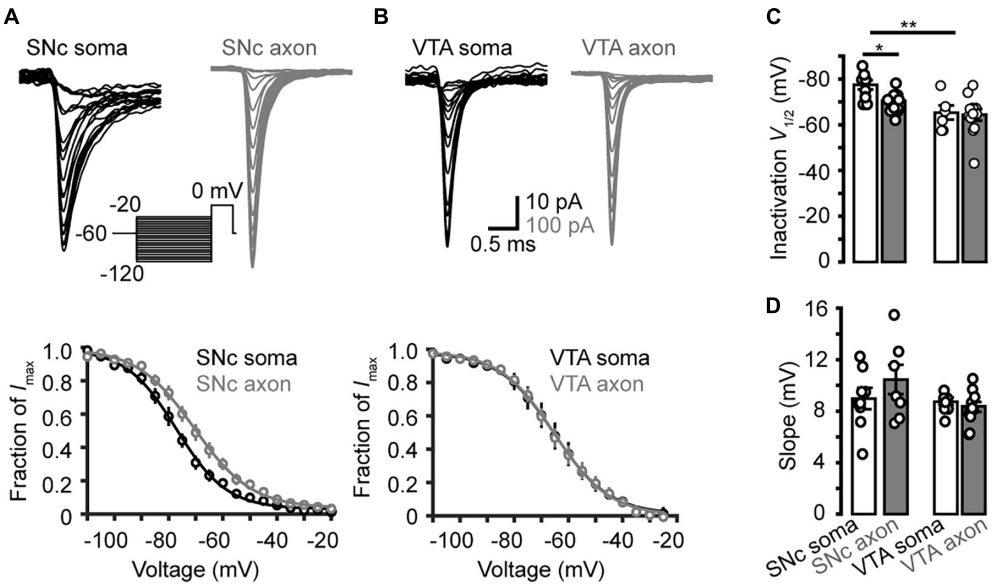


**FIGURE 6 |** Steady-state inactivation of transient $Na^+$ currents in midbrain TH neurons. **(A)** Example families of $Na^+$ currents (top) evoked by the voltage commands (inset) for steady-state channel inactivation in a SNc somatic nucleated patch and an isolated AIS bleb. Bottom, inactivation curves of SNc $Na^+$ currents ($n$ = 7 somatic nucleated patches and 7 isolated AIS blebs). **(B)** Similar as in A but from VTA cells. **(C,D)** Group data comparing the half-inactivation voltages and the inactivation curve slopes. *$p < 0.05$; **$p < 0.01$.

receptors (Cragg and Greenfield, 1997; Gentet and Williams, 2007), we speculate that the lower channel density at the AIS of dopaminergic neurons, as compared with that of pyramidal cells, may ensure a higher sensitivity of AP backpropagation to modulation by dopamine and other neuromodulators.

## Voltage Dependence of Channel Activation and Inactivation

We found surprisingly that somatic and AIS $Na^+$ channels share similar voltage dependence of channel activation in both SNc and VTA cells (**Figure 3**). The half-activation voltage shows no significant difference (ranging from −23 to −27 mV). Activation curves of somatic and axonal channels differ slightly in their slopes; small but significant difference was only found in VTA cells (soma: 6.6 mV vs. AIS: 5.4 mV). In addition, activation kinetics of somatic channels are similar to those of AIS channels, as reflected by their similar rising time (**Figure 4**). The voltage dependence of channel inactivation, however, is more complicated. In the experiments examining the steady-state channel inactivation (availability), we found that SNc somatic channels have the most hyperpolarized half-inactivation voltage than AIS channels in SNc and both somatic and AIS channels in VTA, indicating that at similar $V_m$ levels SNc soma has the lowest channel availability (**Figure 6**). Different from SNc, VTA somatic channels share similar voltage dependence with AIS channels. In general, AIS channels of both SNc and VTA cells show slower onset of inactivation and faster recovery from inactivation as compared with somatic channels (**Figures 7**, **8**).

The difference in the inactivation curves may reflect differences in channel subunits or modulation of channel proteins. Since the expression level of $Na^+$ channels at the soma is extremely low and the antibody staining is not sensitive enough, the molecular identity of somatic channels remains unclear. However, our immunostaining results (**Figures 9**, **10**) together with findings from previous *in situ* hybridization experiments (Gonzalez-Cabrera et al., 2017) indicate that Nav1.2 subunits preferentially express in dopaminergic neurons. In contrast, Nav1.1 and Nav1.6 may only express in other types of neurons, possibly GABAergic inhibitory neurons. Therefore, it is unlikely that the channel subunit difference is attributable to the difference in the inactivation curves of SNc somatic and axonal channels. In comparison to Nav1.6 channels that are refractory to modulation by PKA or PKC (Maurice et al., 2001; Chen et al., 2009), Nav1.2 channels are much more vulnerable to modulation by neuromodulators and protein kinases (Maurice et al., 2001). PKC causes phosphorylation of serine 1506 at the inactivation gate (West et al., 1991) while PKA induces phosphorylation in the I–II loop but not the III–IV loop that is responsible for channel inactivation (Cantrell and Catterall, 2001). Phosphorylation of Nav1.2 induced by PKA and PKC would increase the slow channel inactivation (Carr et al., 2003; Chen et al., 2006, 2008). Therefore, we speculate that the differences in channel inactivation curves as well as those of inactivation and deactivation time courses could be due to differential phosphorylation of somatic and axonal channels. However, it remains unknown what determines the phosphorylation level and whether somatodendritic release of dopamine plays a role in the differential regulation.

Previous studies in neocortical pyramidal cells and inhibitory interneurons reveal distinct voltage-dependent properties of $Na^+$ channels in the soma and the axon (Hu et al., 2009, 2014;

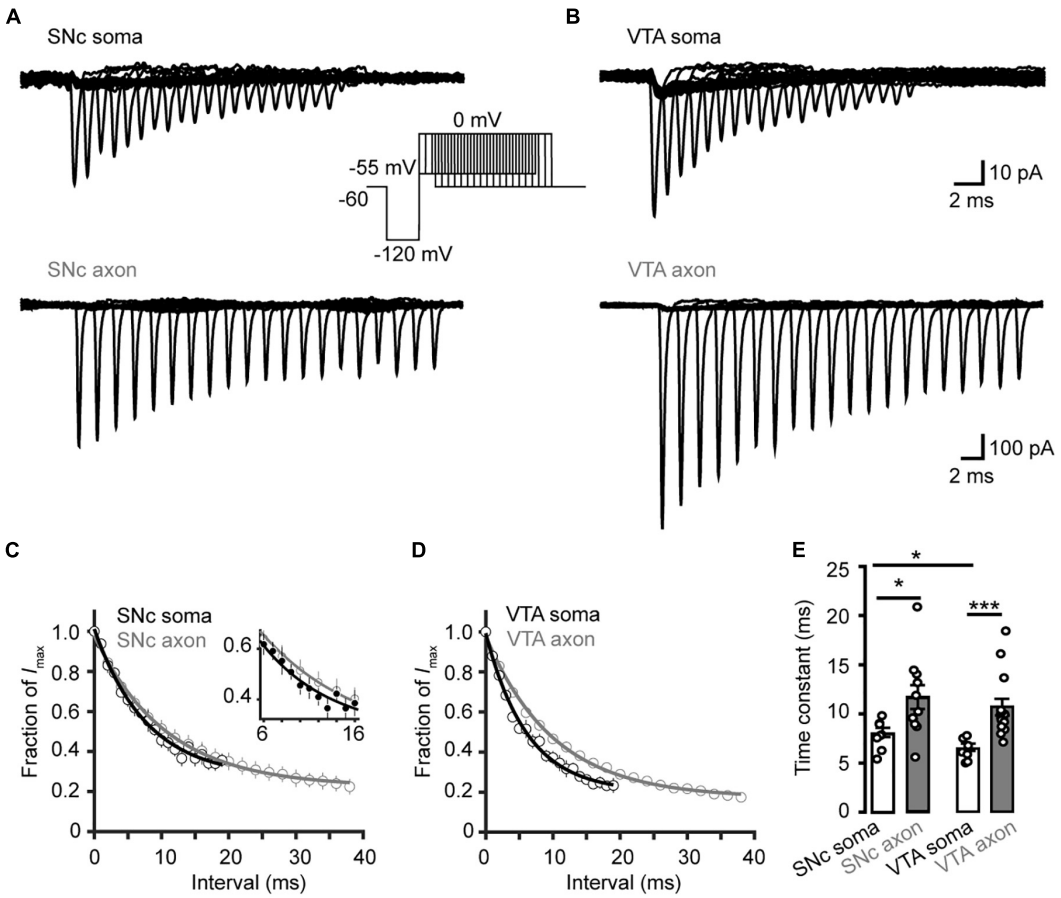


**FIGURE 7 |** Time course of $Na^+$ channel inactivation onset in TH neurons. **(A)** Example currents evoked by the voltage commands (inset) in SNc neurons. The $V_m$ was stepped from a prepulse of –120 mV (20 ms) to –55 mV with varying intervals followed by a test pulse to 0 mV (5 ms). **(B)** Similar as in A but from VTA neurons. **(C,D)** Plots of the currents as a function of intervals. Currents were normalized to the $Na^+$ currents without time interval. The plots were fitted with single exponential functions. Inset, expanded plots showing differences between the two groups. **(E)** Time constants for the development of $Na^+$ channel inactivation at –55 mV. $^*p < 0.05$; $^{***}p < 0.001$.

Li et al., 2014; Ye et al., 2018). The half-activation voltages of channels distributed in distal AIS regions are more hyperpolarized than those in the soma. In midbrain dopaminergic neurons, the similarities in voltage dependence of channel activation at the soma and AIS suggest a more important role of the high channel density and the thin AIS structure in AP initiation (Stuart et al., 1997). In comparison with that of AIS channels of pyramidal cells, the relatively depolarized half-activation voltage of AIS channels would increase the AP threshold and slow down the conduction velocity along the axon. The slower development of channel inactivation and faster recovery ensure higher channel availability in prolonged depolarization levels and with a high firing rate, such as during phasic firing. It remains to be further examined whether biophysical properties of somatic and axonal channels are subject to modulation by neuromodulator receptors.

## Molecular Identity of AIS $Na^+$ Channels

Previous findings (Ding et al., 2011) from single-cell RT-PCR suggest that dopaminergic neurons express all four $Na^+$ channel subtypes in the central nervous system, including Nav1.1, Nav1.2, Nav1.3, and Nav1.6. In addition, quantitative RT-PCR reveal relatively higher expression levels of Nav1.2 in dopaminergic neurons but Nav1.1 and Nav1.6 in GABAergic neurons of the substantial nigra. *In situ* hybridization experiments also revealed that most of the SNc neurons express mRNA of Nav1.2, only a small population contains mRNA of Nav1.6 (Gonzalez-Cabrera et al., 2017). In agreement with these findings, our immunostaining results reveal that, at the protein level, Nav1.2 is the predominant channel subtype at the AIS of TH-expressing neurons in both SNc and VTA (**Figure 9**). In sharp contrast, Nav1.1 and Nav1.6 immunosignals are not detectible in TH-positive cells (**Figure 10**). Immunosignals of Nav1.1 and Nav1.6 are found in some TH-negative neurites, most likely from local GABAergic neurons. Considering that Nav1.3 is mainly expressed during earlier developmental stages (Shah et al., 2001) and has a much lower expression level in juvenile animals as compared with other subunits in single-cell RT-PCR experiments (Ding et al., 2011), we did not examine the expression of this channel subtype in the immunostaining experiments.

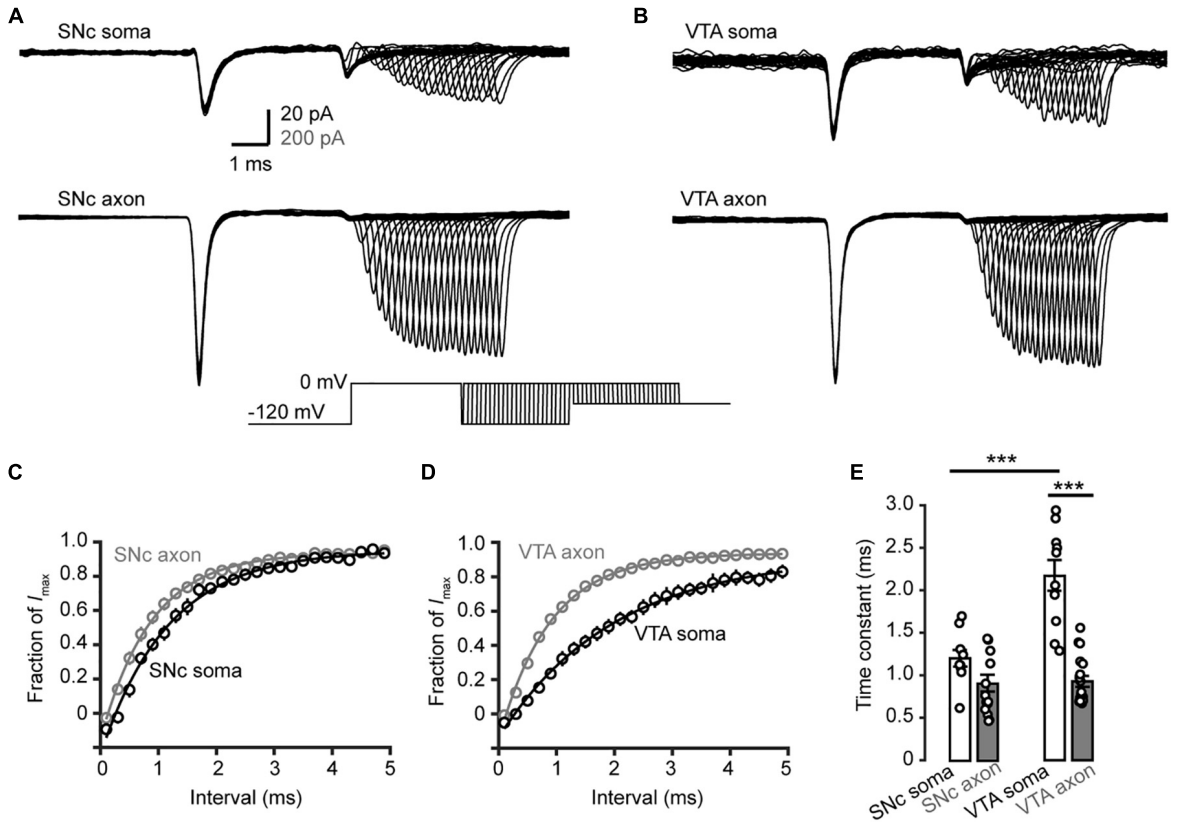


**FIGURE 8 |** Recovery from inactivation of $Na^+$ channels in TH neurons. **(A,B)** Representative currents evoked by two paired pulses (from –120 to 0 mV) with varying intervals (inset) in SNc **(A)** and VTA neurons **(B)**. **(C,D)** Plots of the currents in SNc **(C)** and VTA cells **(D)** as a function of intervals between the two pulses. Currents were normalized to the peak amplitude of the current evoked by the first pulse. **(E)** Comparison of the recovery time constants from inactivation between $Na^+$ currents in different groups. $^{***}p < 0.001$.

The exclusive expression of Nav1.2 at the AIS of dopaminergic neurons suggest a critical role of Nav1.2 in determining the excitability of these neurons. Dysfunction of channels containing the α subunit Nav1.2 may lead to alteration of brain functions, such as motor control, motivation and reward. Indeed, mutations of Nav1.2 have been associated with autism (Sanders et al., 2012; Ben-Shalom et al., 2017) and epilepsy (Kamiya et al., 2004; Lauxmann et al., 2013; Berecki et al., 2018). Thus, this channel subunit could be a potential drug target for the treatment of related brain disorders.

# MATERIALS AND METHODS

## Slice Preparation

The use and care of animals in this study were approved by the Animal Advisory Committee at the State Key Laboratory of Cognitive Neuroscience and Learning, Beijing Normal University. The number of animals used in the experiments was minimized to comply the rules of ethics committee. We used TH-GFP mice (P16-25) for electrophysiological experiments. Mice were anesthetized by sodium pentobarbital (100 mg/kg, i.p.) before decapitation. The brain was dissected out and immersed in an ice-cold slicing solution (in mM: Sucrose 213, KCl 2.5, $NaH_2PO_4$ 1.25, $NaHCO_3$ 26, Dextrose 10, $MgSO_4$ 2, $CaCl_2$ 2), which was bubbled with mixed gas (95% $O_2$, 5% $CO_2$). In this sucrose-based solution, brain slices (200 μm in thickness) containing the midbrain were cut on a vibratome (VT1200S, Leica). Slices were then transferred to an incubator containing the artificial cerebrospinal fluid (ACSF) (in mM: NaCl 126, KCl 2.5, $NaH_2PO_4$ 1.25, $NaHCO_3$ 26, Dextrose 25, $MgSO_4$ 2, $CaCl_2$ 2; 315–325 mOsm, pH = 7.2–7.3) and maintained at 34°C for ∼30–60 min. After incubation, slices were kept in the same solution at the room temperature until use.

## Electrophysiological Recordings

To obtain electrophysiological recordings, we transferred slices to a recording chamber perfused with aerated ACSF at 24–26°C. The GFP-positive cells were considered as putative dopaminergic neurons. They were visualized under an infrared differential interference contrast (IR-DIC) fluorescence microscope (BX51WI, Olympus). Patch pipettes had an impedance of ∼5 MΩ for somatic recording and ∼10 MΩ for axonal bleb recording. Blebs formed at the AIS (60 μm away from the

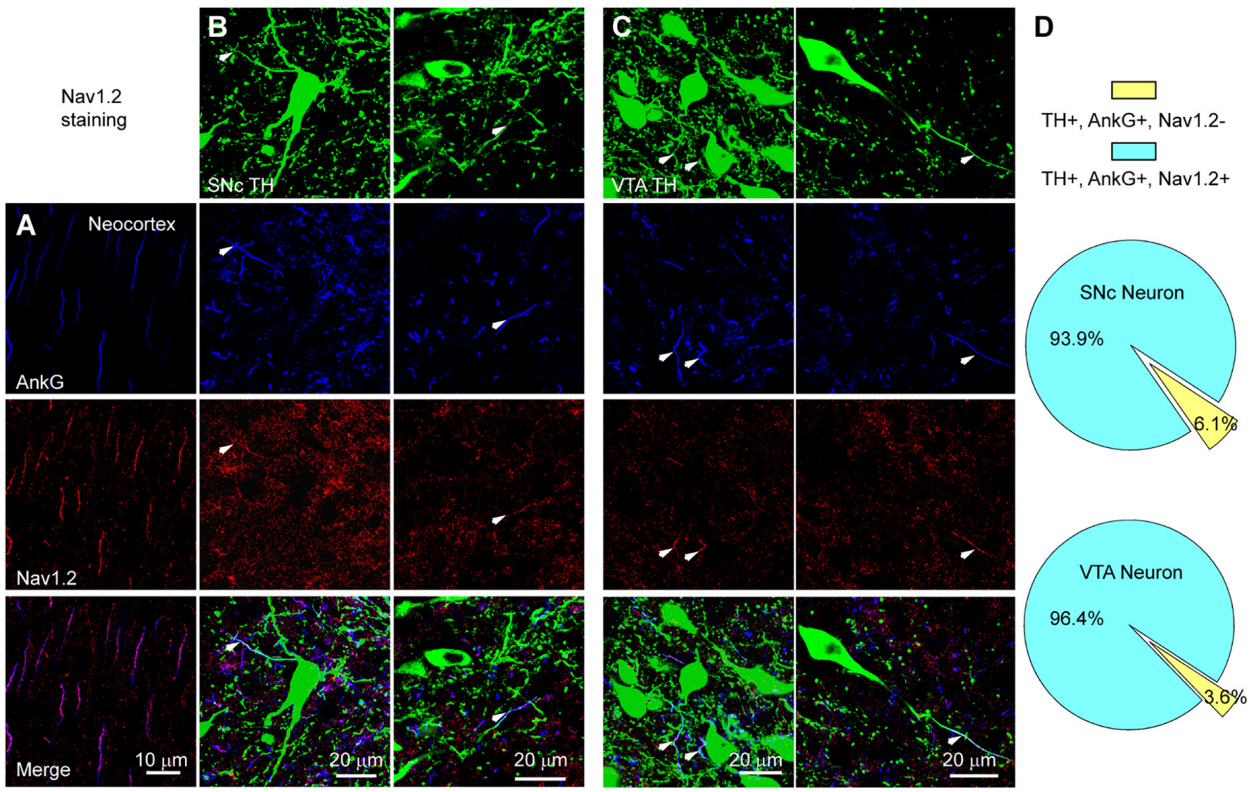


**FIGURE 9 |** The AIS of midbrain TH-positive neurons express Nav1.2. **(A)** Double staining of AnkG (Blue) and Nav1.2 (Red) in neocortex. **(B)** Triple staining of TH (green), AnkG (Blue) and Nav1.2 (Red) in two example SNc cells. White arrowheads indicate neurite segments positive to all three antibodies. **(C)** Similar as in B but for cells in VTA. **(D)** Percentages of TH/AnkG-positive neurites in SNc (top) and VTA (bottom) that are positive (blue) or negative (yellow) to Nav1.2 staining.

branching point of the ABD) were chosen for recording in this study. The TH-positive axons together with their blebs were identified by the expression of GFP. For current clamp recording, pipettes were filled with a $K^+$-based internal solution (in mM: Kgluconate 140, KCl 3, MgCl2 2, HEPES 10, EGTA 0.2, Na2ATP 2; 295–305 mOsm, pH = 7.2). For voltage clamp recordings, pipettes were filled with a $Cs^+$-based solution (in mM: CsCl 140, $MgCl_2$ 2, HEPES 10, EGTA 10, $Na_2ATP$ 2; 295–305 mOsm, pH = 7.2). To obtain local $Na^+$ currents at the soma (nucleated patch) and the axon (isolated axonal bleb), we added 4-AP (3 mM), TEA-Cl (96 mM) and $CdCl_2$ (100 μM) to the ACSF but reduced the concentration of NaCl to 50 mM. Isolation of blebs from the axon was achieved as described previously (Chaudhury et al., 2013). In brief, we swept a patch pipette just below the selected GFP-positive bleb and disconnect it from the main axon. A MultiClamp 700B amplifier (Molecular Devices) was used for whole-cell recording and giant patch (somatic nucleated patch and isolated axonal bleb) recording. Voltage and current signals were acquired by pClamp10 software at a sampling rate of 50 kHz. $Na^+$ current traces were averaged and then filtered with a Gaussian filter. The liquid junction potentials were not corrected for *V*m values shown in the text and figures.

The holding potential of somatic nucleated patches and isolated axonal blebs was −60 mV. For the measurement of $Na^+$ channel density and the investigation of voltage-dependent channel activation, the $V_m$ was stepped from a prepulse (−120 mV, 30 ms) to a series of testing pulses ranging from −70 to +30 mV with increment of 5 mV. The maximal peak amplitude among the evoked families of currents and the membrane area (based on the measured diameter) were used for the estimation of $Na^+$ channel conductance density. The peak amplitudes at different voltage levels were normalized to the maximal amplitude and plotted as a function of the membrane potential (activation curves). We fitted the rise and decay of the evoked currents with single exponential functions to examine the kinetics of channel activation and inactivation. For channel deactivation, 0.2 ms after stepping the membrane potential from −120 to 0 mV, a series of 25-ms voltage pulses from −100 to −30 mV were applied to the patches. The deactivation time constants could be obtained from the tail currents at different voltage levels.

To examine the steady-state inactivation of $Na^+$ channels, we evoked transient $Na^+$ currents by stepping the $V_m$ from a series of prepulses (from −120 to −60 mV, 35 ms) to the 20-ms test pulse at 0 mV. The evoked currents were normalized to the maximal peak amplitude to generate the inactivation curves, i.e., channel availability at different voltages. To examine the time course of channel inactivation onset, we stepped the

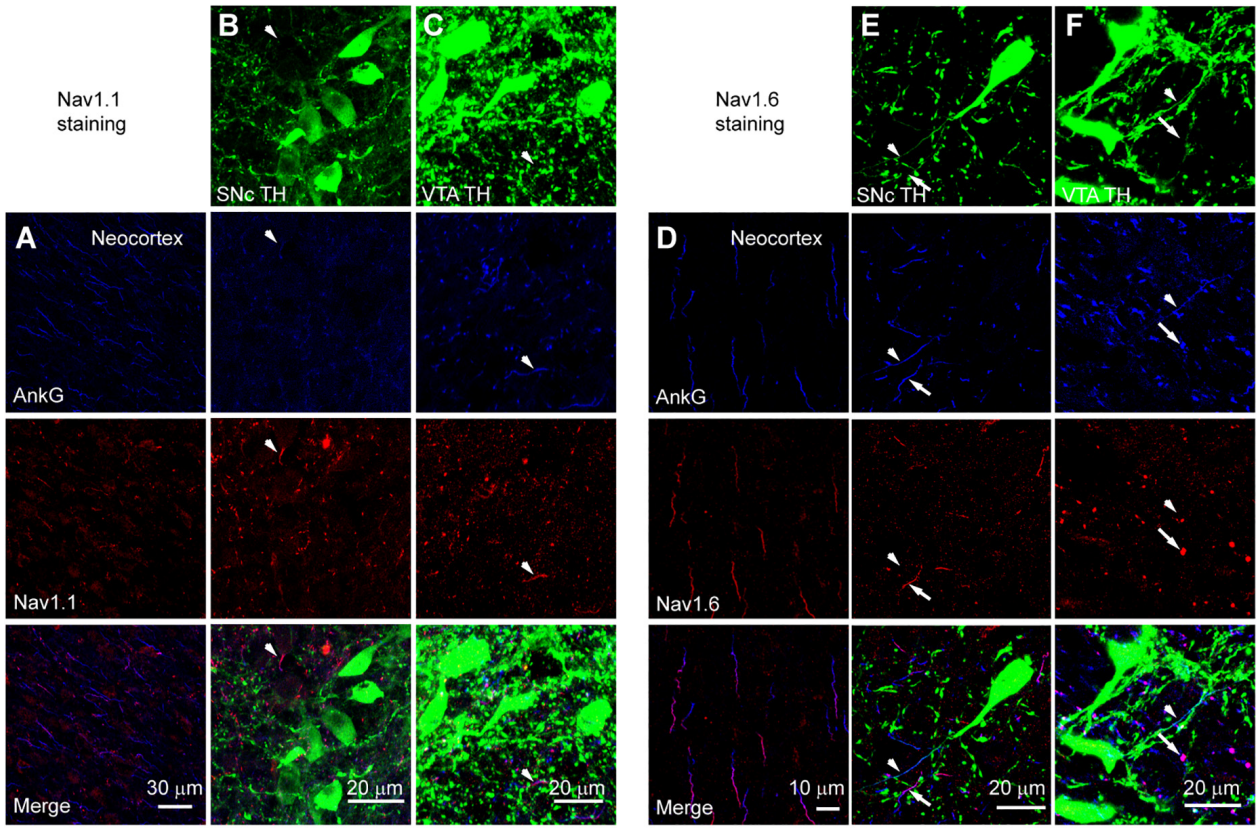


**FIGURE 10 |** Absence of Nav1.1 and Nav1.6 from the AIS of midbrain TH-positive neurons. **(A)** Double staining of AnkG (Blue) and Nav1.1 (Red) in neocortex. **(B)** Triple staining of TH (green), AnkG (Blue) and Nav1.1 (Red) in SNc. White arrowheads indicate neurites positive to AnkG and Nav1.1 but negative to TH. **(C)** Similar as in B but for VTA. **(D–F)** Similar to **A–C** but for Nav1.6 staining in the neocortex **(D)**, SNc **(E)** and VTA **(F)**. Note the absence of Nav1.6 immunosignals from the TH-positive neurites (arrowheads). Arrows indicate neurites positive to AnkG and Nav1.6 but negative to TH.

$V_m$ from a prepulse at −120 to −55 mV and stepped the $V_m$ further to a test pulse of 0 mV after a delay ranging from 0 to 38 ms. Because the recordings from isolated blebs were normally stable for much longer time than that of nucleated patches, we chose to apply relatively longer time intervals in bleb recordings. Channels were supposed to inactivate at −55 mV but in a time-dependent manner. For recovery from inactivation, we applied two paired pulses from −120 to 0 mV (20 ms) with time intervals ranging from 1 to 110 ms. The first pulse in each paired steps lasted for 30 ms. Currents were normalized to the peak amplitude of the current evoked by the first pulse.

## Immunostaining

After anesthesia, animals were perfused through heart with an ice-cold fixative: 0.5∼1% paraformaldehyde (PFA) and 0.5∼1% sucrose (in 0.1 M phosphate buffer, PB). Brain tissues were dissected out and immersed in the same fixative for 2 h. Then the tissues were transferred to 30% sucrose and maintained at 4°C overnight. Tissues were cut into 30 μm-thick sections on a freezing microtome at −20°C. After wash with 0.01 M phosphate buffered saline (PBS), the sections were treated with 0.5% Triton X-100 in PB for 30 min, and then 5% bovine serum albumin and 0.5% Triton for ∼60 min at room temperature. Sections were then incubated in 0.1% Triton solution containing the primary antibodies (mouse anti-Nav1.1, 1:200, NeuroMab, 73-023; rabbit anti-Nav1.6, 1:400, Alomone Labs, ASC-009; mouse anti-Nav1.2, 1:200, NeuroMab, 73-024; goat anti-AnkG, 1:400, Santa Cruz, sc-31778; rabbit Anti-TH,1:400, Millipore, AB152; Mouse anti-TH, 1:400, Millipore, MAB318) at 4°C overnight. After complete wash with 0.01 M PBS, sections were incubated in 0.1% Triton solution containing secondary antibodies (1:1000, Invitrogen: Alexa-488 conjugated donkey anti-rabbit, A21206, Alexa-555 conjugated donkey anti-mouse, A31570, and Alexa-647 conjugated donkey anti-goat, A21447) for 2 hr at the room temperature.

We chose to image non-successive sections (about 2 mm (2 mm) for each experiment so that no cell on the surface would be over-counted. Images were taken on a laser scanning confocal microscope (A1plus, Nikon) with 10×, 20×, and 60× objectives. The acquisition parameters were carefully adjusted to make the fluorescence signals linearly displayed and fall into the maximum dynamic range of the detectors. Z-stack images were collected with a voxel interval of 1 μm.

### Statistics

All values were presented as mean ± SEM. Statistical significance of difference was examined using non-parametric Wilcoxon rank-sum test.

## DATA AVAILABILITY

All datasets generated for this study are included in the manuscript and/or the supplementary files.

## ETHICS STATEMENT

This study was carried out in accordance with the recommendations of the Animal Advisory Committee at the State Key Laboratory of Cognitive Neuroscience and Learning, Beijing Normal University. The protocol was also approved by this committee.

## AUTHOR CONTRIBUTIONS

YS initiated and designed the experiments. JY performed all the patch-clamp recordings and analyzed the data. YX helped in dual soma-axon recordings. LL and ML conducted the immunostaining experiments. QH helped in data analysis. JY and YS wrote the manuscript.

## FUNDING

This work was supported by the National Natural Science Foundation of China Project (31630029, 31661143037, and 31430038).

## REFERENCES

Ben-Shalom, R., Keeshen, C. M., Berrios, K. N., An, J. Y., Sanders, S. J., and Bender, K. J. (2017). Opposing effects on NaV1.2 function underlie differences between SCN2A variants observed in individuals with autism spectrum disorder or infantile seizures. *Biol. Psychiatry* 82, 224–232. doi: 10.1016/j.biopsych.2017.01.009

Berecki, G., Howell, K. B., Deerasooriya, Y. H., Cilio, M. R., Oliva, M. K., Kaplan, D., et al. (2018). Dynamic action potential clamp predicts functional separation in mild familial and severe de novo forms of SCN2A epilepsy. *Proc. Natl. Acad. Sci. U.S.A.* 115, E5516–E5525. doi: 10.1073/pnas.1800077115

Bermudez, M. A., and Schultz, W. (2010). Reward magnitude coding in primate amygdala neurons. *J. Neurophysiol.* 104, 3424–3432. doi: 10.1152/jn.00540.2010

Cantrell, A. R., and Catterall, W. A. (2001). Neuromodulation of Na+ channels: an unexpected form of cellular plasticity. *Nat. Rev. Neurosci.* 2, 397–407. doi: 10.1038/35077553

Cao, J. L., Covington, H. E. III, Friedman, A. K., Wilkinson, M. B., Walsh, J. J., Cooper, D. C., et al. (2010). Mesolimbic dopamine neurons in the brain reward circuit mediate susceptibility to social defeat and antidepressant action. *J. Neurosci.* 30, 16453–16458. doi: 10.1523/JNEUROSCI.3177-10.2010

Carr, D. B., Day, M., Cantrell, A. R., Held, J., Scheuer, T., Catterall, W. A., et al. (2003). Transmitter modulation of slow, activity-dependent alterations in sodium channel availability endows neurons with a novel form of cellular plasticity. *Neuron* 39, 793–806. doi: 10.1016/s0896-6273(03)00531-2

Chan, A. W., Owens, S., Tung, C., and Stanley, E. F. (2007). Resistance of presynaptic CaV2.2 channels to voltage-dependent inactivation: dynamic palmitoylation and voltage sensitivity. *Cell Calcium* 42, 419–425. doi: 10.1016/j.ceca.2007.04.009

Chan, C. S., Gertler, T. S., and Surmeier, D. J. (2009). Calcium homeostasis, selective vulnerability and Parkinson's disease. *Trends Neurosci.* 32, 249–256. doi: 10.1016/j.tins.2009.01.006

Chaudhury, D., Walsh, J. J., Friedman, A. K., Juarez, B., Ku, S. M., Koo, J. W., et al. (2013). Rapid regulation of depression-related behaviours by control of midbrain dopamine neurons. *Nature* 493, 532–536. doi: 10.1038/nature11713

Chen, G., Henter, I. D., and Manji, H. K. (2009). A role for PKC in mediating stress-induced prefrontal cortical structural plasticity and cognitive function. *Proc. Natl. Acad. Sci. U.S.A.* 106, 17613–17614. doi: 10.1073/pnas.0909771106

Chen, Y., Yu, F. H., Sharp, E. M., Beacham, D., Scheuer, T., and Catterall, W. A. (2008). Functional properties and differential neuromodulation of Na(v)1.6 channels. *Mol. Cell. Neurosci.* 38, 607–615. doi: 10.1016/j.mcn.2008.05.009

Chen, Y., Yu, F. H., Surmeier, D. J., Scheuer, T., and Catterall, W. A. (2006). Neuromodulation of Na+ channel slow inactivation via cAMP-dependent protein kinase and protein kinase C. *Neuron* 49, 409–420. doi: 10.1016/j.neuron.2006.01.009

Clark, B. A., Monsivais, P., Branco, T., London, M., and Hausser, M. H. (2005). The site of action potential initiation in cerebellar Purkinje neurons. *Nat. Neurosci.* 8, 137–139. doi: 10.1038/nn1390

Cragg, S. J., and Greenfield, S. A. (1997). Differential autoreceptor control of somatodendritic and axon terminal dopamine release in substantia nigra, ventral tegmental area, and striatum. *J. Neurosci.* 17, 5738–5746. doi: 10.1523/JNEUROSCI.17-15-05738.1997

Dauer, W., and Przedborski, S. (2003). Parkinson's disease: mechanisms and models. *Neuron* 39, 889–909. doi: 10.1016/S0896-6273(03)00568-3

Ding, S., Wei, W., and Zhou, F. M. (2011). Molecular and functional differences in voltage-activated sodium currents between GABA projection neurons and dopamine neurons in the substantia nigra. *J. Neurophysiol.* 106, 3019–3034. doi: 10.1152/jn.00305.2011

Fields, H. L. (2007). Understanding how opioids contribute to reward and analgesia. *Reg. Anesth. Pain. Med.* 32, 242–246. doi: 10.1016/j.rapm.2007.01.001

Geffen, L. B., Jessell, T. M., Cuello, A. C., and Iversen, L. L. (1976). Release of dopamine from dendrites in rat substantia nigra. *Nature* 260, 258–260. doi: 10.1038/260258a0

Gentet, L. J., and Williams, S. R. (2007). Dopamine gates action potential backpropagation in midbrain dopaminergic neurons. *J. Neurosci.* 27, 1892–1901. doi: 10.1523/JNEUROSCI.5234-06.2007

Gonzalez-Cabrera, C., Meza, R., Ulloa, L., Merino-Sepulveda, P., Luco, V., Sanhueza, A., et al. (2017). Characterization of the axon initial segment of mice substantia nigra dopaminergic neurons. *J. Comp. Neurol.* 525, 3529–3542. doi: 10.1002/cne.24288

Grace, A. A., and Bunney, B. S. (1984). The control of firing pattern in nigral dopamine neurons: burst firing. *J. Neurosci.* 4, 2877–2890. doi: 10.1523/JNEUROSCI.04-11-02877.1984

Grace, A. A., Floresco, S. B., Goto, Y., and Lodge, D. J. (2007). Regulation of firing of dopaminergic neurons and control of goal-directed behaviors. *Trends. Neurosci.* 30, 220–227. doi: 10.1016/j.tins.2007.03.003

Gunaydin, L. A., Grosenick, L., Finkelstein, J. C., Kauvar, I. V., Fenno, L. E., Adhikari, A., et al. (2014). Natural neural projection dynamics underlying social behavior. *Cell* 157, 1535–1551. doi: 10.1016/j.cell.2014.05.017

Hausser, M., Stuart, G., Racca, C., and Sakmann, B. (1995). Axonal initiation and active dendritic propagation of action potentials in substantia nigra neurons. *Neuron* 15, 637–647. doi: 10.1016/0896-6273(95)90152-3

Hounsgaard, J., Nedergaard, S., and Greenfield, S. A. (1992). Electrophysiological localization of distinct calcium potentials at selective somatodendritic sites in the substantia nigra. *Neuroscience* 50, 513–518. doi: 10.1016/0306-4522(92)90443-6

Hu, H., Gan, J., and Jonas, P. (2014). Interneurons. Fast-spiking, parvalbumin(+) GABAergic interneurons: from cellular design to microcircuit function. *Science* 345:1255263. doi: 10.1126/science.1255263

Hu, W., Tian, C., Li, T., Yang, M., Hou, H., and Shu, Y. (2009). Distinct contributions of Na(v)1.6 and Na(v)1.2 in action potential initiation and backpropagation. *Nat. Neurosci.* 12, 996–1002. doi: 10.1038/nn.2359

Johnson, S. W., Seutin, V., and North, R. A. (1992). Burst firing in dopamine neurons induced by N-methyl-D-aspartate: role of electrogenic sodium pump. *Science* 258, 665–667. doi: 10.1126/science.1329209

Kamiya, K., Kaneda, M., Sugawara, T., Mazaki, E., Okamura, N., Montal, M., et al. (2004). A nonsense mutation of the sodium channel gene SCN2A in a patient with intractable epilepsy and mental decline. *J. Neurosci.* 24, 2690–2698. doi: 10.1523/JNEUROSCI.3089-03.2004

Khaliq, Z. M., and Bean, B. P. (2010). Pacemaking in dopaminergic ventral tegmental area neurons: depolarizing drive from background and voltage-dependent sodium conductances. *J. Neurosci.* 30, 7401–7413. doi: 10.1523/JNEUROSCI.0143-10.2010

Kole, M. H., Ilschner, S. U., Kampa, B. M., Williams, S. R., Ruben, P. C., and Stuart, G. J. (2008). Action potential generation requires a high sodium channel density in the axon initial segment. *Nat. Neurosci.* 11, 178–186. doi: 10.1038/nn2040

Koob, G. F. (1998). Circuits, drugs, and drug addiction. *Adv. Pharmacol.* 42, 978–982. doi: 10.1016/s1054-3589(08)60910-2

Korotkova, T. M., Sergeeva, O. A., Eriksson, K. S., Haas, H. L., and Brown, R. E. (2003). Excitation of ventral tegmental area dopaminergic and nondopaminergic neurons by orexins/hypocretins. *J. Neurosci.* 23, 7–11. doi: 10.1523/JNEUROSCI.23-01-00007.2003

Kuwahara, T., Koyama, A., Gengyo-Ando, K., Masuda, M., Kowa, H., Tsunoda, M., et al. (2006). Familial Parkinson mutant alpha-synuclein causes dopamine neuron dysfunction in transgenic *Caenorhabditis elegans*. *J. Biol. Chem.* 281, 334–340. doi: 10.1074/jbc.M504860200

Lauxmann, S., Boutry-Kryza, N., Rivier, C., Mueller, S., Hedrich, U. B., Maljevic, S., et al. (2013). An SCN2A mutation in a family with infantile seizures from Madagascar reveals an increased subthreshold Na(+) current. *Epilepsia* 54, e117–e121. doi: 10.1111/epi.12241

Lewis, D. A., and Lieberman, J. A. (2000). Catching up on schizophrenia: natural history and neurobiology. *Neuron* 28, 325–334. doi: 10.1016/S0896-6273(00)00111-2

Li, T., Tian, C., Scalmani, P., Frassoni, C., Mantegazza, M., Wang, Y., et al. (2014). Action potential initiation in neocortical inhibitory interneurons. *PLoS Biol.* 12:e1001944. doi: 10.1371/journal.pbio.1001944

Margolis, E. B., Lock, H., Hjelmstad, G. O., and Fields, H. L. (2006). The ventral tegmental area revisited: is there an electrophysiological marker for dopaminergic neurons? *J. Physiol.* 577, 907–924. doi: 10.1113/jphysiol.2006.117069

Maurice, N., Tkatch, T., Meisler, M., Sprunger, L. K., and Surmeier, D. J. (2001). D1/D5 dopamine receptor activation differentially modulates rapidly inactivating and persistent sodium currents in prefrontal cortex pyramidal neurons. *J. Neurosci.* 21, 2268–2277. doi: 10.1523/JNEUROSCI.21-07-02268.2001

McCormick, D. A., Shu, Y., and Yu, Y. (2007). Neurophysiology: Hodgkin and Huxley model–still standing? *Nature* 445, E1–E2. doi: 10.1038/nature05523

Moubarak, E., Engel, D., Dufour, M. A., Tapia, M., Tell, F., and Goaillard, J. M. (2019). Robustness to axon initial segment variation is explained by somatodendritic excitability in rat substantia nigra dopaminergic neurons. *J. Neurosci.* 39, 5044–5063. doi: 10.1523/JNEUROSCI.2781-18.2019

Neuhoff, H., Neu, A., Liss, B., and Roeper, J. (2002). I(h) channels contribute to the different functional properties of identified dopaminergic subpopulations in the midbrain. *J. Neurosci.* 22, 1290–1302. doi: 10.1523/JNEUROSCI.22-04-01290.2002

Nieoullon, A. (2002). Dopamine and the regulation of cognition and attention. *Prog. Neurobiol.* 67, 53–83. doi: 10.1016/s0301-0082(02)00011-4

Rice, M. E., and Patel, J. C. (2015). Somatodendritic dopamine release: recent mechanistic insights. *Philos. Trans. R. Soc. Lond. B Biol. Sci.* 370:20140185. doi: 10.1098/rstb.2014.0185

Rush, A. M., Dib-Hajj, S. D., and Waxman, S. G. (2005). Electrophysiological properties of two axonal sodium channels, Nav1.2 and Nav1.6, expressed in mouse spinal sensory neurones. *J. Physiol.* 564, 803–815. doi: 10.1113/jphysiol.2005.083089

Sanders, S. J., Murtha, M. T., Gupta, A. R., Murdoch, J. D., Raubeson, M. J., Willsey, A. J., et al. (2012). De novo mutations revealed by whole-exome sequencing are strongly associated with autism. *Nature* 485, 237–241. doi: 10.1038/nature10945

Seutin, V., and Engel, D. (2010). Differences in Na+ conductance density and Na+ channel functional properties between dopamine and GABA neurons of the rat substantia nigra. *J. Neurophysiol.* 103, 3099–3114. doi: 10.1152/jn.00513.2009

Shah, B. S., Stevens, E. B., Pinnock, R. D., Dixon, A. K., and Lee, K. (2001). Developmental expression of the novel voltage-gated sodium channel auxiliary subunit beta3, in rat CNS. *J. Physiol.* 534, 763–776. doi: 10.1111/j.1469-7793.2001.t01-1-00763.x

Stuart, G., Spruston, N., Sakmann, B., and Hausser, M. (1997). Action potential initiation and backpropagation in neurons of the mammalian CNS. *Trends. Neurosci.* 20, 125–131. doi: 10.1016/S0166-2236(96)10075-8

Sulzer, D., Cragg, S. J., and Rice, M. E. (2016). Striatal dopamine neurotransmission: regulation of release and uptake. *Basal Ganglia* 6, 123–148. doi: 10.1016/j.baga.2016.02.001

Tobler, P. N., O'Doherty, J. P., Dolan, R. J., and Schultz, W. (2007). Reward value coding distinct from risk attitude-related uncertainty coding in human reward systems. *J. Neurophysiol.* 97, 1621–1632. doi: 10.1152/jn.00745.2006

Tsai, H. C., Zhang, F., Adamantidis, A., Stuber, G. D., Bonci, A., de Lecea, L., et al. (2009). Phasic firing in dopaminergic neurons is sufficient for behavioral conditioning. *Science* 324, 1080–1084. doi: 10.1126/science.1168878

Tye, K. M., Mirzabekov, J. J., Warden, M. R., Ferenczi, E. A., Tsai, H. C., Finkelstein, J., et al. (2013). Dopamine neurons modulate neural encoding and expression of depression-related behaviour. *Nature* 493, 537–541. doi: 10.1038/nature11740

West, J. W., Numann, R., Murphy, B. J., Scheuer, T., and Catterall, W. A. (1991). A phosphorylation site in the Na+ channel required for modulation by protein kinase C. *Science* 254, 866–868. doi: 10.1126/science.1658937

Wise, R. A. (2004). Rewards wanted: molecular mechanisms of motivation. *Discov. Med.* 4, 180–186.

Ye, M. Y., Yang, J., Tian, C. P., Zhu, Q. Y., Yin, L. P., Jiang, S., et al. (2018). Differential roles of Na(V)1.2 and Na(V)1.6 in regulating neuronal excitability at febrile temperature and distinct contributions to febrile seizures. *Sci. Rep.* 8:753. doi: 10.1038/s41598-017-17344-8

**Conflict of Interest Statement:** The authors declare that the research was conducted in the absence of any commercial or financial relationships that could be construed as a potential conflict of interest.

*Copyright © 2019 Yang, Xiao, Li, He, Li and Shu. This is an open-access article distributed under the terms of the Creative Commons Attribution License (CC BY). The use, distribution or reproduction in other forums is permitted, provided the original author(s) and the copyright owner(s) are credited and that the original publication in this journal is cited, in accordance with accepted academic practice. No use, distribution or reproduction is permitted which does not comply with these terms.*

frontiers in Cellular Neuroscience

METHODS
published: 24 July 2019
doi: 10.3389/fncel.2019.00312

# Dedicated Setup for the Photoconversion of Fluorescent Dyes for Functional Electron Microscopy

*Katharine L. Dobson*[1,2], *Carmel L. Howe*[3], *Yuri Nishimura*[1,4] *and Vincenzo Marra*[1]*

[1] Department of Neuroscience, Psychology and Behaviour, University of Leicester, Leicester, United Kingdom, [2] Centre for Discovery Brain Sciences, University of Edinburgh, Edinburgh, United Kingdom, [3] Department of Bioengineering, Imperial College London, London, United Kingdom, [4] Sussex Neuroscience, School of Life Sciences, University of Sussex, Brighton, United Kingdom

Here, we describe a cost-effective setup for targeted photoconversion of fluorescent signals into electron dense ones. This approach has offered invaluable insights in the morphology and function of fine neuronal structures. The technique relies on the localized oxidation of diaminobenzidine (DAB) mediated by excited fluorophores. This paper includes a detailed description of how to build a simple photoconversion setup that can increase reliability and throughput of this well-established technique. The system described here, is particularly well-suited for thick neuronal tissue, where light penetration and oxygen diffusion may be limiting DAB oxidation. To demonstrate the system, we use Correlative Light and Electron Microscopy (CLEM) to visualize functionally-labeled individual synaptic vesicles released onto an identified layer 5 neuron in an acute cortical slice. The setup significantly simplifies the photoconversion workflow, increasing the depth of photoillumination, improving the targeting of the region of interest and reducing the time required to process each individual sample. We have tested this setup extensively for the photoconversion of FM 1-43FX and Lucifer Yellow both excited at 473 nm. In principle, the system can be adapted to any dye or nanoparticle able to oxidize DAB when excited by a specific wavelength of light.

**Keywords: FM1-43, Lucifer Yellow, synaptic vesicle (SV), functional labeling, electron microscopy, CLEM, correlative light electron microscopy, synapse**

OPEN ACCESS

***Edited by:***
*Federico F. Trigo,*
*Université Paris Descartes, France*

***Reviewed by:***
*Céline Auger,*
*UMR8118 Physiologie Cérébrale, France*
*Jorge E. Moreira,*
*University of São Paulo, Brazil*

***Correspondence:**
*Vincenzo Marra*
*vm120@le.ac.uk*

***Specialty section:***
*This article was submitted to Cellular Neurophysiology, a section of the journal Frontiers in Cellular Neuroscience*

***Received:*** *30 April 2019*
***Accepted:*** *25 June 2019*
***Published:*** *24 July 2019*

***Citation:***
*Dobson KL, Howe CL, Nishimura Y and Marra V (2019) Dedicated Setup for the Photoconversion of Fluorescent Dyes for Functional Electron Microscopy. Front. Cell. Neurosci. 13:312. doi: 10.3389/fncel.2019.00312*

## 1. INTRODUCTION

The study of presynaptic organization requires the analysis of both functional and structural aspects of axons and their synaptic compartments (for a review see Debanne et al., 2011). While, for structurally well-characterized synapses, vesicular release can be studied using mainly electrophysiological methods (Jonas et al., 1993; Neher and Sakaba, 2001; Pulido et al., 2015), the study of central synapses often requires a combination of imaging methods. A number of super-resolution techniques can provide information on the morphology of labeled structures with nanometer accuracy (see Gramlich and Klyachko, 2019), however, Electron Microscopy (EM) is still the only imaging technique able to provide contextual information at the ultrastructural level. Classic EM cannot provide any functional information and, to overcome this limitation, a number of Correlative Light and Electron Microscopy (CLEM) techniques have been developed over the years to study live tissue (Maranto, 1982; Harata et al., 2001; Darcy et al., 2006; Ratnayaka et al., 2011; Shu et al., 2011; Peddie et al., 2017; de Beer et al., 2018). Many CLEM techniques rely on

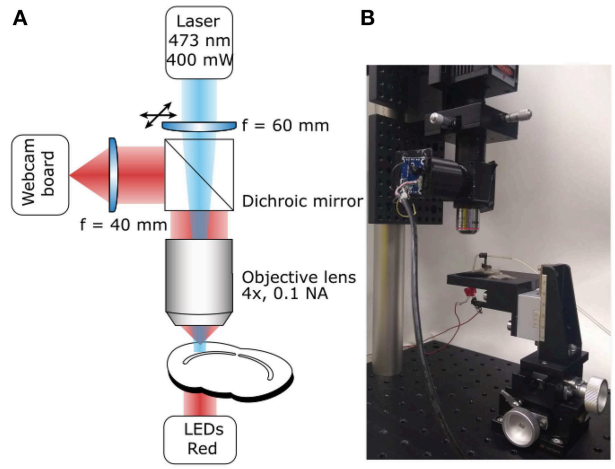


**FIGURE 1 |** Photoconversion Rig. **(A)** Diagram of the light path for both sample illumination (blue) and visualization (red). **(B)** Photograph of a working setup including sample illumination and visualization paths and sample holder.

the conversion of the fluorescent signal into an electron dense one and when this process requires light activation it is generally referred to as photoconversion. For over 30 years, photoconversion of diaminobenzidine (DAB) has been used to observe, at the ultrastructural level, functionally identified neurons (Maranto, 1982; Smith and Bolam, 1990; Viney et al., 2013). Harata et al. (2001) have shown for the first time that FM1-43 photoillumination in fixed cell cultures can be used to precipitate DAB into an osmiophilic polymer selectively in synaptic vesicles that underwent release and endocytosis in the presence of the dye. In spite of its usefulness, DAB photoconversion in thick neuronal tissue has only been employed by a relatively small number of research groups. A number of different protocols have been published to describe the technique in a range of different preparations and using different modes of light delivery to drive the photoconversion (Opazo and Rizzoli, 2010; Marra et al., 2014; Sabeva and Bykhovskaia, 2017).

Here, we present a low-cost system to drive targeted photoconversion of DAB in thick neuronal tissue. The intent of this article is not to describe the entire photoconversion procedure [already presented by Marra et al. (2014)], but to provide instructions to build a photoconversion setup to easily identify and illuminate a region of interest in a controlled manner.

## 2. EQUIPMENT

The photoconversion setup (**Figure 1**) consists of a high-power excitation light laser, an optical microscope for monitoring the sample during photoconversion and a simple stage to hold the sample and supply the oxygen required for DAB polymerization. We have included a list of the components (**Table 1**) required to build the system described here but we have not included general laboratory supplies.

### 2.1. Excitation Light Path

The system's main purpose is to deliver high-power excitation light over a large volume of tissue. The wavelength of the excitation light will depend on the fluorophore used. The system described here is built to photoconvert FM 1-43FX and Lucifer Yellow (excitation peaks at 473 and 425 nm, respectively), for this reason we chose a 473 nm Diode-Pumped Solid State (DPSS) laser as the light source, however, high-power (>300 mW) single-wavelength LEDs would also work. The light path is extremely simple to minimize attenuation (**Figure 1A**), it consists of a lens focussing the laser beam on the back focal aperture of a 4X air objective. Underfilling the objective aperture produces an approximately collimated beam providing a larger volume of evenly photoilluminated tissue compared with what would be achieved overfilling the objective aperture. The light will still be scattered by the tissue but the illuminated region will be effectively thicker driving the reaction over a larger volume for the same exposure time compared to previously reported results (Marra et al., 2014). Photoconverted vesicles can be observed at 85 µm below the slice surface, a 35 µm improvement over the previous method (Marra et al., 2012, ; data not shown). Between the focussing lens and the objective, the light goes through a 505 nm short-pass dichroic mirror. While the dichroic mirror attenuates the laser intensity, it also allows simultaneous visualization of the sample and of the photoilluminated area for precise positioning. This system ensures that over 20% of the laser output reaches the focal plane of the objective with an homogeneously illuminated area of 0.65 mm $^2$. The fine position of the illuminated area can be adjusted using an XY lens translator. This component is not strictly required, however, it allows fine adjustments improving accuracy and reducing the chance for experimenters' error. Given the large volume illuminated, the power density is comparable to the previously reported one (Marra et al., 2014) and unlikely to directly damage fixed tissue. However, non-specific DAB oxidation may lead to precipitates that could obscure or damage the region of interest. The easiest solution to this issue, is to perform live labeling at least 20 µm below the surface of the tissue, when possible.

### 2.2. Sample Visualization Path

A critical step, in the photoconversion procedure, is the identification of the region of interest. In this photoconversion system, the objective used to deliver the excitation light is also used to image the sample which is illuminated from below with dim throughhole red LEDs. The red LEDs' light is unlikely to excite and photobleach the fluorophores and can be used to monitor the progress of the photoconversion reaction. The red light illuminating the sample will reach the objective, be reflected by the dichroic mirror and imaged using a simple webcam (**Figure 1**). We found that a large field of view is useful to identify the region of interest, particularly in acute brain slices. Such large field of view can be obtained by using a camera with a large sensor (e.g., >1/1.8") or by reducing the objective's magnification. Here, we have used an inexpensive webcam with a small sensor 1/4", removed the casing and glued it to a 3D-printed adaptor (**Figure 2A**). The lens creating the image on the webcam sensor is placed at only 70 mm from the objective's back aperture,

**TABLE 1 |** List of components.

| Component | Supplier | Product code | Notes |
|---|---|---|---|
| **EXCITATION LIGHT PATH** | | | |
| 473 nm Laser | Eksma Optics | DPSS-473-H | This could be replaced with any appropriate high-power light source. Single wavelength Macro LEDs are a viable alternative. |
| Main post | Thorlabs | P50/M | The 50 cm post is the main body of the setup. A shorter version (30 cm–P30/M) would be appropriate if space is a concern. |
| Post mounting clamps | Thorlabs | C1545/M | Two are required one to mount the laser, one for the cube holding the dichroic mirror. |
| Spacers | Thorlabs | BA2S8/M | Two are required to mount the laser so that its output is aligned with the rest of the optics. |
| Steel post L=50.8 mm | Edmund Optics | 83–133 | This post is needed to mount the cube holding the dichroic mirror on the mounting clamps. The additional 0.8 mm length compared with the Thorlabs equivalent allowed for a better match with the laser output but may not be required for other systems. |
| Planconvex lens f= 60 mm | Edmund Optics | 47–347 | This lens focusses the laser beam on the back focal plane of the objective. |
| XY lens translator | Thorlabs | ST1XY-S/M | To move the lens used to focus the laser |
| Lens tube spacer | Thorlabs | SM1S10 | To connect the XY lens translator with the cube. |
| Dichroic mirror cube | Thorlabs | CM1-DCH/M | The rest of the optical components will be connected to this cube. |
| Short-pass dichroic mirror | Laser2000 | FF505-SDi01 | This 25 x 36 mm mirror will let over 90% of the laser light through while reflecting the transmitted light to the webcam. |
| SM1 to RMS thread adapter | Thorlabs | SM1A3TS | Allows the objective to be mounted directly on the mirror holding cube. |
| 4X Objective | Thorlabs | RMS4X | Objective used for light delivery and sample imaging. |
| **SAMPLE VISUALIZATION PATH** | | | |
| Lens tube for focussing lens | Thorlabs | SM1L25 | This tube connects to the cube and holds the lens focussing the image on the camera sensor. |
| Bi convex lens f= 40 mm | Thorlabs | LB1027 | This is used to image on the webcam sensor. |
| 3D printed webcam adapter | 3D printed | | See SCAD file. |
| Webcam | | | Any standard webcam would work but its original lens will need to be removed. |
| **STAGE AND OXYGEN DELIVERY** | | | |
| XYZ Stage | Laser2000 | TAR-38405L-M6 | 3-axis translator for sample positioning. |
| Stage | 3D printed | | See SCAD file. |
| Capillary holder | 3D printed | | See SCAD file. |
| Petri dish insert | 3D printed | | See SCAD file. |
| Glass O-ring | Glass blowing workshop | | Normally cut from a 19mm capillary. |

providing an effective magnification of 1.5X. This provides an adequate compromise between magnification and field of view. The ability to identify the region of interest with a large field of view greatly speeds up the positioning process down to a few minutes. Depending on user's experience and region of interest's size, the positioning process can take up to 45 min when using a high power objective and following a "roadmap" acquired before tissue fixation, particularly without the aid of fluorescence.

## 2.3. Stage and Oxygen Delivery

To minimize the cost, a stage was designed using OpenSCAD (openscad.org) and 3D-printed using an Ultimaker2$^+$ 3D-printer. The stage is connected to the 3-axis translator and used to hold and position the sample. Magnetic metal should be glued on the stage to position a capillary holder (**Figure 2C**). The stage includes a support for the throughhole LEDs used to illuminate the sample (**Figures 1B**, **2B**). Once ready for photoconversion, the fixed tissue is placed in a 35 mm petri dish containing a plastic insert (**Figure 2C**) and held down with a glass O-ring (19 mm O.D.) with nylon strings (Marra et al., 2014). Once the user has identified the region of interest, PBS can be replaced with the DAB solution and oxygenated using Carbogen (95% $O_2$ and 5% $CO_2$). Carbogen is delivered using a glass capillary with an opening of $>150\,\mu m$. The capillary is held by a 3D-printed holder (**Figure 2C**) with a magnet glued to its base for positioning. The plastic insert has two functions: keeping the sample and the O-ring in the center of the petri dish and avoiding bubbles from floating over the sample and thus scattering the light (**Figure 2C**).

# 3. MATERIALS AND METHODS

## 3.1. Brain Slice Preparation

This study was conducted in accordance with the UK Animals (Scientific Procedures) Act, 1986 and following institutional regulations by the University of Leicester, animals were sacrificed under Schedule 1 and the project did not require full review and approval by the Home Office. Experiments were performed

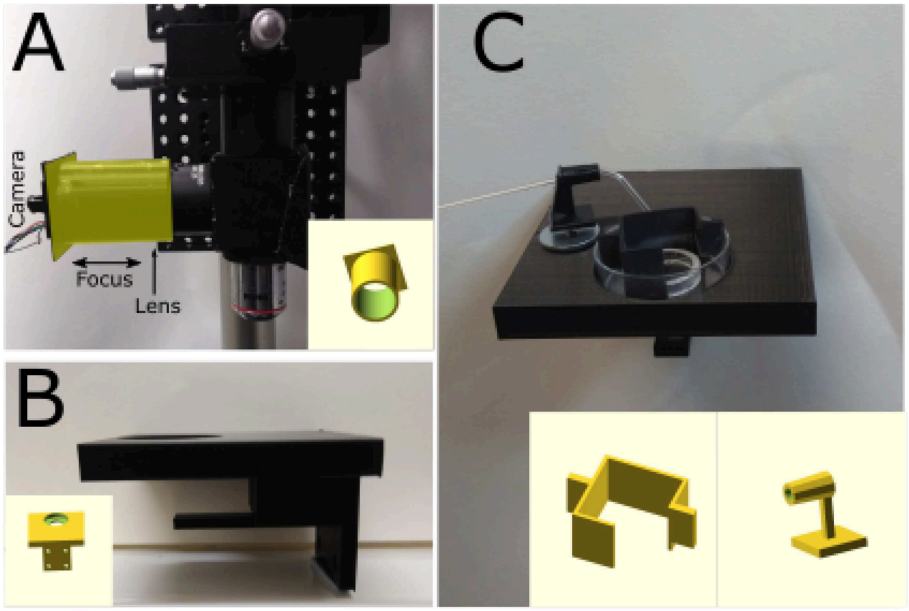


**FIGURE 2 |** 3D-printed components. **(A)** Photograph of a simple adaptor (highlighted in the yellow) for mounting a webcam board onto a Thorlabs 1" lens tube. The lens focusing the image on the sensor is placed inside the tube and the 3D-printed adaptor can be moved to focus the image. Insert: 3D model of the adaptor. **(B)** Photograph of stage mounted on 3-axis translator. Metal disks were glued and covered with transparent plastic to avoid DAB-induced oxidation. Insert: 3D model of the stage. **(C)** Sample in a 35 mm petri dish held in position by a 19 mm glass ring with nylon string across its middle and plastic box that prevents sample movement and bubbles covering the sample.The sample would placed under the glass ring. Glass capillary holder with a magnet mounted at its bottom to hold it in position. The capillary is used to oxygenate the solution and facilitate DAB photoconversion. Insert: 3D model of petri dish box and capillary holder.

in CBA/Ca mice of either sex postnatal day 15—20. Animals were humanely killed by cervical dislocation and cessation of circulation was confirmed by severing the carotid artery. The brain was rapidly removed and placed into ice-cold oxygenated artificial cerebrospinal fluid (aCSF) consisting of (in mM): 125 NaCl, 2.5 KCl, 26 $NaHCO_3$, 1.25 $NaH_2PO_4$, 25 glucose, 1 $MgCl_2$, 2 $CaCl_2$; pH 7.3 when bubbled with 95% $O_2$ and 5% $CO_2$. Auditory cortex slices were cut at a thickness of 350 µm using a vibrating microtome (Leica VT1200S) at an angle of 15° off horizontal to preserve thalamocortical projections (Llano et al., 2014). Slices were allowed to recover for 20 min at 32°C before being cooled to room temperature.

## 3.2. Electrophysiology and Cell Labeling

Whole-cell recordings were made from visually identified layer 5 pyramidal neurons. Intracellular recording solution consisted of (in mM): 115 $KMeSO_4$, 5 KCl, 10 HEPES, 10 creatine phosphate, 0.5 EGTA, 2 MgATP, 2 $Na_2ATP$, 0.3 $Na_2GTP$, 290 mOsm, with the addition of Lucifer Yellow (1 mg/mL, Sigma-Aldrich, ex/em 425/540 nm). After 5 min in whole-cell configuration a Z-stack image of the dye-loaded cell was acquired for later reference. A glass stimulating electrode filled with FM 1-43FX (20 µM in aCSF) (Thermofisher) was positioned ∼ 150 µm from the recorded cell soma at a depth equal to that of the recording electrode. Prior to the onset of dye application the stimulus intensity was set to give a reliable excitatory post-synaptic current (EPSC) amplitude of ∼200 pA, to ensure the recruitment of a large number of presynaptic terminals.

## 3.3. Vesicle Labeling

FM 1-43FX (Thermofisher, ex/em 473/585 nm) dye was locally applied by providing 1.03 bars of positive pressure for a total of 5 min. Two minutes after the start of dye application presynaptic terminals were stimulated at 10 Hz for 60 s using a stimulus isolator (Digitimer). Dye application continued for further 2 min for a total of 5 min dye application and 10 min in whole-cell configuration. The recording electrode was then carefully withdrawn to reseal the recorded cell and minimize Lucifer Yellow leakage.

## 3.4. Fixation and Photoconversion

Fixation and photoconversion were performed ensuring the samples' exposure to light was kept to a minimum and following the protocol of Marra et al. (2014). Slices were carefully removed from the recording chamber and fixed in 6% glutaraldehyde/2% paraformaldehyde in PBS using microwave-assisted fixation. Samples were blocked in 100 mM glycine solution for 1 h, rinsed in 100 mM ammonium chloride for 1 min, then washed in PBS. The sample was then positioned on the photoconversion setup (**Figure 1B**) with a fine bore glass capillary immersed to allow continuous bubbling with Carbogen throughout. PBS was replaced with 1 mg/mL DAB solution prepared in oxygenated PBS and incubated in the dark for 10 min. This was replaced with fresh oxygenated DAB solution and the photoconversion reaction initiated using the 473nm DPSS laser (**Figure 1A**). Before starting the photoconversion reaction, the laser should be set to a low power setting and positioned on the region of interest

using the fine XY lens translator while the transmission LEDs are on, to obtain an unequivocal image of the photoilluminated region on the sample. Reactions were monitored every 5–10 min and terminated when a defined dark region was visible on the slice. Since a number of factors may affect the time required to obtain a successful photoconversion, we recommend monitoring

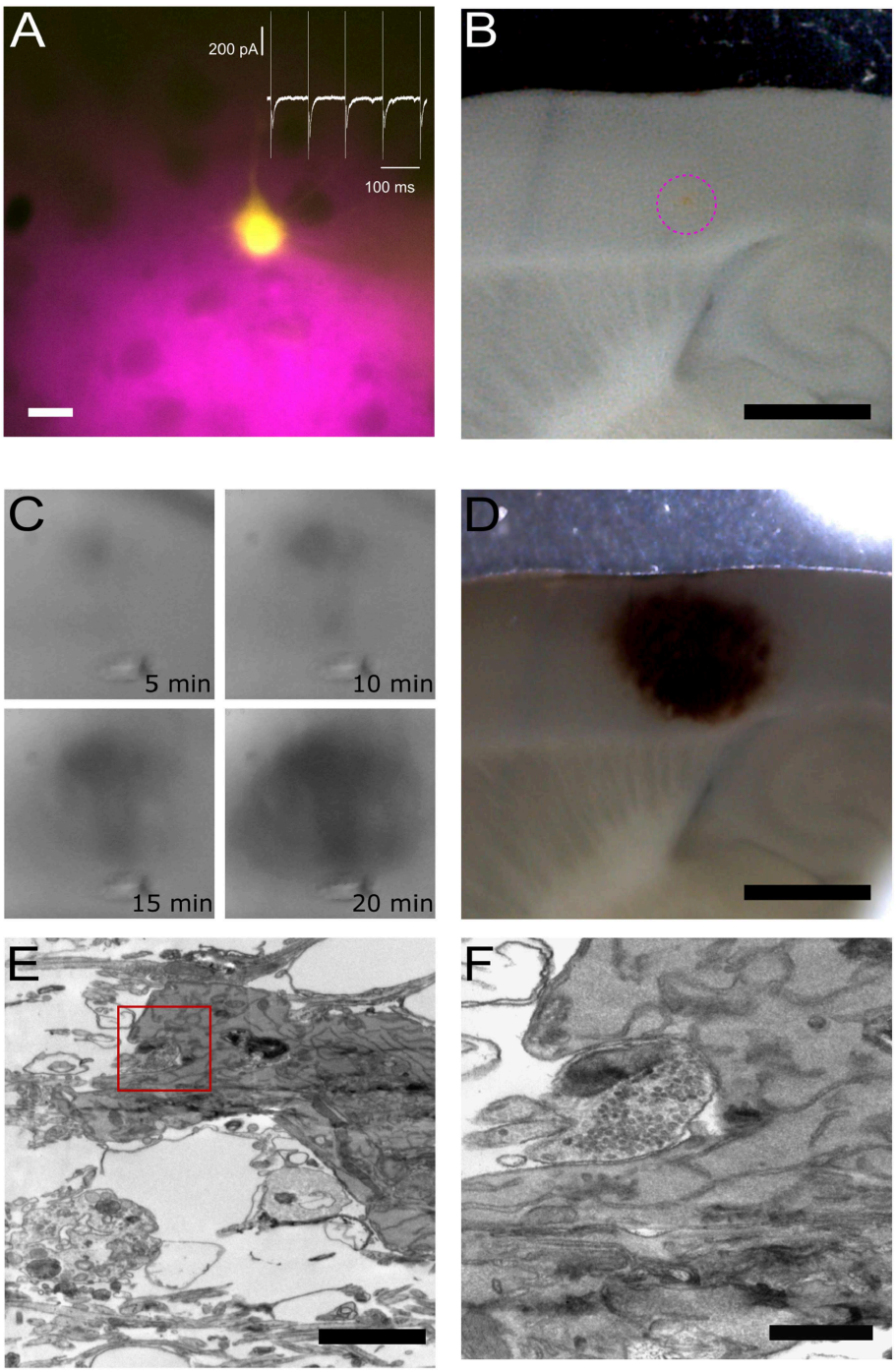


**FIGURE 3 |** Pre- and post-synaptic photoconversion anticipated results. **(A)** Pyramidal neuron loaded with Lucifer Yellow with region of pressure-applied FM dye highlighted in magenta. Insert: whole-cell voltage clamp recording from loaded cell. Scale bar: 20 μm. **(B)** Acute slice following fixation, with FM dye region clearly visible (magenta dashed circle). Scale bar: 1 mm. **(C)** Development of the photoconversion product monitored at 5 min intervals. **(D)** Photoconverted region extending across FM dye region and Lucifer Yellow-loaded neuron. Scale bar: 1 mm. **(E)** Electron micrograph of Lucifer Yellow-loaded neuron. Scale bar: 20 μm. **(F)** Higher magnification electron micrograph of the same spine as **(E)**, with FM-loaded vesicles observed in the presynaptic terminal. Scale bar: 500 nm.

the process at regular intervals (∼5 min) by powering down the laser and measuring the intensity of the transmitted light. In the first 10 min there should be a clear decrease in transmitted light intensity that will plateau when the photoconversion process is complete (see Marra et al., 2014). The photoconversion of FM-stained dead tissue will reduce light penetration as the reaction progresses. Using an approximately collimated beam ensures that a large volume is photoconverted before light penetration becomes an issue. The sample was then washed 3 x 5 min in PBS. An image of the photoconverted slice was captured and the sample trimmed for further processing.

### 3.5. Sample Processing for Electron Microscopy

Processing of the fixed photoconverted tissue for electron microscopy follows the protocol of Deerinck et al. (2010). Briefly, samples were washed with 0.15 M sodium cacodylate buffer prior to osmication (2% $OsO_4$, 1.5% $K4Fe(CN)_6$). Samples were then washed with $dH_2O$ and incubated in 1% thiocarbohydrazide solution. Tissues were rinsed again in $dH_2O$ and thereafter placed in 2% osmium tetroxide. Following this second exposure to osmium the tissues were washed with $dH_2O$ then placed in 1% uranyl acetate at 4°C overnight. As an optional step, samples were then washed again with $dH_2O$ and stained *en bloc* with freshly prepared 20 mM lead aspartate. After further $dH_2O$ washes samples are serially dehydrated using a gradient of ethanol solutions and finally with 100% acetone. Samples were infiltrated with Durcupan$^{TM}$ resin before being transferred to a BEEM capsule for embedding and polymerization. With reference to the image of the photoconverted tissue the sample was trimmed, ultrathin (∼70 nm) sections cut and mounted on copper grids. Sections were imaged on a JEOL 1400 transmission electron microscope equipped with an OptiMos (QImaging).

## 4. ANTICIPATED RESULTS

### 4.1. Simultaneous Photoconversion of FM 1-43FX and Lucifer Yellow

To show potential applications of the photoconversion setup, we have combined electrophysiological recordings of a neuron filled with Lucifer Yellow via a patch pipette with simultaneous loading of synaptic vesicles with FM 1-43FX. FM-loading is obtained by puffing the dye with a glass pipette which is also used to deliver the stimulation required for the labeling of synaptic vesicles (10 Hz, 60 s), vesicular release is monitored recording the post-synaptic neuron in voltage clamp (**Figure 3A**). Importantly, the choice of stimulation frequency and duration will depend on the biological question asked. For example, a 1 Hz stimulation for 30 s can be used to study single site release probability (Branco et al., 2010), stimulation frequencies of 10 Hz or above for 1 or 2 min may be used to label the entire recycling pool (Fornasiero et al., 2012) and higher frequency stimulations for few seconds may be used to label the readily releasable pool (Rey et al., 2015). The stimulation frequency used will also depend on the type of synapse probed. For example, at large release sites such as the Calyx of Held, a giant synapse in the auditory pathway, stimulations > 100 Hz are appropriate to recruit the total recycling pool (Lucas et al., 2018); similarly at neuromuscular junctions long high frequency stimulations (30 Hz, 5 min) may be needed (Denker et al., 2009).

**Figure 3** provides an overview of typical results plus examples of the tissue at each stage of processing. The location of the two fluorophores, FM 1-43FX to label presynaptic vesicles and Lucifer Yellow to fill the post-synaptic cell, is visible throughout processing, thus giving the user confidence in the final structural information correlating with the functional readout from the electrophysiological assay. The site of delivery for FM 1-43FX can be easily visualized at low magnification (**Figure 3B**). Following fixation, the sample is moved to the photoconversion setup where the reaction's progression can be observed as a darkening of the tissue (Marra et al., 2014). Before processing for electron microscopy the photoconverted region appears as a dark spot on the tissue (**Figure 3D**). Electron dense structures are readily identifiable in the resultant electron micrograph as a soma containing DAB precipitate (**Figure 3E**) and photoconverted vesicles observed in the terminal opposite the labeled post-synaptic neuron (**Figure 3F**). Lucifer Yellow's absorption is only 25% at 473 nm and this appears sufficient to drive DAB photoconversion without excessive DAB-damage (**Figure 3E**).

Depending on the stimulation protocol, the approach demonstrated here can be used to investigate a number of key synaptic and cellular parameters, e.g., synaptic sites, release probability, recycling pool organization, and in general the impact of pre- and post-synaptic structures on synaptic function.

## 5. DISCUSSION

The functional study of axonal fine structures often requires a combination of fluorescence and electron microscopy. These measurements can be performed in parallel (Clayton et al., 2008; Cheung et al., 2010; Chung et al., 2010; Ratnayaka et al., 2012) or in a correlative way following the same axons and synapses from light to electron microscopy (reviewed by Branco and Staras, 2009; Begemann and Galic, 2016). In both cases, however, the measurements are limited to dissociated cell cultures. A number of new tools are being developed by commercial and academic research laboratories to simplify the CLEM workflow and to extend it to thick neuronal tissue. Some laboratories are developing new fluorescent proteins able to oxidize DAB in a light-independent way (Shu et al., 2011; Liss et al., 2015; de Beer et al., 2018), while others focus on new microscopes to improve the reliability of CLEM workflow (see Brama et al., 2016).

Here, we presented a simple setup to photoconvert fluorescent signals into electron dense ones. The setup is built to facilitate tracing of the region of interest in thick neuronal tissue improving CLEM workflows for *ex vivo* tissue. A dedicated setup can improve reliability and throughput of the photoconversion; these are the two main limiting factors in the diffusion of the technique. Compared with the use of a standard epifluorescence microscope, our setup increases the depth of photoillumination, improves the targeting of the region of interest and reduces the time required to process each individual sample. Commercial

epifluorescence microscopes have optics to ensure Köhler illumination of the sample, while offering a great advantage for imaging, such optics can attenuate a single wavelength light by ∼90% before it reaches a dichroic mirror and filter, which will further attenuate the light. Additionally, most photoillumination approaches for thick tissue require the "sacrifice" of a high power dipping objective to deliver light (Marra et al., 2014) as, once used for DAB photoconversion, a dipping objective should not be used for live tissue imaging. Additionally, air objectives will not be stained by repeated exposure to DAB, while dipping objectives, even with careful cleaning, will stain over time increasing the photoconversion time and affecting the quality of the image used for positioning.

The budget used for building the setup in 2016 was ∼4500€, with over 50% of the budget used to purchase the laser. However, a suitable 473 nm DPSS laser can now be found for much lower prices or substituted by high-power single-wavelength LEDs, lowering the cost of the entire system to ∼3000€, comparable with the cost of a dedicated high quality dipping objective for photoconversion of thick neuronal tissue (Marra et al., 2014). We demonstrate that the setup described can be used for the simultaneous photoconversion of FM 1-43FX and Lucifer Yellow, allowing the study of cellular ultrastructure and activity and release probability at individual release sites.

## DATA AVAILABILITY

The datasets generated for this study are available on request to the corresponding author.

## ETHICS STATEMENT

This study was carried out in accordance with the recommendations of Animals (Scientific Procedures) as amended in 2012.

## AUTHOR CONTRIBUTIONS

KD acquired the data and tested the setup. YN tested the setup. CH assisted with the design of the setup. VM designed, built and tested the setup. All authors contributed to the manuscript.

## FUNDING

The work was funded by the Wellcome Trust Seed Awards in Science 108201/Z/15/Z.

## ACKNOWLEDGMENTS

The authors would like to thank the Core Bioscience Services for access to the experimental animals, the fluorescence microscope setup by Professor Nicholas Hartell and the electron microscope. In particular, we would like to thank Natalie Allcock for the assistance with the preparation of the samples for electron microscopy and the acquisition of the images. We would also like to thank Amy Richardson for building the PWM laser power regulator and Drs. James McCutcheon and Joern Steinert for lending us components to test the early configuration of the setup. A previous version version of this article was published as preprint on www.biorxiv.org (Dobson et al., 2019).

## REFERENCES

Begemann, I., and Galic, M. (2016). Correlative light electron microscopy: connecting synaptic structure and function. *Front. Synapt. Neurosci.* 8:28. doi: 10.3389/fnsyn.2016.00028

Brama, E., Peddie, C. J., Wilkes, G., Gu, Y., Collinson, L. M., and Jones, M. L. (2016). ultralm and minilm: locator tools for smart tracking of fluorescent cells in correlative light and electron microscopy. *Wellcome open Res.* 1:26. doi: 10.12688/wellcomeopenres.10299.1

Branco, T., Marra, V., and Staras, K. (2010). Examining size-strength relationships at hippocampal synapses using an ultrastructural measurement of synaptic release probability. *J. Struct. Biol.* 172, 203–210. doi: 10.1016/j.jsb.2009.10.014

Branco, T., and Staras, K. (2009). The probability of neurotransmitter release: variability and feedback control at single synapses. *Nat. Rev. Neurosci.* 10, 373–383. doi: 10.1038/nrn2634

Cheung, G., Jupp, O. J., and Cousin, M. A. (2010). Activity-dependent bulk endocytosis and clathrin-dependent endocytosis replenish specific synaptic vesicle pools in central nerve terminals. *J. Neurosci.* 30, 8151–8161. doi: 10.1523/JNEUROSCI.0293-10.2010

Chung, C., Barylko, B., Leitz, J., Liu, X., and Kavalali, E. T. (2010). Acute dynamin inhibition dissects synaptic vesicle recycling pathways that drive spontaneous and evoked neurotransmission. *J. Neurosci.* 30, 1363–1376. doi: 10.1523/JNEUROSCI.3427-09.2010

Clayton, E. L., Evans, G. J., and Cousin, M. A. (2008). Bulk synaptic vesicle endocytosis is rapidly triggered during strong stimulation. *J. Neurosci.* 28, 6627–6632. doi: 10.1523/JNEUROSCI.1445-08.2008

Darcy, K. J., Staras, K., Collinson, L. M., and Goda, Y. (2006). Constitutive sharing of recycling synaptic vesicles between presynaptic boutons. *Nat. Neurosci.* 9, 315–321. doi: 10.1038/nn1640

de Beer, M. A., Kuipers, J., van Bergen En Henegouwen, P. M. P., and Giepmans, B. N. G. (2018). A small protein probe for correlated microscopy of endogenous proteins. *Histochem. Cell Biol.* 149, 261–268. doi: 10.1007/s00418-018-1632-6

Debanne, D., Campanac, E., Bialowas, A., Carlier, E., and Alcaraz, G. (2011). Axon physiology. *Physiol. Rev.* 91, 555–602. doi: 10.1152/physrev.00048.2009

Deerinck, T., Bushong, E., Lev-Ram, V., Shu, X., Tsien, R., and Ellisman, M. (2010). Enhancing serial block-face scanning electron microscopy to enable high resolution 3-d nanohistology of cells and tissues. *Microsc. Microanal.* 16, 1138–1139. doi: 10.1017/S1431927610055170

Denker, A., Kröhnert, K., and Rizzoli, S. O. (2009). Revisiting synaptic vesicle pool localization in the drosophila neuromuscular junction. *J. Physiol.* 587, 2919–2926. doi: 10.1113/jphysiol.2009.170985

Dobson, K. L., Howe, C. L., Nishimura, Y., and Marra, V. (2019). Dedicated setup for the photoconversion of fluorescent dyes for functional electron microscopy. *BioRxiv* [Preprint]. doi: 10.1101/622639

Fornasiero, E. F., Raimondi, A., Guarnieri, F. C., Orlando, M., Fesce, R., Benfenati, F., et al. (2012). Synapsins contribute to the dynamic spatial organization of synaptic vesicles in an activity-dependent manner. *J. Neurosci.* 32, 12214–12227. doi: 10.1523/JNEUROSCI.1554-12.2012

Gramlich, M. W., and Klyachko, V. A. (2019). Nanoscale organization of vesicle release at central synapses. *Trends Neurosci.* 42, 425–437. doi: 10.1016/j.tins.2019.03.001

Harata, N., Ryan, T. A., Smith, S. J., Buchanan, J., and Tsien, R. W. (2001). Visualizing recycling synaptic vesicles in hippocampal neurons by

fm 1-43 photoconversion. *Proc. Natl. Acad. Sci. U.S.A.* 98, 12748–12753. doi: 10.1073/pnas.171442798

Jonas, P., Major, G., and Sakmann, B. (1993). Quantal components of unitary epscs at the mossy fibre synapse on ca3 pyramidal cells of rat hippocampus. *J. Physiol.* 472, 615–663. doi: 10.1113/jphysiol.1993.sp019965

Liss, V., Barlag, B., Nietschke, M., and Hensel, M. (2015). Self-labelling enzymes as universal tags for fluorescence microscopy, super-resolution microscopy and electron microscopy. *Sci. Rep.* 5:17740. doi: 10.1038/srep17740

Llano, D. A., Slater, B. J., Lesicko, A. M., and Stebbings, K. A. (2014). An auditory colliculothalamocortical brain slice preparation in mouse. *J. Neurophysiol.* 111, 197–207. doi: 10.1152/jn.00605.2013

Lucas, S. J., Michel, C. B., Marra, V., Smalley, J. L., Hennig, M. H., Graham, B. P., et al. (2018). Glucose and lactate as metabolic constraints on presynaptic transmission at an excitatory synapse. *J. Physiol.* 596, 1699–1721. doi: 10.1113/JP275107

Maranto, A. R. (1982). Neuronal mapping: a photooxidation reaction makes lucifer yellow useful for electron microscopy. *Science* 217, 953–955. doi: 10.1126/science.7112109

Marra, V., Burden, J. J., Crawford, F., and Staras, K. (2014). Ultrastructural readout of functional synaptic vesicle pools in hippocampal slices based on fm dye labeling and photoconversion. *Nat. Protoc.* 9, 1337–1347. doi: 10.1038/nprot.2014.088

Marra, V., Burden, J. J., Thorpe, J. R., Smith, I. T., Smith, S. L., Häusser, M., et al. (2012). A preferentially segregated recycling vesicle pool of limited size supports neurotransmission in native central synapses. *Neuron* 76, 579–589. doi: 10.1016/j.neuron.2012.08.042

Neher, E., and Sakaba, T. (2001). Combining deconvolution and noise analysis for the estimation of transmitter release rates at the calyx of held. *J. Neurosci.* 21, 444–461. doi: 10.1523/JNEUROSCI.21-02-00444.2001

Opazo, F., and Rizzoli, S. O. (2010). Studying synaptic vesicle pools using photoconversion of styryl dyes. *J. Vis. Exp.* e1790. doi: 10.3791/1790

Peddie, C. J., Domart, M.-C., Snetkov, X., O'Toole, P., Larijani, B., Way, M., et al. (2017). Correlative super-resolution fluorescence and electron microscopy using conventional fluorescent proteins in vacuo. *J. Struct. Biol.* 199, 120–131. doi: 10.1016/j.jsb.2017.05.013

Pulido, C., Trigo, F. F., Llano, I., and Marty, A. (2015). Vesicular release statistics and unitary postsynaptic current at single gabaergic synapses. *Neuron* 85, 159–172. doi: 10.1016/j.neuron.2014.12.006

Ratnayaka, A., Marra, V., Branco, T., and Staras, K. (2011). Extrasynaptic vesicle recycling in mature hippocampal neurons. *Nat. Commun.* 2:531. doi: 10.1038/ncomms1534

Ratnayaka, A., Marra, V., Bush, D., Burden, J. J., Branco, T., and Staras, K. (2012). Recruitment of resting vesicles into recycling pools supports nmda receptor-dependent synaptic potentiation in cultured hippocampal neurons. *J. Physiol.* 590(Pt 7), 1585–1597. doi: 10.1113/jphysiol.2011.226688

Rey, S. A., Smith, C. A., Fowler, M. W., Crawford, F., Burden, J. J., and Staras, K. (2015). Ultrastructural and functional fate of recycled vesicles in hippocampal synapses. *Nat. Commun.* 6:8043. doi: 10.1038/ncomms9043

Sabeva, N. S. and Bykhovskaia, M. (2017). Fm1-43 photoconversion and electron microscopy analysis at the drosophila neuromuscular junction. *Bio Protoc.* 7:e2523. doi: 10.21769/BioProtoc.2523

Shu, X., Lev-Ram, V., Deerinck, T. J., Qi, Y., Ramko, E. B., Davidson, M. W., et al. (2011). A genetically encoded tag for correlated light and electron microscopy of intact cells, tissues, and organisms. *PLoS Biol.* 9:e1001041. doi: 10.1371/journal.pbio.1001041

Smith, A. D., and Bolam, J. P. (1990). The neural network of the basal ganglia as revealed by the study of synaptic connections of identified neurones. *Trends Neurosci.* 13, 259–265. doi: 10.1016/0166-2236(90)90106-K

Viney, T. J., Lasztoczi, B., Katona, L., Crump, M. G., Tukker, J. J., Klausberger, T., et al. (2013). Network state-dependent inhibition of identified hippocampal ca3 axo-axonic cells *in vivo*. *Nat. Neurosci.* 16, 1802–1811. doi: 10.1038/nn.3550

**Conflict of Interest Statement:** The authors declare that the research was conducted in the absence of any commercial or financial relationships that could be construed as a potential conflict of interest.

*Copyright © 2019 Dobson, Howe, Nishimura and Marra. This is an open-access article distributed under the terms of the Creative Commons Attribution License (CC BY). The use, distribution or reproduction in other forums is permitted, provided the original author(s) and the copyright owner(s) are credited and that the original publication in this journal is cited, in accordance with accepted academic practice. No use, distribution or reproduction is permitted which does not comply with these terms.*

frontiers in Cellular Neuroscience

MINI REVIEW
published: 02 August 2019
doi: 10.3389/fncel.2019.00354

# Antidromic Analog Signaling

*Federico F. Trigo*[1,2]*

[1] CNRS UMR8003, SPPIN Laboratory, Cerebellar Neurophysiology Group, Faculté des Sciences Fondamentales et Biomédicales, Université de Paris, Paris, France, [2] Departamento de Neurofisiología Celular y Molecular, Instituto de Investigaciones Biológicas Clemente Estable, Montevideo, Uruguay

Analog signaling describes the use of graded voltage changes as signals in the axonal compartment. Analog signaling has been described originally in invertebrates but more recent work has established its presence in the mammalian brain (Alle and Geiger, 2006; Shu et al., 2006). In recent years, many different groups have contributed to the understanding of the physiological significance of analog signaling from a cellular perspective (for a recent review the reader may take a look at the work by Zbili and Debanne, 2019 in this *Frontiers in Neuroscience* Special Issue). The great majority of the experimental work related to analog signaling, however, concerns the propagation of subthreshold voltage changes from the soma to the axon. Much less attention has been paid to the propagation of subthreshold voltage changes in the opposite direction, from the axon to the soma, or to the propagation of local signals within the axon. In this mini review we will describe these other variants of analog signaling that we call here "antidromic" coupling and "local" coupling.

**Keywords: analog – digital signaling, antidromic, axon, neuron, action potential, subthreshold**

OPEN ACCESS

***Edited by:***
*Sergey M. Korogod, Bogomoletz Institute of Physiology (NASU), Ukraine*

***Reviewed by:***
*Dominique Debanne, Unité de Neurobiologie des Canaux Loniques et de la Synapse, France*
*Sylvain Rama, University College London, United Kingdom*

***Correspondence:**
*Federico F. Trigo*
*federico.trigo@parisdescartes.fr*

***Specialty section:***
*This article was submitted to Cellular Neurophysiology, a section of the journal Frontiers in Cellular Neuroscience*

***Received:*** *30 May 2019*
***Accepted:*** *17 July 2019*
***Published:*** *02 August 2019*

***Citation:***
*Trigo FF (2019) Antidromic Analog Signaling. Front. Cell. Neurosci. 13:354. doi: 10.3389/fncel.2019.00354*

## INTRODUCTION

The term "analog signaling" is used to describe the passive propagation of electrical signals among different neuronal compartments. In recent years it became clear that subthreshold or passive (analog) coupling between the somatodendritic and the axonal compartments is far more prevalent than what was expected 15 years ago (in invertebrate neurons the existence of analog signaling has been recognized a long time ago, Marder, 2006; Zbili and Debanne, 2019). This is probably due, at least in part, to the technical improvements that have been accomplished by different labs around the world, which allow to perform electrophysiological recordings and high-resolution imaging from single axonal varicosities.

Although there are some examples in the literature showing that some synapses can operate on the sub-threshold regime (i.e., in a graded manner, like in the vertebrate photoreceptor, Heidelberger, 2007), the majority of synapses operate in a digital fashion, where release happens when the action potential (AP) reaches the presynaptic varicosity. Nevertheless, the value of the local potential at the release site before the AP can influence the amount of release. This has led to the term "Analog–Digital" transmission, to stress the fact that the membrane potential at the varicosity right before the arrival of a spike can affect the AP shape and hence, release (see section on "Intra-Axonal Analog Signaling").

Even more challenging than this orthodromic analog coupling (**Figure 1**, *Left*), is the idea that the axonal compartment may also be the input compartment of a neuron and that some of the signals that originate in the axon may reach the soma and affect neuronal excitability (**Figure 1**, *Middle*). This idea challenges Ramón y Cajal's dynamic polarization theory, that states that information in the nervous system is unidirectional, flowing from the dendrites to the soma to the axon. In antidromic signaling, the signal goes on the contrary from the axon to the soma. The present review discusses this paradoxical, often neglected form of axonal signaling, as well as another form of analog signaling that can be considered a variant of the previous one, "local" signaling, where axonal voltage changes remain confined to the axonal compartment (**Figure 1**, *Right*).

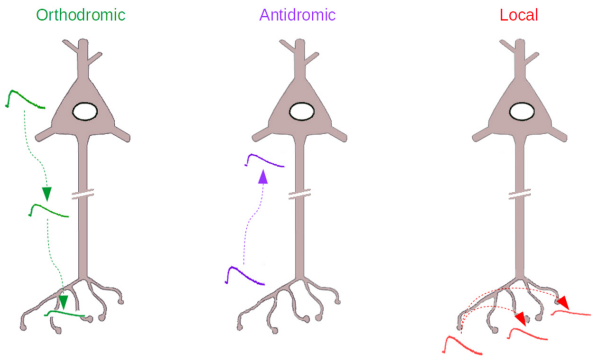


**FIGURE 1 |** The three types of Analog signaling that have been described in the literature. *Left*, the orthodromic signaling, where somatodendritic voltage changes propagate to the axon. *Middle*, the antidromic signaling, where axonal voltage changes propagate backward to the axon initial segment and soma. *Right*, the local signaling, where axonal voltage changes propagate within the axon, to other varicosities, without escaping from the axonal compartment.

## THE AXONAL LENGTH CONSTANT, "λ"

Transmission of electrical signals in the axon can be approached by approximating the axon structure with a cable. The extent of propagation of passive signals in a cable of infinite length at steady state follows an exponential function of distance. The length constant (lambda, "λ") depends on the cable internal resistance (the cytoplasmic resistance, which is a function of the cable diameter) and on the membrane resistance of the axon (Rall, 1969a,b; Rall and Rinzel, 1973).

While the value of lambda does not depend on the direction of the signal propagation for an infinite cable, directionality becomes important for finite length axon cables linked to other axonal or somatic compartments. Specifically, the voltage changes produced either in the soma or in the axon by some current injected in the other compartment will depend on the passive characteristics of the target compartment (the soma when the current is injected in the axon and the axon when the current is injected in the soma), that is, input resistance and membrane capacitance. This was recently studied in detail by Hu and Bean (2018), who made simultaneous patch-clamp recordings from the soma and the axon of cortical pyramidal neurons and quantified the degree of coupling in both directions, ortho and antidromic. In their study, the authors showed that coupling is stronger in the orthodromic than in the antidromic direction, and they attributed this effect to the impedance mismatch between the two compartments: the input resistance being much lower in the soma, an axonally injected current will induce a strong local (i.e., axonal) voltage change and a much smaller somatic voltage change. As pointed out by Thome et al. (2018), who showed a similar asymmetric coupling between the axonal and the somatic compartment of hippocampal pyramidal neurons, the input capacitance of each compartment will also have a kinetic effect: the higher the capacitance (soma), the slower will be the voltage change; the smaller the capacitance (axon), the quicker the voltage change will be.

In their study, Hu and Bean (2018) also showed that the axonal and somatic resting membrane potentials differ by a few millivolts due to the differential expression of different voltage dependent conductances. In the neurons under study, the somatodendritic Ih current strongly influences the axonal membrane potential (blocking Ih equalizes the somatic and the axonal Vm), but the axonal KV7 current has a negligible effect on the somatodendritic potential. This, again, can be explained by the asymmetry between orthodromic and antidromic coupling.

Although asymmetric coupling may be a general feature of mammalian neurons, its extent is expected to vary markedly depending on cell size. In smaller and more compact cells, like GABAergic interneurons or cerebellar granule cells, where the somatic input resistance is much higher, the asymmetry may be expected to be smaller than in big cells (like the cortical pyramidal cells studied by Hu and Bean, 2018). In these cells, one can expect a much bigger influence of axonal activity on the somatic membrane potential. The exact contribution of the size and general morphological features of a cell on the impact of the orthodromic coupling on cellular excitability remains to be characterized. In the next section we will describe some examples.

## ANTIDROMIC SIGNALS MEDIATED BY AXONAL IONOTROPIC RECEPTORS

Axonal, or presynaptic ionotropic receptors have been described in a large variety of neuronal types in the central and peripheral nervous system (MacDermott et al., 1999). The best documented presynaptic receptors are probably $GABA_A$ receptors ($GABA_ARs$), which have been originally described in sensory primary afferents of the spinal cord (for a recent review on axonal $GABA_ARs$ please see Trigo et al., 2008). In this preparation, GABA is released from the presynaptic compartment at axo-axonic synapses, and activation of presynaptic $GABA_ARs$ results in presynaptic inhibition (a decrease in the amount of neurotransmiter released from the presynaptic side).

Following the pioneering work of Frank and Fuortes (1957), axonal $GABA_ARs$ have been found in multiple neuronal cell types, and their mode of action has been studied in detail. In

some cases activation of axonal $GABA_A$ receptors appeared to be transmitted antidromically to the soma. An early example is a study by Pouzat and Marty (1999), who described an autoreceptor $GABA_A$ current recorded from the soma of cerebellar molecular layer interneurons (MLIs, stellate and basket cells, parvalbumin positive GABAergic interneurons of the cerebellar cortex) that depends on the released GABA binding back to $GABA_A$Rs located on the releasing cell (so-called axonal $GABA_A$ autoRs). It was shown later by Mejia-Gervacio and Marty (2006) that $GABA_A$ autoRs can shape MLI firing. In 2010 we extended this work and showed that in MLIs the activation of $GABA_A$Rs in a single varicosity generates a measurable signal (a "premini," from "presynaptic miniature" current) that can back-propagate to the soma. More recently, we used calcium photolysis in single varicosities to demonstrate that the voltage changes associated with preminis are able to change the cell excitability, probably by modifying AP threshold in the AIS (Zorrilla de San Martin et al., 2015).

Interestingly, the voltage changes produced by the activation of axonal $GABA_A$Rs in MLIs are shaped by the activation of voltage-dependent conductances in the axon. In the work by Mejia-Gervacio and Marty (2006), the authors showed that the effects of the autoreceptor-mediated responses on cellular excitability are counterbalanced by the Ih conductance (a cationic conductance that has a depolarized reversal potential and that is activated by membrane potential hyperpolarization; in MLIs, this conductance is located primarily in the axon, Southan et al., 2000; Luján et al., 2005). More recently, we showed that autoR-mediated depolarizations are amplified by a voltage-dependent sodium conductance, probably a persistent sodium current (Zorrilla de San Martin et al., 2015). These experiments highlight the complex interactions that exist between different ligand and voltage-dependent conductances in the axon and stress the necessity to perform direct recordings from the axonal compartment in order to get a clear understanding of axonal physiology.

Cerebellar granule cells constitute another cell type where signals originating in the axon can reach the soma and change the cell excitability. It was first shown in Stell et al. (2007) that granule cell axons, known as parallel fibers, possess $GABA_A$Rs; their activation increases GABA release, which implies a local depolarizing effect. More recently it was shown that these local, $GABA_A$-mediated depolarizations can also reach the somatic compartment and change granule cell excitability (Pugh and Jahr, 2011, 2013; Stell, 2011; Dellal et al., 2012), including by directly inducing spiking in the axon (Pugh and Jahr, 2011) (see section below on "Ectopic APs," EAPs).

In their study, Dellal et al. (2012) provide some details on the mechanism by which axonal $GABA_A$Rs increase granule cell's excitability. By performing a computational model of the cell, the authors show that the increases in local, axonal excitability and those in somatic excitability produced by the antidromic propagation of subthreshold signals are exquisitely sensitive to the exact chloride equilibrium potential. The increase in conduction velocity observed experimentally, on the other hand, is very sensitive to the voltage dependence of sodium channel inactivation, again highlighting the critical role that axonal voltage-dependent conductances have for the behavior of the axon (Dellal et al., 2012).

## ANTIDROMIC SIGNALS MEDIATED BY VOLTAGE-DEPENDENT CONDUCTANCES

It is well established that the axonal compartment has a specific population of voltage-dependent channels that differs from that of the somatodendritic compartment. These channels contribute to axonal AP propagation and fidelity (see, for example, Hu and Jonas, 2014) and determine the exact AP waveform (see, for example, Geiger and Jonas, 2000) and hence, transmitter release. In the Calyx of Held, a giant synaptic terminal of the auditory pathway in the brainstem, different stimulation paradigms produce varying AP trains, with a typical afterhyperpolarization (due to a $Na^+/K^+$ ATPase pump; Kim et al., 2007) and afterdepolarization (sensitive to riluzole, presumably produced by a persistent type of $Na^+$ current; Paradiso and Wu, 2009). By combining direct terminal recordings from the Calyx and extracellular stimulation of the parent axon, Paradiso and Wu (2009) demonstrated that the axonal voltage changes (produced locally in the Calyx) can travel back to the soma for hundreds of microns and affect AP threshold. The exact effect on excitability of the axonal voltage changes described by Paradiso and Wu (either and increase or a decrease in AP probability) depended on the exact spiking pattern, with the afterdepolarization dominating at the beginning of the burst and the afterhyperpolarization taking over at later stages.

The experiments performed by Paradiso and Wu show that the common view that somatodendritic voltage-dependent conductances determine spiking is an oversimplification. These experiments emphasize the role of the axon in regulating the spiking pattern of the neuron, which is extremely relevant for the physiology of the neuron because it controls the characteristics of synaptic release and therefore, plasticity mechanisms.

## INTRA-AXONAL ANALOG SIGNALING

Local or "intra-axonal" analog signaling has been difficult to study for technical reasons: demonstration of this type of coupling requires recording from 2 varicosities simultaneously. To perform such a challenging experiment, it is necessary to select a special preparation such as the cerebellar primary culture preparation (Kawaguchi and Hirano, 2013; Kawaguchi and Sakaba, 2015) where the axon is planar and where individual cells can be transfected with fluorescent markers, greatly facilitating the identification of the varicosities to be patched. Zorrilla de San Martin et al. (2017) recorded from 2 Purkinje cell varicosities simultaneously. When some current was injected in one varicosity it produced a local voltage change and a voltage change in the neighboring varicosity as well. The voltage change decremented exponentially as a function of distance along the axon, as can be expected from a passive phenomenon, with a $\lambda$ close to 100 $\mu$m.

What kind of signal could give rise to local axonal depolarization in Purkinje cells? In their paper, Zorrilla de San Martín et al. found that Purkinje cells boutons express $GABA_A$ receptors. In several neuron types the reversal potential for $GABA_A$ receptors, $E_{GABA}$, has been found to be less negative in the axon than in the soma (Price and Trussell, 2006; Szabadics et al., 2006). Purkinje cell axons are no exception. By performing perforated, cell-attached recordings, it was shown that axonal receptors mediate a response that has a reversal potential around −47 mV, more depolarized than the somatic $E_{GABA}$ (∼ −73 mV). Therefore, local activation of axonal $GABA_A$ receptors in Purkinje cell axons induces a depolarizing signal that is propagated to neighboring varicosities. The upstream signal seems to be axonal firing and subsequent $GABA_A$ autoR activation (like in cerebellar interneurons), but other options such as spillover GABA release from neighboring axons, or GABA release from glia, are also possible. Concerning this last possibility, evidence in other systems indicates that the original signal may come from non-neuronal cells, like astrocytes. Sasaki et al. (2011) showed that glutamate released by astrocytes surrounding the axonal varicosities of CA3 cells can broaden the AP. Although not shown by the authors, this effect may implicate depolarization propagating across varicosities.

Here, it is important to stress the fact that the intra-axonal, local voltage changes, although sub-threshold, can affect release by modulating the availability of voltage-dependent channels in the varicosity and therefore, the shape of the incoming AP. Also, sub-threshold local voltage changes may also affect release without inducing any change in AP shape, for example by modulating the basal calcium levels or the availability of voltage-dependent calcium channels just before release. For an extensive list of references on this issue the reader can consult the recent review by Zbili and Debanne (2019) and notably their Table 1.

While local analog signaling in the axon domain remains scarcely documented, it is probably even more common than the two other forms of axonal analog signaling, ortho- and antidromic signaling. If some axonal signals reach the soma, as previously discussed, then they must also reach other varicosities, simply because the intervaricosity distance is smaller than the varicosity to soma distance. In the case of long-projecting neurons, such as cortical pyramidal neurons or spinal cord motoneurons, where the axonal length reaches tens and sometimes hundreds of millimeters, local, subthresold axonal signals may hardly ever reach the soma but may have a strong influence on neighboring varicosities. In such a case, the axonal compartment may largely operate independently from the soma, opening new and unexpected possibilities for neuronal computation.

## THE CASE OF ECTOPIC ACTIVITY

So far, we have considered coupling between different axonal compartments for voltage signals in the subthreshold regime. However, it is important to appreciate the fact that local events of high amplitude may reach threshold and evoke spiking activity directly in the distal axon. These locally generated action potentials, called EAPs, differ radically from normal APs that are generated in the axon initial segment. They violate Cajal's polarization rule and travel backward to the soma. EAPs have been extensively documented in invertebrates (for an excellent review of EAPs see Pinault, 1995). In recent years, a few groups have shown conclusively the existence of ectopic spikes in the normal and the physiopathological context in mammals. We will highlight here some of the former examples.

Sheffield et al. (2011) showed that repeated current injection into hippocampal interneurons eventually produces persistent firing, a form of spiking that outlasts the current injection for tens of seconds. The authors showed that persistent firing is not initiated in the soma but in the distal axon and is blocked by gap junction blockers (electrical coupling through axonal electrical synapses has already been shown by Schmitz et al., 2001), although it is still present in connexin 36 knockouts (Sheffield et al., 2013). Interestingly, persistent firing can spread from the stimulated cell to a neighboring, non-stimulated cell.

During network oscillations in the hippocampus (*in vitro* gamma frequency), EAPs are generated in the axon of CA3 pyramidal cells but fail to reach the soma (Dugladze et al., 2012) (giving rise to the so-called "spikelets"); according to the author's results, this is because the voltage changes are shunted by axo-axonic GABAergic synapses on the axon initial segment. Surprisingly, axo-axonic cells are more efficient in preventing the back-propagated EAPs to reach the soma than in preventing the generation of orthodromic spikes (which is usually the main function attributed to axo-axonic cells). Spikelets have also been described in CA1 pyramidal cells *in vivo*, where they represent around one third of the spiking activity of the neuron (Epsztein et al., 2010). Interestingly, the spikelet frequency is modulated according to the location of the animal in space, indicating that spikelets play an important role in spatial exploration.

In a recent paper, Thome et al. (2018) showed that EAPs (probably the spikelets in Epsztein's work) can be triggered in hippocampal CA1 pyramidal neurons by axonal stimulation. In their paper, the authors showed that EAPs reliably propagate toward the soma, and further showed that their occurrence can be modulated by subthreshold synaptic activity, either depolarizing or hyperpolarizing, in the somatodendritic compartment. With this paper Thome and collaborators nicely integrated some of the concepts that have been discussed in this review: the analog, ortho and antidromic coupling between the somatodendritic and axonal compartments of CA1 pyramidal neurons is very prominent; in some special occasions, which remain to be exactly determined, the axon may be capable of generating EAPs that reach the soma and whose activity is, at the same time, controlled by somatodendritic activity.

## CONCLUSION AND FUTURE DIRECTIONS

All the experimental data that has been collected during the past two decades or so has progressively changed our view of the physiology of the axonal compartment. Clearly, the axon cannot be considered as a simple transmission cable, and it

rather emerges as a complex computational unit that increases the operational capabilities of the neuron (Debanne et al., 2011). Today, it is generally accepted that sub threshold voltage changes originating primarily in the dendrites can passively propagate to the axon, where they modify voltage-dependent conductances and AP shape. In this mini-review we summarized recent work showing that signals originating primarily in the axon can back-propagate to the soma, giving rise to a type of antidromic (and sometimes local) analog signaling. For technical reasons, the pace of research in the field of axon signaling has been relatively slow up to now. However, we predict that the development of new, brighter and faster, genetically encoded voltage indicators (for a recent review see Panzera and Hoppa, 2019) will soon open new avenues in the study of the axon, notably by allowing the simultaneous imaging of different axonal regions, far away from the somatic compartment of neurons.

## AUTHOR CONTRIBUTIONS

FT wrote the manuscript and prepared the figure.

## FUNDING

This work was supported by a JCJC ANR grant to FT (ANR-17-CE16-0011-01).

## ACKNOWLEDGMENTS

The author would like to thank Dr. Alain Marty for his helpful discussions, critical reading of the manuscript and useful corrections.

## REFERENCES

Alle, H., and Geiger, J. R. P. (2006). Combined analog and action potential coding in hippocampal mossy fibers. *Science* 311, 1290–1293. doi: 10.1126/science.1119055

Debanne, D., Campanac, E., Bialowas, A., Carlier, E., and Alcaraz, G. (2011). Axon physiology. *Physiol. Rev.* 91, 555–602. doi: 10.1152/physrev.00048.2009

Dellal, S. S., Luo, R., and Otis, T. S. (2012). GABAA receptors increase excitability and conduction velocity of cerebellar parallel fiber axons. *J. Neurophysiol.* 107, 2958–2970. doi: 10.1152/jn.01028.2011

Dugladze, T., Schmitz, D., Whittington, M. A., Vida, I., and Gloveli, T. (2012). Segregation of axonal and somatic activity during fast network oscillations. *Science* 336, 1458–1461. doi: 10.1126/science.1222017

Epsztein, J., Lee, A. K., Chorev, E., and Brecht, M. (2010). Impact of spikelets on hippocampal CA1 pyramidal cell activity during spatial exploration. *Science* 327, 474–477. doi: 10.1126/science.1182773

Frank, K., Fuortes, M. G. F. (1957). Presynaptic and postsynaptic inhibition of monosynaptic reflexes. *Fed. Proc.* 16, 39–40.

Geiger, J. R. P., and Jonas, P. (2000). Dynamic control of presynaptic Ca2+ inflow by fast-inactivating K+ channels in hippocampal mossy fiber boutons. *Neuron* 28, 927–939. doi: 10.1016/s0896-6273(00)00164-1

Heidelberger, R. (2007). Mechanisms of tonic, graded release: lessons from the vertebrate photoreceptor. *J. Physiol.* 585, 663–667. doi: 10.1113/jphysiol.2007.137927

Hu, H., and Jonas, P. (2014). A supercritical density of Na(+) channels ensures fast signaling in GABAergic interneuron axons. *Nat. Neurosci.* 17, 686–693. doi: 10.1038/nn.3678

Hu, W., and Bean, B. P. (2018). Differential control of axonal and somatic resting potential by voltage-dependent conductances in cortical layer 5 pyramidal neurons. *Neuron* 97, 1315.e3–1326.e3.

Kawaguchi, S., and Hirano, T. (2013). Gating of long-term depression by Ca2+/calmodulin-dependent protein kinase II through enhanced cGMP signalling in cerebellar Purkinje cells. *J. Physiol.* 591, 1707–1730. doi: 10.1113/jphysiol.2012.245787

Kawaguchi, S., and Sakaba, T. (2015). Control of inhibitory synaptic outputs by low excitability of axon terminals revealed by direct recording. *Neuron* 85, 1273–1288. doi: 10.1016/j.neuron.2015.02.013

Kim, J. H., Sizov, I., Dobretsov, M., and von Gersdorff, H. (2007). Presynaptic Ca2+ buffers control the strength of a fast post-tetanic hyperpolarization mediated by the alpha3 Na(+)/K(+)-ATPase. *Nat. Neurosci.* 10, 196–205. doi: 10.1038/nn1839

Luján, R., Albasanz, J. L., Shigemoto, R., and Juiz, J. M. (2005). Preferential localization of the hyperpolarization-activated cyclic nucleotide-gated cation channel subunit HCN1 in basket cell terminals of the rat cerebellum. *Eur. J. Neurosci.* 21, 2073–2082. doi: 10.1111/j.1460-9568.2005.04043.x

MacDermott, A. B., Role, L. W., and Siegelbaum, S. A. (1999). Presynaptic ionotropic receptors and the control of transmitter release. *Annu. Rev. Neurosci.* 22, 443–485. doi: 10.1146/annurev.neuro.22.1.443

Marder, E. (2006). Neurobiology: extending influence. *Nature* 441, 702–703. doi: 10.1038/441702a

Mejia-Gervacio, S., and Marty, A. (2006). Control of interneurone firing pattern by axonal autoreceptors in the juvenile rat cerebellum. *J. Physiol.* 571, 43–55. doi: 10.1113/jphysiol.2005.101675

Panzera, L. C., and Hoppa, M. B. (2019). Genetically encoded voltage indicators are illuminating subcellular physiology of the axon. *Front. Cell. Neurosci.* 13:52. doi: 10.3389/fncel.2019.00052

Paradiso, K., and Wu, L.-G. (2009). Small voltage changes at nerve terminals travel up axons to affect action potential initiation. *Nat. Neurosci.* 12, 541–543. doi: 10.1038/nn.2301

Pinault, D. (1995). Backpropagation of action potentials generated at ectopic axonal loci: hypothesis that axon terminals integrate local environmental signals. *Brain Res. Brain Res. Rev.* 21, 42–92. doi: 10.1016/0165-0173(95)00004-m

Pouzat, C., and Marty, A. (1999). Somatic recording of GABAergic autoreceptor current in cerebellar stellate and basket cells. *J. Neurosci.* 19, 1675–1690. doi: 10.1523/jneurosci.19-05-01675.1999

Price, G. D., and Trussell, L. O. (2006). Estimate of the chloride concentration in a central glutamatergic terminal: a gramicidin perforated-patch study on the calyx of held. *J. Neurosci.* 26, 11432–11436. doi: 10.1523/jneurosci.1660-06.2006

Pugh, J. R., and Jahr, C. E. (2011). Axonal GABAA receptors increase cerebellar granule cell excitability and synaptic activity. *J. Neurosci.* 31, 565–574. doi: 10.1523/JNEUROSCI.4506-10.2011

Pugh, J. R., and Jahr, C. E. (2013). Activation of axonal receptors by GABA spillover increases somatic firing. *J. Neurosci.* 33, 16924–16929. doi: 10.1523/JNEUROSCI.2796-13.2013

Rall, W. (1969a). Distributions of potential in cylindrical coordinates and time constants for a membrane cylinder. *Biophys. J.* 9, 1509–1541. doi: 10.1016/s0006-3495(69)86468-4

Rall, W. (1969b). Time constants and electrotonic length of membrane cylinders and neurons. *Biophys. J.* 9, 1483–1508. doi: 10.1016/s0006-3495(69)86467-2

Rall, W., and Rinzel, J. (1973). Branch input resistance and steady attenuation for input to one branch of a dendritic neuron model. *Biophys. J.* 13, 648–687.

Sasaki, T., Matsuki, N., and Ikegaya, Y. (2011). Action-potential modulation during axonal conduction. *Science* 331, 599–601. doi: 10.1126/science.1197598

Schmitz, D., Schuchmann, S., Fisahn, A., Draguhn, A., Buhl, E. H., Petrasch-Parwez, E., et al. (2001). Axo-Axonal coupling: a novel mechanism for ultrafast neuronal communication. *Neuron* 31, 831–840. doi: 10.1016/s0896-6273(01)00410-x

Sheffield, M. E. J., Best, T. K., Mensh, B. D., Kath, W. L., and Spruston, N. (2011). Slow integration leads to persistent action potential firing in distal

axons of coupled interneurons. *Nat. Neurosci.* 14, 200–207. doi: 10.1038/nn.2728

Sheffield, M. E. J., Edgerton, G. B., Heuermann, R. J., Deemyad, T., Mensh, B. D., and Spruston, N. (2013). Mechanisms of retroaxonal barrage firing in hippocampal interneurons. *J. Physiol.* 591, 4793–4805. doi: 10.1113/jphysiol.2013.258418

Shu, Y., Hasenstaub, A., Duque, A., Yu, Y., and McCormick, D. A. (2006). Modulation of intracortical synaptic potentials by presynaptic somatic membrane potential. *Nature* 441, 761–765. doi: 10.1038/nature04720

Southan, A. P., Morris, N. P., Stephens, G. J., and Robertson, B. (2000). Hyperpolarization-activated currents in presynaptic terminals of mouse cerebellar basket cells. *J. Physiol.* 526(Pt 1), 91–97. doi: 10.1111/j.1469-7793.2000.t01-1-00091.x

Stell, B. M. (2011). Biphasic action of axonal GABA-A receptors on presynaptic calcium influx. *J. Neurophysiol.* 105, 2931–2936. doi: 10.1152/jn.01125.2010

Stell, B. M., Rostaing, P., Triller, A., and Marty, A. (2007). Activation of presynaptic GABAA receptors induces glutamate release from parallel fiber synapses. *J. Neurosci.* 27, 9022–9031. doi: 10.1523/jneurosci.1954-07.2007

Szabadics, J., Varga, C., Molnár, G., Oláh, S., Barzó, P., and Tamás, G. (2006). Excitatory effect of GABAergic axo-axonic cells in cortical microcircuits. *Science* 311, 233–235. doi: 10.1126/science.1121325

Thome, C., Roth, F. C., Obermayer, J., Yanez, A., Draguhn, A., and Egorov, A. V. (2018). Synaptic entrainment of ectopic action potential generation in hippocampal pyramidal neurons. *J. Physiol.* 596, 5237–5249. doi: 10.1113/JP276720

Trigo, F. F., Marty, A., and Stell, B. M. (2008). Axonal GABAA receptors. *Eur. J. Neurosci.* 28, 841–848. doi: 10.1111/j.1460-9568.2008.06404.x

Zbili, M., and Debanne, D. (2019). Past and future of analog-digital modulation of synaptic transmission. *Front. Cell. Neurosci.* 13:160. doi: 10.3389/fncel.2019.00160

Zorrilla de San Martin, J., Jalil, A., and Trigo, F. F. (2015). Impact of single-site axonal GABAergic synaptic events on cerebellar interneuron activity. *J. Gen. Physiol.* 146, 477–493. doi: 10.1085/jgp.201511506

Zorrilla de San Martin, J., Trigo, F. F., and Kawaguchi, S.-Y. (2017). Axonal GABAA receptors depolarize presynaptic terminals and facilitate transmitter release in cerebellar Purkinje cells. *J. Physiol.* 595, 7477–7493. doi: 10.1113/JP275369

**Conflict of Interest Statement:** The author declares that the research was conducted in the absence of any commercial or financial relationships that could be construed as a potential conflict of interest.

*Copyright © 2019 Trigo. This is an open-access article distributed under the terms of the Creative Commons Attribution License (CC BY). The use, distribution or reproduction in other forums is permitted, provided the original author(s) and the copyright owner(s) are credited and that the original publication in this journal is cited, in accordance with accepted academic practice. No use, distribution or reproduction is permitted which does not comply with these terms.*

frontiers in Synaptic Neuroscience

HYPOTHESIS AND THEORY
published: 01 October 2019
doi: 10.3389/fnsyn.2019.00026

# EGTA Can Inhibit Vesicular Release in the Nanodomain of Single $Ca^{2+}$ Channels

*Yukihiro Nakamura**

*Department of Pharmacology, Jikei University School of Medicine, Tokyo, Japan*

The exogenous $Ca^{2+}$ chelator EGTA (ethylene glycol tetraacetic acid) has been widely used to probe the coupling distance between $Ca^{2+}$ channels and vesicular $Ca^{2+}$ sensors for neurotransmitter release. Because of its slow forward rate for binding, EGTA is thought to not capture calcium ions in very proximity to a channel, whereas it does capture calcium ions at the remote distance. However, in this study, our reaction diffusion simulations (RDSs) of $Ca^{2+}$ combined with a release calculation using vesicular sensor models indicate that a high concentration of EGTA decreases $Ca^{2+}$ and vesicular release in the nanodomain of single channels. We found that a key determinant of the effect of EGTA on neurotransmitter release is the saturation of the vesicular sensor. When the sensor is saturated, the reduction in the $Ca^{2+}$ concentration by EGTA is masked. By contrast, when the sensor is in a linear range, even a small reduction in $Ca^{2+}$ by EGTA can decrease vesicular release. In proximity to a channel, the vesicular sensor is often saturated for a long voltage step, but not for a brief $Ca^{2+}$ influx typically evoked by an action potential. Therefore, when EGTA is used as a diagnostic tool to probe the coupling distance, care must be taken regarding the presynaptic $Ca^{2+}$ entry duration as well as the property of the vesicular $Ca^{2+}$ sensor.

**Keywords: $Ca^{2+}$, $Ca^{2+}$ channel, $Ca^{2+}$ microdomain, reaction diffusion simulation, vesicular sensor, coupling distance, EGTA, transmitter release**

OPEN ACCESS

***Edited by:***
*Federico F. Trigo, Université Paris Descartes, France*

***Reviewed by:***
*Juan D. Goutman, CONICET Instituto de Investigaciones en Ingeniería Genética y Biología Molecular Dr. Héctor N. Torres (INGEBI), Argentina*
*Andreas Ritzau-Jost, University Hospital Leipzig, Germany*

***Correspondence:**
*Yukihiro Nakamura*
*yunakamura@jikei.ac.jp*

***Received:*** *30 April 2019*
***Accepted:*** *02 September 2019*
***Published:*** *01 October 2019*

***Citation:***
*Nakamura Y (2019) EGTA Can Inhibit Vesicular Release in the Nanodomain of Single $Ca^{2+}$ Channels. Front. Synaptic Neurosci. 11:26. doi: 10.3389/fnsyn.2019.00026*

## INTRODUCTION

The release of neurotransmitter is triggered by an increase in the intracellular $Ca^{2+}$ concentration ($[Ca^{2+}]_i$) in the presynaptic nerve terminal (Katz, 1969). This increase in $[Ca^{2+}]_i$ is mediated by voltage-gated calcium channels (VGCCs), activated upon the arrival of action potentials or by sustained depolarizations. Calcium ions entering through a channel pore diffuse to vesicular $Ca^{2+}$ sensors. During this diffusion, part of calcium ions binds to $Ca^{2+}$ buffers present in the cytosol. Thus, the probability of vesicular release, i.e., the output from the presynaptic nerve terminal, is determined by the combination of $Ca^{2+}$ influx, the properties of $Ca^{2+}$ buffers and $Ca^{2+}$ sensors, and the distance between VGCCs and $Ca^{2+}$ sensors. This coupling distance between VGCCs and $Ca^{2+}$ sensors is an important determinant of the $[Ca^{2+}]_i$ sensed by the $Ca^{2+}$ sensor, because the spatial concentration gradient of $Ca^{2+}$ formed around the open channel is steep. This gradient was first postulated using a mathematical model of $Ca^{2+}$ diffusion, referred to as the "$Ca^{2+}$ microdomain" (Chad and Eckert, 1984; Fogelson and Zucker, 1985), and later experimentally observed in the squid giant presynaptic terminal (Llinás et al., 1992) and the frog neuromuscular junction (DiGregorio et al., 1999).

The term microdomain originally had a broad meaning, referring to the high concentration of $Ca^{2+}$ near open VGCCs in general. More recently, the $Ca^{2+}$ microdomain has also referred to a coupling between VGCCs and the vesicular $Ca^{2+}$ sensor together with its counterpart $Ca^{2+}$ nanodomain (Augustine et al., 2003; Fedchyshyn and Wang, 2005; Eggermann et al., 2012; Wang and Augustine, 2015; Bornschein and Schmidt, 2019). To date, there has been no direct measurement of the coupling distance between VGCCs and vesicular $Ca^{2+}$ sensors by microscopic observation because of the technical limitation in identifying/labeling VGCCs together with synaptic vesicles. Alternatively, the quantitative estimate of the coupling distance via intraterminal loading of exogenous $Ca^{2+}$ chelators. The widely used chelators EGTA and BAPTA [1,2-Bis(2-aminophenoxy)ethane-N,N,N′,N′-tetraacetic acid] have similar binding affinities, but the forward binding kinetics of BAPTA is ∼40 times faster than that of EGTA (Naraghi and Neher, 1997). The slow on rate of EGTA is thought to result in its inability to capture $Ca^{2+}$ ions diffusing from VGCCs before they bind to vesicular sensors. By contrast, BAPTA can capture calcium ions, thereby inhibiting vesicular fusion. At locations distal to the VGCCs, both chelators should equally inhibit vesicular release. The magnitude of inhibition of transmitter release by these chelators can be a readout of the coupling distance. Thus, microdomain refers to the loose VGCC–sensor coupling distance that is inhibited by both EGTA and BAPTA, whereas nanodomain refers to the tight coupling inhibited solely by BAPTA (Augustine et al., 2003; Fedchyshyn and Wang, 2005; Wang and Augustine, 2015). The border separating the two domains is proposed to be 50–150 nm (Eggermann et al., 2012; Bornschein and Schmidt, 2019). This overall concept became widely recognized after the striking difference in the effectiveness of EGTA and BAPTA at the squid giant synapse was observed (Adler et al., 1991). The effects of these exogenous chelators have been further examined in a variety of nerve terminals (Borst et al., 1995; Rozov et al., 2001; Hefft and Jonas, 2005; Schmidt et al., 2013; Ritzau-Jost et al., 2014; Vyleta and Jonas, 2014).

However, EGTA might introduce some error when used as a diagnostic tool under certain conditions. Our recent studies using reaction diffusion simulations (RDSs) indicated that EGTA can inhibit vesicular release in the immediate vicinity (∼20 nm) of VGCCs, in the nanodomain coupling distance (Nakamura et al., 2015, 2018). Although an early study pointed out the ability of EGTA to reduce $[Ca^{2+}]_i$ at channel pores (Neher, 1986), little attention has been paid to this. In this article, I will examine how EGTA affects the $Ca^{2+}$ microdomain around a single VGCC (single domain; Stanley, 2015) as well as the resultant vesicular release to precisely understand the inhibitory effect of EGTA on transmitter release.

# MATERIALS AND METHODS

## Linearized Buffer Approximation (LBA)

First, I estimated local $[Ca^{2+}]_i$ around an open VGCC using linearized buffer approximation (LBA; Naraghi and Neher, 1997). Among several analytical solutions, LBA has been widely used to calculate local $[Ca^{2+}]_i$ because it reliably estimates $[Ca^{2+}]_i$ at an arbitrary distance from the channel in the presence of multiple $Ca^{2+}$ buffer species (Neher, 1998a), without time-consuming numerical simulations. All parameters were the same as those in the RDS (see below), except that the endogenous fixed buffer (EFB) was inherently excluded from LBA (Naraghi and Neher, 1997). The calculations were performed using Microsoft Excel.

## Reaction Diffusion Simulations (RDS)

To estimate $[Ca^{2+}]_i$ gradients around an open VGCC, I mostly used RDS. In contrast to LBA, which calculates a single $[Ca^{2+}]_i$ at steady state (Naraghi and Neher, 1997), RDS can deduce time-dependent $[Ca^{2+}]_i$ changes in the presence and absence of buffers. Moreover, it can incorporate the geometry of the presynaptic terminal, which is of huge importance when analyzing diffusion in confined environments such as small presynaptic terminals. In this study, the same simulation environment and parameters were used as those described by Nakamura et al. (2018). $Ca^{2+}$ entry, diffusion, and binding with buffers were calculated by numerically integrating partial differential equations applying an explicit finite-element (Euler) method using the Java-based simulation environment D3D. The total simulation volume was set to 1.0 ($x$) × 1.0 ($y$) × 1.0 ($z$) μm, which was divided into the elemental simulation voxels of 10 × 10 × 10 nm for finite difference calculations. With this voxel size, a concentration of 1 mM is equal to 602 molecules per voxel. The time step of simulation was 0.06 μs, and the resultant $Ca^{2+}$ wave outputs were at 100 kHz. In this dimension, one simulation trial (10 ms in duration) typically took ∼7 h using a Windows 10 PC equipped with Intel Xeon CPU (E5-2640, 2.6 GHz).

A single VGCC was placed at the center of a single surface ($z$ = 0). The current amplitude of a single VGCC was 0.3 pA, assuming the single channel conductance for $Ca_V2$ is 2.7 pS (Weber et al., 2010) and the driving force for $Ca^{2+}$ is ∼110 mV, when the terminal membrane potential at rest is −65 mV, and the reversal potential for $Ca^{2+}$ is +43 mV in 2 mM extracellular $Ca^{2+}$ (Sheng et al., 2012). Although the single VGCC current under physiological conditions can vary depending on membrane potential, the amplitude was fixed at 0.3 pA in this study, as our previous study using amplitudes ranging from 0.075 to 0.6 pA produced similar tendencies [see Figures 2, 4 in the study by Nakamura et al. (2018)]. This current amplitude corresponds to an influx of 936 $Ca^{2+}$ ions per millisecond. The resting free $[Ca^{2+}]$ was set at 50 nM and the $Ca^{2+}$ diffusion coefficient ($D_{Ca}$) was 220 $\mu m^2/s$ (Allbritton et al., 1992). The parameters for buffers were set to match those of previous recordings performed in the dialyzed calyx of Held presynaptic terminal at room temperature (22–24°C) when possible (Nakamura et al., 2015). Free ATP was set at 200 μM, assuming the presence of 2 mM ATP (total concentration) and 3 mM $Mg^{2+}$ (calculation using Maxchelator). The values for $Ca^{2+}$ binding to ATP were as follows: $K_{D,Ca}$ = 200 μM, $k_{on,Ca}$ = 5 × $10^8$ $M^{-1}s^{-1}$ (Baylor and Hollingworth, 1998), $D_{ATP}$ = 220 $\mu m^2/s$. The parameters for EGTA were $k_{on}$ = 1.05 × $10^7$ $M^{-1}s^{-1}$ and $K_D$ = 70 nM (Nägerl et al., 2000). The parameters for BAPTA

were $k_{on}$ = 4.0 × $10^8$ $M^{-1}s^{-1}$ and $K_D$ = 220 nM (Naraghi and Neher, 1997). The diffusion coefficients of EGTA and BAPTA were 220 $\mu m^2/s$ (Naraghi and Neher, 1997). In the simulations with EFB, EFB was evenly distributed throughout the simulation volume. EFB and mobile buffers are similar, except that the EFB diffusion coefficient is 0 $\mu m^2/s$. The parameters for EFB were as follows: $K_D$ = 100 μM (Xu et al., 1997), $k_{on}$ = 1 × $10^8$ $M^{-1}s^{-1}$, $Ca^{2+}$ binding ratio (κ) = 40 (Helmchen et al., 1997). To focus on diffusion and buffering, $Ca^{2+}$ extrusion was not implemented in this study. The resultant $[Ca^{2+}]_i$ waves were imported into IgorPro 8 (WaveMetrics) and analyzed using NeuroMatic (Rothman and Silver, 2018).

## Simulations of Vesicular Release Probability (Pv)

A five-site model of $Ca^{2+}$-dependent vesicle fusion derived from experiments in the mature calyx of Held (Kochubey et al., 2009) was used to simulate vesicular transmitter release. The model was integrated using a forward Euler numerical integration routine (IgorPro 8), using the $[Ca^{2+}](t)$ generated from RDS. The probability over time of arriving in the fused state is considered the probability that a single vesicle will be released as a function of time (single vesicular release rate). The cumulative release rate, which is equivalent to the vesicular release probability (Pv), was estimated from the integral of the single vesicular release rate over a window from the onset of VGCC opening to 10 ms after closing. With the assumption that the $Ca^{2+}$ sensors for vesicular release are juxtaposed to the release face membrane, Pvs were calculated only in the voxels on the synaptic surface ($z = 0$).

# RESULTS

## Calculation of $[Ca^{2+}]_i$ Using Linearized Buffer Approximation

To quantify the $[Ca^{2+}]_i$ gradient around a single open VGCC, I first used the analytical solution. When a calcium ion enters a channel pore, it is unbound (free ion) and starts diffusing. The increment in $[Ca^{2+}]_i$ ($\Delta[Ca^{2+}]_i$) by diffusion is inversely proportional to the distance ($r$) from the channel pore. Assuming that $Ca^{2+}$ is diffusing into a hemisphere adjacent to the plasma membrane, it is calculated by:

$$\Delta[Ca^{2+}]_i = i_{Ca}/(4\pi \cdot F \cdot D_{Ca} \cdot r) \quad (1)$$

where $i_{Ca}$ is the amplitude of the constant $Ca^{2+}$ current of a single VGCC, $F$ is the Faraday constant, and $D_{Ca}$ is the diffusion coefficient of free $Ca^{2+}$ (Neher, 1986). When the single channel current amplitude was 0.3 pA (Weber et al., 2010), $\Delta[Ca^{2+}]_i$ was 56.3 μM at 20 nm and 11.3 μM at a 100 nm distance in the absence of buffers (**Figures 1A,B**, left gray bars).

However, because several $Ca^{2+}$ buffers are present in the presynaptic terminal, a calcium ion often binds to a buffer molecule before it reaches vesicular $Ca^{2+}$ sensors; $Ca^{2+}$ buffers dampen the $\Delta[Ca^{2+}]_i$. To calculate the $[Ca^{2+}]_i$ gradient in the presence of buffers, I used LBA, which reliably estimates $[Ca^{2+}]_i$ in the immediate vicinity of VGCC in the presence of multiple mobile buffer species (Neher, 1998a). The theoretical background of this approximation is based on the assumption that a steady $[Ca^{2+}]_i$ gradient is immediately established upon an opening of VGCCs if the concentration of free $Ca^{2+}$ buffer is very high compared with $[Ca^{2+}]_i$.

In the presence of an excess amount of buffer, it is assumed that $Ca^{2+}$ influx through a VGCC does not substantially change the free buffer concentration. Under such conditions, a free calcium ion diffuses randomly until it is captured by a buffer molecule. This requires on the average time:

$$\tau = 1/([B] \cdot k_{on}) \quad (2)$$

where $[B]$ and $k_{on}$ represent the concentration and forward binding constant of the buffer, respectively. During this time, a calcium ion will travel a distance:

$$\lambda = \sqrt{(D_{Ca}/([B] \cdot k_{on})} \quad (3)$$

The buffer decreases the average distance that calcium ions travel, and space constant λ is supplemented to Eq. 1. Thus, in the presence of buffer, $\Delta[Ca^{2+}]_i$ at a given location is calculated by (for more detail, see Stern, 1992; Neher, 1998a; Ait-Haddou et al., 2010):

$$\Delta[Ca^{2+}]_i = i_{Ca}/(4\pi \cdot F \cdot D_{Ca} \cdot r) \cdot exp(-r/\lambda) \quad (4)$$

λ may also be considered the border of the "non-equilibrium" domain (Neher, 1998b). If $r >> \lambda$, the contribution of diffusional $Ca^{2+}$ to total $[Ca^{2+}]_i$ becomes minor as $\Delta[Ca^{2+}]_i$ becomes close to zero. In this distance range, the buffering reaction is at an equilibrium. By contrast, if $r << \lambda$, the value calculated for Eq. 4 becomes close to that for Eq. 1, indicating that diffusion primarily determines $[Ca^{2+}]_i$. $Ca^{2+}$ exists as free ions and is not at an equilibrium. Within this non-equilibrium domain, because free buffer molecules and $Ca^{2+}$-bound buffer molecules diffuse each other, the $Ca^{2+}$ concentration remains at a steady state (Neher, 1998a). Space constant λ can be used to indicate the extent of the $Ca^{2+}$ microdomain determined by the buffer.

According to Eqs 2 and 3, τ and λ for 0.1 mM EGTA were 1.63 ms and 599 nm, respectively. Thus, when the basal resting $[Ca^{2+}]_i$ was 50 nM, LBA calculates $[Ca^{2+}]_i$ as 54.4 μM at 20 nm and 9.6 μM at 100 nm, slightly decreased from the no-buffer condition (**Figures 1A,B**, left bar graphs). Similarly, $[Ca^{2+}]_i$ in the presence of 10 mM EGTA (τ = 16 μs, λ = 59.9 nm) was 40.3 μM at 20 nm and 2.2 μM at 100 nm. The addition of free ATP (0.2 mM), which widely exists in the cytosol and acts as a rapid-binding low-affinity mobile buffer, further decreased $[Ca^{2+}]_i$, and 10 mM BAPTA (τ = 0.3 μs, λ = 8.2 nm) strongly decreased $[Ca^{2+}]_i$ to 4.8 μM even at a distance of 20 nm (in the presence of ATP).

## Calculation of $[Ca^{2+}]_i$ Using Reaction Diffusion Simulation

Although LBA is a useful method for calculating local $[Ca^{2+}]_i$ at an arbitrary distance from the VGCC, it has several limitations because of its assumptions. First, under low-buffered conditions,

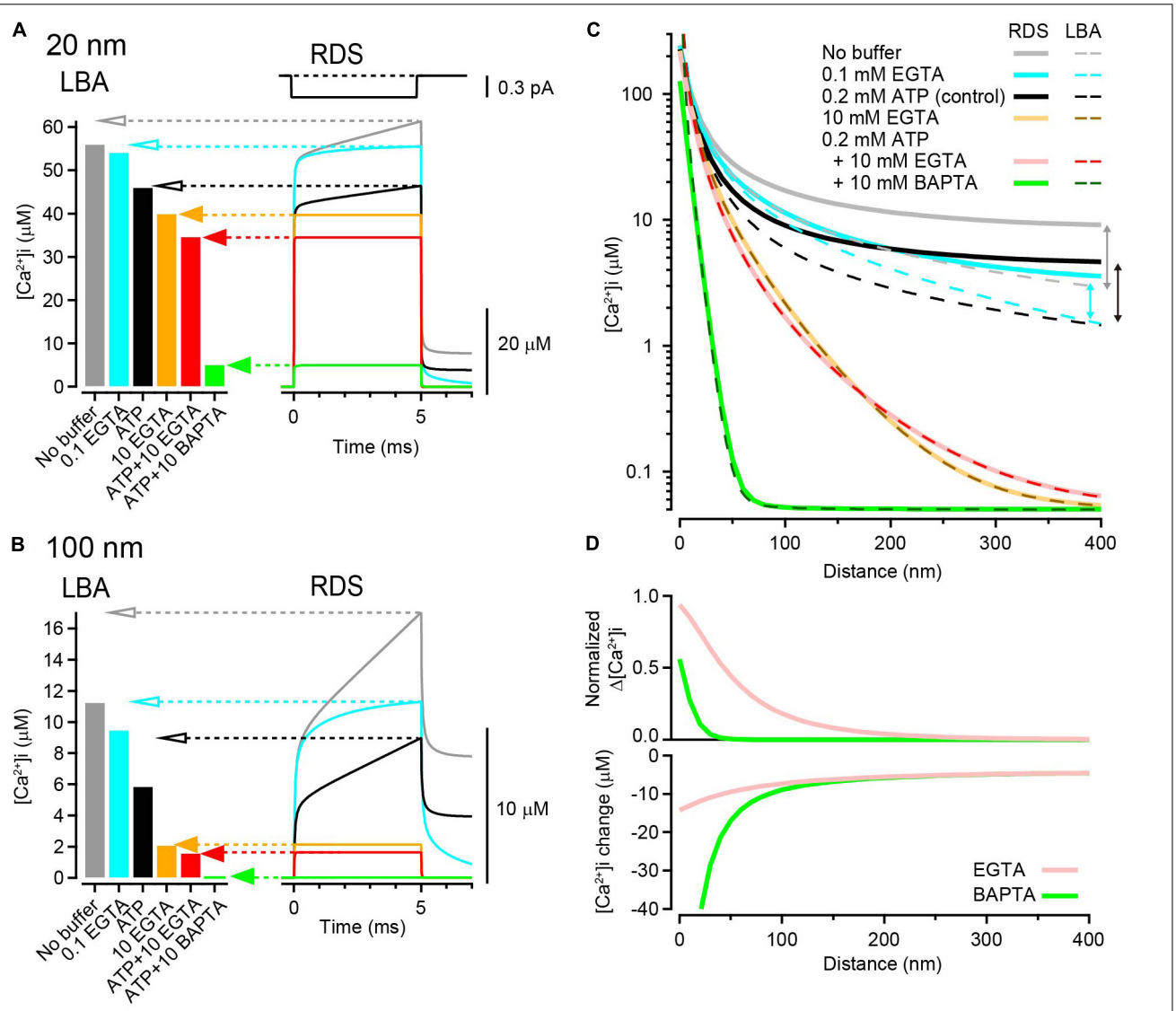


**FIGURE 1 |** Calculation of $[Ca^{2+}]_i$ gradients around an open VGCC. **(A)** left, $[Ca^{2+}]_i$ at 20 nm from the VGCC calculated using LBA under various buffer conditions. Single channel current amplitude was 0.3 pA. Right, Time dependent $[Ca^{2+}]_i$ changes calculated using RDS. Channel open duration was 5 ms (top). Under heavily buffered conditions, both estimates agreed (filled arrows), whereas under the weak or no-buffer conditions, LBA predicted lower $[Ca^{2+}]_i$ than the peak $[Ca^{2+}]_i$ of transients in RDS (open arrows). Resting $[Ca^{2+}]_i$ was 50 nM. **(B)** Same as **(A)** but at 100 nm from the VGCC. **(C)** Spatial gradients of $[Ca^{2+}]_i$ from LBA (dashed) and RDS (solid) in various buffer conditions. The vertical arrows indicate discrepancies between the two estimates. **(D)** Reduction of $[Ca^{2+}]$ by 10 mM EGTA (pink) and BAPTA (green) against distance. Top, the reduction is represented as the ratio of the peak $[Ca^{2+}]_i$ in the presence of the chelator to that in the control (0.2 mM ATP). Bottom, the reduction is represented as the difference between the peak $[Ca^{2+}]_i$ in the presence of the chelator and that in the control.

LBA does not provide reliable estimates because $Ca^{2+}$ influx could substantially alter the free buffer concentration. Second, as LBA assumes an instantaneous establishment of steady-state $\Delta[Ca^{2+}]_i$ gradient after channel opening and calculates the steady-state $\Delta[Ca^{2+}]_i$, it does not provide for time-dependent changes in $[Ca^{2+}]_i$. To circumvent these limitations, I next estimated local $[Ca^{2+}]_i$ gradients using RDS. To simulate time-dependent $[Ca^{2+}]_i$ changes, I used a single channel current of 0.3 pA (Weber et al., 2010) for 5 ms. The resultant $[Ca^{2+}]_i$ transient at 20 nm rose immediately after channel opening and gradually increased further until the end of the $Ca^{2+}$ current. The peak $[Ca^{2+}]_i$ was 62 μM in the absence of $Ca^{2+}$ buffers (**Figure 1A** right, gray trace). The addition of free ATP (0.2 mM) reduced the peak $[Ca^{2+}]_i$ to 47 μM by affecting both the fast and slow components (**Figure 1A**, black). By contrast, the addition of a low concentration (0.1 mM) of EGTA reduced the peak $[Ca^{2+}]_i$ to 56 μM, only affecting the slow component (**Figure 1A**, blue). Increasing the EGTA concentration to 10 mM eliminated this slow component and resulted in a steady-state $[Ca^{2+}]_i$ at 40 μM (**Figure 1A**, orange and red). Steady-state $[Ca^{2+}]_i$ was also attained in the presence of 10 mM BAPTA but with an amplitude as small as 5 μM (**Figure 1A**, green). At a 100 nm

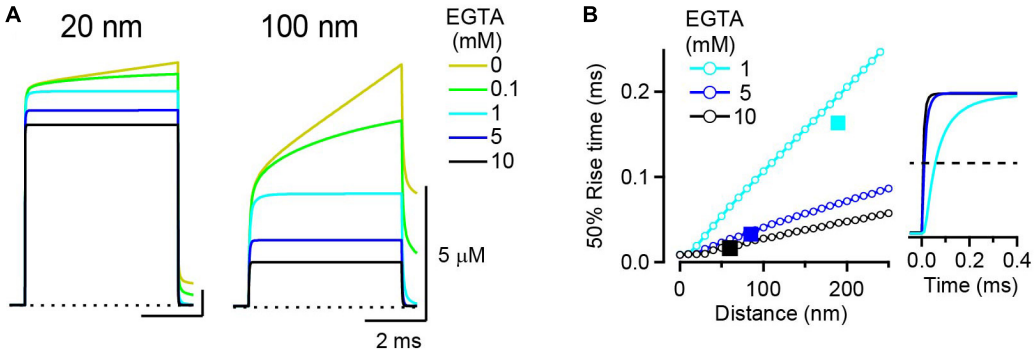


**FIGURE 2 |** Rise kinetics of $[Ca^{2+}]_i$ transients. **(A)** $[Ca^{2+}]_i$ transient at 20 nm (left) and 100 nm (right) from a VGCC in the presence of various concentrations of EGTA. Single VGCC current was 0.3 pA in amplitude and 5 ms in duration. **(B)** Relationship between $[Ca^{2+}]_i$ transient kinetics and the distance; 50% rise time of $[Ca^{2+}]$ transients from RDS in the presence of 1, 5, and 10 mM EGTA was plotted against voxel distance from the VGCC. For comparison, the time constant [τ (ms)] from LBA plotted against the space constant [λ (nm)] for each EGTA concentration is denoted as a filled square. Traces in the right panel represent $[Ca^{2+}]_i$ transients (normalized with amplitude) at the voxel closest to the distance λ (190 nm for 1 mM; 80 nm for 5 mM; 60 nm for 10 mM EGTA). Horizontal dashed line denotes 50% rise of the transients.

distance, $[Ca^{2+}]_i$ transients became smaller in amplitude with slower rising kinetics (**Figure 1B**).

When comparing $[Ca^{2+}]_i$ from LBA with the peak $[Ca^{2+}]_i$ from RDS, the two estimates matched in the presence of 10 mM EGTA or BAPTA (**Figures 1A,B**, filled arrows). Indeed, $[Ca^{2+}]_i$ immediately reached steady state in RDS under these highly buffered conditions. By contrast, LBA deduced smaller $[Ca^{2+}]_i$ under weak- or no-buffer conditions than RDS (open arrows). This difference became apparent in the plot showing entire spatial $[Ca^{2+}]_i$ gradients (**Figure 1C**). The discrepancy is partly accounted by the difference in diffusional spaces (Nakamura et al., 2018). Many analytical solutions, including LBA, assume an infinite diffusion volume, whereas RDS uses limited diffusional space, which tends to cause an accumulation of $Ca^{2+}$. Furthermore, under weakly buffered conditions, $Ca^{2+}$ influx substantially alters the free buffer concentration, violating the assumption of a linear buffer regime for LBA. The slower component of $[Ca^{2+}]_i$ in RDS is due to the limited diffusional space and the lower buffer condition. Thus, to estimate of $[Ca^{2+}]_i$ gradient in low-buffered condition, the use of RDS is preferable. However in highly buffered condition, LBA provides a powerful method for estimating steady-state $[Ca^{2+}]_i$, as there is a good agreement between the two estimates throughout the entire spatial gradients (**Figure 1C**).

To quantify the inhibition of the spatial gradient of $[Ca^{2+}]_i$ by EGTA and BAPTA, I compared $\Delta[Ca^{2+}]_i$ under the control condition (0.2 mM ATP) with that in the presence of 10 mM chelators. As LBA cannot reliably predict $[Ca^{2+}]_i$ under low-buffered control conditions, I used $[Ca^{2+}]_i$ calculated from RDS. As predicted, both EGTA and BAPTA nearly completely inhibited $\Delta[Ca^{2+}]_i$ at more distal locations (400 nm, <1% of control). By contrast, at a 10 nm distance from the VGCC, EGTA inhibited $\Delta[Ca^{2+}]_i$ by only 15%, whereas BAPTA inhibited it by 83%. Thus, EGTA was much less potent in inhibiting $\Delta[Ca^{2+}]_i$ than BAPTA at locations close to the channel (**Figure 1D**, top). However, it should be noted that EGTA still decreased $[Ca^{2+}]_i$ at this distance. When calculating the difference in $[Ca^{2+}]_i$ between control and chelator conditions, EGTA decreased the peak $[Ca^{2+}]_i$ by 13 μM, and BAPTA decreased $[Ca^{2+}]_i$ by 64 μM at a 10 nm distance (**Figure 1D**, bottom). Although EGTA was less potent than BAPTA, this reduction by EGTA was not negligible. These results indicate that a high concentration of EGTA can reduce $[Ca^{2+}]_i$ at all distances on the release surface, including the nanodomain of VGCCs.

## Buffer Property Affects the Rising Kinetics of the $[Ca^{2+}]_i$ Transient

I next examined the effect of buffers on the kinetics of the $[Ca^{2+}]_i$ transient. In the analytical solution, the average time to reach steady-state $[Ca^{2+}]_i$ after the onset of channel opening is inversely related to the forward binding kinetics and the concentration of buffers (see Eq. 2). When the EGTA concentration is, for example, 10 mM, τ is 16 μs (this is quite fast and approaches the assumption of LBA). However, because each free calcium ion randomly moves in a Brownian motion, the establishment of steady-state $[Ca^{2+}]_i$ might take longer at more distal locations. To examine this possibility, the 50% rise time of $[Ca^{2+}]_i$ transients was measured. At EGTA concentrations of <0.1 mM, $[Ca^{2+}]_i$ transients never reached steady state during the 5 ms channel opening, both at 20 nm and at 100 nm distances (**Figure 2A**). To attain steady-state $[Ca^{2+}]_i$ EGTA concentration of >1 mM was necessary. The 50% rise times at 20 nm were 19, 9.9, and 9.5 μs for 1, 5, and 10 mM EGTA, respectively. At 100 nm, they became longer, at 106, 41, and 28 μs, respectively. The rise time proportionally increased with the voxel distance (**Figure 2B**), indicating that steady-state $[Ca^{2+}]_i$ is attained in the proximity of the channel and then spreads to distal locations.

To compare these simulated rise times with the prediction from the analytical solution, I plotted τ (Eq. 2) against λ (Eq. 3) on the same graph (**Figure 2B**, squares). τ values for 5 and 10 mM EGTA appeared just on the lines that show a 50% rise time of RDS $[Ca^{2+}]_i$ transients against voxel distance, indicating that the ratio τ/λ corresponds to the slope of the 50% rise time of

$[Ca^{2+}]_i$ transients against distance. However, τ for 1 mM EGTA went below its corresponding line. This was probably because the $[Ca^{2+}]_i$ transients in the RDS did not attain a true steady state. Indeed, in the presence of 1 mM EGTA, the peak amplitude of the $[Ca^{2+}]_i$ transient in RDS (**Figure 2A**, light blue trace) was slightly larger than the estimate from LBA (not shown); thus the 50% rise time was longer than τ. This means that EGTA concentrations of <1 mM deviate from a linear range and that the LBA should be avoided under these conditions.

## Effect of Endogenous Fixed Buffer on the $[Ca^{2+}]_i$ Transient

In addition to mobile buffers, presynaptic terminals also contain an EFB (Helmchen et al., 1997; Neher and Taschenberger, 2013; Delvendahl et al., 2015; Nakamura et al., 2015). The exact molecular identity of the EFB is not known, but it is believed that ubiquitous proteins and lipids anchored to the membrane or cytoskeleton act as fixed low-affinity buffers (Schwaller, 2010). Calmodulin attached to presynaptic proteins (Eggermann et al., 2012) and $Ca^{2+}$ sensors on vesicles might also act as EFBs. Calcium ions bound by mobile buffers retain their mobility because they diffuse together with their shuttle, whereas those bound by an EFB cannot diffuse. The EFB retards the distribution of calcium ions and delays the establishment of steady-state $[Ca^{2+}]_i$ by competing with mobile buffers. In LBA, the contribution of EFB is omitted because once the $[Ca^{2+}]_i$ reaches steady state, the standing $[Ca^{2+}]_i$ gradients are identical to those without an EFB (Stern, 1992; Naraghi and Neher, 1997). However, how long EFB might delay the establishment of steady-state $[Ca^{2+}]_i$ has not been examined in detail. To quantify the effect of EFB on the rise time of the $[Ca^{2+}]_i$ transient, I next tested EFBs with three different $Ca^{2+}$ binding ratios (κ) and affinities. Because EFB κ is low in most presynaptic terminals, I used a κ of 15 (Neher and Taschenberger, 2013; Delvendahl et al., 2015) or 40 (Helmchen et al., 1997) but also tested a higher value (κ = 100). In the presence of 10 mM EGTA, the addition of low-affinity EFB ($K_D$ = 100 μM) increased the time to reach steady state without affecting the steady-state amplitude of $[Ca^{2+}]_i$ (**Figure 3A**). The rising kinetics of the increase in $[Ca^{2+}]_i$ in the presence of EFB had multiple components, a rapid rise immediately after the onset of the $Ca^{2+}$ current, followed by a gradual increase. Because the 50% rise time was not a reliable measure in this case, I then estimated the mean time constant to reach steady state. Increasing κ from 0 (10 mM EGTA alone) to 100 (10 mM EFB) increased the time constant for the $[Ca^{2+}]_i$ transient at all distances (**Figure 3B**). I next tested different $K_D$s, including 2 (Meinrenken et al., 2002; Bucurenciu et al., 2008), 10, and 100 μM (Xu et al., 1997; DiGregorio et al., 1999; Nakamura et al., 2015), by altering $k_{off}$. To keep κ constant (40), the EFB concentration was concomitantly adjusted in this simulation. The lowest $K_D$ (100 μM) slowed the rise kinetics the most. At the 20 nm distance, the rise time increased ∼20-fold from 3.4 to 66 μs (**Figures 3C,D**).

In these simulations, EFB did not affect the amplitude of steady-state $[Ca^{2+}]_i$ for a 5 ms channel opening (**Figures 3A,C**). However, the slower rise kinetics of $[Ca^{2+}]_i$ transients in the presence of EFB might reduce the peak amplitude $[Ca^{2+}]_i$ evoked by brief channel openings. To test this possibility, a Ca current waveform evoked by the action potential in the mature calyx of Held (half duration, 0.19 ms; Nakamura et al., 2015) was used in the simulation, because this waveform is an example of the shortest evoked $Ca^{2+}$ influx in the CNS and contrasts the longer square pulses. The addition of low-affinity EFB ($K_D$ = 100 μM) reduced the peak $[Ca^{2+}]_i$ from 41 μM to 34 μM at 20 nm from VGCC (**Figure 3E**). The reduction in $[Ca^{2+}]_i$ was pronounced in more distal locations (**Figure 3F**) because $Ca^{2+}$ influx terminated before the $[Ca^{2+}]_i$ reached steady state. Although I have presented the simulation result of EFB in the presence of 10 mM EGTA here, EFB also reduces the peak $[Ca^{2+}]_i$ in low concentrations of mobile $Ca^{2+}$ buffers (see Nakamura et al., 2018). Thus, to estimate the $[Ca^{2+}]_i$ evoked by a brief $Ca^{2+}$ influx, such as that induced by an action potential, the presence of EFB cannot be neglected and the RDS is preferred.

## Saturation of the Vesicular Release Sensor Masks the Reduction in $[Ca^{2+}]_i$

I next examined the effect of EGTA on the Pv, which was estimated from the waveform of $[Ca^{2+}]_i$ transients from RDS using the five-site model of $Ca^{2+}$-dependent vesicular fusion (Kochubey et al., 2009). In this simulation, the control condition included 0.2 mM ATP and 4 mM low-affinity EFB. For the $[Ca^{2+}]_i$ transient induced by 5 ms voltage steps, the Pv at 20 nm rapidly (within 1 ms) reached 1 under the control condition. The addition of 10 mM EGTA reduced $[Ca^{2+}]_i$ and slightly slowed the rise of Pv, but the Pv similarly reached and remained at 1 (**Figure 4A**), indicating that EGTA had no effect on the final Pv at this distance. At 100 nm, an increase in Pv was observed only in the control condition, which was completely inhibited by EGTA. Under both control and EGTA conditions, the Pv decreased with distance, but this decrement occurred at a shorter distance in the presence of EGTA (**Figure 4B**). To quantify the relationship between Pv and $Ca^{2+}$, Pvs were plotted against the time integral of $[Ca^{2+}]_i$ for each voxel location (**Figure 4C**). In proximity to VGCC (<40 nm in this example), EGTA caused a leftward shift of the points, indicating a decrease in $[Ca^{2+}]_i$. But because vesicular release sensors remained at a saturated level ($Pv$ = 1), this decrease in $[Ca^{2+}]_i$ did not affect the Pv. At distal locations (>50 nm), the decrease in $[Ca^{2+}]_i$ by EGTA was seen as a decrease in the Pv, because the vesicular $Ca^{2+}$ sensor entered a linear range.

Next, Pv with action potentials was examined. For this brief $Ca^{2+}$ influx, EGTA reduced the peak $[Ca^{2+}]_i$ from 41 μM to 35 μM (by 15%) and the Pv from 0.07 to 0.03 (by 52%) at a 20 nm distance from the VGCC (**Figure 4D**). The Pv also decreased with distance, but this decrement occurred at shorter distance than for the voltage step (**Figure 4E**). For action potential-induced brief $Ca^{2+}$ influx, the vesicular $Ca^{2+}$ sensor showed no indication of saturation (**Figure 4F**). As the time integral of $[Ca^{2+}]_i$ at the channel pore (0 nm) was already in or near the linear range of the vesicular sensor, even a small decrease in $[Ca^{2+}]_i$ directly decreased the Pv. To examine how EGTA differently affects the $Ca^{2+}$ release relationship for voltage steps and action potentials,

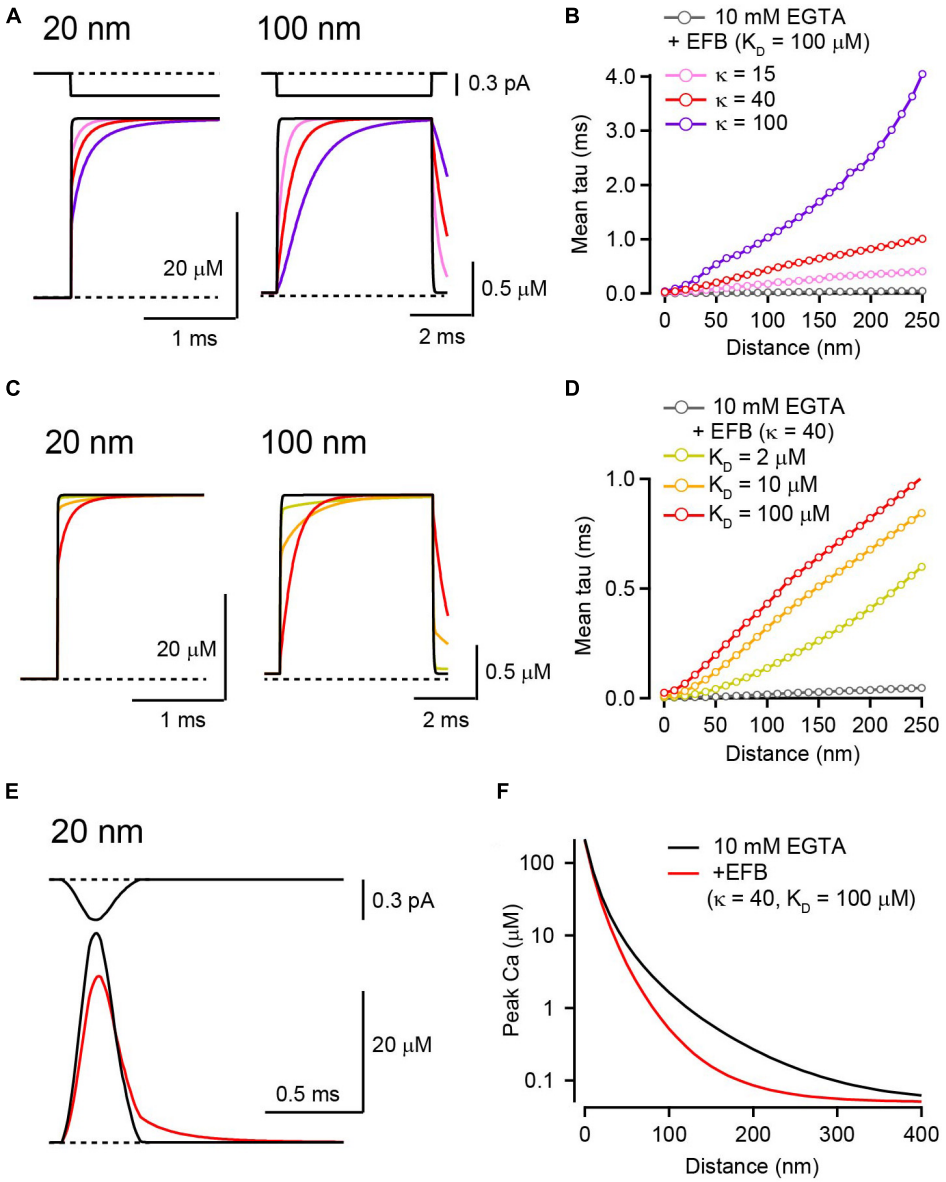


**FIGURE 3 |** The effect of EFB on $[Ca^{2+}]$ transients in the presence of 10 mM EGTA. **(A)** $Ca^{2+}$ current through a VGCC (top) and the resultant $[Ca^{2+}]_i$ transients for 20 nm (left) and 100 nm (right) distances in the presence of EFB with various κ values. I tested κ of 15 (pink), 40 (red), and 100 (purple) by altering EFB concentration. $K_D$ was 100 μM. **(B)** Mean rise times of $[Ca^{2+}]$ transients for different EFB κ values were plotted against voxel distance. **(C)** $[Ca^{2+}]$ transients for 20 nm (left) and 100 nm (right) distances with various affinities of EFB. We tested $K_D$ of 2 (yellow), 10 (orange), and 100 (red) μM. κ was set at 40. Black and red traces are identical to those in **(A)**. **(D)** Mean rise times of $[Ca^{2+}]$ transients for different EFB affinities. **(E)** Action potential-evoked $[Ca^{2+}]$ transients 20 nm from VGCC in the absence (black) and presence (red) of EFB. The current waveform (top) was obtained from whole-presynaptic terminal $Ca^{2+}$ current at the calyx of Held evoked by action potential waveform voltage command and scaled to 0.3 pA. **(F)** Spatial gradients of peak $[Ca^{2+}]$ transients evoked by an action potential in the presence of low-affinity EFB.

the change in Pv (EGTA/control) was plotted against that in $[Ca^{2+}]_i$ in each voxel location. For voltage step-evoked release, the decrease in the Pv occurred when 10 mM EGTA reduced the $[Ca^{2+}]_i$ to 60% or less (**Figure 4G**, squares on solid blue line). For action potential-evoked release, the smaller decrease in the $[Ca^{2+}]_i$ (to ∼80%) decreased the Pv (circles on solid green line). For lower EGTA concentrations, the decreases in Pv and $[Ca^{2+}]_i$ were smaller (triangles and diamonds on dashed lines).

The results from the simulation and analysis indicate that the saturation of vesicular sensors primarily determines the inhibition of Pv by EGTA. In the proximity of VGCCs, voltage step-induced large $[Ca^{2+}]_i$ transients saturate vesicular sensors masking the effect of EGTA on release. By contrast, action potential-induced brief $Ca^{2+}$ influx drives the Pv within a linear range of the sensor, revealing the effect of EGTA on the inhibition of vesicular release. At the same distance, the

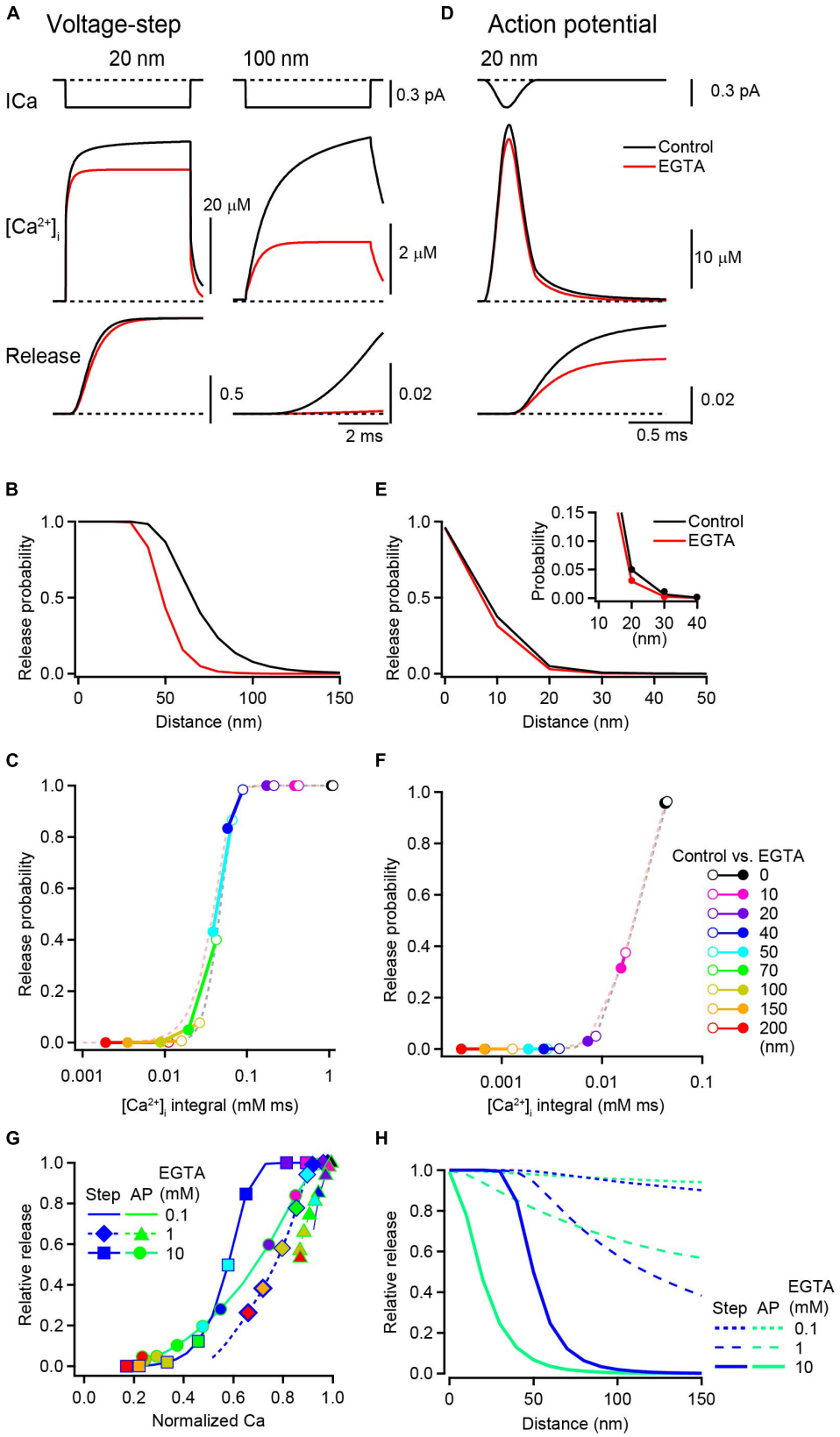


**FIGURE 4 |** Continued

**FIGURE 4 |** Inhibitory effect of EGTA on vesicular release probability. **(A)** [$Ca^{2+}$] transients (middle) and the cumulative release probabilities (bottom) at 20 nm (left) and 100 nm (right) distances under the control condition (black) and in the presence of 10 mM EGTA (red), induced by a 5 ms depolarization. Single channel $Ca^{2+}$ current is shown in the top row. **(B)** Spatial profile of Pv induced by voltage steps in the control (black) and in the presence of 10 mM EGTA (red). **(C)** Relationship between Pv and the time integral of $[Ca^{2+}]_i$ induced by voltage steps. Each circle pair represents $Ca^{2+}$-Pv coupling under control (open) and EGTA (filled) conditions at various distances. Dashed lines represent the properties of $Ca^{2+}$ secretion in relation to the vesicular sensor. **(D)** [$Ca^{2+}$] transient (middle) and the resultant cumulative release probability (bottom) at 20 nm, evoked by an action potential. The top trace is a channel current in response to an action potential. **(E,F)** Same as in **(B,C)** but induced by action potentials. To better represent the decrease in Pv by EGTA at a 20 nm distance, the closer location is expanded in the inset. **(G)** The reduction in Pv by EGTA ($Pv_{\_EGTA}/Pv_{\_Control}$) was plotted against that in the time integral of $[Ca^{2+}]_i$ ($Ca_{\_EGTA}/Ca_{\_Control}$) at each location. Symbols on lines show the data from representative voxel distances from the VGCC [from left to right: 200, 150, 100, 70, 50, 40, 20, 10, and 0 nm, color code as in panel **(F)**]. 0.1 mM EGTA (dashed line) induced small reductions both in $Ca^{2+}$ and Pv. Increased EGTA concentrations of 1 mM (diamonds and triangles on dashed lines) and 10 mM (circles and squares on solid lines) shifted the curve toward the lower left of the panel. **(H)** Spatial profiles of the inhibitory effect of various concentrations of EGTA on Pv evoked by voltage steps (blue) and by action potentials (green).

magnitude of inhibition of release by EGTA varies depending on the duration of $Ca^{2+}$ influx (**Figure 4H**). In addition to the two above-described $Ca^{2+}$ influx waveforms, I performed simulations using a $Ca^{2+}$ current step followed by tail $Ca^{2+}$ currents (**Supplementary Figure S1**). The spatial profile of the effects of EGTA on release also shifted depending on the duration of the $Ca^{2+}$ current step. Thus, the duration of $Ca^{2+}$ influx is a key determinant of the magnitude by which EGTA inhibits vesicular release (Nakamura et al., 2018).

## Duration of $Ca^{2+}$ Influx Alters the Spatial Profile of the EGTA Effect on Transmitter Release

To more systematically examine how the duration of channel opening influences the effect of EGTA, the step duration was varied from 0.1 to 30 ms. In this simulation, $[Ca^{2+}]_i$ transients evoked by brief steps were regarded as equivalent to those evoked by action potentials, whereas $[Ca^{2+}]_i$ transients evoked by longer influxes corresponded to voltage step-induced VGCC currents. ATP (0.2 mM) and the low-affinity EFB (4 mM) were included in this simulation. The peak $[Ca^{2+}]_i$ produced a spatiotemporal gradient (**Figure 5A**), but the spatial gradient (horizontal) was more apparent than the temporal gradient (vertical), especially for higher concentrations (>1 mM) of EGTA. This is because the steady-state $[Ca^{2+}]_i$ rapidly established in the presence of the buffer diminished the temporal gradient (see **Figure 1**). The gradients for the Pv values (**Figure 5B**) were less steep than those for $[Ca^{2+}]_i$, because the sensor saturation masked the $[Ca^{2+}]_i$ change at higher concentrations. The sensor saturation (shown as light green) covered the upper left corners of the graphs, in the proximity of the VGCC, and expanded along the temporal axis. An increase in the EGTA concentration decreased the Pv, especially at distal locations for long channel openings. By contrast, at close locations, EGTA minimally affected Pv.

To visualize the inhibitory effect of EGTA on release, I calculated the ratios of Pv (various concentrations of EGTA/control, **Figure 5C**). In the presence of 0.1 mM EGTA, most of the area was red colored, representing no effect of EGTA. A reduction in release was observed only at distal locations for longer channel openings. An increase in the EGTA concentration enlarged the blue area, representing complete inhibition of release. In the presence of 10 mM EGTA, the blue occupied the area from the distal end to 50 nm from the VGCC. On the contrary, the red area was restricted to the proximity of the VGCC (<50 nm) for long durations of channel opening (>20 ms). For very brief channel openings (<0.5 ms), the red area was further restricted to within 10 nm. In the intermediate area shown in the color gradient, EGTA partially inhibited vesicular release. As predicted, 10 mM BAPTA further inhibited the release.

In summary, EGTA inhibits vesicular release at locations distal from the VGCC for a wide range of channel open durations. At distances greater than 100 nm, EGTA completely diminishes the Pv, regardless of how long the channel is open. By contrast, the effect of EGTA in the vicinity of the channel critically depends on the time the channel is open; EGTA does not affect the Pv when the channel is open for a long time but decreases the Pv for brief openings. Thus, the duration of $Ca^{2+}$ influx critically determines the inhibitory effect of EGTA on neurotransmitter release.

# DISCUSSION

To precisely understand the effect of EGTA on the spatiotemporal gradients of $[Ca^{2+}]_i$ and vesicular release, I performed RDS of $[Ca^{2+}]_i$ transients following a single VGCC opening and simulations of vesicular release using a simplified version of the presynaptic terminal. RDS indicated that EGTA decreases $[Ca^{2+}]_i$ in the proximity of the channel (**Figure 1D**). Although this decrement in the $[Ca^{2+}]_i$ accounted for a minor fraction of the total $[Ca^{2+}]_i$, the subsequent release simulation suggested that EGTA decreases release, especially for a brief $Ca^{2+}$ influx, such as that evoked by action potentials (**Figures 4E–G**). Thus, EGTA can inhibit vesicular release, at least partially, in the nanodomain of VGCCs. The saturation of vesicular sensors near the VGCC accounts for the lack of an effect of EGTA on vesicular release. EGTA decreases $[Ca^{2+}]_i$ at all distances from the VGCC, but the $[Ca^{2+}]_i$ in the presence of EGTA is sufficient to saturate sensors close to the channel when the duration of $Ca^{2+}$ influx is long. In such cases, one cannot observe the decrease in $[Ca^{2+}]_i$ as a reduction in release. I propose that the property of the vesicular sensor and the $Ca^{2+}$ influx duration critically determine the inhibitory effect of EGTA on release. When interpreting the results from synaptic experiments showing an inhibition of vesicular transmitter release by EGTA, these biophysical parameters must be considered.

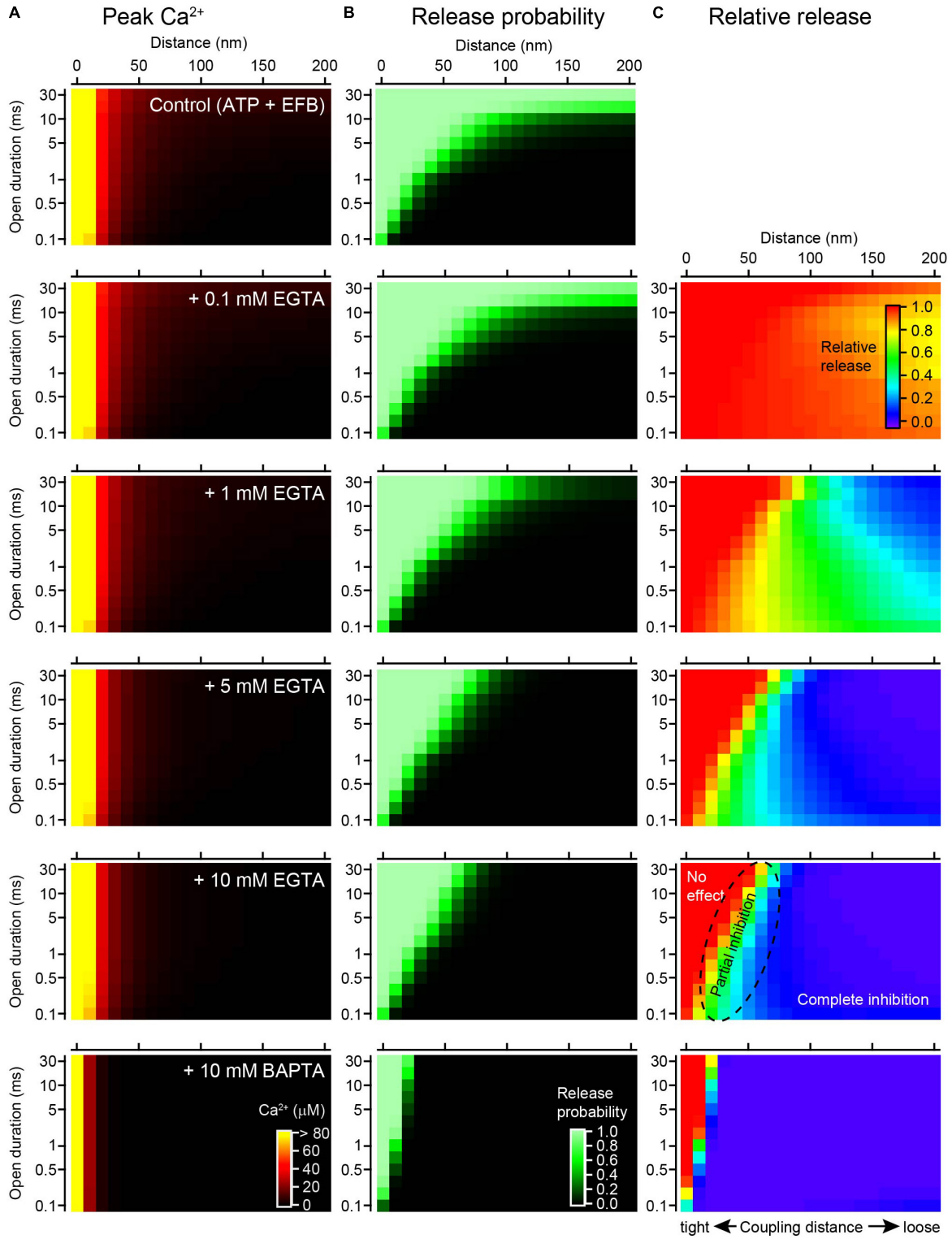


**FIGURE 5 |** Channel open duration affects the inhibitory effect of EGTA on vesicular release. **(A)** Spatiotemporal profiles of peak $[Ca^{2+}]_i$ in response to a single channel opening under the control condition (0.2 mM ATP + EFB) and with 0.1, 1, 5, and 10 mM EGTA and 10 mM BAPTA (from top to bottom). The amplitude of the single VGCC current was 0.3 pA. Note that $[Ca^{2+}]_i$ of >80 μM is colored yellow to magnify the concentration gradient near $K_D$ of the $Ca^{2+}$ sensor. **(B)** Spatiotemporal profiles of Pvs calculated from $Ca^{2+}$ transients in panel **(A)** using the five-site release model. **(C)** Spatiotemporal profiles of the inhibitory effect of various chelator concentrations of EGTA and 10 mM BAPTA on Pv. The graph for each chelator condition was calculated from the ratio of Pv in the chelator to that in the control.

## The Estimation of Coupling Distance Using EGTA in Combination With RDS

For more than two decades, EGTA has been widely tested in a variety of synapses to probe the coupling distance between VGCCs and vesicular $Ca^{2+}$ sensors. insights from analytical solutions including LBA (Naraghi and Neher, 1997), the lack of the EGTA effect on vesicular transmitter release has been explained by an the inaccessibility of EGTA to calcium ions in the proximity of the VGCC and is thus regarded as an indication of nanodomain coupling. On the contrary, the inhibition of vesicular release by EGTA is considered an indication of microdomain coupling (Augustine et al., 2003; Eggermann et al., 2012; Wang and Augustine, 2015; Bornschein and Schmidt, 2019). However, the discrimination of the nanodomain from the microdomain solely on the basis of the inhibitory effect of EGTA is less physiologically relevant, because the excessively buffered conditions achieved experimentally with exogenous chelators are artificial. In the unperturbed presynaptic terminal, the spatial extent of the $Ca^{2+}$ microdomain can be determined by the diffusion coefficient, and by the product of the concentrations and binding kinetics of the endogenous buffers (Eq. 3). With the assumption that buffer properties vary among cell types, the absolute length $\lambda$ is cell specific and can range from orders of nanometers to micrometers. Whether the vesicular $Ca^{2+}$ sensors are located within or beyond this $\lambda$ is more important because the effects of endogenous $Ca^{2+}$ buffers on Pv and short-term plasticity depend on the distance of the sensor from the VGCCs. In this context, the physical distance between vesicular $Ca^{2+}$ sensors and VGCCs (coupling distance) is important. EGTA should be used to measure the absolute distance rather than to discriminate nano/microdomains. The knowledge of the absolute distance would help to understand the complex molecular composition governing vesicular release.

Reaction diffusion simulation can provide valuable insights regarding the effect of EGTA on the spatial gradients of $[Ca^{2+}]_i$ around VGCCs. This simulation has several advantages, including the incorporation of the time course of $Ca^{2+}$ entry and the property of endogenous buffers, including EFBs. Moreover, by combining release simulations, we can incorporate the property of the vesicular sensor to estimate the effect of EGTA on release. In this study, I focused on the $Ca^{2+}$ microdomain formed around a single channel (single domain; Stanley, 2015). However, RDS can be used for the more complex geometry of presynaptic terminals, including for the distribution of VGCCs at the release site (Nakamura et al., 2015; Miki et al., 2018). As computer power has increased enormously, RDS has become less time consuming. EGTA and simulations together make a powerful diagnostic tool for estimating the coupling distance. **Figure 5C** provides useful insight into past and future experiments. In the following sections, I will review some of the previous synaptic experiments using EGTA and discuss how we can interpret them on the basis of the results from the present simulation study.

## No Inhibition

The lack of an effect of EGTA on neurotransmitter release has been reported for a variety of central synapses. Bath application of EGTA-AM has a negligible effect on the amplitude of excitatory postsynaptic currents (EPSCs) in climbing fiber-Purkinje synapses (Matsui and Jahr, 2003), granule cell-to-molecular layer interneuron synapses (Satake and Imoto, 2014), and mature cerebellar granule cell-to-Purkinje cell synapses (Schmidt et al., 2013; Baur et al., 2015). EGTA-AM also shows no effect on inhibitory postsynaptic currents (IPSCs) in synapses between molecular layer interneurons (Christie et al., 2011) or between hippocampal basket cells and granule cells (Hefft and Jonas, 2005). Unfortunately, as the cytosolic EGTA concentration is uncertain in these experiments using this membrane permeable derivative of EGTA, it is impossible to estimate the absolute coupling distance. However, because the duration of channel opening must be as brief as 0.5 ms for these action potential-evoked transmitter releases, the data are likely situated near the left bottom corners of the plots in **Figure 5C**. Thus, only a tight coupling between vesicular sensors and channels can account for the experimental observation that EGTA has no effect on release.

A lack of an effect with EGTA has also been reported for voltage step stimulation with longer channel openings. EGTA (5 mM) does not affect the fast release components for responses at cerebellar mossy fiber-granule synapses (Ritzau-Jost et al., 2014), Purkinje cell and granule cell terminals in culture (Kawaguchi and Sakaba, 2015, 2017), and the mature calyx of Held (Chen et al., 2015). A high concentration of EGTA also does not affect the fast release component of responses at auditory hair cell ribbon synapses (Moser and Beutner, 2000; Johnson et al., 2017) or retinal ribbon synapses (Singer and Diamond, 2003). These fast release components are thought to be mediated by vesicular sensors near the channels (Wadel et al., 2007; Chen et al., 2015) because the $[Ca^{2+}]_i$ at distal locations is not sufficient to trigger vesicular release under high-EGTA conditions (**Figure 1C**). In response to voltage step-induced long $Ca^{2+}$ influx, $Ca^{2+}$ sensors near the channels are likely to be saturated; thus EGTA effect cannot be seen as the reduction of release. The distance from the channel at which EGTA shows no inhibition can range from 0 to 50 nm depending on channel open duration.

The most famous example showing a lack of an effect of EGTA was at the squid giant synapse, in which ∼80 mM EGTA had no effect on transmitter release but BAPTA diminished it (Adler et al., 1991). Although this pioneer study opened the door to this field, the squid synapse is unique, such that a high concentration of EGTA had no effect on action potential-evoked, i.e., a brief $Ca^{2+}$ influx-induced, vesicular release. In mammalian synapses, EGTA is typically tested at concentrations ranging between 1 and 30 mM, and the high concentration (>10 mM) resulted in some inhibition of release. There are several possible reasons for the difference between squid and mammalian synapses. First, the forward binding of EGTA is slower in the squid synapse because of the lower temperature and higher ionic concentration. Thus, it is possible that the $[Ca^{2+}]_i$ gradient in the presence of EGTA in squid synapses is less steep than that in mammalian terminals. Second, the time course of $Ca^{2+}$ entry during a presynaptic action potential (∼1 ms; Llinás et al., 1981) is longer than that in typical mammalian synapses (Borst and Sakmann, 1998; Bischofberger et al., 2002; Ritzau-Jost et al., 2014; Nakamura et al., 2015),

increasing the time window for the lack of an observed effect of EGTA. Third, the higher external [$Ca^{2+}$] causes a larger single channel current, enhancing the saturation of sensors. All these factors might contribute to the reduced effect of EGTA at the squid synapse. Although Adler et al. (1991) accounted for these factors and adjusted the EGTA parameters, these biophysical parameters in the squid should be investigated further.

## Complete Inhibition

Our simulations indicate that complete inhibition of release by EGTA is robust evidence for "microdomain" coupling. If the sensor is located beyond 100 nm from a channel, EGTA completely inhibits vesicular release regardless of how long the channel is open (**Figure 5C**). However, complete inhibition of action potential-induced vesicular release by EGTA has not been reported, at least for the first pulse of evoked synchronous release. This is partly because an action potential-evoked brief $Ca^{2+}$ influx thorough single VGCC hardly induce detectable Pv at distal locations from the channel (**Figure 5B**; Stanley, 2015). For synchronous release, EGTA most often exhibits no effect or partial inhibition. Complete inhibition by EGTA was demonstrated for delayed release at cerebellar granule cell-to-stellate cell synapses (Atluri and Regehr, 1998), and asynchronous release at autaptic hippocampal synapses (Otsu et al., 2004) and retinal ribbon synapses (Singer and Diamond, 2003). Although there is debate regarding the origins, pools, and sensors for these different release modes (Schneggenburger and Rosenmund, 2015), it is interesting to examine whether asynchronous release might occur at more distal locations relative to synchronous release. The 5-site release model (Schneggenburger and Neher, 2000; Kochubey et al., 2009) used in the present study encompasses the $[Ca^{2+}]_i$ range for synchronous release. To investigate the coupling distance for asynchronous, delayed, and spontaneous release, other $Ca^{2+}$ sensor models incorporating low $[Ca^{2+}]_i$ (Lou et al., 2005) might be more useful. Nevertheless, the comparison of BAPTA and EGTA provides clues on the coupling distance for spontaneous release (Goswami et al., 2012; Williams et al., 2012).

## Partial Inhibition

At most central synapses, high concentrations of EGTA partially inhibit vesicular release. This experimental observation and its underlying mechanism should be interpreted with caution because the coupling distance generating partial inhibition ranges several tens of nanometers (**Figure 5C**), covering nanodomain to microdomain distances (depending on the definitions). In response to a long voltage step, vesicular release has fast and slow release components. Although the fast component is insensitive to EGTA, 5–20 mM EGTA reduces the slow component at cerebellar mossy fiber-granule synapses (Ritzau-Jost et al., 2014), the mature calyx of Held (Chen et al., 2015), and hair cell ribbon synapses (Moser and Beutner, 2000; Johnson et al., 2017). The slow components might use different $Ca^{2+}$ sensors (Wölfel et al., 2007), but could be explained by release from locations distal from the channel (Wadel et al., 2007) because 20 mM EGTA preferentially blocks vesicular release at $>50$ nm (Chen et al., 2015). Thus, for experiments using long voltage steps, a high concentration of EGTA dissects the location of vesicular release and can be used as a diagnostic tool to discriminate nanodomain and microdomain coupling distances.

Partial inhibition by EGTA has also been reported for action potential-evoked release. The first example reported in a central synapse was for the calyx of Held, in which presynaptic loading with 10 mM EGTA from a patch pipette reduced action potential-evoked release (Borst and Sakmann, 1996). Although the effect of EGTA becomes smaller throughout postnatal development, EGTA inhibits EPSCs by 22–69% (Fedchyshyn and Wang, 2005; Nakamura et al., 2015). At synapses between layer 2/3 pyramidal neurons and interneurons, the EPSC is reduced by dialyzing millimolar concentrations of EGTA into the presynaptic pyramidal neuron (Rozov et al., 2001). In hippocampal autaptic synapses, EGTA-AM reduces EPSCs by 20% (Otsu et al., 2004). IPSCs at hippocampal basket cell-to-granule cell synapses are reduced by injecting the presynaptic cell with 30 mM EGTA (Bucurenciu et al., 2008). Similarly, 10–30 mM EGTA reduces IPSCs at cerebellar basket cell-Purkinje cell synapses (Arai and Jonas, 2014). The inhibitory effect of EGTA on postsynaptic currents was originally thought to indicate loose "microdomain" coupling, but more recent simulations indicate that the coupling distance ranges from 10 to 20 nm in these inhibitory terminals (Bucurenciu et al., 2008; Arai and Jonas, 2014) and from 10 to 40 nm in the calyx depending on the developmental stage (Nakamura et al., 2015). Direct patch clamp recordings from the calyx revealed that the half duration of $Ca^{2+}$ influx during an action potential is 0.36 ms (Borst and Sakmann, 1998). This brief $Ca^{2+}$ influx prevents the sensor from becoming saturated; thus the reduction in presynaptic $[Ca^{2+}]_i$ by EGTA immediately affects vesicular release. Indeed, it was shown that $Ca^{2+}$ sensors are not saturated at these synapses because higher external [$Ca^{2+}$] increases Pv (Bucurenciu et al., 2008; Koike-Tani et al., 2008). As with these studies, the possibility of sensor saturation should be always examined at the synapse. Presynaptic $Ca^{2+}$ uncaging experiments can also provide information on vesicular $Ca^{2+}$ sensors (Schneggenburger and Neher, 2000).

A robust inhibitory effect of EGTA was also reported for the hippocampal mossy fiber-CA3 pyramidal cell synapse, in which 10 mM EGTA reduces EPSCs to merely 8% (Vyleta and Jonas, 2014). Combined with the BAPTA experiments, the coupling distance is estimated at ∼70 nm. Whether this loose coupling can be classified as "microdomain" distance depends on the definition and on the number of $Ca^{2+}$ channels triggering release (Bornschein and Schmidt, 2019). As the duration of $Ca^{2+}$ influx during an action potential is short (0.58 ms; Bischofberger et al., 2002), the coupling distance at this synapse can be determined via plots, as in **Figure 5C**.

# CONCLUSION

The present study sheds light on two points that have received little attention: the slow $Ca^{2+}$ chelator EGTA can access $Ca^{2+}$

ions to decrease $[Ca^{2+}]_i$ in the proximity of a channel, and the saturation of the vesicular sensor masks the effect of EGTA on vesicular release. When $Ca^{2+}$ influx is triggered by an action potential, a small reduction of $[Ca^{2+}]_i$ by EGTA causes an immediate reduction of vesicular release because the vesicular $Ca^{2+}$ sensor is in a linear range. Thus, the experimental observation that EGTA inhibits synaptic transmission alone does not directly indicate that the coupling is within the microdomain. A more accurate interpretation requires the consideration of additional biophysical parameters, of which, the most important is the duration of $Ca^{2+}$ influx.

## DATA AVAILABILITY STATEMENT

All datasets generated for this study are included in the manuscript/**Supplementary Files**.

## AUTHOR CONTRIBUTIONS

YN conceived the research, performed the simulation, wrote the manuscript, and prepared the figures.

## FUNDING

This work was supported by the Japan Society for the Promotion of Science (KAKENHI Grant JP17K07064) and the Takeda Science Foundation.

## ACKNOWLEDGMENTS

The author thanks Jason Rothman for developing D3D simulator and Taro Ishikawa for critical reading of the manuscript.

## SUPPLEMENTARY MATERIAL

The Supplementary Material for this article can be found online at: https://www.frontiersin.org/articles/10.3389/fnsyn.2019.00026/full#supplementary-material

**FIGURE S1 |** The effect of tail $Ca^{2+}$ currents on $[Ca^{2+}]_i$ and release simulations. **(A)** Top, $Ca^{2+}$ current waveforms used in this simulation consisted of steady step current (0.15 pA) and subsequent tail current. Durations of step currents varied from 0.5 to 5 ms. The peak amplitude of the tail current was 0.3 pA, which decayed exponentially with the fast (0.2 ms, 90%) and slow (1.0 ms, 10%) time constants. Middle, $[Ca^{2+}]_i$ transients at a 20 nm distance in the control (0.2 mM ATP and EFB, solid line) and in the presence of 10 mM EGTA (dashed line). The tail current additionally increased $[Ca^{2+}]_i$ upon the steady-state $[Ca^{2+}]_i$ induced by the preceding step current. Bottom, cumulative release probability. Pv increased with the duration of the step. **(B)** Spatial profiles of Pvs evoked using $Ca^{2+}$ current with tail current in the control and in the presence of EGTA. **(C)** Spatial profiles of the inhibitory effect of EGTA on release. Spatial profile shifted with the increase in step duration. **(D–F)** Same as **(A–C)** but without tail current. When the duration of step component was sufficiently long (e.g., 5 ms, red traces), the spatial profiles of Pv **(B,E)** and the effect of EGTA on release **(C,F)** showed similar distributions, because Pv and the effect of EGTA were exclusively determined by the $[Ca^{2+}]_i$ increase during the step. By contrast, when the step duration was shorter (e.g., 0.5 ms, blue traces), the tail current additionally elevated Pv, and the effect of EGTA decreased. **(G)** For comparison, release rate traces under the control condition for 0.5 and 5 ms steps with/without tail current are shown. This simulation indicates that the tail current significantly contributes only when the channel is open for a short time. It should be noted that an action potential-induced brief $Ca^{2+}$ current is mostly mediated by a tail component.

## REFERENCES

Adler, E. M., Augustine, G. J., Duffy, S. N., and Charlton, M. P. (1991). Alien intracellular calcium chelators attenuate neurotransmitter release at the squid giant synapse. *J. Neurosci.* 11, 1496–1507. doi: 10.1523/jneurosci.11-06-01496.1991

Ait-Haddou, R., Kurachi, Y., and Nomura, T. (2010). On calcium–buffer dynamics within the excess buffer regime. *J. Theor. Biol.* 264, 55–65. doi: 10.1016/j.jtbi.2010.01.017

Allbritton, N. L., Meyer, T., and Stryer, L. (1992). Range of messenger action of calcium ion and inositol 1,4,5- trisphosphate. *Science* 258, 1812–1815. doi: 10.1126/science.1465619

Arai, I., and Jonas, P. (2014). Nanodomain coupling explains Ca2+ independence of transmitter release time course at a fast central synapse. *eLife* 3:e04057. doi: 10.7554/eLife.04057

Atluri, P. P., and Regehr, W. G. (1998). Delayed release of neurotransmitter from cerebellar granule cells. *J. Neurosci.* 18, 8214–8227. doi: 10.1523/jneurosci.18-20-08214.1998

Augustine, G. J., Santamaria, F., and Tanaka, K. (2003). Local calcium signaling in neurons. *Neuron* 40, 331–346. doi: 10.1016/s0896-6273(03)00639-1

Baur, D., Bornschein, G., Althof, D., Watanabe, M., Kulik, Á, Eilers, J., et al. (2015). Developmental tightening of cerebellar cortical synaptic influx-release coupling. *J. Neurosci.* 35, 1858–1871. doi: 10.1523/JNEUROSCI.2900-14.2015

Baylor, S. M., and Hollingworth, S. (1998). Model of sarcomeric Ca2+ movements, including ATP Ca2+ binding and diffusion, during activation of frog skeletal muscle. *J. Gen. Physiol.* 112, 297–316. doi: 10.1085/jgp.112.3.297

Bischofberger, J., Geiger, J. R. P., and Jonas, P. (2002). Timing and efficacy of Ca2+ channel activation in hippocampal mossy fiber boutons. *J. Neurosci.* 22, 10593–10602. doi: 10.1523/jneurosci.22-24-10593.2002

Bornschein, G., and Schmidt, H. (2019). Synaptotagmin Ca2+ sensors and their spatial coupling to presynaptic Cav channels in central cortical synapses. *Front. Mol. Neurosci.* 11:494. doi: 10.3389/fnmol.2018.00494

Borst, J. G. G., Helmchen, F., and Sakmann, B. (1995). Pre- and postsynaptic whole-cell recordings in the medial nucleus of the trapezoid body of the rat. *J. Physiol.* 489, 825–840. doi: 10.1113/jphysiol.1995.sp021095

Borst, J. G. G., and Sakmann, B. (1996). Calcium influx and transmitter release in a fast CNS synapse. *Nature* 383, 431–434. doi: 10.1038/383431a0

Borst, J. G. G., and Sakmann, B. (1998). Calcium current during a single action potential in a large presynaptic terminal of the rat brainstem. *J. Physiol.* 506, 143–157. doi: 10.1111/j.1469-7793.1998.143bx.x

Bucurenciu, I., Kulik, Á, Schwaller, B., Frotscher, M., and Jonas, P. (2008). Nanodomain coupling between Ca2+ channels and Ca2+ sensors promotes fast and efficient transmitter release at a cortical GABAergic synapse. *Neuron* 57, 536–545. doi: 10.1016/j.neuron.2007.12.026

Chad, J. E., and Eckert, R. (1984). Calcium domains associated with individual channels can account for anomalous voltage relations of Ca-dependent responses. *Biophys. J.* 45, 993–999. doi: 10.1016/s0006-3495(84)84244-7

Chen, Z., Das, B., Nakamura, Y., DiGregorio, D. A., and Young, S. M. (2015). Ca2+ channel to synaptic vesicle distance accounts for the readily releasable pool kinetics at a functionally mature auditory synapse. *J. Neurosci.* 35, 2083–2100. doi: 10.1523/JNEUROSCI.2753-14.2015

Christie, J. M., Chiu, D. N., and Jahr, C. E. (2011). Ca2+-dependent enhancement of release by subthreshold somatic depolarization. *Nat. Neurosci.* 14, 62–68. doi: 10.1038/nn.2718

Delvendahl, I., Jablonski, L., Baade, C., Matveev, V., Neher, E., and Hallermann, S. (2015). Reduced endogenous Ca2+ buffering speeds active zone Ca2+ signaling. *Proc. Natl. Acad. Sci. U.S.A.* 112, E3075–E3084. doi: 10.1073/pnas.1508419112

DiGregorio, D. A., Peskoff, A., and Vergara, J. L. (1999). Measurement of action potential-induced presynaptic calcium domains at a cultured neuromuscular junction. *J. Neurosci.* 19, 7846–7859. doi: 10.1523/jneurosci.19-18-07846.1999

Eggermann, E., Bucurenciu, I., Goswami, S. P., and Jonas, P. (2012). Nanodomain coupling between Ca2+ channels and sensors of exocytosis at fast mammalian synapses. *Nat. Rev. Neurosci.* 13, 7–21. doi: 10.1038/nrn3125

Fedchyshyn, M. J., and Wang, L. Y. (2005). Developmental transformation of the release modality at the calyx of Held synapse. *J. Neurosci.* 25, 4131–4140. doi: 10.1523/jneurosci.0350-05.2005

Fogelson, A. L., and Zucker, R. S. (1985). Presynaptic calcium diffusion from various arrays of single channels. implications for transmitter release and synaptic facilitation. *Biophysics* 48, 1003–1017. doi: 10.1016/s0006-3495(85)83863-7

Goswami, S. P., Bucurenciu, I., and Jonas, P. (2012). Miniature IPSCs in hippocampal granule cells are triggered by voltage-gated Ca2+ channels via microdomain coupling. *J. Neurosci.* 32, 14294–14304. doi: 10.1523/JNEUROSCI.6104-11.2012

Hefft, S., and Jonas, P. (2005). Asynchronous GABA release generates long-lasting inhibition at a hippocampal interneuron–principal neuron synapse. *Nat. Neurosci.* 8, 1319–1328. doi: 10.1038/nn1542

Helmchen, F., Borst, J. G. G., and Sakmann, B. (1997). Calcium dynamics associated with a single action potential in a CNS presynaptic terminal. *Biophys. J.* 72, 1458–1471. doi: 10.1016/s0006-3495(97)78792-7

Johnson, S. L., Olt, J., Cho, S., von Gersdorff, H., and Marcotti, W. (2017). The coupling between Ca2+ channels and the exocytotic Ca2+ sensor at hair cell ribbon synapses varies tonotopically along the mature cochlea. *J. Neurosci.* 37, 2471–2484. doi: 10.1523/JNEUROSCI.2867-16.2017

Katz, B. (1969). *The Release of Neural Transmitter Substances*. Springfield, IL: Charles C. Thomas.

Kawaguchi, S. Y., and Sakaba, T. (2015). Control of inhibitory synaptic outputs by low excitability of axon terminals revealed by direct recording. *Neuron* 85, 1273–1288. doi: 10.1016/j.neuron.2015.02.013

Kawaguchi, S. Y., and Sakaba, T. (2017). Fast Ca2+ buffer-dependent reliable but plastic transmission at small CNS synapses revealed by direct bouton recording. *Cell Rep.* 21, 3338–3345. doi: 10.1016/j.celrep.2017.11.072

Kochubey, O., Han, Y., and Schneggenburger, R. (2009). Developmental regulation of the intracellular Ca2+ sensitivity of vesicle fusion and Ca2+-secretion coupling at the rat calyx of Held. *J. Physiol.* 587, 3009–3023. doi: 10.1113/jphysiol.2009.172387

Koike-Tani, M., Kanda, T., Saitoh, N., Yamashita, T., and Takahashi, T. (2008). Involvement of AMPA receptor desensitization in short-term synaptic depression at the calyx of Held in developing rats. *J. Physiol.* 586, 2263–2275. doi: 10.1113/jphysiol.2007.142547

Llinás, R., Steinberg, I. Z., and Walton, K. (1981). Presynaptic calcium currents in squid giant synapse. *Biophys. J.* 33, 289–321. doi: 10.1016/s0006-3495(81)84898-9

Llinás, R., Sugimori, R., and Silver, R. B. (1992). Microdomains of high calcium concentration in a presynaptic terminal. *Science* 256, 677–679. doi: 10.1126/science.1350109

Lou, X., Scheuss, V., and Schneggenburger, R. (2005). Allosteric modulation of the presynaptic Ca2+ sensor for vesicle fusion. *Nature* 435, 497–501. doi: 10.1038/nature03568

Matsui, K., and Jahr, C. E. (2003). Ectopic release of synaptic vesicles. *Neuron* 40, 1173–1183. doi: 10.1016/s0896-6273(03)00788-8

Meinrenken, C. J., Borst, J. G. G., and Sakmann, B. (2002). Calcium secretion coupling at calyx of Held governed by nonuniform channel-vesicle topography. *J. Neurosci.* 22, 1648–1667. doi: 10.1523/jneurosci.22-05-01648.2002

Miki, T., Nakamura, Y., Malagon, G., Neher, E., and Marty, A. (2018). Two-component latency distributions indicate two-step vesicular release at simple glutamatergic synapses. *Nat Commun.* 9:3943. doi: 10.1038/s41467-018-06336-5

Moser, T., and Beutner, D. (2000). Kinetics of exocytosis and endocytosis at the cochlear inner hair cell afferent synapse of the mouse. *Proc. Natl. Acad. Sci. U.S.A.* 97, 883–888. doi: 10.1073/pnas.97.2.883

Nägerl, U. V., Novo, D., Mody, I., and Vergara, J. L. (2000). Binding kinetics of calbindin-D(28k) determined by flash photolysis of caged Ca2+. *Biophys. J.* 79, 3009–3018. doi: 10.1016/s0006-3495(00)76537-4

Nakamura, Y., Harada, H., Kamasawa, N., Matsui, K., Rothman, J. S., Shigemoto, R., et al. (2015). Nanoscale distribution of presynaptic Ca2+ channels and its impact on vesicular release during development. *Neuron* 85, 145–158. doi: 10.1016/j.neuron.2014.11.019

Nakamura, Y., Reva, M., and DiGregorio, D. A. (2018). Variations in Ca2+ influx can alter chelator-based estimates of Ca2+ channel-synaptic vesicle coupling distance. *J. Neurosci.* 38, 3971–3987. doi: 10.1523/JNEUROSCI.2061-17.2018

Naraghi, M., and Neher, E. (1997). Linearized buffered Ca2+ diffusion in microdomains and its implications for calculation of [Ca2+] at the mouth of a calcium channel. *J. Neurosci.* 17, 6961–6973. doi: 10.1523/jneurosci.17-18-06961.1997

Neher, E. (1986). Concentration profiles of intracellular calcium in the presence of a diffusible chelator. *Exp. Brain Res.* 14, 80–96. doi: 10.1007/978-3-642-70744-5_8

Neher, E. (1998a). Usefulness and limitations of linear approximations to the understanding of Ca++ signals. *Cell Calcium* 24, 345–357. doi: 10.1016/s0143-4160(98)90058-6

Neher, E. (1998b). Vesicle pools and Ca2+ microdomains: new tools for understanding their roles in neurotransmitter release. *Neuron* 20, 389–399. doi: 10.1016/s0896-6273(00)80983-6

Neher, E., and Taschenberger, H. (2013). Transients in global Ca2+ concentration induced by electrical activity in a giant nerve terminal. *J. Physiol.* 591, 3189–3195. doi: 10.1113/jphysiol.2012.248617

Otsu, Y., Shahrezaei, V., Li, B., Raymond, L. A., Delaney, K. R., and Murphy, T. H. (2004). Competition between phasic and asynchronous release for recovered synaptic vesicles at developing hippocampal autaptic synapses. *J. Neurosci.* 24, 420–433. doi: 10.1523/jneurosci.4452-03.2004

Ritzau-Jost, A., Delvendahl, I., Rings, A., Byczkowicz, N., Harada, H., Shigemoto, R., et al. (2014). Ultrafast action potentials mediate kilohertz signaling at a central synapse. *Neuron* 84, 152–163. doi: 10.1016/j.neuron.2014.08.036

Rothman, J. S., and Silver, R. A. (2018). NeuroMatic: an Integrated open-source software toolkit for acquisition, analysis and simulation of electrophysiological data. *Front. Neuroinform.* 12:14. doi: 10.3389/fninf.2018.00014

Rozov, A., Burnashev, N., Sakmann, B., and Neher, E. (2001). Transmitter release modulation by intracellular Ca2+ buffers in facilitating and depressing nerve terminals of pyramidal cells in layer 2/3 of the rat neocortex indicates a target cell-specific difference in presynaptic calcium dynamics. *J. Physiol.* 531, 807–826. doi: 10.1111/j.1469-7793.2001.0807h.x

Satake, S., and Imoto, K. (2014). Cav2.1 channels control multivesicular release by relying on their distance from exocytotic *Ca*2+ sensors at rat cerebellar granule cells. *J. Neurosci.* 34, 1462–1474. doi: 10.1523/JNEUROSCI.2388-13.2014

Schmidt, H., Brachtendorf, S., Arendt, O., Hallermann, S., Ishiyama, S., Bornschein, G., et al. (2013). Nanodomain coupling at an excitatory cortical synapse. *Curr. Biol.* 23, 244–249. doi: 10.1016/j.cub.2012.12.007

Schneggenburger, R., and Neher, E. (2000). Intracellular calcium dependence of transmitter release rates at a fast central synapse. *Nature* 406, 889–893. doi: 10.1038/35022702

Schneggenburger, R., and Rosenmund, C. (2015). Molecular mechanisms governing Ca2+ regulation of evoked and spontaneous release. *Nat. Neurosci.* 18, 935–941. doi: 10.1038/nn.4044

Schwaller, B. (2010). Cytosolic Ca2+ buffers. *Cold Spring Harb. Perspect. Biol.* 2:a004051. doi: 10.1101/cshperspect.a004051

Sheng, J., He, L., Zheng, H., Xue, L., Luo, F., Shin, W., et al. (2012). Calcium-channel number critically influences synaptic strength and plasticity at the active zone. *Nat. Neurosci.* 15, 998–1006. doi: 10.1038/nn.3129

Singer, J. H., and Diamond, J. S. (2003). Sustained Ca2+ entry elicits transient postsynaptic currents at a retinal ribbon synapse. *J. Neurosci.* 23, 10923–10933. doi: 10.1523/jneurosci.23-34-10923.2003

Stanley, E. (2015). Single calcium channel domain gating of synaptic vesicle fusion at fast synapses; analysis by graphic modeling. *Channels* 9, 324–333. doi: 10.1080/19336950.2015.1098793

Stern, M. D. (1992). Buffering of calcium in the vicinity of a channel pore. *Cell Calcium* 13, 183–192. doi: 10.1016/0143-4160(92)90046-u

Vyleta, N. P., and Jonas, P. (2014). Loose coupling between Ca2+ channels and release sensors at a plastic hippocampal synapse. *Science* 347, 665–670. doi: 10.1126/science.1244811

Wadel, K., Neher, E., and Sakaba, T. (2007). The coupling between synaptic vesicles and Ca2+ channels determines fast neurotransmitter release. *Neuron* 53, 563–575. doi: 10.1016/j.neuron.2007.01.021

Wang, L. Y., and Augustine, G. J. (2015). Presynaptic nanodomains: a tale of two synapses. *Front. Cell Neurosci.* 8:455. doi: 10.3389/fncel.2014.00455

Weber, A. M., Wong, F. K., Tufford, A. R., Schlichter, L. C., Matveev, V., and Stanley, E. F. (2010). N-type Ca2+ channels carry the largest current: implications for nanodomains and transmitter release. *Nat. Neurosci.* 13, 1348–1350. doi: 10.1038/nn.2657

Williams, C., Chen, W., Lee, C. H., Yaeger, D., Vyleta, N. P., and Smith, S. M. (2012). Coactivation of multiple tightly coupled calcium channels triggers spontaneous release of GABA. *Nat. Neurosci.* 15, 1195–1197. doi: 10.1038/nn.3162

Wölfel, M., Lou, X., and Schneggenburger, R. (2007). A mechanism intrinsic to the vesicle fusion machinery determines fast and slow transmitter release at a large CNS synapse. *J. Neurosci.* 27, 3198–3210. doi: 10.1523/jneurosci.4471-06.2007

Xu, T., Naraghi, M., Kang, H., and Neher, E. (1997). Kinetic studies of $Ca^{2+}$ binding and $Ca^{2+}$ clearance in the cytosol of adrenal chromaffin cells. *Biophys. J.* 73, 532–545. doi: 10.1016/s0006-3495(97)78091-3

**Conflict of Interest:** The author declares that the research was conducted in the absence of any commercial or financial relationships that could be construed as a potential conflict of interest.

*Copyright © 2019 Nakamura. This is an open-access article distributed under the terms of the Creative Commons Attribution License (CC BY). The use, distribution or reproduction in other forums is permitted, provided the original author(s) and the copyright owner(s) are credited and that the original publication in this journal is cited, in accordance with accepted academic practice. No use, distribution or reproduction is permitted which does not comply with these terms.*

# Advantages of publishing in Frontiers

**OPEN ACCESS**
Articles are free to read for greatest visibility and readership

**FAST PUBLICATION**
Around 90 days from submission to decision

**HIGH QUALITY PEER-REVIEW**
Rigorous, collaborative, and constructive peer-review

**TRANSPARENT PEER-REVIEW**
Editors and reviewers acknowledged by name on published articles

**Frontiers**
Avenue du Tribunal-Fédéral 34
1005 Lausanne | Switzerland

**Visit us:** www.frontiersin.org
**Contact us:** info@frontiersin.org | +41 21 510 17 00

**REPRODUCIBILITY OF RESEARCH**
Support open data and methods to enhance research reproducibility

**DIGITAL PUBLISHING**
Articles designed for optimal readership across devices

**FOLLOW US**
@frontiersin

**IMPACT METRICS**
Advanced article metrics track visibility across digital media

**EXTENSIVE PROMOTION**
Marketing and promotion of impactful research

**LOOP RESEARCH NETWORK**
Our network increases your article's readership